ANTI-CORROSION PROPERTIES OF A NON-CHROMATE CONVERSION COATING FOR AEROSPACE ALUMINUM ALLOYS – PERFORMANCE OPTIMISATION AND EARLY STAGE FAILURE MECHANISMS

By

Shruthi Tiruchirapalli Kumar Raj

A DISSERTATION

Submitted to
Michigan State University
in partial fulfilment of the requirements
for the degree of

Chemistry - Doctor of Philosophy

2020

ABSTRACT

ANTI-CORROSION PROPERTIES OF A NON-CHROMATE CONVERSION COATING FOR AEROSPACE ALUMINUM ALLOYS – PERFORMANCE OPTIMISATION AND EARLY STAGE FAILURE MECHANISMS.

By

Shruthi Tiruchirapalli Kumar Raj

The aerospace industry uses a variety of metal alloys as structural components in aircraft. Corrosion and degradation of these metals in service is typically inhibited using a multi-layer coating system (conversion coating + primer + topcoat). Historically used conversion coatings and primers contain Cr(VI) as the active corrosion inhibitor. Due to human health and environmental concerns, there is a world-wide effort to eliminate chromate from use and to replace these coatings with more environment-friendly and equally-as-effective coatings. The trivalent chromium process (TCP) conversion coating is the leading replacement candidate. A challenge with implementing this conversion coating for protecting high Cu aluminum alloys is that it is not as good as the legacy chromate coatings for reasons that remain poorly understood. In this dissertation project, fundamental research was conducted to better understand how to improve the anti-corrosion properties of TCP on AA2024-T3, a high Cu containing aerospace alloy.

A focus was on understanding system-level interactions between the coating and alloy surface, and how it correlates with early-stage failure of alloys. The overall objective of this dissertation project was to improve the corrosion performance of TCP conversion coatings through:

(i) process parameter optimization

(ii) a better understanding of early-stage failure mechanisms, specifically, the sites where alloy corrosion initiates and the coating composition and structure on and around these sites.

The final chapters of this dissertation also focus on the use of TCP as a sealant for surface modified (anodized) AA2024-T3 and compare the effectiveness of a TCP seal against other industrially used sealing methods.

ACKNOWLEDGEMENTS

I would like to acknowledge the support and contributions received from the following colleagues, family and friends in completing this dissertation.

Thanks to Prof. Greg Swain for his continued academic and emotional support throughout these years. His academic expertise and words of wisdom helped me get through challenging times during my PhD journey. Without his consistent help and guidance, this dissertation would not have been possible. I could not have asked for a better mentor to guide me through this wonderful learning experience.

I would also like to thank my committee members Dr. Gary Blanchard, Dr. Thomas Hamann, and Dr. Carl Boehlert for their professional guidance, which has helped me motivate myself and helped transform me into a better researcher.

My sincere thanks to my group members Jack Walton, Sarah McFall-Boegeman, Fatemeh Parvis, Dr. Catherine Munson, Brandon Whitman and all other current and former members of Dr. Swain's lab for their valuable research insights and for maintaining a pleasant working atmosphere.

I thank all members of the CAM facility and Per Askeland from the Material Characterization Facility in the College of Engineering for providing guidance, training and expertise with the scanning electron microscopy and the x-ray photoelectron spectroscopy measurements.

Finally, I would like to thank my family and friends who always believed in me and encouraged my decision to pursue a Ph.D. Thanks to my friends, Vijay Pandian, Dr. Satish Kumar, Kamalambika Muthukumar and Ashwin Ramanujam for their emotional support during challenging times and for continuously inspiring me to succeed in life.

Thanks to the Office of Naval Research, CHEMEON Surface Technology, and Henkel Technologies for providing financial support to conduct this dissertation research.

TABLE OF CONTENTS

LIST OF TABLES

LIST OF FIGURES

KEY TO ABBREVIATIONS

AA	Aluminum alloy
DI	Deionized
SHE	Standard Hydrogen Electrode
TCP	Trivalent chrome process
CCC	Chromate conversion coating
OCP	Open circuit potential
E_{pit}	Pitting potential
APC	Anodic polarisation curve
CPC	Cathodic polarization curve
IMP	Intermetallic particle
R_p	Polarisation resistance
EIS	Electrochemical impedance spectroscopy
RDE	Rotating disk electrode
ORR	Oxygen reduction reaction
SEM	Scanning electron microscope
FIB	Focused ion beam
XPS	X-ray photoelectron spectroscopy
NSS	Neutral salt spray
TLM	Thin layer mist
RT	Room temperature
DCFH-DA	2’,7’-dichlorohydrofluorescein diacetate

DCF	dichlorofluorescein
Na_2SO_4	Sodium sulfate
NaCl	Sodium chloride
H_2O_2	Hydrogen peroxide
NiAc	Nickel acetate
HW	Hot water

CHAPTER 1. INTRODUCTION, LITERATURE REVIEW & MOTIVATIONS FOR STUDY

1.1 ALUMINUM

Aluminum offers a wide range of favorable properties such as high strength-to-weight ratio, easy of workability, high fracture toughness and low cost, which permits the design and manufacture of strong, lightweight structural components.[1–4] When appropriately treated and alloyed, the mechanical properties of aluminum can be significantly improved - making it a useful structural material for aircrafts and space vehicles.[2,3] Aluminum is used in the manufacture aircraft components such as engines, frames, fuselage, accessories, and tankage.[5] Although aluminum is a highly reactive metal, it has high corrosion resistance due to a naturally occurring protective surface oxide layer. Unlike other metals, such as steel, that continuously oxidise to form rust, aluminum oxide possesses self-healing properties that resist progressive oxidation of the metal.[6]

1.2 ALUMINUM ALLOYS: NOMENCLATURE, PROPERTIES & APPLICATIONS

Aluminum is generally alloyed with other metals to enhance its properties and usefulness.[1–4,7] The properties of these alloys, depend on their non-aluminum elemental composition, the distribution of these second-phase particles, and the microstructure. Copper, magnesium, manganese, zinc and silicon are some of the major alloying elements used.[1,7] The Aluminum Association uses a four-digit system to classify Al alloys based on their composition. The International Alloy Designation System (IADS) gives a four-digit number for each wrought alloy based on the principal alloying element. The first digit denotes the principal alloying element. The second digit indicates the modifications made to the alloy. The third and fourth digits serve little meaning and are used primarily to identify the alloy within the series. In addition to the four- digit nomenclature, a temper nomenclature was also adopted by the IADS to identify the type of heat

treatment the alloy was subjected to achieve certain mechanical properties. Heat treated alloys are designated with a letter 'T' followed by a digit to identify the series of thermal treatment processes performed during the alloy manufacturing process. For example: For AA2024-T3 alloy, 2 denotes that Cu is the primary alloying element, 0 indicates that the alloy was not subjected to any further modifications, 24 helps identify the alloy in the 2xxx series, T denotes that the alloy was heat treated during manufacturing and 3 denotes that the alloy was heat treated, cold worked and naturally aged.[2] Table 1.1 summarizes the different classes of alloys, principal alloying elements and common industrial applications.

Table 1.1 Classification of aluminum alloys based on principal alloying elements.

Alloy type	**Principle alloying element**	**Application**
1xxx	Pure Al	Electrical and chemical industries
2xxx	Cu	Aerospace industry
3xxx	Mn	Architectural industry
4xxx	Si	Welding industry
5xxx	Mg	Marine industry
6XXX	Mg and Si	Architectural and Automotive industry
7xxx	Zn	Aerospace industry
8xxx	Ti, Li and/or Fe	Miscellaneous applications

Of the different alloy classes, the 2xxx and 7xxx series Al alloys are widely used in the aerospace sector due to their high yield strength while manufacturing stressed aircraft components.[8,9] Although alloying provides improved mechanical properties, a reduction in

corrosion resistance and increased susceptibility to pitting corrosion, stress corrosion cracking and intergranular corrosion is often observed.[4]

1.3 CORROSION OF ALUMINUM AND ALUMINUM ALLOYS

Aluminum is a thermodynamically reactive metal with a standard oxidation potential of -1.7 V vs SHE. It reacts spontaneously with atmospheric oxygen to form a thin passivating oxide layer. This surface oxide bonded to the metal surface is self-healing and protects the metal from further oxidation. Thus, aluminum is naturally corrosion resistant. Under conditions when self-repair of the oxide cannot occur, corrosion of the underlying metal takes place.[10] The conditions of thermodynamic stability of the native oxide are indicated in the potential vs. pH (Pourbaix) plot presented in Figure 1.1. The alloy is immune to corrosion at potentials negative of -2.0 V vs. SCE (~-1.7 V vs. SHE) , except at the most alkaline pH. The metal is passivated between a pH range of 4 – 9 at potentials from -2.0 to +1.2 V vs. SCE. Under very acidic or alkaline conditions, the metal is susceptible to dissolution at potentials positive of the standard reduction potential. Al oxidizes to form Al^{3+} ions under acidic conditions and aluminate (AlO_2^-) ions under basic conditions. The limits shown in the graph are not absolute and vary with external factors like temperature and presence of corrosive salts/ soluble species in the environment.[10]

Corrosion of aluminum alloys is a complicated process. The metal matrix of an aluminum alloy consists of several coarse and microscopic secondary phase particles formed during the alloying process. These second-phase particles are generally cathodic to the aluminum. Because these particles have electrochemical potentials different from the surrounding aluminum matrix, localized galvanic cells are formed throughout the alloy. A difference in corrosion potential

between aluminum and the cathodic microconstituents of the localized cells is generally the cause for corrosion initiation. In most cases of localised corrosion, the reaction proceeds as follows:

$$Al \rightarrow Al^{3+} + 3e^{-} \quad (1)$$

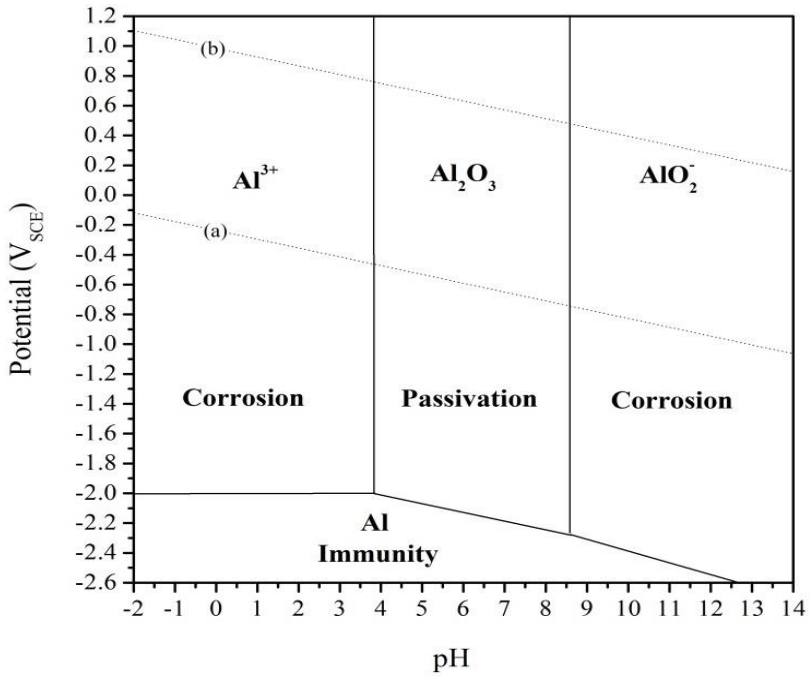

Figure 1.1 Potential vs. pH diagram showing the thermodynamic stability of native aluminum oxide. The immunity and passivation regions indicate conditions under which the surface oxide film is stable. Figure adapted from book chapter in the Atlas of Electrochemical Equilibria in Aqueous Solutions (Pourbaix 1974). [10]

The degree of corrosion seen in aluminum alloys depends on the degree to which it is polarized in the galvanic cell. In other words, effects of localised corrosion increase when the difference in electrode potential between the alloying elements (cathode) and Al (anode) is greater. [1,2,4] 2xxx series aluminum alloys are more susceptible to pitting corrosion because of the highly cathodic nature of Cu. (E^o = +0.337 V vs SHE). In the localised galvanic cells, secondary phase particles act as cathodes and aluminum serves as the anode. The rate of corrosion also depends on other environmental factors such as temperature, halide concentration, pH etc. Of all commercial aluminum alloys, the relative pitting resistance is as: [4]

5xxx > 3xxx > 6xxx > 7xxx > 2xxx

Pitting is the most common type of corrosion seen on aluminum alloys. Pits initiate at localized discontinuities in the native oxide, usually in areas surrounding intermetallics. Pits can propagate quickly, if undetected and can significantly reduce the mechanical strength of the material over time, especially when formed at locations of high fatigue stress. Although pitting corrosion by itself is not dangerous, other severe forms of corrosion, like stress-corrosion cracking are initiated from pits. Once initiated, fatigue cracks can propagate quickly and weaken the entire structure.[4,11] Figure 1.2 shows the different types of pits formed as a result of pitting corrosion.

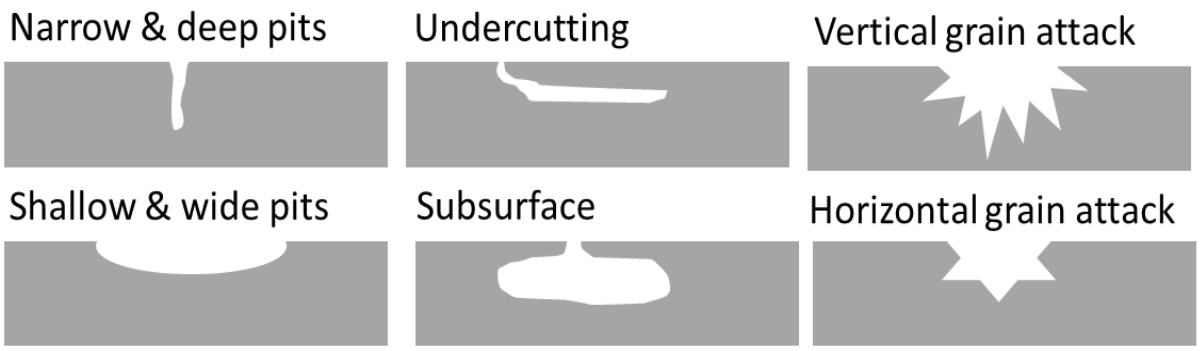

Figure 1.2 Types of pits commonly observed on metal substrates as a result of pitting corrosion in corrosive environments.

Filiform corrosion is another common type of degradation observed on 2xxx and 7xxx series aluminum alloys.[12–14] This form of corrosion is accelerated in high chloride environments, such as when an aircraft is in service over oceans or in coastal regions. The most common aircraft components affected by this type of corrosion are fuselage skin, lower wing skin, pylon tank, and all areas around steel fasteners. Figure 1.3 shows an image of filiform corrosion of an aircraft wing.

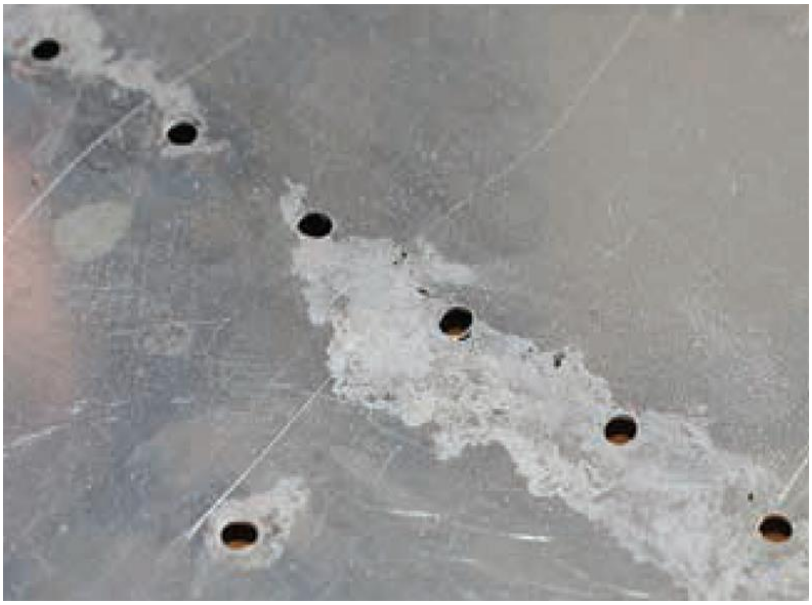

Figure 1.3 Filiform corrosion attack on an aircraft wing. Areas around fastener holes are most affected by corrosion. Imaged obtained from online source: Aviation safety experts (http://www.dviaviation.com/aircraft-corrosion.html).

In general, metal corrosion initiates and propagates when the following conditions prevail:

1. Presence of an active corrosion site consisting of an anode and cathode
2. Electrical contact between anode and cathode
3. Presence of a cathodic reactant or electrolyte such as water, H_2 or O_2.

The electrochemical reactions occurring during corrosion are:[15]

Anodic half reaction:

$$Al \rightarrow Al^{3+} + 3e^- \quad (2)$$

Cathodic half reaction:

$$O_2 + 2H_2O + 4e^- \rightarrow 4OH^- \ (neutral\ or\ alkaline) \quad (3)$$

$$2H^+ + 2e^- \rightarrow H_2 \ (acid) \quad (4)$$

The rate of cathodic reactions occurring on a metal surface directly affects the rate of corrosion of the metal.[15,16] Eliminating oxygen and electrolyte contact with the metal is an effective method to prevent corrosion. This is done by introducing an insoluble and insulating organic or inorganic barrier layer (coating) on the metal surface. The coatings help suppress cathodic reactions occurring on the metal surface by limiting transport of electrolyte, water and oxygen to the substrate. Transportation of electrons is also inhibited, thereby reducing the rate of anodic reaction that might take place on the substrate as well.[15,16]

1.4 CORROSION PREVENTION

The aerospace industry relies on a multi-component coating system to protect metals against environmental corrosion. A thin (50 – 200 nm) conversion coating constitutes the first layer of the coating system. It is usually an inorganic layer that enhances corrosion protection and activates the alloy surface for better paint receptivity. The primer (second layer) is generally a pigmented organic resin matrix, approximately 50 – 250 μm thick. The main function of the primer layer is to provide corrosion protection to the substrate and to promote adhesion with a topcoat. The third layer is a topcoat that serves as the principal barrier layer protecting the substrate from extreme environmental conditions and UV radiation. It also is applied for aesthetic or appearance reasons. Figure 1.4 shows the schematic of a typical aircraft coating system.[15]

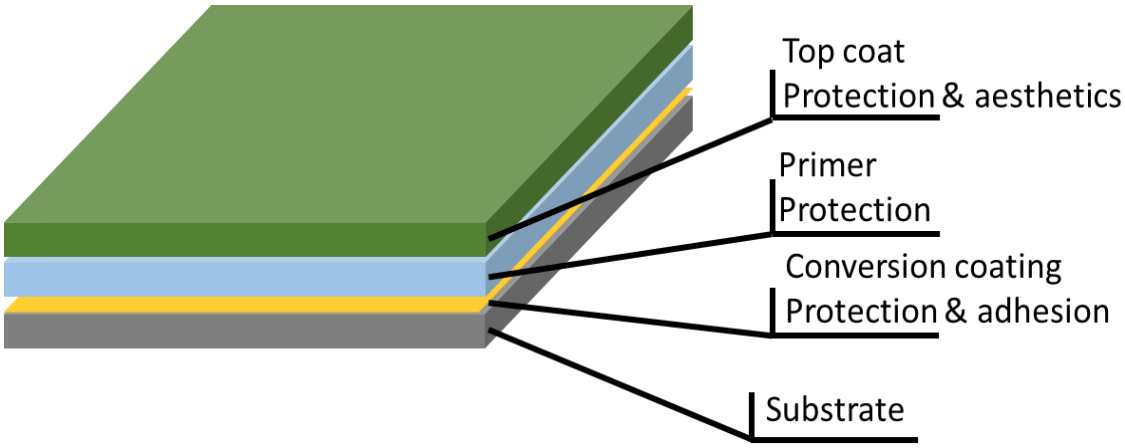

Figure 1.4 Schematic of a multi-layer coating system used to protect aircraft components.

In addition to coatings, several other corrosion prevention techniques are used to protect aerospace aluminum alloys including plasma ablation, plasma deposition, cathodic magnetron sputtering, anodization etc.

Of the many techniques available, anodization of aluminum alloys has gained attention for protecting aircraft parts with complex shapes which cannot otherwise be protected by spray coating or electrodeposition. Anodizing a substrate involves modifying the metal surface to create a barrier oxide layer (micrometer). The oxide is electrochemically grown on the alloy surface at a constant voltage or current in an acid medium. When a sufficient anodic potential is maintained, the alloy undergoes oxidation to form a porous oxide according to the following reaction:[17]

$$2Al + 3H_2O \rightarrow Al_2O_3 + 6H^+ + 6e^- \quad (5)$$

The oxide thus formed consists of two layers – a barrier layer and a porous layer. The barrier layer is thin, dense and non-porous while the porous layer is thick and is a network of 10-20 nm

size pores.[17] A schematic of an electrochemically grown oxide layer on the surface of an aluminum alloy is shown below in Figure 1.5.

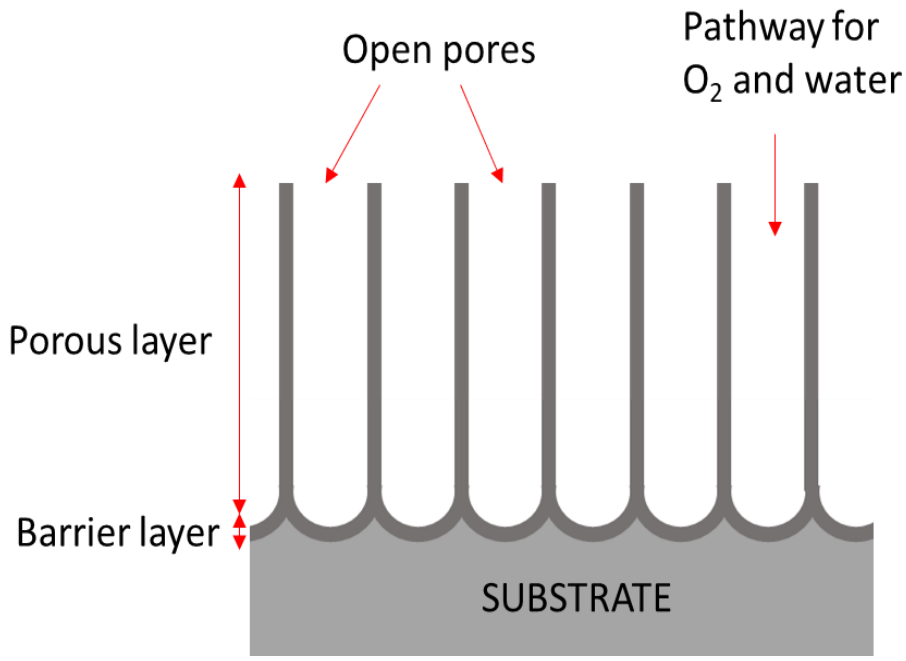

Figure 1.5 Schematic of an aluminum oxide layer grown by electrochemical oxidation of an aluminum alloy surface showing the barrier and porous layers of the oxide.

The electrochemically grown aluminum oxide is non-conducting and suppresses the rate of electron transfer reactions happening on the metal surface. However, pores in the oxide layer provide pathways for diffusion of electrolyte and oxygen to the substrate promoting cathodic reactions to occur on the substrate. Therefore, the porous oxide is typically 'sealed' by immersing the anodized alloy in baths containing corrosion inhibitors such as chromate, nickel acetate, nickel fluoride. The sealant forms a thin non-porous film over the oxide and within the pores, acting as a barrier preventing diffusion of electrolyte and water through the pores.[18] Figure 1.6 shows the schematic of a sealed aluminum oxide layer.

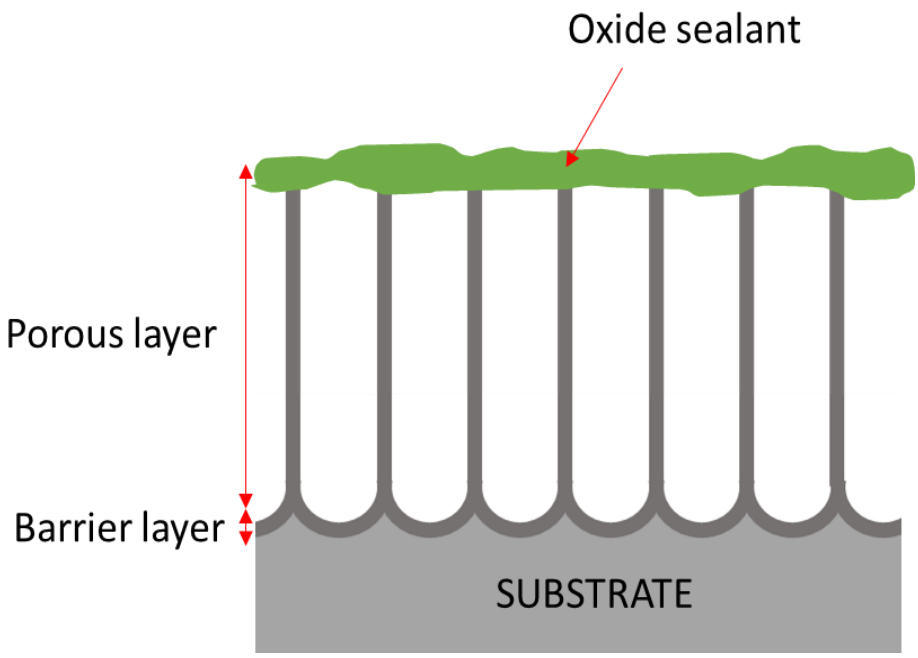

Figure 1.6 Schematic of an electrochemically grown aluminum oxide layer sealed with a conversion coating.

Coatings in the aerospace industry – chromates.

Since the 1900's, the aerospace industry has relied on hexavalent chromium-based conversion coatings, primers and sealants to protect ferrous and non-ferrous alloys from corrosion. Hexavalent chromium, or chromate, is known to be the most effective corrosion inhibitor for aerospace aluminum alloys. It is used in the form of conversion coatings, anodization baths and corrosion inhibitor pigments in primers. However, strict regulations have been placed since 1982 to limit the use of Cr(VI) due to its high carcinogenicity. The use of Cr(VI) has been limited by the Environmental Protection Agency (EPA) through various acts including Toxic Substance Control Act (TSCA), Clean Air Act, Clean Water Act etc and Cr(VI) was listed as one among the 188 Hazardous Air Pollutants (HAP). Cr^{6+} undergoes reduction to Cr^{5+} which when ingested or inhaled can cause DNA damage, lung cancer and other serious illnesses. The current public health service exposure limit for Cr is 0.05 mg/l. [16, 19,20,21]

Alternates to chromates.

Federal mandates on the use of chromate and chromate containing compounds has resulted in economic challenges for the aerospace industry in the form of increased costs for environmental compliance and increased liability claims of Cr(VI) exposure in workplaces. This has led to funds being allocated towards research for the development of suitable replacements for chromate. Enormous research work is underway in both academia and industry to find suitable replacement corrosion inhibitors to protect aerospace aluminum alloys. Some alternates to chromates are mentioned below.

(i) Rare-earth based coatings

Cerium and lanthanum-based inhibitors were investigated in the 1980's as candidates for chromate replacement on aluminum alloys.[22,23] Complexes of Ce and La precipitate as their respective oxides and hydroxides on the alloy surface at pH > 10 and inhibit the kinetics of cathodic reactions that occur on underlying metal surface. Rare-earth salts have been used to successfully protect Zn, steel, Mg and Al alloys. They are easy to use as they integrate well in coatings and primers. However, coatings formed from rare-earth salts are unstable in acidic conditions and dissolve at lower pH. These coatings are therefore not durable for aerospace applications.[22,23]

(ii) Vanadate-based coatings

Sodium metavanadate was studied as a potential corrosion inhibitor for steel in the 1960's. Vanadate-based coatings were reported to adsorb on cathodic sites on AA2024-T3 and significantly inhibit oxygen reduction reactions.[24,25] However, vanadium compounds are carcinogenic and have been proven to cause tumors making it a non-viable chromate replacement.[24,25]

(iii) Li-based coatings

Li-based coatings were investigated in 1996 as candidates for the corrosion protection of Al alloys. [26,27] The size of Li enabled ready intercalation into the $Al(OH)_3$ matrix thus stabilizing the protective film under corrosive conditions. It was reported that a compact polycrystalline Al-Li double hydroxide layer forms on aluminum alloys and enhances the corrosion resistance of the substrate significantly. Polyurethane coatings containing Li-salts possess self-healing properties and have been suggested as replacements for chromate primers. These coatings have shown promising results in ASTM B117 tests and are yet to be industrialized.[26,27]

(iv) Organic coatings and nanocomposites

Organic corrosion inhibitors include polymeric and sol-gel based coatings. Organic coatings used to protect aluminum alloys, despite being multi-layered, allow permeation of moisture and oxygen through the coating structure. This leads to substrate degradation. Such polymeric coatings are often interspersed with active corrosion inhibitors such as $SrCrO_4$ to improve barrier characteristics of coatings and primers. Graphene-nanocomposite based coatings have been used to protect steel and iron substrates by increasing path length of oxygen from reaching the substrate. Graphene-polyvinyl butyral coatings have shown significant resistance to coating delamination. However, the cost of mass production of graphene limits the use of this technology. Another class of “smart organic coatings” are also being researched as viable alternatives to chromates. These coatings respond to external stimulus such as pH change or moisture ingress and release corrosion inhibitors in response to such changes. Smart coatings include conducting polymers, polyelectrolyte-based coatings and other organic inhibitors like mercaptobenzimidazole, benzotriazole, salicylaldoxime. The key limitation for implementation of these smart coatings is

the cost associated with the industrialization of these processes. Also, these coatings are still in an experimental stage and do not meet the industry standards to replace chromates.[28–30]

(v) Zirconium-based coatings

Zirconium-based coatings are increasingly used in the aerospace industry (fighter jet and space shuttles) due to superior corrosion protection, ease of application and good adhesion properties. [31,32] However, the extent of corrosion protection offered by these coatings is still inferior to chromates and therefore are not viable alternatives to completely replace chromates in the aerospace industry. These coatings are used as chromate replacements in other industries like coil coating, automotive, extrusion and appliances.[31,32]

(vi) Trivalent chromium coatings

Trivalent chromium coatings (TCP) are the leading replacement for chromate coatings. [33-35] These Cr(VI)-free coatings possess excellent corrosion resistance and good adhesion properties. These coatings are similar in composition to the zirconium conversion coatings but contain small amounts of Cr(III) salts added to improve cathodic protection. According to Class IA of MIL-SPEC-ETL-5541F, TCP conversion coatings meet industry standards to replace chromates and can be used to protect aerospace aluminum alloys.[33,34]

In the past, reports have been published describing the structure, formation mechanism, and electrochemical behaviour of TCP coatings formed on various aerospace aluminum alloys including AA6061, AA7075 and AA2024. It has been found that TCP provides corrosion protection on a level comparable to chromate conversion coatings. The protection tends to be both anodic (reduced rate of metal oxidation) and cathodic (reduced rate of reduction reaction, oxygen reduction) in nature. However, inconsistencies in corrosion protection behaviour by TCP has been observed for the high Cu containing 2xxx series aluminum alloys (Ex: AA2024-T3).[35] It is

envisioned that these inconsistencies could be a result of variations in surface preparation techniques. Thus, a major focus of this dissertation work focuses on understanding the role of process parameters in improving the overall corrosion performance of TCP on AA2024-T3. Another aspect of this work aims at determining the early-stage failure mechanism of TCP on AA2024-T3.

1.5 INTRODUCTION TO TRIVALENT CHROME PROCESS (TCP) SURFACE PRETREATMENT

The trivalent chrome process (TCP) conversion coating is the leading replacement for chromate conversion coatings to protect aerospace aluminum alloys.[35-39] This coating was first developed by Agarwala and colleagues at NAVAIR, who reported the electrochemical behavior of TCP-coated aluminum alloys.[15, 35-40, 45-53, 57] TCP is a Cr(VI)-free conversion coating with a composition similar to commercial zirconium-based coatings, but enriched in Cr(III) salts for additional corrosion protection and better primer adhesion. The TCP coating bath is made of ~60 wt.% zirconium salts like hexafluorozirconate and 5 wt.% Cr(III) salts. The remaining 35% is composed of coatings promoters and stabilizers.[40-43] TCP is currently marketed by several vendors: Henkel (Bonderite T5900), Chemeon (TCP-HF), Luster-On (Aluminescent), SurTec (ChromitAL 650).[40-43] The coating formed by immersion on aluminum alloys is 100-200 nm thick, composed of hydrated zirconia ($ZrO_2.nH_2O$) and oxyhydroxides of Cr(III) ($Cr(OH)_3$ and Cr_2O_3). The uniformity of TCP formation and its corrosion inhibition performance on aluminum alloys depends greatly on surface preparation techniques i.e. the cleanliness of the surface, surface morphology of the alloy (surface roughness, pit density), chemical composition of the alloy surface.[42-44]

The alloy surface is generally subjected to the following pretreatment steps before forming a protective coating:

1. Manual polishing or abrading – To reduce surface roughness and remove smut.
2. Degreasing – To remove grease and oil from the alloy surface using an alkaline surfactant.
3. Deoxidation – To dissolve the natural oxide layer using a highly acidic fluoride solution.

The conversion coating is then formed on a clean, low oxygen surface by spray or immersion techniques. Each of these pretreatment steps, particularly the deoxidation or desmutting step, can influence the alloy surface texture and elemental composition by altering surface pit density or second-phase particle distribution, which in turn affects the corrosion resistance of the TCP layer subsequently formed. A poorly prepared surface can result in non-uniform coating coverage and negatively affect corrosion performance of the coating during service conditions.[42-44]

1.6 TCP FORMATION

The TCP conversion coating bath primarily consists of hexaflorozirconate with added Cr(III) salts. Accelerators and stabilisers are added in small quantities to accelerate coating formation reactions and increase coating shelf life. Fluoride salts are added to initiate aluminum oxide dissolution.[41,45] The bath is completely free of hexavalent chromium. The first step towards TCP formation over an alloy involves dissolution of the surface oxide layer by fluoride ions. Oxide dissolution reactions are shown below: [46-50]

$$Al_2O_3 + 6HF \leftrightarrow 2AlF_3 + 3H_2O \quad (6)$$

$$Al + 6HF + 3H^+ \leftrightarrow AlF_6^{3+} + 3H_2 \quad (7)$$

Dissolution of surface oxide by fluoride ions forms an interfacial fluoroaluminate layer of ~40 nm thickness. Removal of the passivating oxide shifts the interfacial potential to more cathodic values driving cathodic reactions like oxygen reduction and hydrogen evolution on the surface. Reactions occurring at the alloy surface at negative potentials are shown below: [46,47,49]

$$Al + 6F^- \rightarrow AlF_6^{3-} + 3e^- \quad (8)$$

$$O_2 + 2H_2O + 4e^- \rightarrow 4OH^- \quad (3)$$

$$2H^+ + 2e^- \rightarrow H_2 \quad (4)$$

These proton consuming cathodic reactions occurring at the alloy surface, cause an increase in interfacial pH and drive the hydrolysis of hexafluorozirconate and Cr(III) species in the coating bath. Oxides and hydroxide of Zr(IV) and Cr(III) co-precipitate to form the TCP coating. Hydrolysis reactions occurring at the interface at elevated pH are shown below:

$$ZrF_6^{2-} + 4OH^- \rightarrow ZrO_2.2H_2O + 6F^- \quad (9)$$

$$Cr^{3+} + 8OH^- + 3e^- \rightarrow Cr(OH)_3 + 5OH^- \quad (10)$$

A schematic of the biphasic structure of TCP formed over an aluminum alloy substrate is shown in Figure 1.7. [41,45]

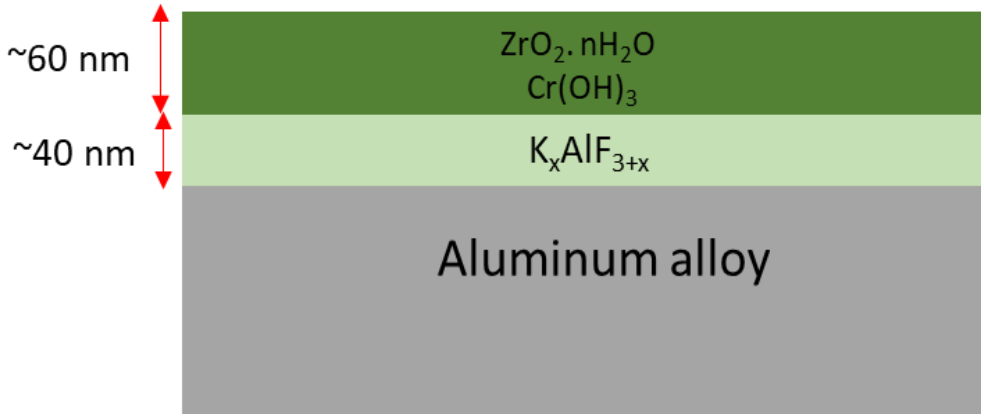

Figure 1.7 Schematic of the biphasic TCP structure formed on an aluminum alloy.

1.7 TCP CHARCTERIZATION

Physical and chemical characterization.

The morphology, chemical composition, electrochemical behaviour and corrosion resistance of TCP conversion coatings formed on aluminum alloys have been studied and reported on in prior publications. [41-45,48] Ellipsometry and XPS results have shown the thickness of a TCP coating formed by 5-10 min immersion to be ~100 nm. SEM, EDX and Raman spectroscopic data have revealed that the coating is mainly composed of Cr $(OH)_3$, Cr_2O_3 and ZrO_2. XPS and Auger electron spectroscopy data have been used to confirm the biphasic structure of TCP with elevated signals of F, Al, and O in the interfacial region (~40 nm), and signals for ZrO_2 and Cr in the outer layer up to a thickness of ~100 nm. [40,51-53]

Electrochemical characterization.

The corrosion inhibition of protective coatings can be assessed using potentiodynamic polarization curves.[54] Figure 1.8 shows the anodic and cathodic polarization curves for an uncoated and TCP-coated AA2024-T3 in a sodium sulfate plus sodium chloride electrolyte. Open circuit potential (OCP), or otherwise called E_{corr} is the equilibrium potential of the alloy under conditions of zero current flow.[54] An anodic polarization curve is obtained by scanning the potential in the positive direction from the OCP and a cathodic polarization curve is obtained by scanning the potential in the negative direction. At potentials more positive than the OCP, aluminum dissolution is favored along with stable pit formation and growth, if the potential is sufficiently positive. At potentials more negative, cathodic reactions are favored such as the reduction of dissolved oxygen. The current measured as a function of potential sheds light on the redox reactions occurring and their rate.[54] The presence of a protective coating generally suppresses electrochemical reaction kinetics on the alloy surface. This results in lower anodic and cathodic polarization curve currents.

Anodic and cathodic currents are generally suppressed by 10-100x on TCP-coated aluminum alloys, as compared to the uncoated alloy controls. The anodic potential at which a sudden increase in current is observed for smaller changes in the applied potential is called the pitting potential, E_{pit}. Pitting corrosion of aluminum alloys is accelerated in the presence of chloride in the supporting electrolyte. Beyond this potential, the substrate undergoes stable pit formation and growth. This produces severe damage to the alloy. For surfaces protected by a coating, E_{pit} is generally more positive than the value for the uncoated controls.[54] This indicates the alloy is more resistant to corrosion. Generally, a TCP- coated substrate has a slightly more positive OCP indicating surface passivation and also an E_{pit} shifted positive by ~300 mV, or more. [54-57]

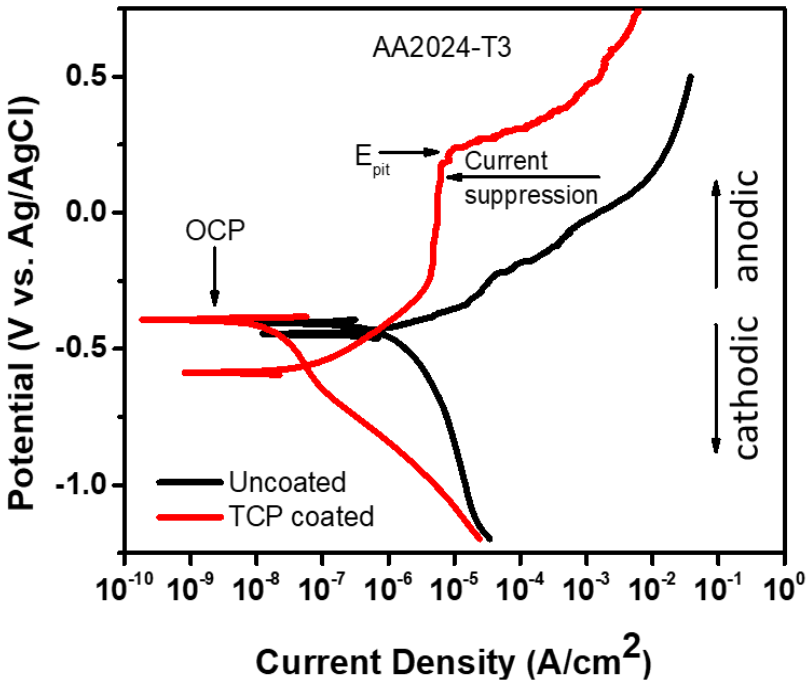

Figure 1.8. Potentiodynamic polarization curves for uncoated and TCP coated AA2024-T3 in sodium sulfate + sodium chloride electrolyte. The graph shows important electrochemical parameters such as OCP and E_{pit}. A suppression in anodic and cathodic currents by the coating is also indicated.

1.8 MOTIVATIONS FOR STUDY

At present, there is considerable information available in the scientific literature regarding the the formation and electrochemical behavior of TCP coatings on several aluminum alloys. The evidence is that these coatings do provide good stand-alone corrosion resistance to aluminum alloys when exposed to neutral salt spray environments, comparable to the protection observed for legacy chromate conversion coatings. The corrosion protection provided by TCP tends to be inferior to that provided by chromate conversion coatings when applied to high Cu aluminum alloys (e.g., AA2024-T3 and AA7075-T6). The reasons for this are unclear. To this end, basic research was conducted to better understand the mechanisms by which TCP inhibts corrosion on aluminum alloys, the role of Cr(III) in the inhibition mechanism, and the importance of different surface pretreatments on the TCP coating performance. In addition, research was conducted to determine the mechanism and effectiveness of TCP as a sealant for anodic oxide coatings on aluminum alloys.

REFERENCES

REFERENCES

(1) Davis, J. R. Alloying: Understanding the Basics-Light Metals and Alloys. **2001.**

(2) Polmear, I. J. Light Alloys. **2005**.

(3) Kaufman, J. G.; International, A. S. M. Introduction to Aluminum Alloys and Tempers. **2000**.

(4) Davis, J. R. Corrosion of Aluminum and Aluminum Alloys. **1999**.

(5) Lang, L.; Li, T.; An, D.; Chi, C.; Nielsen, K. B.; Danckert, J. Investigation into Hydromechanical Deep Drawing of Aluminum Alloy-Complicated Components in Aircraft Manufacturing. *Mater. Sci. Eng. A* **2009**, *499* (1–2), 320–324.

(6) Zähr, J.; Oswald, S.; Türpe, M.; Ullrich, H. J.; Füssel, U. Characterisation of Oxide and Hydroxide Layers on Technical Aluminum Materials Using XPS. *Vacuum* **2012**, *86* (9), 1216–1219.

(7) Mondolfo, L. F. Aluminum Alloys: Structure and Properties. **1979.**

(8) Eswara Prasad, N.; Wanhill, R. J. H. Aerospace Materials and Material Technologies, Volume 1: Aerospace Materials, Indian Institute of Metals Series. **2017**, *1*, 586.

(9) Das, S. K. Recycling Aluminum Aerospace Alloys. *Adv. Mater. Process.* **2008**, *166* (3), 34–35.

(10) Pourbax. M. Atlas of Electrochemical Equilibria in Aqueous Solutions. Brussels **1966.**

(11) Z. Szklarska-Smialowska. Insights Into The Pitting Corrosion Behavior Of Aluminum Alloys. *Corros. Sci.* **1992**, *33* (8), 1193–1202.

(12) Le Bozec, N.; Persson, D.; Nazarov, A.; Thierry, D. Investigation of Filiform Corrosion on Coated Aluminum Alloys by FTIR Microspectroscopy and Scanning Kelvin Probe. *J. Electrochem. Soc.* **2002**, *149* (9), B403.

(13) Huang, R. S.; Lin, C. J.; Isaacs, H. S. A Difference-Imaging Technique Used to Study Streaking Corrosion of Aluminum Alloys AA7075 and AA8006 in Chloride Solution. *Electrochem. Solid-State Lett.* **2006**, *9* (2), 11–14.

(14) Williams, G.; McMurray, H. N. Anion-Exchange Inhibition of Filiform Corrosion on Organic Coated AA2024-T3 Aluminum Alloy by Hydrotalcite-like Pigments. *Electrochem. Solid-State Lett.* **2003**, *6* (3), 9–11.

(15) Twite, R. L.; Bierwagen, G. P. Review of Alternatives to Chromate for Corrosion Protection

of Aluminum Aerospace Alloys. *Prog. Org. Coat.* **1998**, *33* (2), 91–100.

(16) Gharbi, O.; Thomas, S.; Smith, C.; Birbilis, N. Chromate Replacement: What Does the Future Hold? NPJ *Mater. Degrad.* **2018**, *2* (1), 23–25.

(17) Abrahami, S. T.; de Kok, J. M. M.; Terryn, H.; Mol, J. M. C. Towards Cr(VI)-Free Anodization of Aluminum Alloys for Aerospace Adhesive Bonding Applications: A Review. *Front. Chem. Sci. Eng.* **2017**, *11* (3), 465–482.

(18) Priet, B.; Odemer, G.; Blanc, C.; Giffard, K.; Arurault, L. Effect of New Sealing Treatments on Corrosion Fatigue Lifetime of Anodized 2024 Aluminium Alloy. *Surf. Coat. Technol.* **2016**, *307*, 206–219.

(19) James, B. R.; Bartlett, R. J. Behavior of Chromium in Soils: VII. Adsorption and Reduction of Hexavalent Forms. *J. Environ. Qual.* **1983**, *12* (2), 177–181.

(20) Das, A.; Mishra, S. Hexavalent Chromium (VI) : Environment Pollution and Health Hazard. *J. Environ. Res. Dev.* **2008**, *2* (3), 386–392.

(21) Nadler, G. R Eflections On. *J. Manage.* **2004**, *13* (Fall 2008), 239–246.

(22) Hinton, B. R. W. Corrosion Inhibition with Rare Earth Metal Salts. *J. Alloys Compd.* **1992**, *180* (1–2), 15–25.

(23) Zhang, S. H.; Kong, G.; Lu, J. T.; Che, C. S.; Liu, L. Y. Growth Behavior of Lanthanum Conversion Coating on Hot-Dip Galvanized Steel. *Surf. Coat. Technol.* **2014**, *259*, 654–659.

(24) Bienstock, D.; Field, J. H. Corrosion Inhibitors For Hot Carbonate Systems. *Corrosion* **1961**, *17* (12), 571t-574t.

(25) Ehrlich, V. A.; Nersesyan, A. K.; Atefie, K.; Hoelzl, C.; Ferk, F.; Bichler, J.; Valic, E.; Schaffer, A.; Schulte-Hermann, R.; Fenech, M.; et al. Inhalative Exposure to Vanadium Pentoxide Causes DNA Damage in Workers: Results of a Multiple End Point Study. *Environ. Health Perspect.* **2008**, *116* (12), 1689–1693.

(26) Buchheit, R. G. An Anodic Dissolution-Based Mechanism For The Rapid Cracking, "Pre-Exposure" Phenomenon Demonstrated By Al-Li-Cu Alloys. *U.S. Dep. Energy Contract no. DE-AC04-94A185000*.

(27) Rangel, C. M.; Travassos, M. A. The Passivation of Aluminium in Lithium Carbonate/Bicarbonate Solutions. *Corros. Sci.* **1992**, *33* (3), 327–343.

(28) Yasakau, K. A.; Tedim, J.; Zheludkevich, M. L.; Ferreira, M. G. S. Smart Self-Healing Coatings for Corrosion Protection of Aluminium Alloys. Handbook of Smart Coatings for Materials Protection **2014**, 224 - 274.

(29) Glover, C. F.; Richards, C.; Baker, J.; Williams, G.; McMurray, H. N. In-Coating Graphene Nano-Platelets for Environmentally-Friendly Corrosion Protection of Iron. *Corros. Sci.* **2017**, *114*, 169–172.

(30) Buchheit, R. G.; Guan, H.; Mahajanam, S.; Wong, F. Active Corrosion Protection and Corrosion Sensing in Chromate-Free Organic Coatings. *Prog. Org. Coat.* **2003**, *47* (3–4), 174–182.

(31) Buchheit, R. G.; Hughes, A. E. Chromate and Chromate Free Conversion Coatings, ASM Handbook: Fundamentals, Testing and Protection **2003.**

(32) Nordlien, J. H.; Walmsley, J. C.; Østerberg, H.; Nisancioglu, K. Formation of a Zirconium-Titanium Based Conversion Layer on AA 6060 Aluminium. *Surf. Coat. Technol.* **2002**, *153* (1), 72–78.

(33) Nickerson, W,C.; Lipnickas, E. TriService Corrosion Conference Proceedings **2003**.

(34) Mitton, D. B.; Carangelo, A.; Acquesta, A.; Monetta, T.; Curioni, M.; Bellucci, F. Selected Cr(VI) Replacement Options for Aluminum Alloys: A Literature Survey. *Corros. Rev.* **2017**, *35* (6), 365–381.

(35) Milosev. I.; Frankel, G. S. Review - Conversion Coatings Based on Zirconium and/or Titanium. *J. Electrochem. Soc.* **2018**, *165* (3), C127–C144.

(36) Nickerson, B. C.; Lipnickas, E. Proceedings of the 2003 Tri-Service Corrosion Conference: Las Vegas, NV, Nov. 17-21, **2003**.

(37) Alodine® T 5900 RTU. MSDS 756387; Henkel Corporation: Madison Heights, MI, **2011**.

(38) Pearlstein, F.; Agarwala, V. S. Trivalent Chromium Solutions for Applying Chemical Conversion Coatings to Aluminum Alloys or for Sealing Anodized Aluminum. *Plat. Surf. Fin.* **1994**, *81* (7), 50–55.

(39) Pearlstein, F.; Agarwala, V. S. Trivalent Chromium Solution for Sealing Anodizing Aluminum. *NAVAIR Warfare Center Aircraft Division (NAWCAD)* **1994**, *298* (0704).

(40) Dardona, S.; Jaworowski, M. In Situ Spectroscopic Ellipsometry Studies of Trivalent Chromium Coating on Aluminum. *Appl. Phys. Lett.* **2010**, *97* (18), 1–4.

(41) Li, L. L.; Desouza, A. L.; Swain, G. M. In Situ pH Measurement during the Formation of Conversion Coatings on an Aluminum Alloy (AA2024). *Analyst* **2013**, *138* (15), 4398–4402.

(42) Li, L. L.; Desouza, A. L.; Swain, G. M. Effect of Deoxidation Pretreatment on the Corrosion Inhibition Provided by a Trivalent Chromium Process (TCP) Conversion Coating on

AA2024-T3. *J. Electrochem. Soc.* **2014**, *161* (5), C246–C253.

(43) Van Westing E. P. M.; Campestrini P.; De Wit J. H. W. Influence of Surface Preparation On Performance Of Chromate Conversion Coatings On Alclad 2024 Aluminium Alloy: Part I: Nucleation And Growth. *Electrochim. Acta*. **2001**, *46*, 2553.

(44) Moffitt, C. E.; Wieliczka, D. M.; Yasuda, H. K. An XPS Study of The Elemental Enrichment on Aluminum Alloy Surfaces from Chemical Cleaning. *Surf. Coat. Technol*. **2001**, *137* (2-3), 188-196.

(45) Li, L. L.; Swain, G. P.; Howell, A.; Woodbury, D.; Swain, G. M. The Formation, Structure, Electrochemical Properties and Stability of Trivalent Chrome Process (TCP) Coatings on AA2024. *J. Electrochem. Soc.* **2011**, *158* (9), C274.

(46) Dong, X.; Wang, P.; Argekar, S.; Schaefer, D. W. Structure and Composition of Trivalent Chromium Process (TCP) Films on Al Alloy. *Langmuir* **2010**, *26* (13), 10833–10841.

(47) Dong, X.; Argekar, S.; Wang, P.; Schaefer, D. W. In Situ Evolution of Trivalent Chromium Process Passive Film on Al in a Corrosive Aqueous Environment. *ACS Appl. Mater. Interfaces* **2011**, *3* (11), 4206–4214.

(48) Qi, J. T.; Hashimoto, T.; Walton, J. R.; Zhou, X.; Skeldon, P.; Thompson, G. E. Trivalent Chromium Conversion Coating Formation on Aluminium. *Surf. Coat. Technol.* **2015**, *280*, 317–329.

(49) Shruthi, T. K.; Swain, G. M. Communication—Role of Trivalent Chromium on the Anti-Corrosion Properties of a TCP Conversion Coating on Aluminum Alloy 2024-T3. *J. Electrochem. Soc.* **2018**, *165* (2), C103–C105.

(50) Cho, K. W.; Shankar Rao, V.; Kwon, H. S. Microstructure and Electrochemical Characterization of Trivalent Chromium Based Conversion Coating on Zinc. *Electrochim. Acta* **2007**, *52* (13), 4449–4456.

(51) Qi, J.; Hashimoto, T.; Walton, J.; Zhou, X.; Skeldon, P.; Thompson, G. E. Formation of a Trivalent Chromium Conversion Coating on AA2024-T351 Alloy. *J. Electrochem. Soc.* **2016**, *163* (2), C25–C35.

(52) Qi, J.; Walton, J.; Thompson, G. E.; Albu, S. P.; Carr, J. Spectroscopic Studies of Chromium VI Formed in the Trivalent Chromium Conversion Coatings on Aluminum. *J. Electrochem. Soc.* **2016**, *163* (7), C357–C363.

(53) Liangliang Li; G. M. Swain, Formation and Structure of Trivalent Chromium Process Coatings on Aluminum Alloys 6061 and 7075. *J. Electrochem. Soc*. **2013**, *69* (12), 1205-1216.

(54) Getting Started with Electrochrmical Corrosion Measurement, Application Note - Gamry

Instruments.

(55) Na, K. H.; Pyun, S. Il. Comparison of Susceptibility to Pitting Corrosion of AA2024-T4, AA7075-T651 and AA7475-T761 Aluminium Alloys in Neutral Chloride Solutions Using Electrochemical Noise Analysis. *Corros. Sci.* **2008**, *50* (1), 248–258.

(56) Shapovalov, E. T.; Gerasimov, V. V. The Electrochemical Behavior of Uranium. *Sov. At. Energy* **1969**, *27* (4), 1045–1049.

(57) Walton, J.; Shruthi, T. K.; Yancey, D.; Vlasak, P.; Westre, S.; Swain, G. M. Evaluation of a Trivalent Chromium Process (TCP) Conversion Coating on AA2024-T3 That Requires No Surface Pretreatment. *J. Electrochem. Soc.* **2019**, *166* (15), C589–C599.

CHAPTER 2. SURFACE PREPARATION, ELECTROCHEMICAL TESTING & CHARACTERIZATION OF AA2024-T3.

2.1 REAGENTS

All chemicals used were analytical grade quality or better and were used without additional purification. Sodium sulfate (Na_2SO_4), sulfuric acid (H_2SO_4), sodium chloride (NaCl), potassium dichromate ($K_2Cr_2O_7$), nickel (II) acetate tetrahydrate, boric acid (H_3BO_3), sodium carbonate ($NaHCO_3$), calcium chloride ($CaCl_2$), 2',7'–dichlorodihydrofluorescein diacetate (DCFH-DA) and sodium hydroxide (NaOH) were analytical grade quality, or better, and were purchased from Sigma-Aldrich (St. Louis, MO). Nitric acid (HNO_3) was purchased from Fisher Scientific (Hampton, NH). Hydrogen peroxide (30 wt. %) was purchased from CCI Chemical (Vernon, CA). Industrial grade Cleaner 1000, TCP-NP and TCP-HF conversion coating baths were obtained from CHEMEON Surface Technology (Minden, NV). Turco 6849 degreaser, Turco Smut-Go deoxidizer, Bonderite T5900 and T5900-NC coating baths were obtained from Henkel (Madison Heights, MI). The 133 degreaser and 495L deoxidiser were provided by SurTec Inc. (Brunswick. OH). The pH of all TCP baths was adjusted to 3.85 using 1 wt. % NaOH or 0.5 M H_2SO_4, as required. All solutions were prepared using ultrapure water from a Barnstead E-Pure system with a resistivity >17 MΩ-cm. No solution filtration was applied to remove solid particulates from the coating baths prior to use.

2.2 SPECIMEN PREPARATION

Aluminum alloy 2024-T3 specimens were obtained as 2 mm-thick sheets (www.metalsonline.com) and were cut into $1in^2$ pieces for the studies. The specimens were mechanically abraded for 4 min using 1500 grit wet aluminum oxide paper to smooth the surface. This was followed by a fine polish using 0.3 μm alumina grit (Buehler) slurried with ultrapure

water on a felt polishing pad for 4 min. A 20-min ultrasonic cleaning in ultrapure water was performed after each abrading and polishing step. Polished specimens were then degreased at 55 °C for 10 min followed by a 2-min ultrapure water rinse. The degreased specimens were then deoxidized for 2 min at room temperature followed by a 2-min ultrapure water rinse. The degreased and deoxidized specimens were then dried with a flow of N_2 before being immersion coated in a TCP bath at room temperature. Different degreasers and deoxidisers were used throughout this work and the respective immersion times and temperature used are in accordance with the supplier recommendations. The coated specimens were then immersed in tap water for 2 min with no agitation. This was followed by aging/drying overnight in a covered dish before further testing. The schematic of specimen preparation is shown in Figure 2.1. Several commercial variants of TCP were used for the experiments reported in the upcoming chapters, each pre-treated with the respective degreaser and deoxidizer as provided by the company. Immersion times vary for different variants of TCP.

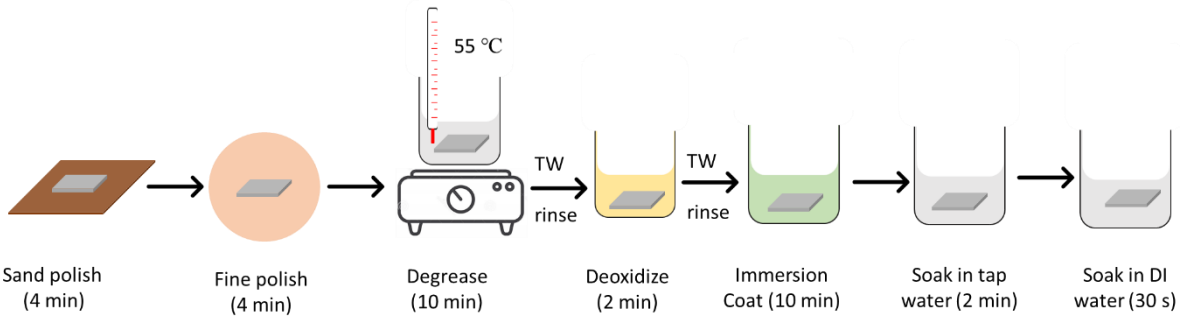

Figure 2.1 Schematic of the alloy surface preparation process as performed in the laboratory.

2.3 ELECTROCHEMICAL ANODIZATION AND SEALING

Degreased and deoxidized specimens were electrochemically anodized for 23 min total in 9.8 wt. % H_2SO_4. AA2024-T3 panels were the anode and a stainless-steel plate of the same dimension

was employed as the cathode. The two electrodes were mounted vertically and parallel to one another using plastic alligator clips separated by of 5 cm. The aluminum alloy was connected to the positive terminal and the stainless-steel plate was connected to the negative terminal of a DC power supply (Tenma, 30 V and 5A (150 W)). The electrodes were lowered into a beaker such that 2/3 of the specimen was immersed in the acid. Anodization was initiated by applying a 1 V/12 s ramp to 15 V DC (3 min). This voltage was then maintained for 20 min producing a total anodization time of 23 min. The current density ranges from 25 – 35 mA/cm^2 during the process with a progressive increase during the anodization period. The anodized specimens were then removed and rinsed copiously with ultrapure water. This was followed by immersion in room temperature ultrapure water for 20 min to fully dissolve aluminum hydroxysulfate salts (anodization smut) that sometimes formed on the surface. The specimens were then dried with N_2 and stored overnight in a desiccator before further testing. The stainless-steel cathode was abraded with 1500 grit wet aluminum oxide paper to refresh the surface prior to each anodization run. Although anodization was performed with an acid at ambient temperature, resistive heating caused the solution to warm during the process. Figure 2.2 shows the schematic and photograph of the anodization set up used to grow the oxide layer on AA2024-T3.

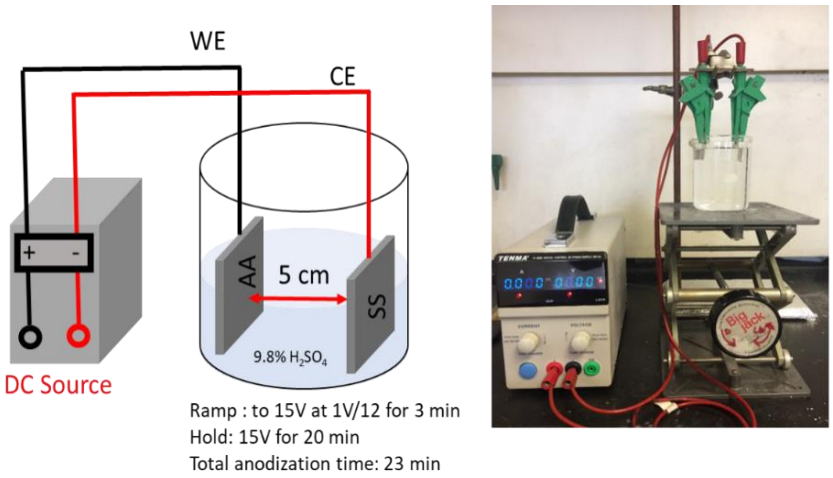

Figure 2.2 Schematic and photograph of the electrochemical anodization setup used in the laboratory for anodizing AA2024-T3 under controlled potential at room temperature.

The anodized specimens were immersion sealed in various coating baths to compare the corrosion inhibition performance of the sealants. Four different sealants were used:

(i) TCP NP seal: TCP-NP coating bath was prepared by mixing 0.5% (v/v) and 5% (v/v) of the two bath components: parts A and B. A 5 min immersion in the TCP NP bath (pH: 3.85) was followed for sealing.

(ii) Potassium dichromate seal: 15 min immersion in 5 wt. % potassium dichromate solution at 90°C.

(iii) Nickel acetate seal: 15 min immersion in 5 g/l nickel acetate + 1 g/l cobalt acetate + 8 g/l boric acid solution at 85°C.

(iv) Hot water seal: 30 min immersion in ultrapure water at 90°C.

All immersion sealed specimens, except hot water sealed, were immersed in DI water for 2 min after sealing and aged overnight in laboratory conditions before testing. The sealing conditions used are optimized conditions for each sealant.

2.4 MATERIAL CHARACTERIZATION

Scanning Electron Microscopy/ Energy Dispersive X-Ray Spectroscopy.

Scanning electron microscopy was performed using two microscopes – JEOL 6610 and JEOL 7500 (JEOL Ltd, Tokyo, Japan). The plan view electron micrographs obtained were used to understand the surface morphology of coated and uncoated alloys.

Elemental maps of the alloys and coatings were obtained on Aztec system detector (Oxford Instruments, UK) attached to the electron microscope and the obtaine data were analyzed (version 3.1) using the system software (Aztech Energy analysis). Spectra were recorded using a 15 keV accelerating voltage. The x-ray analysis was primarily used to identify coating components such as Zr, Cr, F and O. All measurements were made at the Centre for Advanced Microscopy (CAM) facility in MSU.

A focused ion beam (FIB) was sometimes used to mill through specimens to obtain cross-sections. A Ga ion gun attached to the SEM was used to mill through samples. The gun was attached at a 45° angle. An accelerating voltage of 30k eV and 4 nA current was used to mill. A 600 pA current was used for fine sectioning.

Digital Microscopy.

A Keyence VHX 600 digital optical microscope was used to obtain 3-dimensional images, morphology data and surface depth profiles of specimens before and after accelerated degradation tests. The instrument generated 3D maps of surfaces that helped distinguish IMPs from pits formed during testing. The micrographs also provided useful information such as pit depths, surface roughness and pit densities. The depth resolution of the microscope was determined to be *ca.* 0.2 μm.

UV-Vis Spectroscopy.

UV-Vis absorbance spectra were obtained with a UV-2401 PC series spectrophotometer (Shimadzu Corp., Kyoto, Japan). A quartz cuvette of 1 cm path length was used to collect the spectra. The instrument was used to detect a fluorophore dihydrofluorescien (DCF) with absorption intensity (λ_{max} = 502 nm). Beer's law (A = εbc) was used to calculate the concentrating of DCF from the recorded absorption spectra.

Raman Spectroscopy.

Raman Spectroscopy was performed using a Renishaw *inVia* Confocal microscope equipped with a Nd:YAG laser (Max. power 45W). The excitation wavelength used was 532 nm along with a 1200 line/mm grating. 5 – 10% laser power was used for all measurements. An internal Si wafer standard was used to calibrate the instrument. The technique was used to probe for the presence, or absence of Cr(III)-O ($Cr(OH)_3$) and Cr(VI)-O (CrO_4^{2-} or $HcrO_4^-$) vibrational modes in the TCP coated and sealed specimens. Signal averaging of 3 scans per measurement was using to smooth spectral signals.

Contact Profilometry.

Scanning contact profilometry (Nanomap 500LS, Germany) with a 0.5 nm resolution along z axis was used to measure surface roughness, pit depth and pit densities on specimen surfaces. The stylus is made of tungsten carbide and had a sharp 2 μm tip diameter with a 60◦ taper. Image analysis was done using Nanomap SPIP software. A contact load of 3 mg was used throughout the scan. The zero-position tip placement was established on a region of the specimen away from any damaged area. Pit densities were calculated by dividing the total pit number by the geometric area scanned. Three 1mm x 1mm area spots were investigated on each sample.

2.5 ELECTROCHEMICAL CHARACTERISATION

Electrochemical measurements were conducted in a 1 cm^2 flat cell using a computer-controlled electrochemical workstation (Gamry Instruments, Inc, Reference 600, Warminster, PA). Figure 2.3 shows a schematic of the flat cell. The working electrode (alloy specimen) was mounted in the cell against a Viton® O-ring that defined the exposed geometric area, 1 cm^2. All currents reported herein, are normalized to this geometric area. The image below shows the setup of the assembled electrochemical cell. The counter electrode was a Pt flag and the reference was a home-made Ag/AgCl electrode (4 M KCl, E^0 = +0.197 V vs. NHE) that was housed in a Luggin capillary with a cracked glass tip. All measurements were made in naturally aerated Na_2SO_4 or NaCl electrolyte at room temperature.

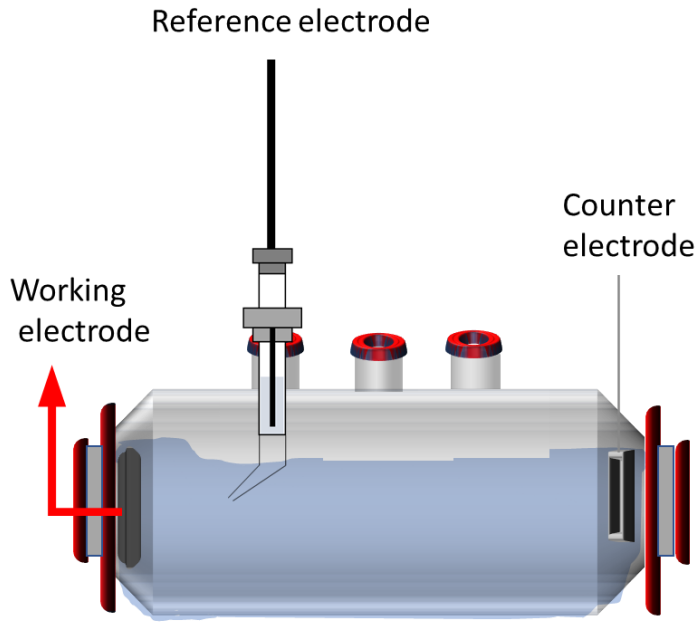

Figure 2.3 Schematic of the flat cell used for electrochemical measurements. Positioning of the reference electrode (RE), working electrode (WE) and counter electrode (CE) are indicated.

The electrochemical testing protocol used is as follows:

(i) Recording the open circuit potential (OCP) for 60 min.

(ii) Collecting electrochemical impedance spectra (EIS) from 1 MHz to 10 mHz at the OCP. A rms AC sine wave with 10 mV amplitude was used. 7 points/decade were recorded.

(iii) Recording a linear polarization curve ± 20 mV vs. OCP. The slope of the curve (R_p = V/I) was used to determine the polarization resistance, R_p

(iv) Recording a potentiodynamic anodic or cathodic scan from OCP to +0.2V or -1.2V vs. Ag/AgCl, respectively. APC and CPC were recorded at a scan rate of 1 mV/s.

The OCP was re-established between each measurement step.

2.6 ROTATING DISK ELECTRODE (RDE) MEASUREMENTS

The RDE voltammetric measurements were performed using home-made aluminum alloy disk electrode with an Autolab rotator with maximum rotation speed of 10000 rpm. The RDE was prepared by press fitting a AA2024-T3 rod into a Teflon shroud. The diameter of the disk electrode was 6 mm (0.28 cm^2). The shroud was 5 cm long and 12 mm in diameter. A three-compartment glass cell as shown in Figure 2.4 was used for all RDE measurements.

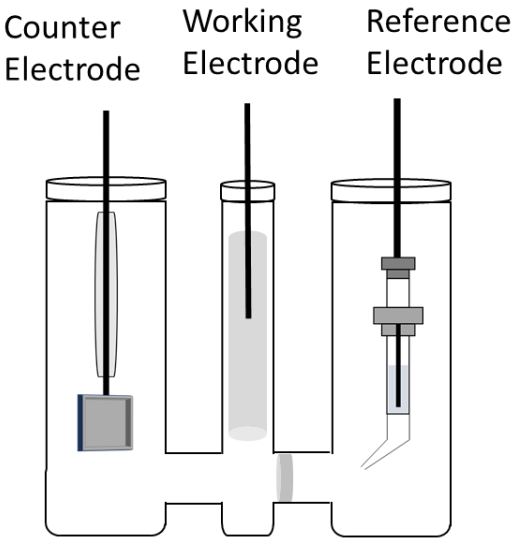

Figure 2.4 Schematic of the three-compartment cell used for RDE measurements. Positioning of the AA2024-T3 working electrode, Pt flag counter electrode and Ag/AgCl reference electrode is indicated.

2.7 ACCELERATED DEGRADATION TESTS

Laboratory electrochemical experiments are predictive only about the the corrosion protection provided by a coating. These data do not necessarily reflect how the coating will perform during environmental exposure. Accelerated degradation tests are used to mimic the conditions a coated specimen will experience in service. One legacy accelerated degradation test is the neutral salt spray exposure (ASTM B117). Military specifications (Mil spec doc.??) call for conversion coating assessment on aluminum alloys during salt-spray exposure for 14 days. Other accelerated degradation tests include - full solution immersion in a salt solution and a so-called, a thin layer mist test developed in our laboratory t. Post testing, specimens are generally cleaned with concentrated nitric acid for 1-2 minutes to remove corrosion product from the surface. The degree of corrosion damage is then analysed by specimen mass loss measurements (mass gain indicates corrosion product build up and mass loss indicates metal oxidation) and other tools to assess the surface texture such as scanning optical profilometry and digital microscopy.

5-Day Full Immersion Test.

The AA2024-T3 specimens were fully immersed in 3.5 wt. % NaCl for 5 days at room temperature in a $1cm^2$ flat cell. The cell was left undisturbed during the test period. Orifices in the cell ensured oxygen replenishment in the electrolyte. OCP and EIS measurements at the OCP were recorded daily to monitor changes in the electrochemical behavior of coated and uncoated aluminum alloys.

14-Day Neutral Salt Spray (NSS) Test – ASTM B117.

The aluminum alloy specimens were exposed to a 14-day neutral salt spray (NSS) (ASTM B117, 5 wt. % NaCl and 35 ± 1°C) in a commercial 4 ft^3 salt-spray chamber (MX 9204, Associated Environmental Systems). The test was conducted according to standard ASTM practice. The salt

solution in the chamber was refilled daily. Figure 2.5 shows an image of the ASTM B117 test chamber used to conduct the test under controlled conditions.

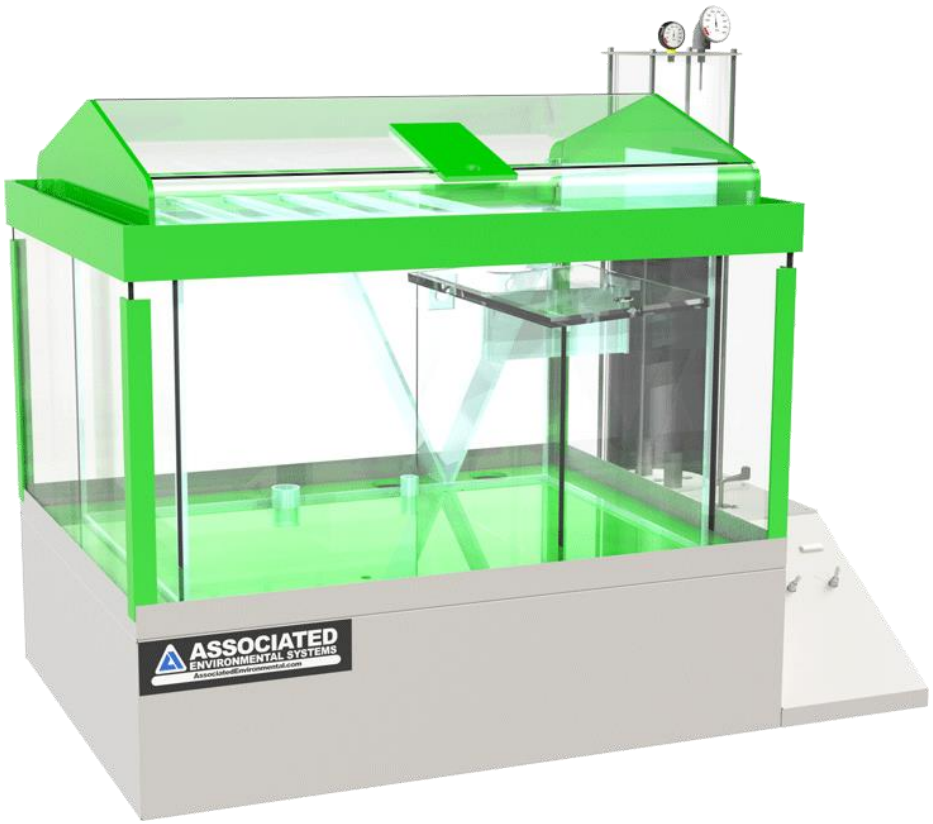

Figure 2.5 Photograph of the salt spray chamber apparatus used for 14-day ASTM B117 test.

14-Day Thin Layer Mist (TLM) Test.

This test was developed to understand the effects of moisture condensate on aluminum alloy surfaces. AA2024-T3 specimens were positioned horizontally on a platform in a container with DI water. Specimens are sprayed with a thin mist of 0.25% $NaHCO_3$ + 0.9% NaCl + 0.1% $CaCl_2$ solution. The container is then sealed and placed in an over at 55°C and 100% RH. After every 24-h, the specimens are removed from the oven and allowed to cool for 1-h. The specimens are then allowed to re-heat for 1-h before re-misting. This allows for a thermal stress cycle. The specimens are placed back in the over after re-misting. The test is conducted for 14 days. At the end of the

period, specimens are thoroughly rinsed with DI water and dried before examination. Figure 2.6 shows a schematic of the TLM test set up.

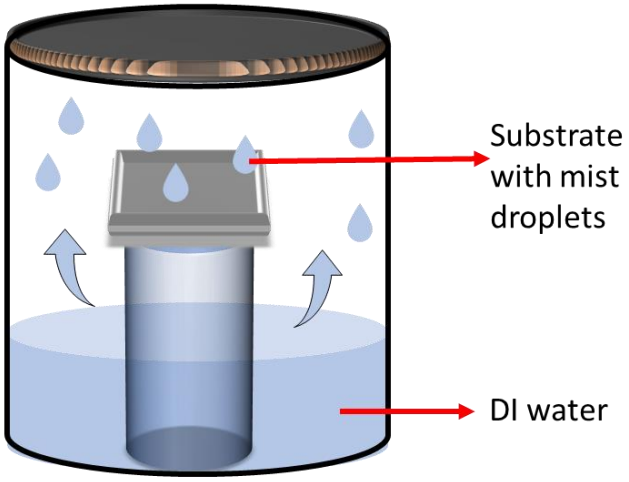

Figure 2.6 Schematic of the thin layer mist (TLM) test setup showing mist droplets on the substate surface and humidity within the container.

CHAPTER 3. EFFECT OF DEOXIDATION ON SURFACE MORPHOLOGY AND CORROSION PERFORMANCE OF TCP COATED AA2024-T3.

3.1 INTRODUCTION

The structure, formation mechanisms and corrosion resistance of conversion coatings formed on aluminium alloys is influenced by the alloy surface chemistry. Surface pretreatment processes aid in obtaining a clean, low oxide surface prior to formation of a conformal conversion coating.[1,2] Thus, it is essential to understand how pretreatment affects the alloy surface chemistry and microstructure. Typical surface pretreatment involves: (i) degreasing and (ii) deoxidation or desmutting.[3-5] Degreasers are weakly alkaline solutions containing mainly surfactants and phosphates that remove residual oil and grease contaminants from the alloy surface. The deoxidation step helps dissolve the pre-existing aluminum oxide layer. [5] The deoxidation step, in addition to removing the surface oxide layer also causes dealloying of surface intermetallics and subsequent redistribution of nanometer-sized domains of these metals across the surface . [6-9] Previous research work has shown that deoxidation pretreatment does influence the formation and performance of chromate conversion coatings and TCP coatings. [10-12]

In this work, the effect of two commercially available deoxidisers (Turco Liquid Smut Go and SurTec 495L) on the formation of TCP pre-treated AA2024-T3 was studied. To date, there have been few reports on how surface pretreatment affects TCP coating formation and properties and if such processes could be detrimental to coating performance. Our group has previously studied the effects of increased deoxidiser exposure time on the performance of Bonderite T5900 (TCP) coated on AA2024-T3. It was reported that increased exposure to deoxidiser produces a roughened surface texture and increased pitting. Buchheit et al, reported that the deoxidation step affects the formation of conversion coating by altering the surface chemistry of the alloy. [13-15] Therefore,

proper surface pretreatment is critical for forming a continuous, defect-free conversion coating. [2,6,8,16-17]

The hypothesis tested is that the formation of a low-defect TCP coating on an alloy surface is strongly influenced by deoxidation time as this alters the surface chemistry and texture of a metal prior to forming a conversion coating. In addition to deoxidation time, the chemical makeup of the different variants of commercially available deoxidisers could also play a role in altering the alloy surface chemistry. Fluoride ions present in deoxidisers are responsible for oxidatively attacking the surface oxide and providing a low oxide surface for TCP formation.[5] A higher fluoride ion concentration in some deoxidisers results in Al metal dissolution in addition to oxide layer removal producing a pitted surface with pits that are several microns deep. Therefore, the optimal deoxidiser exposure time depends on the product used. This chapter presents evidence to show that increased deoxidiser exposure time increases surface roughness, surface pit depth and pit densities for both deoxidisers but to varying degrees. TCP formed on such surfaces is defective and incompletely protects the surface, exposing many regions of unprotected metal to the environment. These regions become potential sites for corrosion initiation. In this study, two commercially available deoxidisers (Turco Smut Go and SurTec 495L) have been compared to show effects on surface morphology of AA2024-T3 after 1, 2- and 4-min exposure times. The performance of a TCP coating formed on AA2024-T3 deoxidised for 1, 2- and 4-minute time intervals is also reported.

3.2 MATERIALS AND METHODS

Reagents.

Turco 6849 (20% v/v, Henkel Corp., Madison Heights, MI) and SurTec 133 (4% w/v SurTec Inc, Brunswick, Ohio) were used as degreasers. Industrial grade Turco liquid Smut-Go (20% v/v,

Henkel Corp.) and SurTec 495 L (20% v/v, SurTec Inc) were the commercial deoxidisers evaluated. Two commercial TCP coatings, Alodine T5900 RTU (Henkel Corp.) and SurTec ChromitAL 650 (20% v/v, SurTec Inc) was used to study the effects of the respective deoxidisers. All solutions were prepared with ultrapure water (Barnsted E-pure) having a resistivity of >17 MΩ-cm.

Specimen Preparation.

The AA2024-T3 specimens were abraded, polished and degreased according to the protocol described in Chapter 2 (Section 2.2). The degreased specimens were then deoxidised at room temperature in one of two commercial deoxidisers (Turco Liquid Smut-Go or SurTec 495L) for 1, 2 or 4 min. This was followed by a city tap water rinse for 2 min. The deoxidised samples were then immersion coated in one of the TCP coating baths. Specimens were coated in Alodine T5900 bath for 10 min at room temperature or in SurTec ChromitAL 650 for 4 min at 30-40 ℃. After coating, the specimens were rinsed in city tap water for 2 min followed by 30 s ultrapure water rinse. The TCP-coated specimens were aged overnight in a loosely covered petri dish prior to any testing.

3.3 TESTING & CHARACTERIZATION

Accelerated Degradation Tests – Neutral Salt-Spray Test (ASTM B117).

A commercial $4ft^3$ chamber (MX92004, Associated Environmental Systems) was employed for the neutral salt spray exposure, as per ASTM B117. Specimens were exposed for 7 days (168 h) to a neutral salt spray (5 wt.% NaCl at 35 ℃). The salt solution in the tower was refilled each day to maintain a constant fog composition throughout the test.

***Electrochemical Characterization*.**

All electrochemical measurements were conducted in a single-compartment glass cell using a computer-controlled electrochemical workstation (Gamry Instruments Inc.). The coated alloy was mounted at the bottom of the cell with an O-ring defining the geometric area (0.48 cm^2) exposed to the electrolyte. A Pt foil served as the counter electrode and a home-made Ag/AgCl (3 M KCl) electrode was used as the reference. All measurements were made at room temperature in naturally-aerated 0.5 M Na_2SO_4 + 0.05 M NaCl.

Electrochemical testing was conducted according to the protocol summarized in Chapter 2 (Section 2.3). Separate specimens were used for the anodic and cathodic polarization measurements. The polarisation resistance was calculated by fitting the experimental EIS data using ZView software to an equivalent circuit representative of metal/coating interface. Figure 3.1 shows the equivalent circuit used to fit EIS data for TCP coated samples.[18]

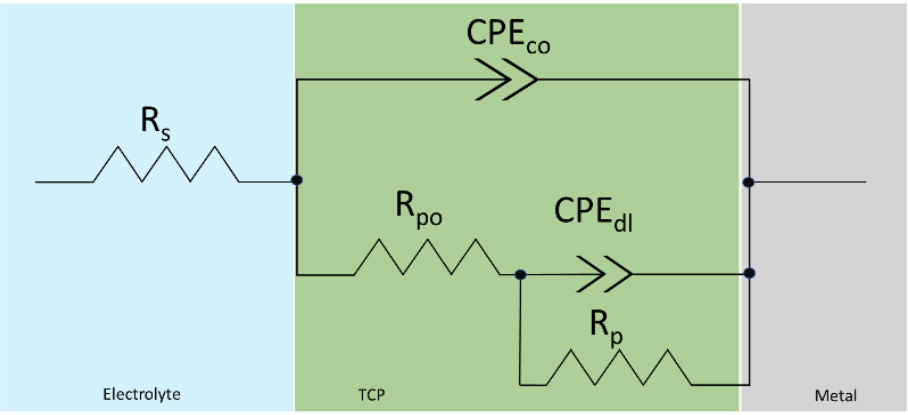

Figure 3.1 Equivalent circuit model used to represent the surface of a degreased, deoxidised and TCP-coated AA2024-T3.

The interface is modelled to represent the TCP coating as a barrier layer with pores and defects allowing oxygen and electrolyte solution penetration to underlying alloy. In the equivalent circuit, R_s is the solution resistance. R_{po} and R_p represent the pore resistance and polarisation resistance,

respectively. CPE_{co} is the constant phase element representing coating capacitance and CPE_{dl} is the metal-solution interfacial layer capacitance in the pores.[18] For statistical analysis, all measurements were repeated three times with values being reported as mean ± standard deviation.

Chemical Analysis.

Analysis of the fluoride ion concentration in the coating bath was made potentiometrically with a fluoride ion selective electrode (Orion, Thermo Scientific). Quantitation was performed using response curves generated with external standards (0.1-100 ppm).

Surface Characterization.

Scanning contact profilometry (Nanomap 500LS, Germany) used to measure surface roughness, pit depth and pit densities of the specimen.

Scanning electron micrographs were obtained on JEOL 6610 scanning electron microscope (Tokyo, Japan). Energy Dispersive Spectra were obtained through Aztec software. Detailed description of measurement conditions is provided in Chapter 2.

A Digital microscope (Keyence VHX 600) was also used to obtain 3-Dimensional pit depth information after the salt-spray exposure. The depth resolution with the microscope was 0.2 µm. Detailed description of measurement conditions is provided in Chapter 2.

3.4 RESULTS

Figure 3.2 summarizes effect of deoxidation time on the surface texture morphology of AA2024-T3 for the two deoxidisers used. Surface roughness, pit density and pit depth data are presented in Figure 3.2. The data were obtained by scanning contact profilometry. Data are presented as mean ± std. dev. for three 1mm x 1mm areas on each specimen. Results show that both deoxidisers increase the surface roughness, pit density and pit depth of the alloy with increase in deoxidation time. The degree of surface roughening and pitting, however, appears slightly lower

for the Turco Smut Go deoxidised specimen as compared to SurTec 495L deoxidised specimens for all times. Similarly, the maximum pit depths are much higher for specimens deoxidised with SurTec 495L as compared to Turco Smut-Go.

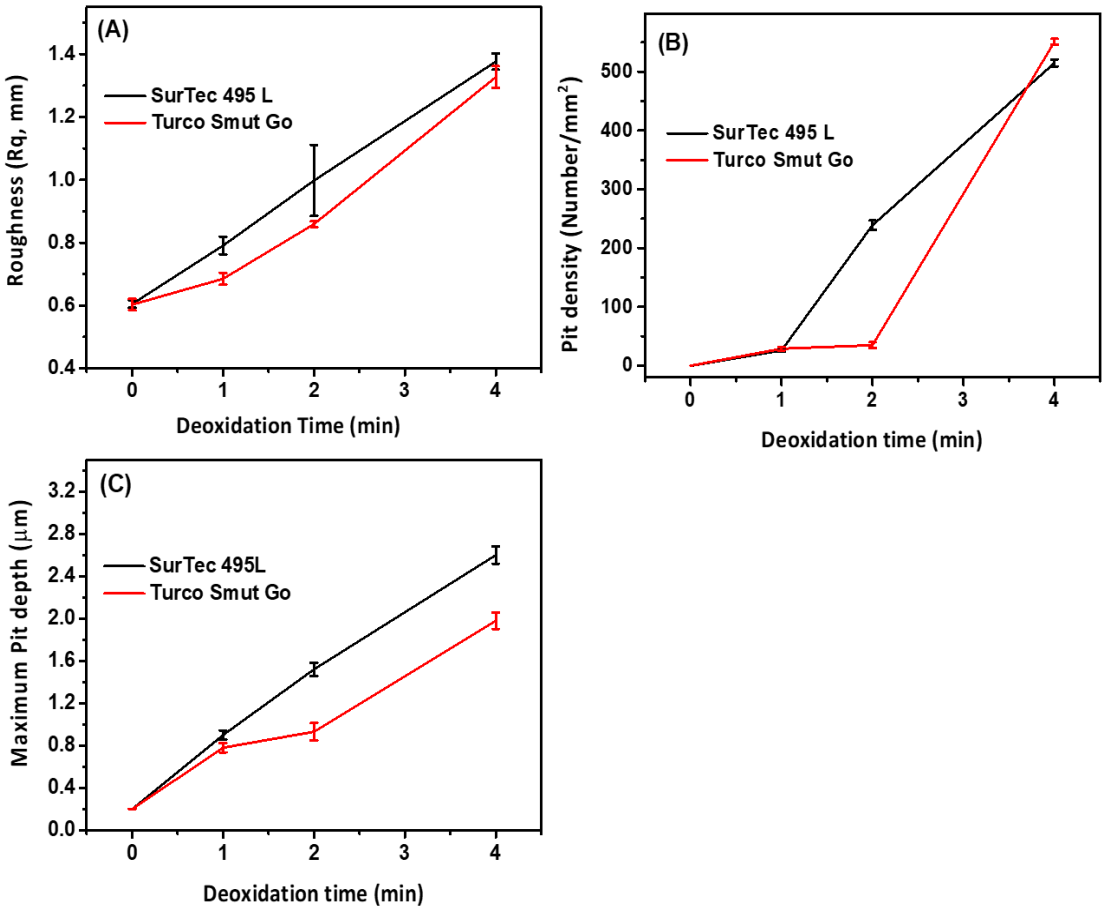

Figure 3.2 Contact profilometry data showing (A) surface roughness (B) pit density and (C) maximum pit depth for SurTec 495L and Turco Smut-Go deoxidised AA2024-T3 specimens. Data are presented as average ± std. dev. for areas on each specimen.

The SEM micrographs shown in Figure 3.3 are consistent with profilometry data showing increased surface damage, growing pit diameters, and pit densities with increasing deoxidation time. The morphological changes appear dependent on the type of deoxidiser used with SurTec 495L deoxidised surfaces showing a greater degree of pitting and surface roughening within 2 min of exposure. Between 2 and 4 min, the Turco Smut-Go deoxidised surface shows increase in pit

numbers, but pit diameters appear unchanged whereas an increase in both pit number and pit diameter is seen for SurTec 495L deoxidised surfaces.

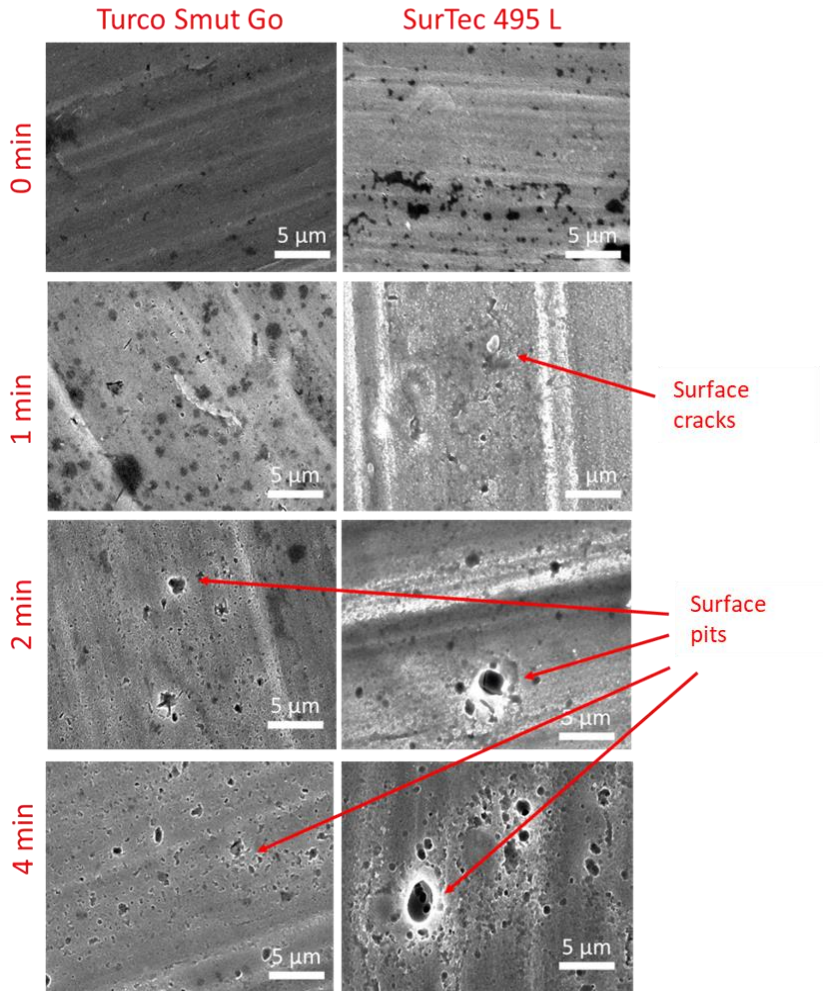

Figure 3.3 SEM micrographs of degreased AA2024-T3 surface deoxidised for 0, 1, 2 and 4 minutes in Turco Smut-Go (left) and SurTec 495L (right). Arrows indicate changes in surface morphology caused by the deoxidation process.

Figure 3.4 shows the potentiodynamic polarisation curves for AA2024-T3 specimens pre-treated in the two deoxidisers for 1, 2 and 4 min. All figures show a common trend of increasing anodic and cathodic current with increase in deoxidation time. The magnitude of current increase is dependent on the deoxidiser type. Increasing deoxidation time resulted in a less positive E_{pit}

value – the onset potential for stable pit formation and growth (indicated by arrows). The anodic and cathodic polarisation curves for 1 and 2 min deoxidised AA2024-T3, behave identical when deoxidised with Turco Smut Go while the two samples behave very differently for 495L treated specimen. Current increase within the initial 2 min is more evident for 495L deoxidised specimens indicating a greater surface modification within a short time. This observation is consistent with the SEM micrographs shown in Figure 3.3. On the other hand, the pitting potential, anodic and cathodic currents for samples deoxidised with Turco Smut-Go are similar for the initial 2 minutes indicating minimal changes in surface intermetallic chemistry. Overall, for specimens deoxidised in 495L, anodic currents increase significantly with immersion time. The pitting potential, E_{pit}, also shifts to more negative potentials with increasing deoxidation time. The cathodic current for 4 min deoxidised specimen is 6x higher than that of a 2 min deoxidised specimen. On the contrary, the anodic and cathodic currents for samples deoxidised in Turco Smut-Go only increase slightly and no statistical difference in pitting potentials are observed. It is reasonable to conclude that SurTec 495L is more aggressively altering alloy surface morphology as compared to Turco Smut Go.

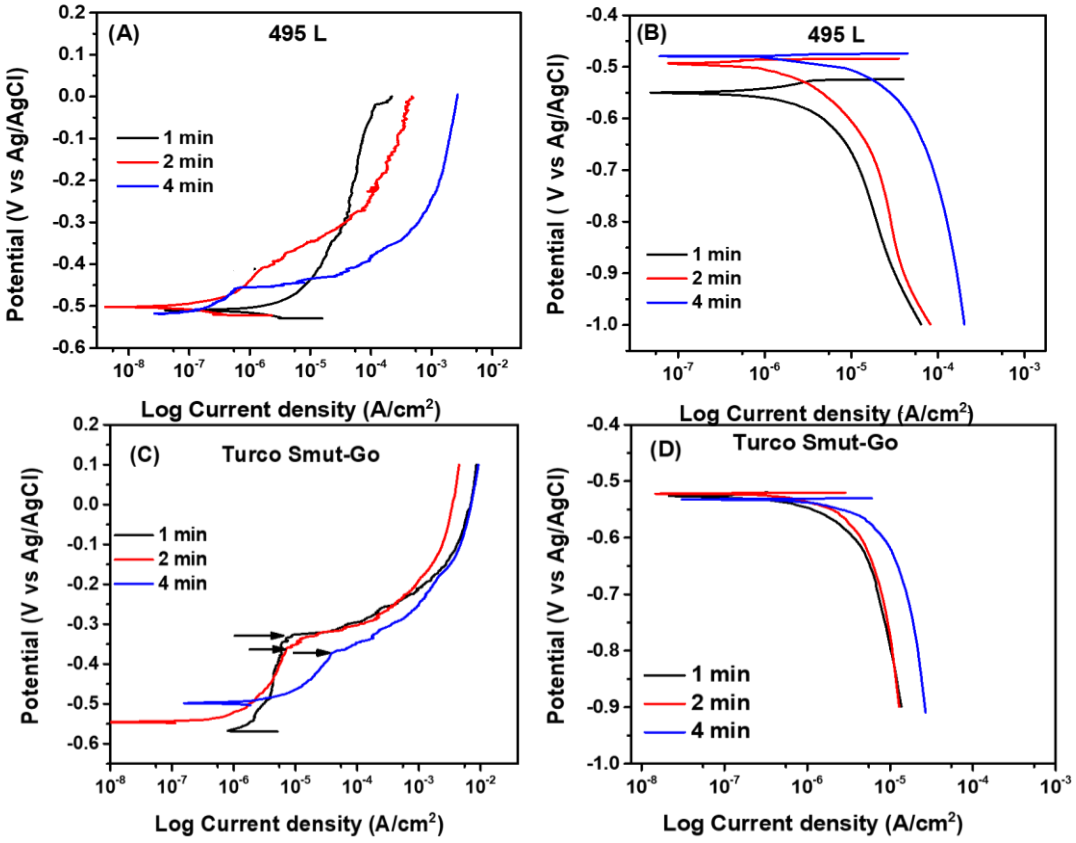

Figure 3.4 Anodic (A) and cathodic (B) potentiodynamic polarization curves for degreased AA2024-T3 deoxidised in SurTec 495L for 1, 2 and 4 min. Anodic (C) and cathodic (D) polarization curves for degreased AA2024-T3 deoxidised in Turco Smut-Go for 1,2 and 4 min. Naturally- aerated 0.5 M Na2SO4 + 0.05 M NaCl was used as electrolyte. Arrows indicate pitting potentials (E_{pit}).

The effect of the deoxidation treatment on the elemental composition of the alloy was investigated using SEM with EDXS analysis. Figure 3.5 shows the scanning electron micrographs and Al and Cu elemental maps for AA2024-T3 deoxidised specimens with 495L for 1,2 and 4 min. Elemental maps reveal that with increased deoxidation time, larger areas of Cu-containing second phase particles are exposed to the surface due to etching of surrounding Al. After 1 min, initial trenching around second phase particles is seen. Trenching around these particles becomes more extensive with deoxidation time. After 4 min, the diameter of Cu particles exposed, is almost 3x

larger than the initial size. This increases the surface area available on these cathodic particles for oxygen reduction. This leads to increased cathodic currents.

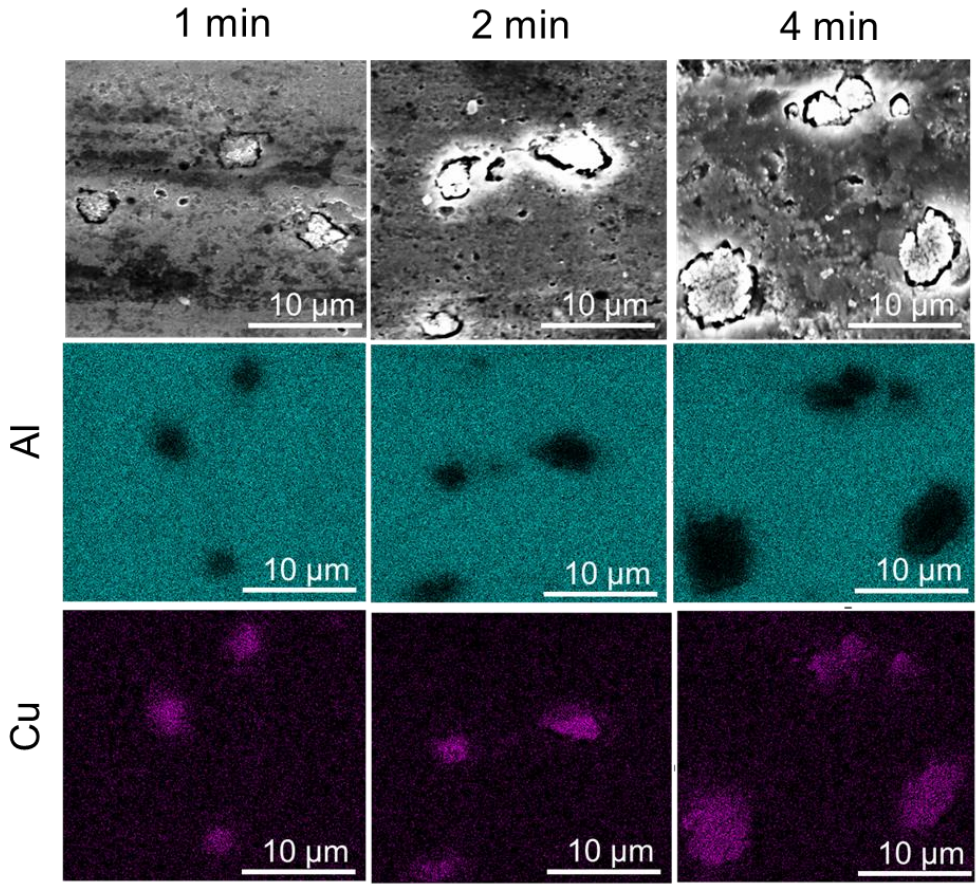

Figure 3.5 Scanning electron micrographs and EDX elemental maps showing the distribution of Al and Cu across AA2024-T3 specimen deoxidised in 495L for 1, 2 and 4 min.

Figure 3.6 and Table 3.1 presents a summary of numerical electrochemical parameters for uncoated and TCP-coated AA2024-T3 specimens pretreated in 495L for different deoxidation times. TCP provides anodic and cathodic inhibition to uncoated aluminum alloys by suppressing currents by a factor of 10-100x. However, TCP coated samples deoxidised for longer durations (4 min) exhibit electrochemical behavior comparable to uncoated control specimens deoxidised for 1 min. The pitting potentials shifts more negative (less noble) with increasing deoxidation time for both uncoated and TCP-coated samples. For example, the 4 min deoxidised + TCP coated

specimen surface appears to start pitting 200mV earlier than the 1 min deoxidised + TCP coated specimen. A 5x increase in anodic and cathodic currents is also seen for 4 min deoxidised + TCP coated AA2024-T3 as compared to 1 min deoxidised + TCP coated AA2024-T3. In fact, the anodic and cathodic currents for a 4 min deoxidised + TCP coated sample are comparable to an uncoated specimen deoxidised for 1 min.

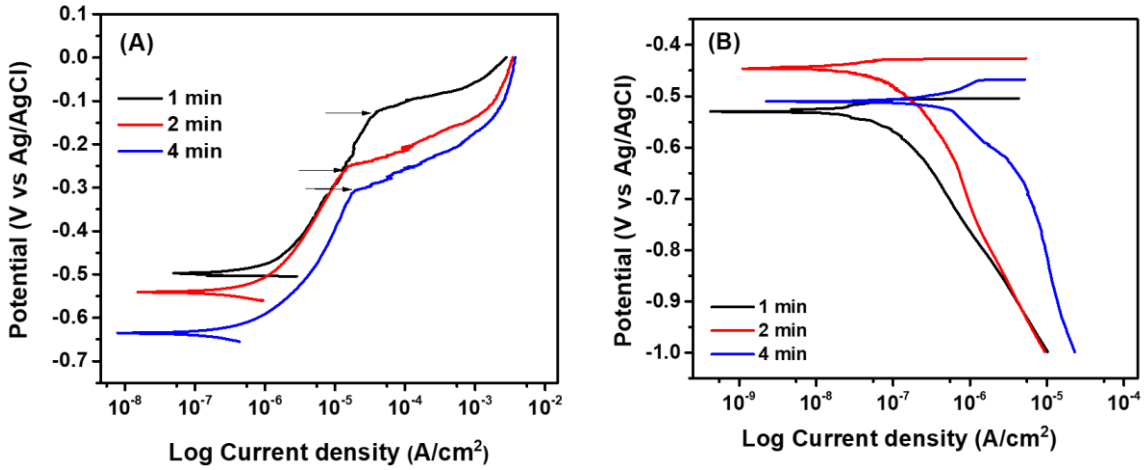

Figure 3.6 (A) Anodic and (B) cathodic polarisation curves for TCP-coated AA2024-T3 specimens deoxidised in SurTec 495L for 1, 2 and 4 minutes.

Table 3.1 summarizes the effect of deoxidation time on crucial electrochemical parameters for uncoated and TCP-coated AA2024-T3. The general trend is:

(i) Presence of TCP-coating inhibits surface anodic and cathodic reactions but excessive deoxidation results in a defective TCP coating incapable of providing superior corrosion protection.

(ii) Increase in deoxidation time causes earlier breakdown of TCP coating on the alloy surface.

(iii) Increase in deoxidation time results in increased anodic and cathodic currents for both uncoated and TCP-coated AA2024-T3.

Table 3.1 Summary of electrochemical parameters measured for TCP coated and uncoated AA2024-T3 deoxidised with 495L for varying time intervals.

.

	Uncoated AA2024-T3			TCP-coated AA2024-T3		
	1 min	**2 min**	**4 min**	**1 min**	**2 min**	**4 min**
E_{pit} (V)	-0.35 ± 0.036	-0.39 ± 0.003	-0.46 ± 0.008	-0.11 ± 0.003	-0.25 ± 0.006	-0.32 ± 0.007
log i @ -0.3V ($\mu A/cm^2$)	33 ± 16	32 ± 9	842 ± 75	6 ± 15	6 ± 7	10 ± 11
log i @ -0.7V ($\mu A/cm^2$)	21 ± 7	53 ± 15	287 ± 28	0.91 ± 4	1 ± 13	11 ± 16

Figure 3.7A shows the cyclic voltammograms of TCP-coated AA2024-T3 specimens deoxidised for 1, 2 and 4 min. Voltammograms were collected by scanning potential from OCP to -0.75V and back to -0.25V. The area under the voltammogram represents charge associated with aluminum dissolution. A defective surface accumulates more charge indicating non-uniform coating. As seen in the figure, TCP formed over after excessive deoxidation (4 min), leads to earlier coating breakdown and greater charge accumulation.

Figure 3.7B presents the electrochemical impedance data (Nyquist plot) comparing TCP coated AA2024-T3 deoxidised for 2 and 4 min. The R_{ct} was obtained from the diameter of the semicircle on the real axis. A lower charge transfer resistance indicates faster electron transfer kinetics between the metal and its environment, in other words, faster aluminium dissolution kinetics. A 5x decrease in charge transfer resistance from 0.37 ± 0.03 M Ω cm^2 to 0.075 ± 0.09 M Ω cm^2 was seen on increasing deoxidation time from 2 to 4 min. The polarisation resistance for 4 min deoxidised + TCP coated surface was comparable to an uncoated control (0.074 ± 0.06 M Ω cm^2). In addition to lower charge transfer resistance, the pore resistance of the TCP coated

specimen also decreases with increasing deoxidation time. R_{po} for TCP coated specimen decreases 12x times from 172 ± 31 Ω cm^2 for 2 min deoxidised surface to 15 ± 6 Ω cm^2 for 4 min deoxidised surface. This can be attributed to the highly discontinuous and porous coating formed on a surface roughened and pitted by deoxidation. Such an incoherent coating will more likely expose many regions of uncoated metal to atmospheric oxygen and electrolyte. The higher pore resistance observed for a 2 min deoxidised + TCP coated specimen is presumably due to a comparatively non-porous coating.

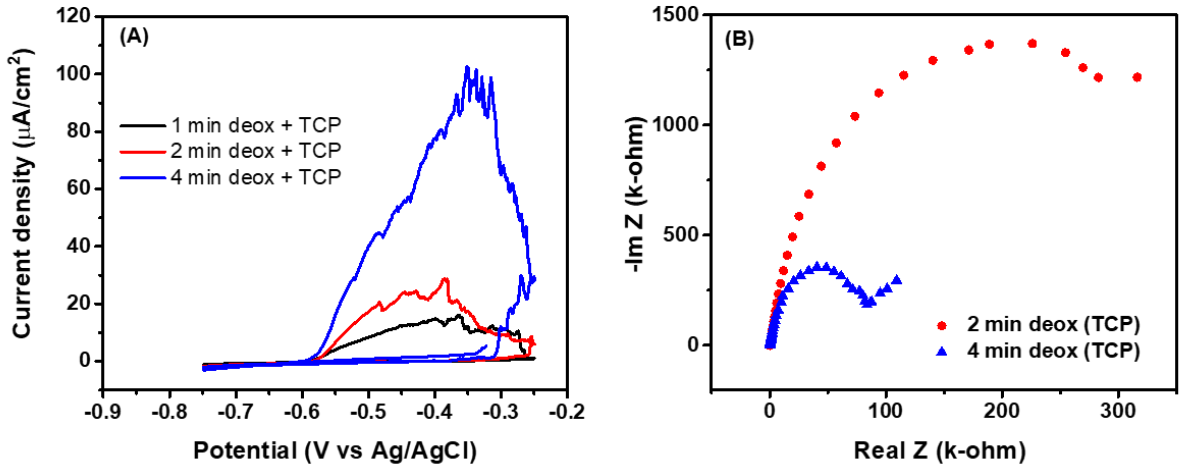

Figure 3.7 (A) Cyclic Voltammograms of SurTec E coated AA2024-T3 deoxidised for 1,2 and 4 min (B) Nyquist Plot of uncoated and SurTec E coated AA2024-T3.

TCP coated specimen deoxidised for 1, 2 and 4 minutes were subjected to 7-day Neutral Salt Spray test (B117) to evaluate their performance under corrosive conditions and validate laboratory results. Figure 3.8 shows the surface maps of TCP coated alloys post degradation testing. The red dots represent pits on the surface formed during the B117 test. Data reveals that TCP coating formed over surfaces deoxidised for longer durations provides inferior corrosion protection during the test period with greater pit density and pit diameters. The histogram shows pit size distributions across the surface. Pit diameters and densities increase as a function of deoxidation time. This is

consistent with electrochemical data indicating earlier TCP breakdown for excessively deoxidised surfaces.

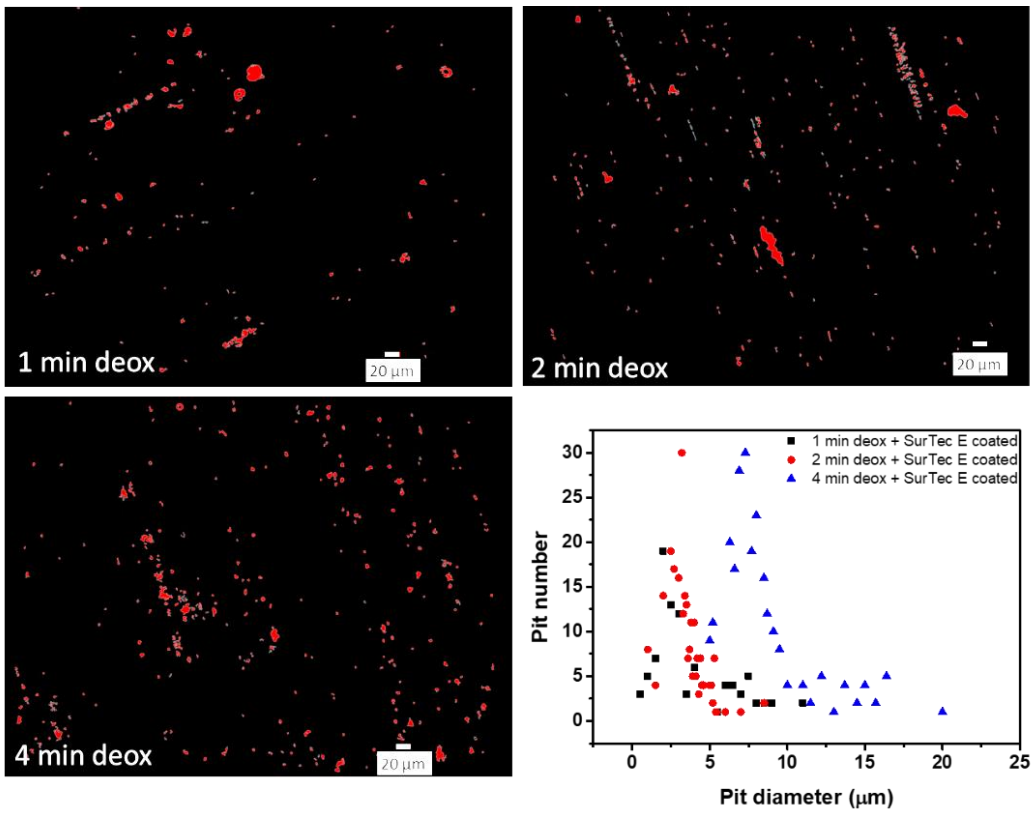

Figure 3.8 Digital maps of pit distribution across AA2024-T3 specimens deoxidised for 1, 2- and 4-min after 7-day neutral salt spray exposure. time intervals. The histogram shows the minimum pit diameter vs pit number distribution across the surface.

3.5 DISCUSSION

The naturally occurring aluminum oxide layer is thin and defective around second phase particles in the alloy. These are sites for preferential aluminum dissolution during deoxidation in the acidic fluoride medium. Excessively deoxidising metal surfaces creates a highly irregular alloy surface with pits consisting of steep walls and ridges. It is reasonable to assume that the TCP forms non-uniformly. Therefore, the degree of corrosion protection provided by a TCP coating will decrease as the alloy surface is more damaged. Figure 3.9 shows a schematic of a proposed TCP coating structure on a properly deoxidised and excessively deoxidised AA2024-T3 surface.

Results indicate that the deoxidation step significantly affects alloy surface texture by altering surface roughness, pit depth and density. Controlling the deoxidation time during specimen pretreatment is therefore critically important for optimum corrosion protection by the coating. Commercial deoxidising solutions have different chemical compositions with varying fluoride ion concentrations and pH. When the alloy is deoxidised, fluoride ions adsorb on the surface and oxidatively attack the passive aluminium oxide layer.[5] Increased exposure to deoxidiser results in extensive surface attack in addition to passivation layer breakdown. Thus, knowledge about fluoride ion concentration in the deoxidiser is critical in understanding its effect on alloy surface chemistry. Estimation of fluoride ion concentration in the deoxidisers revealed that SurTec 495L (1.475 ppm) contained 35% higher fluoride concentration as compared to Turco Smut Go (1.086 ppm). The increased surface roughening observed for 495 L exposed surfaces within shorter time durations can be attributed to the higher fluoride ion concentration. However, for longer exposure times, both deoxidisers have a deleterious effect on the metal surface. Excessive deoxidation also causes increase in surface area of secondary phase intermetallic particles and redistribution of those IMPs in the alloy matrix as supported by EDS data. With increasing deoxidation time, larger intermetallic area is exposed to the surface due to dissolution of surrounding Al. This leads to increased current for the reduction of dissolved oxygen and therefore an increased rate of aluminum dissolution under open circuit conditions. The conservation of charge requires that the total cathodic current must be equal to the total anodic current. Increasing one current necessarily causes the increase in the other current. Since, corrosion protection provided by a TCP coating depends on the surface microstructure of the alloy over which the coating is formed. A highly roughened alloy surface caused by excessive deoxidation contains several sharp edges and steep walls which are unlikely to be passivated by the coating (Figure 3.9). These walls are mostly

around IMPs leaving these areas unprotected which become potential sites for corrosion initiation and propagation. TCP formed over excessively deoxidised surfaces thus provides inferior corrosion protection due to non-uniform surface coverage.

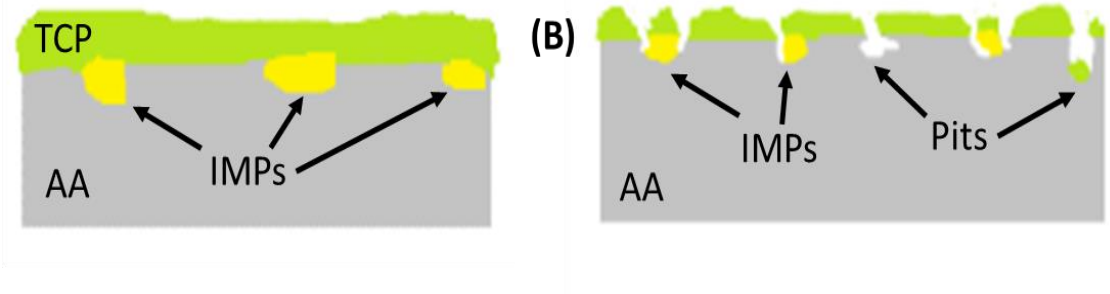

Figure 3.9 Proposed TCP structure on (A) degreased, cleaned and less defective surface (B) degreased, cleaned and excessively damaged surface.

Corrosion inhibition provided by TCP on AA2024-T3 was assessed in naturally aerated 0.5 M Na_2SO_4 +0.05 M NaCl. The breakdown potential for pit initiation was observed to shift to less positive potentials as a function of deoxidation time. The anodic and cathodic currents also increased with increased deoxidation time for both uncoated and TCP coated AA2024-T3. The electrochemical performance of TCP formed over an excessively deoxidised AA2024-T3 surface resembled that of an uncoated alloy. The polarization resistance, R_p, for 4 min deoxidised + TCP coated substrate is of the same order as an uncoated alloy. In addition, the low pore resistance likely provides a path for mass transport of dissolved O_2 to the underlying metal surface. Accelerated degradation tests also comply with the hypothesis of a less protective TCP coating. TCP coated AA2024-T3 after a 4 min deoxidation performed worse during salt spray test with greater pit density and pit diameter. The histogram revealed that most pits for this specimen had diameters ranging from 5-10 microns and few larger pits with diameters (20-25 µm) were also

observed. The 1 and 2 min deox + TCP coated samples however showed pits ranging in diameters between 0-5 μm.

3.6 CONCLUSIONS

In this work, the effect of deoxidation time on surface chemistry and microstructure on AA2024-T3 using two different commercial deoxidisers was investigated. It was found that deoxidation affects surface roughness, pit depths and densities and therefore is an important parameter to control during pre-treatment processes. Increased deoxidiser exposure increases surface roughening and promotes pit formation and growth on the alloy. The extent of surface damage is dependent on the type of deoxidiser and varies with the concentration of fluoride ions in the deoxidiser. Non-uniformly coated surfaces are more prone to corrosion attack than a conformally coated surface. A TCP coating formed over an excessively damaged surface behaves electrochemically similar to an uncoated control. A continuous, defect free conversion coating has high polarisation, pore resistance and serves as a barrier to oxygen/ electrolyte diffusion. Thus, it provides superior corrosion protection under laboratory conditions and during accelerated degradation testing. Post-test analysis revealed inferior TCP performance with increased deoxidation time. Increased deoxidiser exposure leads to the formation of deep irregularly shaped surface pits with steep walls. Such areas are not uniformly covered by the TCP coating and are potential sites for corrosion initiation and coating failure.

Although the deoxidation pre-treatment step causes issues with regard to coating formation and protection, it is an important pre-treatment process as it removes unnecessary smut and the natural oxide layer from the alloy surface required to form a coherent TCP coating. Therefore, the process cannot be eliminated entirely but care should be taken in controlling the deoxidiser time to minimize deleterious modifications to surface microstructure of the alloy.

REFERENCES

REFERENCES

(1) U. S. Military Specification, MIL-DTL-5541F: Detail Specification: Chemical Conversion Coatings on Aluminum and Aluminum Alloys, Department of Defense, **2006**.

(2) Hagans, P. L.; Hass, C. M. Influence Of Metallurgy On The Protective Mechanism of Chromium-Based Conversion Coatings on Aluminum–Copper Alloys. *Surf. Interface Anal*. **1994**, *21*, 65.

(3) Moffitt, C. E.; Wieliczka, D. M.; Yasuda, H. K. An XPS Study of The Elemental Enrichment on Aluminum Alloy Surfaces from Chemical Cleaning. *Surf. Coat. Technol*. **2001**, *137* (2-3), 188-196.

(4) Cherepy, N. J.; Shen, T. H.; Esposito, A. P.; Tillotson, T. M. Characterization Of An Effective Cleaning Procedure for Aluminum Alloys: Surface Enhanced Raman Spectroscopy And Zeta Potential Analysis. *J. Colloid Interf. Sci*. **2005**, *282* (1), 80-86.

(5) Li L. L.; Desouza A. L.; Swain, G. M. Effect of Deoxidation Pretreatment on the Corrosion Inhibition Provided by a Trivalent Chromium Process (TCP) Conversion Coating on AA2024-T3. *J. Electrochem. Soc*. **2014**, *161* (5) C246-C253.

(6) Van Westing E. P. M.; Campestrini P.; De Wit J. H. W. Influence of Surface Preparation On Performance Of Chromate Conversion Coatings On Alclad 2024 Aluminium Alloy: Part I: Nucleation And Growth. *Electrochim. Acta*. **2001**, *46*, 2553.

(7) Li, R.; Sun, X.; Wong, K. C.; Mitchell, K. A. R.; Foster, T. Surface Effects In Chromate Conversion Coatings On 2024-T3 Aluminum Alloy. *J. Mater. Sci*., **2001,** *36*, 3215.

(8) Keams, J. R.; Halada, G. P.; Clayton, C. R.; Kendig, M. W.; Jeanjaquest, S. L.; Peterson, G. G.; Shea-Mccarthy, G. The Electrochemical Meeting Abstracts, *Vol. 98-2*, Abstract 231, Boston, MA, Nov. 1-6, **1998**.

(9) Maddela, S.; Pinc, W. R.; O'Keefe, M. J.; Fahrenholtz, W. G. Formation Of Subsurface Crevices In Aluminum Alloy 2024-T3 During Deposition Of Cerium-Based Conversion Coatings. *Surf. Coat. Technol*., **2010**, *204*, 4095.

(10) Guo, Y.; Frankel, G. S.; Characterization Of Trivalent Chromium Process Coating On AA2024-T3. *Surf. Coat. Technol*., **2012**, *206*, 3895.

(11) Grant, J. T.; De Rosa, R. L.; Katsen, L.; Donley, M.; Bierwagen, G. P. *Corrosion* (Houston), 56, *395*, **2000**.

(12) Lunder, O.; Nisancioglu, K. *Corrosion* (Houston), 44, *414*, **1988**.

(13) Pinner, R.; Wernick, S.; Sheasby, P. G. The Surface Treatment and Finishing of Aluminum

and its Alloys, 5th ed.: ASM International, **1987**.

(14) Hughes A. E.; Buchheit, R. G. ASM Handbook, Vol. 13A, ASM International **2003,** 720-735.

(15) Ressier, L.; Lacrois, L.; Blanc,C.; Mankowski, G. Combination Of AFM, SKPFM, And SIMS To Study The Corrosion Behavior Of S-Phase Particles In AA2024-T351. *J. Electrochem. Soc.,* **2008**, *155*, C131.

(16) Taylor, R. J.; Hughes, A. E.; Hinton, B. R. W. Chromate Conversion Coatings on 2024 Al Alloy. *Surf. Interf. Anal*., **1997**, *25*, 223.

(17) Clayton, C. R.; Chidambaram, D.; Kendig, M. W.; Halada, G. P. Surface Pretreatments of Aluminum Alloy AA2024-T3 and Formation of Chromate Conversion Coatings. *J. Electrochem. Soc.*, **2004**, *151*, B613.

(18) Orazem, M. E.; Tribollet, B. Electrochemical Impedance Spectroscopy, 1st ed: Wiley, John & Sons, Incorporated **2008**, 5.

CHAPTER 4. EFFECT OF Cr(III) CONCENTRATION ON THE CORROSION RESISTANCE OF TCP CONVERSION COATING ON AA2024-T3.

Chapter adapted from *J. Electrochem. Soc.*, 165 (2), C103-C105 (2018). Copyright 2018, The Electrochemical Society.

Article: T. K. Shruthi and Greg. M. Swain, Communication – The role of trivalent chromium on the anti-corrosion properties of a TCP-conversion coating on aluminum alloy 2024-T3.

4.1 INTRODUCTION

TCP conversion coating bath, developed by NAVAIR, is the leading non-chromate replacement coating for aluminum alloys in the market.[1-28]sThe composition of TCP conversion coating bath is similar to Zr-based conversion coating baths containing fluorozirconate (H_2ZrF_6 or K_2ZrF_6) as the leading inhibitor component.[5,6] TCP, however, contains some added Cr(III) salts (≤5 wt.%).[7–9] While the actual composition of the TCP baths are proprietary, the coating bath is known to contain potassium hexafluorozirconate (K_2ZrF_6), fluoroboric acid (HBF_4) and Cr(III) salts ($Cr_2(SO_4)_3$).[7-9] Although, TCP is the leading replacement coating, little knowledge exists about the role of its coating components in the level of corrosion protection provided to AA2024-T3. Reports published previously indicate that fluoroboric acid added to the coating bath aids in dissolution of any native aluminum oxide layer present on the alloy surface and enables formation of a uniform conversion coating over the alloy surface. During coating formation, fluorozirconate in the coating bath precipitate over aluminum alloy surface as hydrated zirconia. The low electronic conductivity and high band gap of zirconia helps in reducing the rate of electron transfer reactions (anodic inhibition) occurring on the alloy surface. It is also known to improve adhesion with the primer layer. A plethora of reports have been published describing the mechanism by

which Zr-based conversion coatings baths protect aluminum alloys and other metals from corrosion.[10–15] However, no insight exists about the effect of added Cr(III). Chen et al., have reported adding Cr(III) to TCP conversion coating bath results in the formation of a denser coating, but the effect of Cr(III) on corrosion prevention of aluminum alloys was not explored.[16]

Results presented herein show the role of Cr(III) in the corrosion protection offered by TCP conversion coating formed on AA2024-T3. Potentiodynamic polarization, rotating disk voltammetric data and accelerated degradation tests show that Cr(III) plays a crucial role in suppressing cathodic reactions on the alloy surface by blocking sites for oxygen chemisorption on cathodically-active intermetallics.

4.2 MATERIALS AND METHODS

Reagents.

The degreaser (Turco 6849), deoxidizer (Turco Liquid Smut-go) and the two TCP conversion coatings (Bonderite T5900 RTU and T5900-NC) used were provided by Henkel Corp. (Madison Heights, MI). Ultrapure water (>17 MΩ·cm) used for all solution preparations was obtained from a Barnstead E-Pure system.

Specimen Preparation.

The uncoated and TCP-coated AA2024-T3 specimens were prepared according to procedure explained in Chapter 2 (Section 2.2). The degreaser and deoxidiser solutions were both diluted to 20 v/v % using ultrapure water. Two TCP baths were used – Bonderite T5900 RTU and T5900-NC. The chemical compositions for both conversion coating baths were similar except that no Cr(III) salts were added to T5900-NC (No Chrome). Both TCP conversion coatings were used as received. The coatings T5900 RTU and T5900-NC will henceforth be referred as TCP and TCP-NC respectively.

4.3 TESTING & CHARACTERISATION

Accelerated Degradation Test.

A 7-day neutral salt spray (NSS) test was conducted to evaluate the role of Cr(III) in the corrosion protection of AA2024-T3. The test was conducted according to ASTM B117 protocol explained in Chapter 2.

Electrochemical Characterization.

All electrochemical measurements were made in a three-compartment glass cell with a pre-treated AA2024-T3 as the working electrode, platinum flag counter electrode and a home-made Ag/AgCl (3M, E^o= +0.197 V vs NHE) reference electrode. A photograph of the cell used is shown in Chapter 2 (Figure 2.4). All measurements were made in naturally-aerated 0.5 M Na_2SO_4 + 0.1% NaCl at room temperature (23 ± 2 ^oC). The RDE used for studying oxygen reduction reactions (ORR) was pre-treated and immersion coated with TCP and TCP-NC exactly as described in Chapter 2.

Surface Characterization.

Secondary electron micrographs and energy dispersive spectra of conversion coated AA2024-T3 were obtained using a scanning electron microscope to study changes in coating morphology and composition caused by the presence of Cr(III) in the coating. Specifications of the instrument and conditions used to collect the micrographs are outlined in Chapter 2 (Section 2.7).

4.4 RESULTS

Figure 4.1 shows the potentiodynamic polarization curves for uncoated (bare) and conversion coated AA2024-T3 alloys in naturally-aerated 0.5 M Na_2SO_4 + 0.1% NaCl. Two conversion-coated specimens were compared: TCP (T5900) and TCP-NC (T5900-NC). Figure 4.1A shows the anodic polarization curves for all three specimens revealing anodic current suppression

provided by both conversion coatings. The curves show a negative shift of ~50-70 mV in OCP for both the TCP and TCP-NC-coated panels. However, statistically, the OCP for the uncoated and coated AA2024-T3 are similar. The electrochemical data are summarized in Table 4.1. Anodic currents in the passive region of the curve (-0.5 to -0.1V) are at least 10x lower for the coated specimens as compared to the current for the uncoated specimens. The magnitude of current suppression in the passive region between the OCP and E_{pit} is similar for both the conversion coatings. The pitting potential, E_{pit}, for the coated specimens is shifted positive by ~200-300 mV for the TCP and TCP-NC coated specimens. The uncoated specimen starts to pit at the OCP (-0.425 V) while the pitting poetntials were at -0.150 V for the TCP-NC-coated specimen and -0.100 V for the TCP-coated specimen. The suppressed anodic current and positive shift in E_{pit} seen for both conversion coatings suggests similar levels of anodic inhibition provided by the coatings.

The cathodic polarization curves shown in Figure 4.1B reveal differences in the corrosion protection mechanism of the two conversion coatings analyzed. The cathodic current in the potential range between -0.550V and -0.900 V arises from the reduction of dissolved oxygen in the electrolyte solution. The ORR current is largest for the uncoated AA2024-T3 specimen. The greatest suppression of oxygen reduction current was seen for the TCP-coated specimen – about 10x lower at -0.700 V. Although a suppressed current is observed for the TCP-NC-coated specimen, it is only half as much as for the TCP-coated specimen. The suppression in cathodic currents suggests that the conversion coatings also inhibit corrosion by reducing surface oxygen

reduction reaction kinetics. The highest suppression in ORR kinetics for the TCP-coated specimen suggests that Cr(III) plays an important in suppressing the cathodic rather than the anodic current.

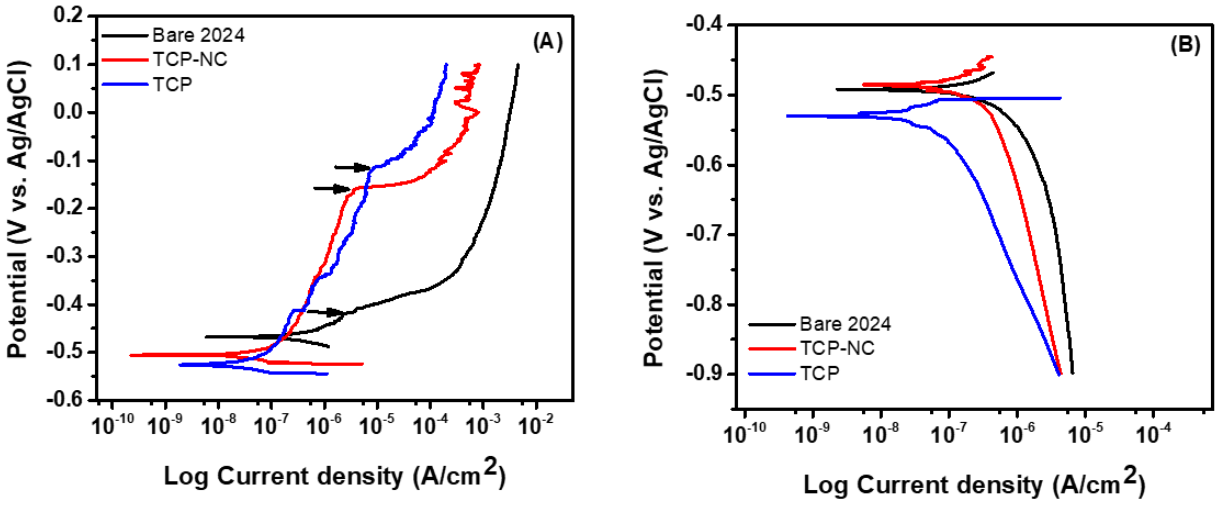

Figure 4.1 Potentiodynamic (A) Anodic and (B) Cathodic polarization curves of uncoated (bare) and conversion-coated AA2024-T3 in naturally-aerated 0.5 M Na_2SO_4 + 0.1% NaCl at room temperature. Scan rate = 1 mV/s. Arrows indicate E_{pit}.

Table 4.1 Summary of electrochemical data for uncoated and conversion coated AA2024-T3. Values reported as mean ± std. dev.

N = 3	**OCP (V)**	**log i @ -0.1V ($\mu A/cm^2$)**	**log i @ -0.7V ($\mu A/cm^2$)**
Uncoated (bare)	0.48 ± 0.08	2293 ± 333	3.5 ± 0.6
TCP-NC	0.44 ± 0.02	192.3 ± 86.1	1.1 ± 0.7
TCP	0.40 ± 0.09	15.15 ± 5.53	0.5 ± 0.4

Figure 4.2 shows the cathodic polarization curves obtained on a RDE for uncoated AA2024-T3 in naturally-aerated 0.5 M Na_2SO_4 + 0.1% NaCl. The measurements were recorded at rotation speeds from 0 to 2000 rpm. A positive shift in OCP was observed from -0.575 V at 0 rpm to *ca.* -0.400 V for the electrode under rotation. This can be attributed to the increased flux of O_2 to the electrode with convection. To compensate the increased exchange current during high rotation rates for oxygen reduction, the exchange current for metal dissolution also increases resulting in a positive shift in OCP. The plot shows a proportional increase in diffusion-limited oxygen reduction currents with increasing scan rate. Currents recorded at lower rotation speeds were lower than expected currents, likely due to a problem with the rotator. Nevertheless, the limiting current increased with the rotation rate.

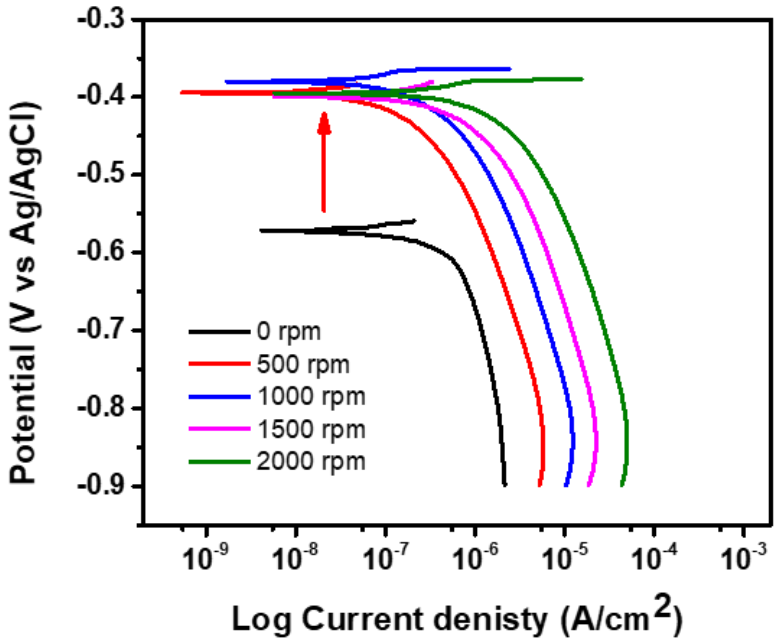

Figure 4.2 Cathodic polarization curves for uncoated AA2024-T3 at different rotation rates in naturally-aerated 0.5 M Na_2SO_4 + 0.1% NaCl. Curves were recorded with a rotating disk electrode at rotation rates from 0 to 2000 rpm. Arrow shows positive shift in OCP. Scan rate = 1mV/s.

Figure 4.3A and B show cathodic polarization curves obtained on TCP-NC and TCP-coated AA2024-T3 RDE in naturally aerated 0.5 M Na_2SO_4 + 0.1% NaCl. As expected, a slight positive shift in OCP was observed for both TCP-NC and TCP coated specimens. The OCP shifted from -0.4V to *ca.* -0.350 V for TCP-NC coated specimen and from -0.55V to -0.5V for TCP coated specimen. The shift in OCP for the conversion coated specimen is not as evident in the coated specimens as in the uncoated specimen because the coating inhibits oxygen reduction reaction kinetics on the alloy surface and therefore the rate of metal dissolution is not significantly increased. The ORR current at -0.7V for TCP-NC coated RDE was smaller than the uncoated specimen at all rotation rates. The diffusion-limited oxygen reduction current increased only slightly with rotation rate. The ORR current for TCP coated RDE, however, was independent of the rotation rate suggesting that Cr(III) plays an important role in inhibiting oxygen reduction on the surface of the alloy.

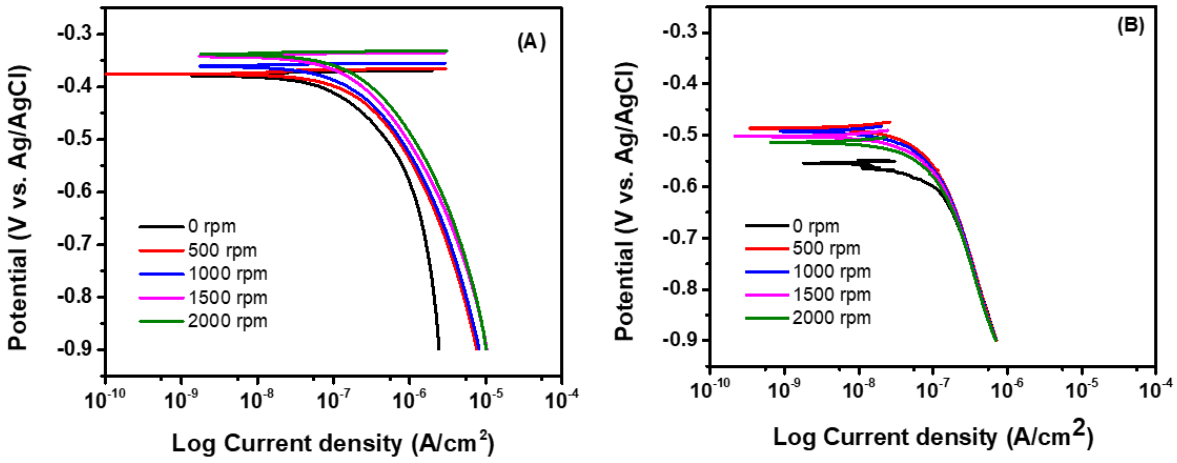

Figure 4.3 Cathodic polarization curves for (A) TCP-NC and (B) TCP coated AA2024-T3 in naturally-aerated 0.5 M Na_2SO_4 + 0.1% NaCl at different rotation rates. Curves were recorded with a rotating disk electrode at rotation rates from 0 to 2000 rpm. Scan rate = 1 mV/s.

Figure 4.4 shows the scanning electron micrographs of TCP and TCP-NC coated AA2024-T3. The surface morphology of both specimens look similar except that more coating precipitates can be easily identified on the surface of TCP coated AA2024-T3. These precipitates have been reported to be Cr and Zr oxides and hydroxides that settle on the alloy surface during coating formation process. No such precipitates were observed on the surface of TCP-NC coated specimens.

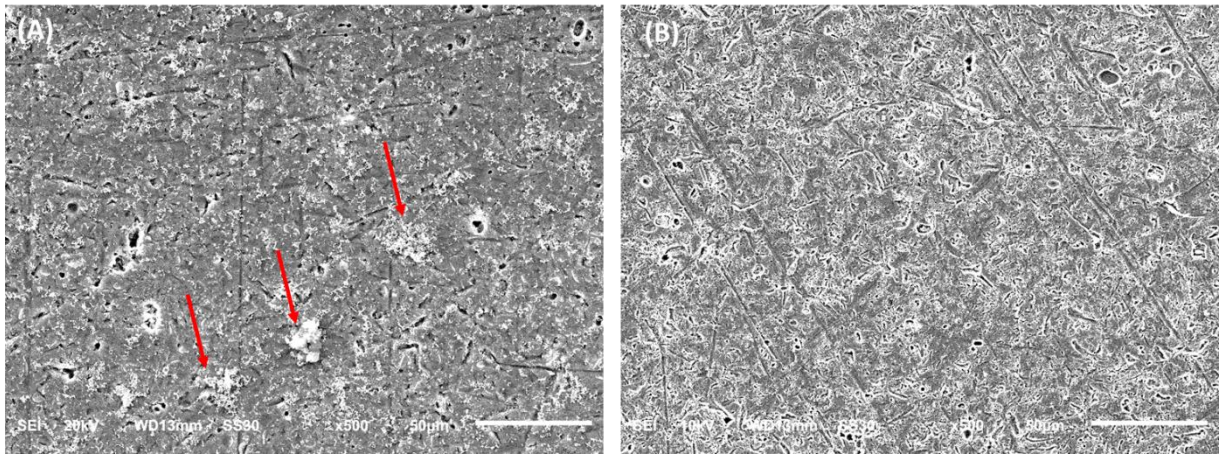

Figure 4.4 Scanning electron micrographs of (A) TCP and (B) TCP-NC coated AA2024-T3 at a 500x magnification. Arrows on the micrograph indicates coating precipitates found on the surface.

To further investigate the role of Cr(III) in the corrosion protection of AA2024-T3, a 7-day NSS test was conducted. Six specimens, three TCP and three TCP-NC coated were tested. Figure 4.5 shows the photographs of the test specimens before and after the 7-day salt exposure period. Clearly, specimens coated with TCP provide better stand-alone corrosion protection, as evidenced by the absence of any visible corrosion damage on all three specimens. No coating discoloration was seen for these specimens. In contrast, TCP-NC coated AA2024-T3 specimens show severe corrosion damage. Pits were seen as early as Day 4 on these specimens and grew in size through-

out the rest of the test period. Corrosion products were removed from the surface through a short nitric acid cleaning step before obtaining optical micrographs of the damaged surface.

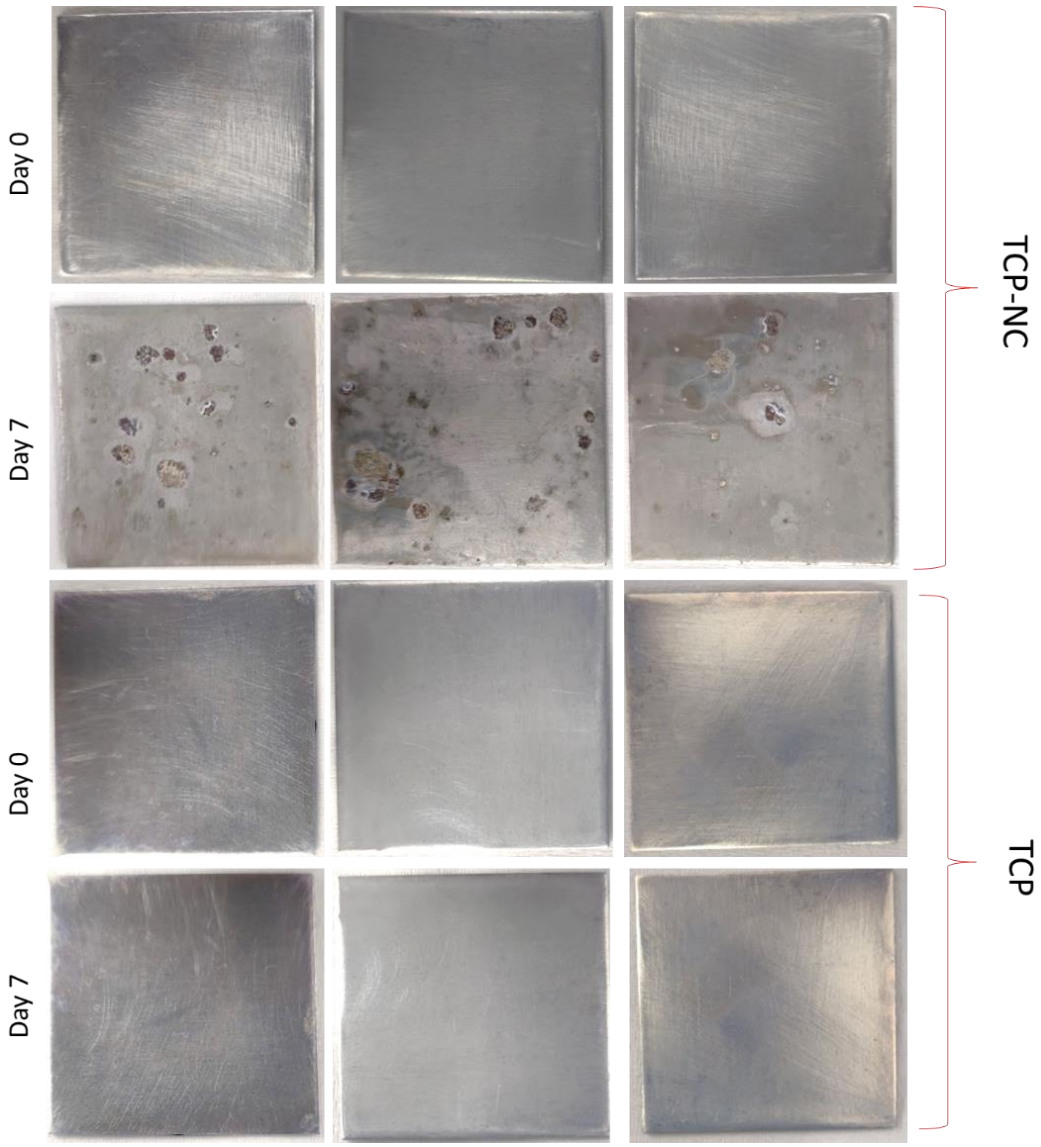

Figure 4.5 Photographs of TCP and TCP-NC coated AA2024-T3 before and after a 7-day B117 test. The brown discoloration seen on TCP-NC coated specimens are pits formed during salt spray exposure. No such discoloration was seen on TCP coated AA2024-T3.

Table 4.2 summarizes the surface topographical parameters obtained before and after the 7-day NSS test. Data show a significant increase in surface roughness for the TCP-NC coated

specimens after the test. This increase in surface roughness arises from the topographical inhomogeneities caused by formation of surface pits. The TCP coated specimens do not show significant surface roughening indicating low surface damage and a superior level of corrosion protection provided by TCP in high chloride environments.

Table 4.2 Summary of surface topographical data for conversion coated AA2024-T3. Values reported as mean ± std. dev.

N=3	**Surface roughness (nm)**		**Pit density (#/in^2) ***	
	Day 0	**Day 7**	**Day 0**	**Day 7**
TCP	239 ± 46	222 ± 18	-	-
TCP-NC	246 ± 33	396 ± 21	-	8 ± 2

4.5 DISCUSSION

Figure 4.6 shows the plot of limiting current density vs rotation rate^{½} for all three specimens. According to Levich equation (Eq. 11), diffusion limited current is directly proportional to the square root of rotation rate.

$$I_L = 0.62\ nFAC * D^{2/3} * w^{1/2} * v^{-1/6} * C \quad (11)$$

where,

i_L = diffusion limited current (A)

n = moles of electrons transferred in the half reaction

F = Faraday's constant (C/mol)

A = area of the electrode (cm^2)

D = diffusion coefficient of the analyte (cm^2/s)

w = angular rotation rate of the electrode (rad/s)

v = kinematic viscosity (cm^2/s)

C = analyte concentration (mol/cm^3)

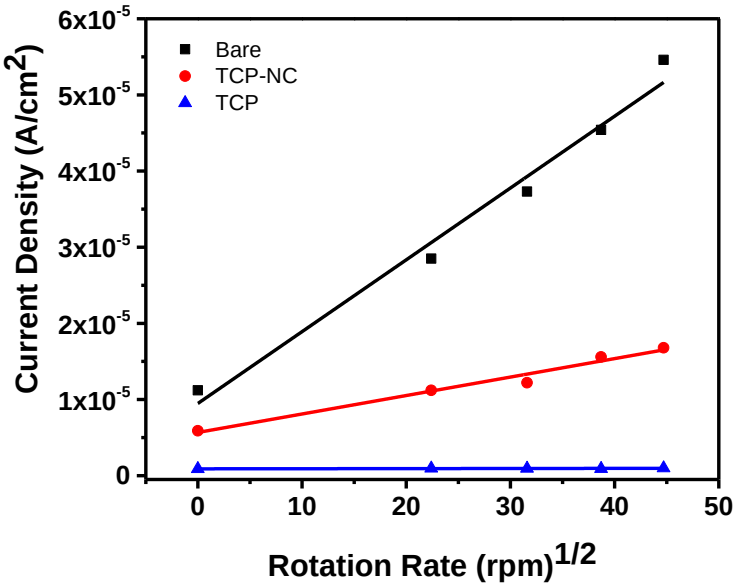

Figure 4.6 Graph of current density vs square root of rotation rate for uncoated, TCP-NC and TCP coated AA2024-T3. Measurements were made in naturally-aerated 0.5 M Na_2SO_4 + 0.1% NaCl at room temperature at a scan rate of 1 mV/s.

The linear dependence of oxygen reduction current on the square root of rotation rate for uncoated specimen confirms that oxygen reduction current is limited by diffusion of oxygen to the electrode surface. Oxygen reduction reaction is known to occur on Cu-rich IMPs present on the alloy. Previous reports have shown that TCP forms on and around intermetallic particles serving as an oxygen diffusional barrier. Cr(III) precipitates as $Cr(OH)_3$ on the Cu-rich IMPs during coating formation process, thereby blocking active sites for oxygen chemisorption. Figure 4.7 shows the schematic of the mechanism by which TCP provides anodic and cathodic inhibition to the underlying alloy.

The reduced slope for TCP-NC coated specimen in Figure 4.6 can be attributed to the lesser number of active IMPs available for oxygen reduction reaction. The near-zero slope for TCP

coated specimen confirms the role of Cr(III) as an oxygen diffusional barrier aiding in inhibiting oxygen reduction reaction kinetics.

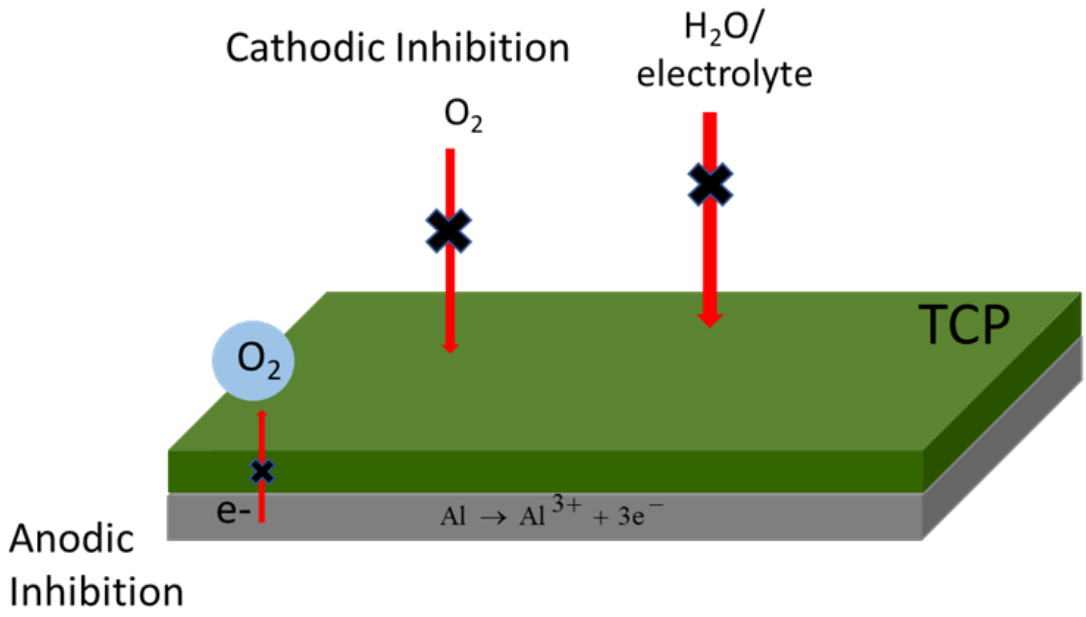

Figure 4.7 Schematic of anodic and cathodic inhibition provided by TCP on AA2024-T3.

Accelerated degradation tests performed on specimens coated with the two conversion coatings also confirms that the presence of Cr(III) helps in preventing early formation of pits on the alloy surface. This could be due to the presence of higher concentration of Cr and Zr-O/OH precipitates on TCP coated surfaces as evidenced by scanning electron micrographs in Figure 4.4.

4.6 CONCLUSIONS

Electrochemical polarization curves and RDE voltammetric data show that Cr(III) present in the TCP conversion coating plays a role in inhibiting the cathodic half reaction *i.e.* oxygen reduction reaction occurring at the alloy surface. The anodic currents were similar for TCP-NC and TCP coated AA2024-T3, while lower cathodic currents were recorded for TCP coated AA2024-T3 as compared to TCP-NC coated specimen. TCP provides corrosion protection to the

underlying metal by acting as a physical barrier preventing contact between the alloy and oxygen/electrolyte from the environment. Also, $Cr(OH)_3$ precipitates formed over IMPs during the coating formation block oxygen chemisorption sites preventing oxygen reduction reactions. The presence of Cr(III) in the conversion coating bath prevents early pitting on AA2024-T3 alloys.

REFERENCES

REFERENCES

(1) Suib, S. L.; La Scala, J.; Nickerson, W.; Fowler, A.; Zaki, N. Determination of Hexavalent Chromium in NAVAIR Trivalent Chromium Process (TCP) Coatings and Process Solutions. *Met. Finish.* **2009**, *107* (2), 28-31,33-34.

(2) Dong, X. C.; Wang, P.; Argekar, S.; Schaefer, D. W. Structure and Composition of Trivalent Chromium Process (TCP) Films on Al Alloy. *Langmuir* **2010**, *26* (13), 10833–10841.

(3) Guo, Y.; Frankel, G. S. Characterization of Trivalent Chromium Process Coating on AA2024-T3. *Surf. Coat. Technol.* **2012**, *206* (19–20), 3895–3902.

(4) Iyer, A.; Willis, W.; Frueh, S.; Nickerson, W.; Fowler, A.; Barnes, J.; Hagos, L.; Escarsega, J.; La Scala, J.; Suib, S. L. Characterization of NAVAIR Trivalent Chrome Process (TCP) Coatings and Solutions. *Plat. and Surf. Fin.* Technical Article, May **2010**.

(5) Li, L. L.; Kim, D. Y.; Swain, G. M. Transient Formation of Chromate in Trivalent Chromium Process (TCP) Coatings on AA2024 as Probed by Raman Spectroscopy. *J. Electrochem. Soc.* **2012**, *159* (8), C326–C333.

(6) Qi, J. T.; Hashimoto, T.; Walton, J. R.; Zhou, X.; Skeldon, P.; Thompson, G. E. Trivalent Chromium Conversion Coating Formation on Aluminium. *Surf. Coat. Technol.* **2015**, *280*, 317–329.

(7) Qi, J.; Němcová, A.; Walton, J. R.; Zhou, X.; Skeldon, P.; Thompson, G. E. Influence of Pre- and Post-Treatments on Formation of a Trivalent Chromium Conversion Coating on AA2024 Alloy. *Thin Solid Films* **2016**, *616*, 270–278.

(8) Twite, R. L.; Bierwagen, G. P. Review of Alternatives to Chromate for Corrosion Protection of Aluminum Aerospace Alloys. *Prog. Org. Coat.* **1998**, *33* (2), 91–100.

(9) Li. L. L.; Swain, G. M. Effects of Aging Temperature and Time on the Corrosion Protection Provided by Trivalent Chromium Process Coatings on AA2024-T3 *ACS Appl. Mater. Inerfaces* **2013**, *5*, 7923-7930.

(10) Chidambaram, D.; Clayton, C. R.; Halada, G. P. The Role of Hexafluorozirconate in the Formation of Chromate Conversion Coatings on Aluminum Alloys. *Electrochim. Acta* **2006**, *51* (14), 2862–2871.

(11) Yu, J. J.; Boyd, I. W. ZrO_2 Films Deposited by Photo-CVD at Low Temperatures. *Appl. Phys. A Mater. Sci. Process.* **2002**, *75* (4), 489–491.

(12) Hirai, S.; Shimakage, K.; Aizawa, S.; Wada, K. Alkaline Corrosion Resistance of Anodized Aluminum Coated with Zirconium Oxide by a Sol-Gel Process. *J. Am. Ceram. Soc.* **1998**, *81* (12), 3087–3092

(13) Li, L. L.; Desouza, A. L.; Swain, G. M. Effect of Deoxidation Pretreatment on the Corrosion Inhibition Provided by a Trivalent Chromium Process (TCP) Conversion Coating on AA2024-T3. *J. Electrochem. Soc.* **2014**, *161* (5), C246–C253.

(14) Nordlien, J. H.; Walmsley, J. C.; Østerberg, H.; Nisancioglu, K. Formation Of A Zirconium-Titanium Based Conversion Layer On AA 6060 Aluminium. *Surf. Coat. Technol.***2002**, *153*, 72-78.

(15) George, F. O.; Skeldon, P.; Thompson, G. E. Formation of Zirconium-Based Conversion Coatings on Aluminium and Al-Cu Alloys. *Corros. Sci.* **2012**, *65*, 231–237.

(16) Golru, S. S.; Attar, M. M.; Ramezanzadeh, B. Morphological Analysis and Corrosion Performance of Zirconium Based Conversion Coating on the Aluminum Alloy 1050. *J. Ind. Eng. Chem.* **2015**, *24*, 233–244.

(17) Li, L. L.; Swain, G. P.; Howell, A.; Woodbury, D.; Swain, G. M. The Formation, Structure, Electrochemical Properties and Stability of Trivalent Chrome Process (TCP) Coatings on AA2024. *J. Electrochem. Soc.* **2011**, *158*, C274.

(18) Guo, Y.; Frankel, G. S. Active Corrosion Inhibition of AA2024-T3 by Trivalent Chrome Process Treatment. *Corrosion* **2012**, *68*, 045002.

(19) Li, L. L.; Swain, G. M. Formation and Structure of Trivalent Chromium Process Coatings on Aluminum Alloys 6061 and 7075. *Corrosion* **2013,** *69*, 1205.

(20) Li, L. L.; Doran, K. P.; Swain, G. M. Electrochemical Characterization of Trivalent Chromium Process (TCP) Coatings on Aluminum Alloys 6061 and 7075. *J. Electrochem. Soc.*, **2013,** *160*, C396.

(21) Qi, J.; Hashimoto, T.; Walton, J.; Zhou, X.; Skeldon, P.; Thompson, G. E. Formation of a Trivalent Chromium Conversion Coating on AA2024-T351 Alloy. *J. Electrochem. Soc.*, **2016,** *163*, C25.

(22) Qi, J.; Hashimoto, T.; Thompson, G. E.; Carr, J. Influence of Water Immersion Post-Treatment Parameters on Trivalent Chromium Conversion Coatings Formed on AA2024-T351 Alloy. *J. Electrochem. Soc.*, **2016,** *163*, C131.

(23) Feng, Z.; Boerstler, J.; Frankel, G. S.; Matzdorf, C. A. Effect of Surface Pretreatment on Galvanic Attack of Coated Al Alloy Panels. *Corrosion*, **2015,** *71*, 771.

(24) Qi, J.; Walton, J.; Thompson, G. E.; Albu, S. P.; Carr, J. Spectroscopic Studies of Chromium VI Formed in the Trivalent Chromium Conversion Coatings on Aluminum. *J. Electrochem.* Soc., **2016,** *163*, C357.

(25) Song, L. L.; Li, J. F.; Cai, C. Corrosion Resistance and Self-Repairing Behaviour of Cr (III) Contained Conversion Coating on AA2024-T3. *Corrosion Engr. Sci. Technol.*, **2016,**

51, 263.

(26) Munson, C. A.; Swain, G. M. Structure and Chemical Composition of Different Variants of a Commercial Trivalent Chromium Process (TCP) Coating on Aluminum Alloy 7075-T6. *Surf. Coat. Technol*., **2017,** *315*, 150.

(27) Munson, C. A.; Zutim, P.; Swain, G. M. Electrochemical Characterization of Different Variants of a Commercial Trivalent Chromium Process (TCP) Coating on Aluminum Alloy 7075-T6. *Corrosion*, **2018,** *74*, 50.

(28) Kendig M. W.; Buchheit, R. G. Corrosion Inhibition of Aluminum and Aluminum Alloys by Soluble Chromates, Chromate Coatings, and Chromate-Free Coatings. *Corrosion*, **2003,** *59*, 379.

CHAPTER 5. EFFECT OF AGING ON TCP COATED AA2024-T3 – FORMATION OF TRANSIENT Cr(VI).

Chapter adapted from *J. Electrochem. Soc*., 166, C3284 (2019). Copyright 2019, The Electrochemical Society.

Article: T. K. Shruthi and Greg M. Swain, Detection of H_2O_2 from the reduction of dissolved oxygen on TCP-coated AA2024-T3: Impact on the transient formation of Cr(VI).

5.1 INTRODUCTION

TCP on AA2024-T3 formed through immersion coating primarily consists of $Cr(OH)_3$, CrOOH and Cr_2O_3 along with hydrated ZrO_2. [1-3] Freshly formed TCP consists of imperfections and hydrated channels in the coating structure similar to that observed in CCC's which serve as pathways for Cr(VI) transport.[4-8] Previous reports have suggested that aging TCP coated AA2024-T3 dehydrates and densifies the coating by collapsing the hydrated channels and defects. An apparent decrease in coating porosity was seen indicating fewer pathways for oxygen and ion transport to the underlying metal.[9]

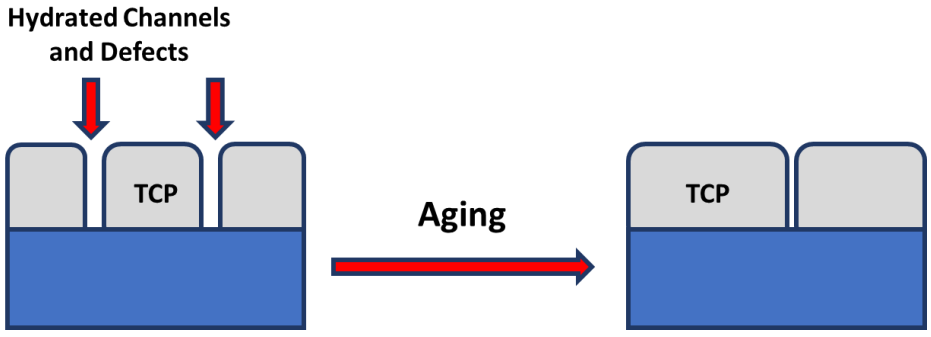

Figure 5.1 Schematic showing dehydration of a TCP coating resulting in reduced hydrated channels caused by aging. Figure adapted from *ACS Applied Materials and Interfaces* **2013**, *5*, 7923 – 7930.

It was envisioned that such structural modifications to the coating could affect the corrosion protection offered by TCP. Thus, short-term and long-term tests were conducted to verify the effects of aging on coating stability. To assess the short-term stability of TCP formed on AA2024-T3, a test was performed by measuring EIS of the specimen during continuous immersion in 0.5M Na_2SO_4 at 55°C for 4h. Figure 5.2A shows the measured impedance profiles before and after the test. Data showed no loss in impedance during the test period confirming TCP's structural and chemical stability for the 4h test period.[10] Li et al., studied the effects of aging on TCP-coated AA2024-T3 and its long-term effects on corrosion protection of the coating. Contact angle measurements comparing a hexafluorozirconate coated and TCP coated AA2024-T3 aged for 8 days showed that the TCP becomes progressively hydrophobic with aging time. The contact angle increased from 5.6 (±1.8)° after overnight aging to 63.1 (±0.3)° after 7 days (Figure 5.2B). An improvement in corrosion performance was also seen for TCP, with the polarization resistance, R_p, increasing 4x from 2 x 10^5 ohm-cm^2 (aging overnight) to 8 x 10^5 ohm-cm^2 (after 7-day aging) with aging at room temperature. This improvement in corrosion protection was attributed to the increasing hydrophobicity of the coating.[9]

Another important effect of aging TCP is the transient formation of Cr(VI). Several reports have been published confirming the presence of Cr(VI) in TCP coated aluminum alloys aged in the presence of oxygen.[11-14] It is important to note that the TCP conversion coating bath contains no Cr(VI) and the Cr(VI) detected was transiently formed when TCP-coated specimens were aged in the presence of oxygen. It has been hypothesized that Cr(III) in the TCP can be oxidized to Cr(VI) in the presence of oxygen and water and that longer immersion times, higher working temperatures and high coating bath pH accelerate the formation of Cr(VI) in the coating.[1]

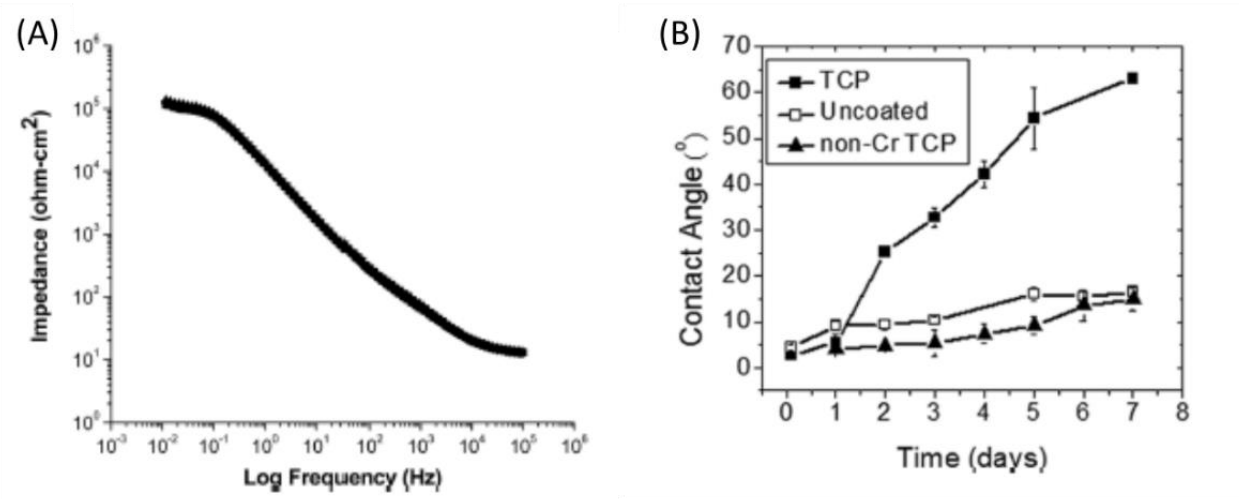

Figure 5.2 (A) EIS profiles for TCP coated AA2024-T3 before and after a 4h exposure to 0.5 M Na_2SO_4 at 55°C. The four curves collected at 1h intervals overlap. (B) static contact angle for water on uncoated, TCP coated and non-Cr TCP coated AA2024-T3 measured for 8 days at RT. Image A adapted from *Journal of The Electrochemical Society* **2011**, *158* (9), C274-C283. Image B adapted from *ACS Applied Materials and Interfaces* **2013**, *5*, 7923 – 7930.

In one report, four different TCP coatings were analysed for Cr(VI) – ST-301, Jishen A01-234C, JASCO TR-173A, Macdermid 21 and all TCP coatings showed the presence of Cr(VI). The concentration of hexavalent chromium was also shown to have increased with increasing aging period. For example, the concentration of Cr(VI) in ST-301 conversion coating was 0.13 mg/L after 4 days which quickly increased to 0.63 mg/L after 30 days of aging at room temperature. The Cr(VI) concentration for the other TCP coatings after 30 days was reported to be 0.7 mg/L and 0.66 mg/L (Jishen A01-234C and JASCO TR-173A respectively).[15] Literature evidence also confirm that the B117 test conditions within the salt spray chamber had sufficient capability to oxidize Cr(III) in the TCP to Cr(VI).[16]

Formation of Cr(VI) during aging TCP is important to study because of the active corrosion protection provided by chromate ions. Active corrosion protection could result if the transiently formed Cr(VI) could migrate through a TCP coating through the hydrated channels to nearby corroding sites and undergo reduction to form a passive layer of $Cr(OH)_3$ similar to the CCCs.[17-

[20] The net redox reaction for aluminum oxidation and the subsequent passivation by $Cr(OH)_3$ through Cr(VI) reduction is shown below: [21]

$$Al + CrO_4^{2-} + 5H^+ \rightarrow Cr(OH)_3 + H_2O + Al^{3+} \text{ (net redox reaction)} \qquad (12)$$

Primary evidence for transient formation of Cr(VI) aged in air has come from Raman spectroscopic data. The spectral peak at *ca.* 850 cm^{-1} corresponding to Cr(VI)-O vibrational mode is the key diagnostic indicator.[22-24] Cr(III)-O vibrational mode is observed at *ca.* 540 cm^{-1}.

Our group has published several reports proposing a mechanism for the transient formation of Cr(VI) species in TCP conversion coatings. [22-28] According to the mechanism, insoluble $Cr(OH)_3$ in TCP is oxidized to soluble and labile Cr(VI) by H_2O_2 produced from the reduction of dissolved oxygen at IMPs in the alloy. Figure 5.3 shows the proposed model for transient formation of Cr(VI) through Cr(III) oxidation by H_2O_2.

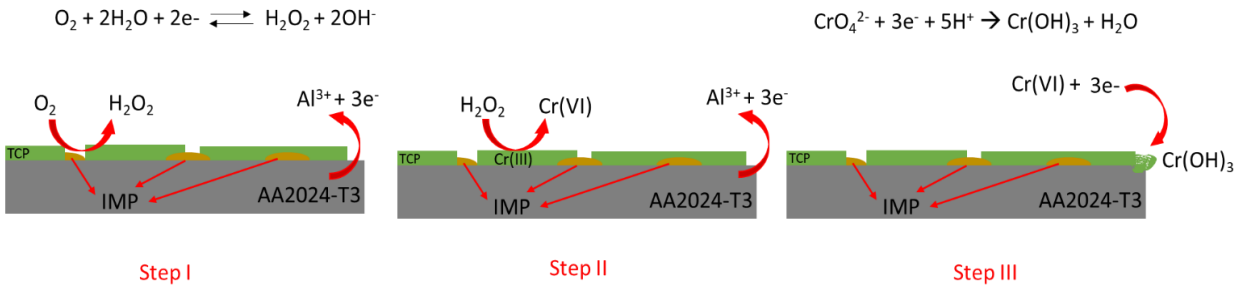

Figure 5.3 Proposed model for the transient formation of Cr(VI) in TCP conversion coatings and the reactions showing active corrosion protection mechanism by Cr(VI) ions. Figure adapted from *Journal of The Electrochemical Society* **2019**, *166* (11), C3284-C3289.

Several experiments were conducted and reported to prove:

(i) The role of dissolved oxygen in the transient formation of Cr(VI) in TCP

(ii) Ability of H_2O_2 to oxidize Cr(III) to Cr(VI)

(iii) Cr(VI) presence in corroding sites on the alloy surface

Results conclusively proved that Cr(VI) was formed in TCP only in the presence of atmospheric/dissolved oxygen. No Cr(VI) peaks were detected when TCP was aged under deoxygenated/ vacuum conditions. Concentration of Cr(VI) increased with increasing concentrations of H_2O_2 in the solution exposed to TCP coated AA2024-T3.[23] However, the missing piece of this model is the direct evidence for H_2O_2 formation.

Results reported herein, provide direct evidence for the formation of H_2O_2 in TCP coated AA2024-T3. Successfully detecting H_2O_2 has enabled to complete the model for how TCP inhibits corrosion on aluminum alloys. In the present work, linear sweep voltammetry and spectrophotometric assay of 2',7'-dichlorohydrofluorescein diacetate (DCFH-DA) were used to detect H_2O_2 produced on uncoated and TCP-coated AA2024-T3 specimens. The oxidation of DCFH-DA (colorless) to fluorescent, dichlorofluorescein (DCF) has been extensively used to detect H_2O_2 produced in biological cells. The reaction of H_2O_2 mediated oxidation of DCFH-DA to DCF is shown in Figure 5.4.[29-32] Experiments involved measuring (i) the reduction current for H_2O_2 formed at the surface of AA2024-T3 immersed in 0.5M Na_2SO_4 solution with a Au disk electrode and (ii) the absorption spectra of DCF formed in electrolyte solutions in contact with uncoated and TCP-coated alloys. DCFH-DA is a widely used probe for detecting intracellular oxidants, like H_2O_2, during oxidative stress.[29-32] Within cells, DCFH-DA is deacetylated by enzymes and is hydrolysed to produce DCFH. This DCFH is then oxidized to DCF by reactive oxygen species like OH•, O_2^-, H_2O_2, etc. The DCF formed is strongly fluorophoric and turns the colorless DCFH solution to a greenish-yellow color.

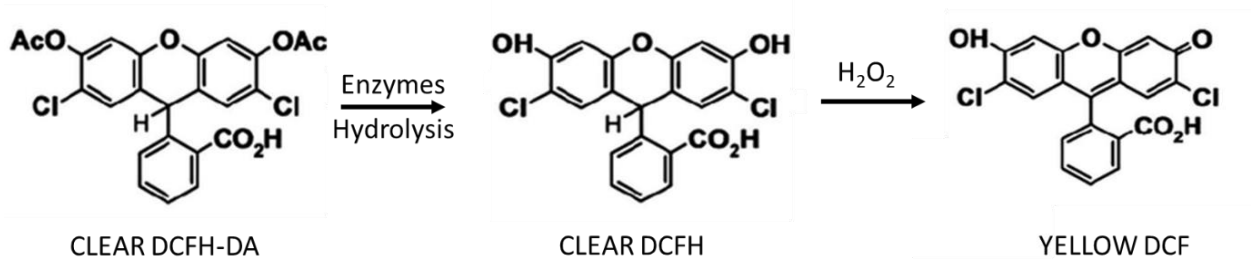

Figure 5.4 Oxidation of DCFH-DA to green fluorescing DCF by hydrogen peroxide. Figure adapted from *Scientific Reports* **2016**, 6, 38145.

5.2 MATERIALS AND METHODS

Reagents.

All chemicals used were analytical grade quality or better and were used without additional purification. Sodium sulfate (Na_2SO_4) and 2',7'–dichlorodihydrofluorescein diacetate (DCFH-DA) were purchased from Sigma-Aldrich (St. Louis, MO). Hydrogen peroxide (30 wt. %) was purchased from CCI Chemical (Vernon, CA). Nitric acid was purchased from Fisher Scientific (Hampton, New Hampshire). The cleaner 1000 and TCP-HF conversion coating bath were obtained from CHEMEON Surface Technology (Minden, NV). The degreaser was prepared to a concentration of 45 g/l. 35 % (v/v) nitric acid (HNO_3) was used for deoxidation. The TCP bath was diluted to 30% (v/v) with ultrapure water. All solutions were prepared using ultrapure water (Barnstead) with a resistivity >17 MΩ-cm.

Specimen preparation.

Uncoated and TCP coated AA2024-T3 specimen were prepared according to the procedure explained in Chapter 2 (Section 2.2).

Au disk electrode preparation.

A Au disk electrode (diameter = 3 cm) of area 0.47 cm^2 was used for in-situ detection of H_2O_2 produced at the surface of the alloy. The electrode was hand polished with alumina grit (1, 0.3 and

0.05 µm) for 20 min on a felt pad to activate the surface. The electrode was subjected to 30-min ultrasonic cleaning in ultrapure water between each polishing step. Cyclic voltammograms were recorded from 0 to +1.5V in 0.5 M H_2SO_4 (20 scans) to condition the electrode and verify electrode cleanliness. Well-defined Au oxidation and oxide stripping peaks were observed, confirming an activated Au electrode surface.

5.3 TESTING & CHARACTERIZATION

Immersion Testing.

Uncoated and TCP-coated AA2024-T3 specimens were immersed in naturally-aerated 0.5 M Na_2SO_4 + 0.1 mM DCFH-DA electrolyte solution. Reduction of dissolved oxygen at the intermetallic sites produced H_2O_2 over time which turned the colorless electrolyte to a greenish-yellow color, due to the oxidation of DCFH to DCF in the solution. The produced DCF was detected spectrophotometrically.

UV-Vis Spectroscopy.

The absorption intensity of the fluorescein probe (DCFH-DA) (λ_{max} = 502 nm) was used to calculate the concentration of DCF formed as a result of H_2O_2 mediated oxidation of DCFH. Extinction coefficient of DCF at 527 nm has been reported to be 59,500 M^{-1} cm^{-1}.[21] Concentration of DCF formed was calculated from Beer's law ($A=\varepsilon bc$) and is directly related to the concentration of H_2O_2 present in the solution as a result of oxygen reduction at the alloy surface.

Electrochemical characterization.

Measurement of H_2O_2 using Au disk electrode. A single compartment glass cell was used for all voltammetric measurements using a computer-controlled electrochemical workstation (Gamry Instruments, Inc, Reference 600, Warminster, PA). The activated Au disk electrode was used as the working electrode to detect the reduction of H_2O_2, Pt foil was used as the counter electrode

and a home-made Ag/AgCl (4M KCl) served as the reference electrode as shown in figure 5.5. The Au disk electrode was positioned at a fixed distance of *ca*.1 mm from the alloy surface. The cell was fitted with a cap to ensure the Au electrode was held firmly in place. All electrochemical measurements were made in naturally-aerated 0.5 M Na_2SO_4. The uncoated and TCP-coated specimens were soaked in the electrolyte solution for 10 h before making any voltammetric measurements. This ensured ample time for the formation of H_2O_2.

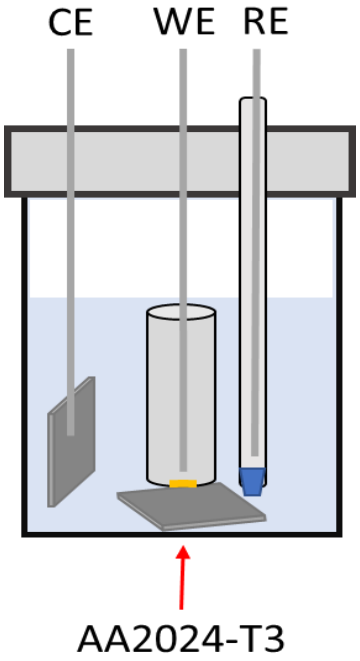

Figure 5.5 Schematic of the electrochemical cell used for the detection of H_2O_2 using Au disk electrode at room temperature. 0.5 M Na_2SO_4 was used as the electrolyte. Scan rate= 50 mV/s.

5.4 RESULTS

Photographs of naturally-aerated 0.5 M Na_2SO_4 + 0.1 mM DCFH-DA solutions with (A) no alloy, (B) in contact with uncoated and (C) TCP-coated AA2024-T3 specimens before and after a 24-h period is shown in Figure 5.6. The solution unexposed to AA2024-T3 produces no H_2O_2 and remains colorless after 24-h. This was a control experiment performed to eliminate potential

problems such as oxidation by adsorbed oxygen or intermediates. The absence of any detectable color change confirms that dissolved oxygen does not oxidize DCFH-DA under these conditions. In contrast, naturally-aerated solutions exposed to uncoated and TCP-coated alloys turn greenish-yellow during the 24h exposure period. This is due to oxidation of DCFH-DA by H_2O_2 to produce DCF. It was observed that the intensity of color change was greatest for the solution exposed to the uncoated alloy. This is because the uncoated alloy has a higher rate of oxygen reduction as compared to the TCP-coated alloy. Therefore, more H_2O_2 is produced, oxidizing a greater number of DCFH molecules to DCF to produce an intense color change. The TCP coating blocks surface IMPs resulting in lesser active surface area for oxygen reduction i.e. H_2O_2 production. Thus, a lower intensity of color change was observed for the solution exposed to TCP-coated AA2024-T3.

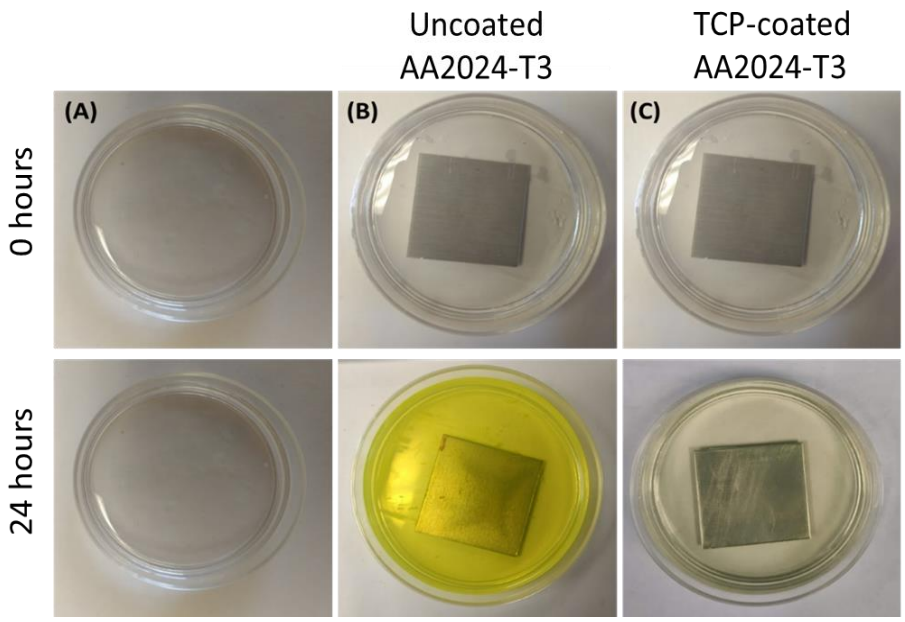

Figure 5.6 Photographs of naturally-aerated 0.5 M Na_2SO_4 + 0.1 mM DCFH-DA solutions before and after a 24-h period (A) with no alloy, (B) in contact with uncoated AA2024-T3 specimen under open circuit conditions, and (C) in contact with a TCP-coated AA2024-T3 specimen under open circuit conditions.

A second experiment was performed to further confirm the role of dissolved oxygen in the formation of H_2O_2. In this experiment, a TCP-coated AA2024-T3 specimen was first exposed to deoxygenated 0.5 M Na_2SO_4 + 0.1 mM DCFH-DA for 48 h. Visual inspection revealed no visible color change due to the relative absence of O_2. Figure 5.7 shows photographs of the solution before and after the 48h exposure period. The same solution was then allowed to equilibrate with ambient air for an additional 48 h. After a total of 96 h, the solution turned greenish-yellow. Figure 5.7 shows evidence for the observed color change. Figure 5.7C shows the set of photographs for a 0.5 M Na_2SO_4 + 0.1 mM DCFH-DA solution spiked with 3% H_2O_2. An intense visible color change was observed after 6 h. Overall, the two sets of immersion tests in 0.5 M Na_2SO_4 + 0.1 mM DCFH-DA confirm that dissolved oxygen has a key role in the transient formation of H_2O_2 at the electrode surface.

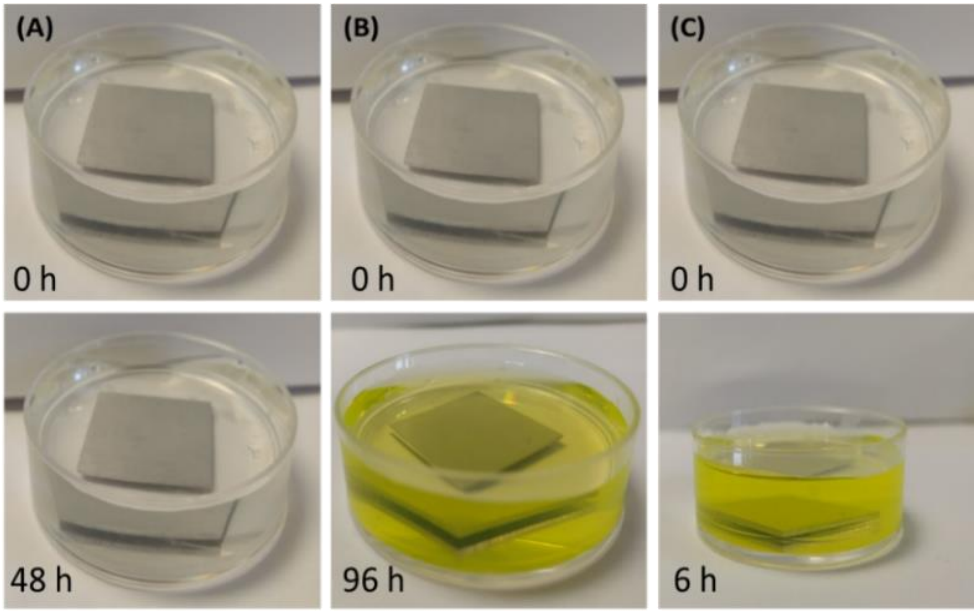

Figure 5.7 Photographs of TCP-coated AA2024 specimens in (A) deoxygenated 0.5 M Na_2SO_4 + 0.1 mM DCFH-DA after 48 h, (B) naturally-aerated 0.5 M Na_2SO_4 + 0.1 mM DCFH-DA after 48 h of exposure to the deaerated solution and an additional 48-h period in contact with the naturally-aerated solution, and (C) naturally-aerated 0.5 M Na_2SO_4 + 0.1 mM DCFH-DA with externally added 3% H_2O_2 after 6 h.

Figure 5.8A shows the *i*-E curves for H_2O_2 reduction on Au disk electrode in 0.5 M Na_2SO_4 with varying concentrations of externally added H_2O_2. For all three curves, the reduction current for H_2O_2 is at -0.1 V and reaches a maximum at -0.2 V. Reports in the literature also confirm the reduction potential for H_2O_2 Au at *ca.* -0.2 V in this medium.[33-34] Figure 5.8B shows the voltammetric *i-E* curve for reduction of H_2O_2 on the Au disk electrode positioned near an uncoated AA2024-T3 specimen. The current was recorded after allowing the alloy to equilibrate in the electrolyte for 10 h. The red curve shows the reduction peak for H_2O_2 formed during oxygen reduction on the IMPs on the alloy surface. The blue curve shows the current response curve recorded after 10 h for the Au disk electrode in 0.5 M Na_2SO_4 with no alloy present. As no H_2O_2 is produced, no current peak was observed in the absence of the alloy. The black curve is the current response of the Au disk electrode in 0.5 M Na_2SO_4 + 3% H_2O_2, shown for comparison. Figure 5.8C shows an enlarged view of the *i-E* response curves in Figure 5.8B. The reduction peak for H_2O_2 was observed at -0.15 V. Figure 4.8D shows the voltammetric *i*-E curve for the reduction of dissolved oxygen in naturally-aerated 0.5 M Na_2SO_4. Oxygen reduction on Au electrode occurs at a more positive potential, ca. 0.10 V. This confirms that the peak observed at -0.15V is due to H_2O_2 reduction on the surface of the Au electrode.

Using UV/visible absorption spectrophotometry , the DCF produced during immersion tests was used to directly quantify H_2O_2 formed at the surface of AA2024-T3 alloy. Figure 5.9 5.9 shows the UV-Vis absorption spectra for freshly prepared naturally-aerated 0.5 M Na2SO4 + 0.1 mM DCFH-DA solution, and for the solution after a 24-h contact with uncoated (blue curve) and TCP-coated (red curve) AA2024-T3 specimens. The DCF absorption intensity seen at 502 nm is higher for the solution in contact with the uncoated AA2024-T3 specimen. This is due to higher oxygen reduction rates, thereby higher H2O2 production at the uncoated surface.

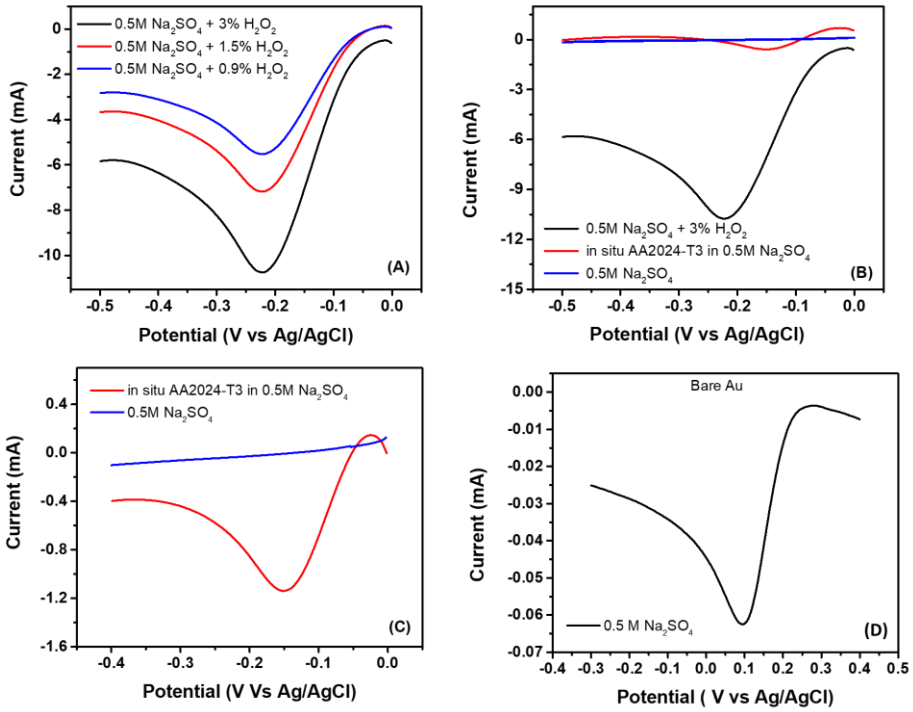

Figure 5.8 Potential sweep voltammetric curves recorded on a Au disk electrode (A) in deoxygenated 0.5 M Na_2SO_4 + 0.9, 1.5 and 3% H_2O_2, (B) in naturally-aerated 0.5 M Na_2SO_4 with uncoated AA2024-T3 alloy immersed for 10-h. The black curve is an overlaid voltammogram of Au disk electrode in 0.5 M Na_2SO_4 + 3% H_2O_2, (C) an expanded view of the voltammetric responses shown in Figure 4.8B and (D) in naturally aerated 0.5 M Na_2SO_4 showing oxygen reduction current at +0.1 V. Electrode geometric area = 0.47 cm^2. Scan rate = 50 mV/s.

. The concentration of DCF was calculated using Beer's law (A= εbC) which was then correlated to obtain the concentration of H_2O_2 produced. After 24-h, the concentration of H_2O_2 formed at the uncoated alloy was calculated to be 6.2 µM. which corresponds to an apparent production rate of 2.6 x 10^{-7} M/h. For the TCP-coated alloy, the H_2O_2 concentration was calculated to be 1.3 µM after 24-h period which corresponds to a production rate of 5.4 x 10^{-8} M/h. The 5x decrease in H_2O_2 concentration is consistent with cathodic inhibition by the TCP coating.

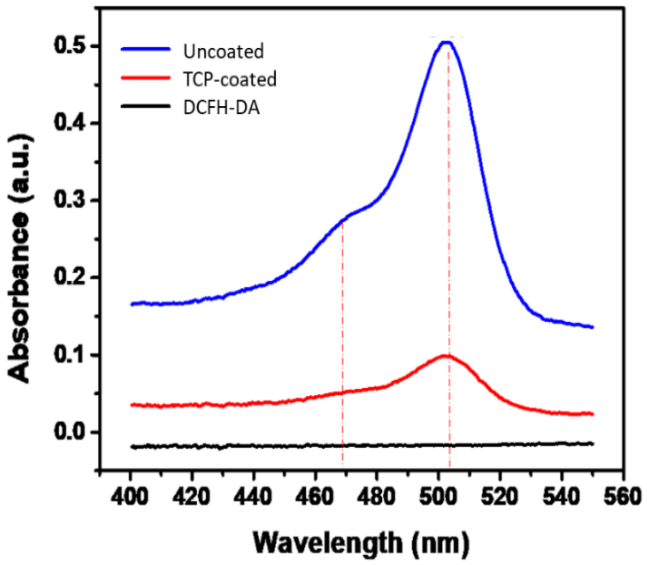

Figure 5.9 UV-Vis absorbance spectra for 0.5 M Na_2SO_4 + 0.1 mM DCFH-DA in contact with uncoated (blue) and TCP-coated (red) AA2024-T3 for 24 h. Background absorbance spectrum (black) for DCFH-DA is shown for comparison.

5.5 DISCUSSION

Results obtained from the experiments show evidence supporting the mechanism of transient formation of Cr(VI) in TCP coatings through the reduction of dissolved oxygen by a $2H^+/2e^-$ mechanism to produce H_2O_2. The formation of a strong oxidant like H_2O_2 at exposed cathodic intermetallic phases (Al_2Cu, Al_2CuMg, Al_7CuFe) on the aluminum alloy surface leads to the oxidation of nearby Cr(III). H_2O_2 oxidizes $Cr(OH)_3$ in the coating to soluble chromate, CrO_4^{2-}, or hydrogen chromate, $HcrO_4^-$, depending on the local solution pH. CrO_4^{2-} is supposed to be the primary transiently-formed active corrosion inhibitor.[5,8,35]

The electrochemical reduction of H_2O_2 on Au disk electrode and spectrophotometric UV-Vis measurements of DCFH-DA exposed to AA2024-T3 provide direct evidence for H_2O_2 formation. The probe molecule, DCFH-DA (colorless), is a very selective molecule and reacts with oxidants such as H_2O_2, to produce an optically-active compound (DCF) which produces a greenish/yellow

color that can be detected in the visible region of the electromagnetic spectrum.[30-32] Both uncoated and TCP-coated AA2024-T3 specimens were tested for H_2O_2 formation in naturally-aerated electrolyte solutions. Although, both specimens showed a visible color change within 24-h, the intensity of the change was noticeably less for the TCP-coated alloy than for the uncoated alloy. This is due to the suppressed oxygen reduction reaction kinetics at IMPs on TCP coated AA2024-T3 where the coating precipitates, presumably $Cr(OH)_3$, partially passivate cathodic sites preventing oxygen chemisorption.[36]

The transiently formed Cr(VI) is mobile and can diffuse through the coating to nearby corroding Al sites to produce a passivating and insoluble layer of $Cr(OH)_3$. The redox reaction is shown below: [21]

$$CrO_4^{2-} + 5H^+ + 3e^- \rightarrow Cr(OH)_3 + H_2O \quad (13)$$

TCP coating does not consist of any Cr(VI) species when formed. The transient formation of Cr(VI) through oxidation of Cr(III) by H_2O_2 produces Cr(VI) which imparts active corrosion protection properties to the coating. The concentration of transiently formed Cr(VI) was estimated to be 676 ppm using the below calculations:

$$C_{H_2O_2}\left(\frac{mol}{L}\right) \times solution\ vol.(L) = Moles\ of\ H_2O_2$$

$$Moles\ of\ H_2O_2 \times \frac{2\ Cr(VI)}{3\ H_2O_2} = Moles\ of\ Cr(VI)\ formed$$

$$\frac{Moles\ of\ Cr(VI) formed}{TCP\ thickness \times geometric\ area} = Moles\ of\ Cr(VI) per\ unit\ vol.$$

$$Moles\ of\ Cr(VI)\ fomred\ per\ cm^3 \times \frac{1000\ cm^3}{L} \times 52\frac{g}{mol} = concentration\ of\ Cr(VI)\ \left(\frac{g}{L}\right)$$

5.6 CONCLUSIONS

Aging TCP coating formed on an aluminum alloy surface in the presence of oxygen leads to improved corrosion resistance. One reason for this improved corrosion resistance is the active corrosion protection provided by Cr(VI). Oxygen reduction reactions occurring at IMPs on the alloy surface through a 2H+/2e- pathway, produce H_2O_2 which oxidizes nearby Cr(III) to Cr(VI). Direct evidence for H_2O_2 formation on the surface of AA2024-T3 during oxygen reduction has been provided. The oxidant is necessary for oxidation of Cr(III) to Cr(VI) within the coating. Cr(VI) concentration has been observed to increase with increasing aging time.

REFERENCES

REFERENCES

(1) Payne, B. P.; Biesinger, M. C.; Mclntyre, N. S., X-Ray Photoelectron Spectroscopy Studies of Reactions on Chromium Metal and Chromium Oxide Surface. *J. Electron Spectros. Relat. Phenomena* **2011**, *184* (1-2), 29-37.

(2) Chen, W. K.; Lee, J. L.; Bai, C. Y.; Hou, K. H.; Ger, M. D., Growth and Characteristics of Cr(III) Based Conversion Coating on Aluminum Alloy. *J. Taiwan Inst. Chem. Eng.* **2012**, *43*, 989-995.

(3) Qi, J.; Hashimoto, J.; Walton, J.; Zhou, X.; Skeldon, P.; Thompson, G. E., Formation of A Trivalent Chromium Conversion Coating on AA2024-T351 Alloy. *J. Electrochem. Soc.* **2016**, *163* (2), C25-C35.

(4) Clark, W. J.; McCreery, R. L., Inhibition of Corrosion-Related Reduction Processes Via Chromium Monolayer Formation. *J. Electrochem. Soc.* **2002**, *149* (9), B379–B386.

(5) Zhao, J.; Xia, L.; Sehgal, A.; Lu, D.; McCreery, R. L.; Frankel, G. S., Effects of Chromate and Chromate Conversion Coatings on Corrosion of Aluminum Alloy 2024-T3. *Surf. Coat. Technol.* **2001**, *140* (1), 51-57.

(6) Xia, L.; Akiyama, E.; Frankel, G. S.; McCreery, R. L., Storage and Release of Soluble Hexavalent Chromium from Chromate Conversion Coatings- Equilibrium Aspects of Cr VI Concentration. *J. Electrochem. Soc.* **2002**, *149* (9), B379–B386.

(7) Ramsey, J. D.; McCreery, R. L., In Situ Raman Microscopy of Chromate Effects on Corrosion Pits in Aluminum Alloy. *J. Electrochem. Soc.* **1999**, *146* (11), 4076-4081.

(8) Zhao, J.; Frankel, G. S.; McCreery, R. L., Corrosion Protection of Untreated AA2024-T3 In Chloride Solution by A Chromate Conversion Coating Monitored by Raman Spectroscopy. *J. Electrochem. Soc.* **1998**, *145* (7), 2258-2264.

(9) Li, L.; Swain, G. M., Effects of Aging Temperature and Time on The Corrosion Protection Provided by Trivalent Chromium Process Coatings on AA2024-T3. *ACS Appl. Mater. Interfaces* **2013**, *5*, 7923-7930.

(10) Li, L.; Swain, G. P.; Howell, A.; Woodbury, D.; Swain, G. M., The Formation, Structure, Electrochemical Properties and Stability of Trivalent Chrome Process (TCP) Coatings on AA2024-T3. *J. Electrochem. Soc.* **2011**, 158 (9), C274-C283.

(11) Guo, Y.; Frankel, G. S., Active Corrosion Inhibition of AA2024-T3 By Trivalent Chrome Process Treatment. *Corrosion* **2012**, 68 (4) 1-10.

(12) Ely, M.; Swiatowska, J.; Seyeux.; Zanna S.; Marcus, P., Role of Post-Treatment in Improved Corrosion Behaviour Of Trivalent Chromium Protection (TCP) Coating Deposited On Aluminum Alloy 2024-T3. *J. Electrochem. Soc.* **2017**, *164* (6), C276-C284.

(13) Suib, S. L.; Scala, J. L.; Nickerson, W.; Fowler, A.; Zaki, N., Determination of Hexavalent Chromium in NAVAIR Trivalent Chromium Process (TCP) Coatings and Process Solutions. *Met. Finish*. **2009**, ESA-STM 276, 29-39.

(14) Qi, J.; Gao, L.; Liu, Y.; Hashimoto, T.; Wang, Z.; Thompson, G. E., Chromate Formed in a Trivalent Chromium Conversion Coating on Aluminum. *J. Electrochem. Soc.* **2017**, *164* (7), C442-C449.

(15) Li, J.; Yao, C.; Liu, Y.; Li, D.; Zhou, B.; Cai, W., The Hazardous Hexavalent Chromium Formed on Trivalent Chromium Conversion Coating: The Origin, Influence Factors and Control Measures. *J. Hazard. Mater*. **2012**, 221-222, 56-61.

(16) Rochester, T.; Kennedy, Z. W., Unexpected Results from Corrosion Testing of Trivalent Passivates. *Plating Surf. Finish*. **2007**, 14-18.

(17) Meng, Q.; Frankel, G. S., Characterization of Chromate Conversion Coating on AA7075-T6 Aluminum Alloy. *Surf. Interface Anal*. **2004**, *36*, 30-42.

(18) Kending, M. W.; Davenport, A. J.; Isaacs, H. S., The Mechanism of Corrosion Inhibition by Chromate Conversion Coatings from X-Ray Absorption Near Edge Spectroscopy (XANES). *Corros. Sci*. **1993**, *34* (1), 41-49.

(19) Lunder, O.; Walmsley, J. C.; Mack, P.; Nisancioglu, K., Formation and Characterization of a Chromate Conversion Coating on AA6060 Aluminum. *Corros. Sci*. **2005**, *47*, 1604-1624.

(20) Akiyama, E.; Markworth, A. J.; McCoy, J. K.; Frankel, G. S.; Xia, L.; McCreery, R. L., Storage and Release of Soluble Chromium from Chromium Conversion Coatings on Al Alloys. *J. Electrochem. Soc*. **2003**, *150* (2), B83-B91.

(21) Shruthi, T. K.; Swain, G. M., Detection of H_2O_2 From the Reduction of Dissolved Oxygen On TCP-Coated AA2024-T3: Impact on The Transient Formation of Cr(VI). *J. Electrochem. Soc.* **2019**, *166* (1), C3284-C3289.

(22) Munson, C. A.; McFall-Boegeman, S. A.; Swain, G. M., Cross Comparison of TCP Conversion Coating Performance on Aluminum Alloys During Neutral Salt Spray and Thin-Layer Mist Accelerated Degradation Testing. *Electrochim. Acta* **2018**, *282*, 171-184.

(23) Qi, J. T.; Hashimoto, T.; Walton, J. R.; Zhou, X.; Skeldon, P.; Thompson, G. E., Trivalent Chromium Conversion Coating Formation on Aluminum. *Surf. and Coat. Technol*. **2015**, *280*, 317-329.

(24) Li, L.; Kim, D. Y.; Swain, G. M., Transient Formation Of Chromate In Trivalent Chromium Process (TCP) Coatings On AA2024-T3 As Probed By Raman Spectroscopy. *J. Electrochem. Soc.* **2012**, *159* (8), C326-C333.

(25) Li, L.; Swain., Formation And Structure Of Trivalent Chromium Process Coatings Onaluminum Alloys 6061 and 7075. *Corros. Sci*. **2013**, *69* (12), 1205-1216.

(26) Li, L.; Doran, K. P.; Swain, G. M., Electrochemical Characterization Of Trivalent Chromium Process (TCP) Coatings On Aluminum Alloys 6061 And 7075. *J. Electrochem. Soc*. **2013**, *160* (8), C396-C401.

(27) Munson, C. A.; Swain, G. M., Structure And Chemical Composition Of Different Variants Of A Commercial Trivalent Chromium Process (TCP) Coating On Aluminum Alloy 7075-T6. *Surf. Coat. Technol*. **2017**, *315*, 150-162.

(28) Munson, C. A.; Zutim, P.; Swain, G. M., Electrochemical Characterization Of Different Variants Of A Commercial Trivalent Chromium Process (TCP) Coating On Aluminum Alloy 7075-T6. *Corros. Sci*. **2018**, *74* (1), 50-65.

(29) Qin, Y.; Lu, M.; Gong, X., Dihydrorhodamine 123 Is Superior To 2,7-Dichlorodihydrofluorescein Diacetate 6G In Detecting Intracellular Hydrogen Peroxide In Tumour Cells. *Cell Biol. Int.* **2008**, *32*, 224-228.

(30) Kalyanaraman, B.; Darley-Usmar, V.; Davies, K. J. A.; Dennery, P. A.; Forman, H. J.; Grisham, M. B.; Mann, G. E.; Moore, K.; Roberts II, L. J.; Ischiropoulos, H., Measuring Reactive Oxygen And Nitrogen Species With Fluorescent Probes: Challenges And Limitations. *Free Radic. Biol. Med*. **2012**, *52*, 1-6.

(31) Aranda, A.; Sequedo, L.; Tolosa, L.; Quintas, G.; Burello, E.; Castell J. V.; Gombau, L., Dicholor-Dihydro-Fluorescein Diacetate (DCFH-DA) Assay: A Quantitative Method For Oxidative Stress Assessment Of Nanoparticle-Treated Cells. *Toxicol. In Vitro* **2013**, *27*, 954-963.

(32) Zamojc, K.; Zdrowowicz, M.; Jacewicz, D.; Wyrzykowski, D.; Chmurzynski, L., Fluorescent Probes Used For Detection Of Hydrogen Peroxide Under Biological Conditions. *Crit. Rev. Anal. Chem.* **2016**, *46* (3), 171-200.

(33) Mason, J.; Batchelor-McAuley, C.; Compton, R. G., Surface Modification Imparts Selectivity, Facilitating Redox Catalytic Studies: Quinone Mediated Oxygen Reduction. *Phys. Chem. Chem. Phys.* **2013**, *15*, 8362-8366.

(34) Tian, C.; Zhang, S.; Zhuang X.; Wang, H.; Chen, D.; Luan, F.; He, T.; He, W.; Qiu, Y., Preparation Of Gold Nanoparticles Supported On Graphene Oxide With Flagella As The Template For Nonenzymatic Hydrogen Peroxide Sensing. *Anal. Bioanal. Chem.* **2018**, *410*, 5915-5921.

(35) Xia, L.; McCreery, R. L., Chemistry Of A Chromate Conversion Coating On Aluminum Alloy AA2024-T3 Probed By Vibrational Spectroscopy. *J. Electrochem. Soc.* **1998**, *145* (9), 3083-3089.

(36) Shruthi, T. K.; Swain, G. M., Communication-Role Of Trivalent Chromium On The Anti-Corrosion Properties Of A TCP Conversion Coating On Aluminum Alloy 2024-T3. *J. Electrochem. Soc.* **2018**, *165* (2), C103-C105.

CHAPTER 6. EARLY STAGE CORROSION OF COATED 6xxx SERIES ALUMINUM ALLOY HEM FLANGE JOINTS DURING ACCELERATED DEGRADATION TESTING

6.1 INTRODUCTION

Automotive OEM's are in a constant search for opportunities to reduce vehicle weight to improve energy efficiency. Replacing heavier ferrous alloys used to construct automotive exterior closure panels with lighter non-ferrous alloys, like Mg and Al, has been a manufacturing approach used. A 30 – 50 % weight saving can be achieved by using aluminum alloy closures as compared to steel or polymer composites.[1-4] 6xxx series aluminum alloys (Mg, Cu, Si additions) are commonly used for automobile hoods and deck lids.[5-8] Although aluminum alloys have some natural corrosion resistance due to a passivating oxide layer that naturally forms, alloying elements that are non-uniformly distributed within the aluminum increases the corrosion susceptibility of the metal by creating localized galvanic cells [9-11] Corrosion protection is typically achieved by a multilayer coating system consisting of a conversion coating surface treatment, a primer, and a topcoat, such as an electrophretically-applied (e-coat) paint. [12-16]

Corrosion protection is particularly critical at hem joints where an outer panel is hemmed over an inner panel forming a crevice for moisture and salt collection. A hem flange is a mechanical joint that connects inner and outer panels, such as doors and hoods. The gap between the hemmed panels is typically filled with an adhesive coating that strengthens the joint, improves crash performance, reduces noise from vibrations, and provides some level of corrosion protection. [17-19] Sealants are often applied over the joint to inhibit moisture and electrolyte penetration, thereby preventing corrosion. In service, these joints may or may not have a sealant layer applied. Hem

edges, when unsealed, are common corrosion initiation sites.[20] Unsealed hem edges are prone to filiform corrosion, especially in snowy/salty environments. Figure 6.1 shows a common example of corrosion on the inside of an automobile door panel at a hem joint. Even though these joints are not in direct contact with the environment, corrosion often initiates here. The coating system originally applied to this vehicle no longer protects the joint effectively. Hem joint edges, particularly those that are unsealed, are prone to filiform corrosion. This degradation of especially problematic in snowy/salty environments. Multiple factors, such as the adhesive uniformity in the joint, its chemical stability, and defective top-coat coverage all impact hem joint corrosion susceptibility.[20]

Figure 6.1. Photograph of an actual hem joint on the inside of an automobile door panel where corrosion has developed along the joint edge during service.

Even though hem joint corrosion is well known to occur, there are several technical issues that need to be better understood for improved mitigation strategies including (i) the role of the adhesive coating, (ii) the role of the surface treatment type and chemistry, (iii) the role of

imperfections in surface treatment layers as initiation sites, and (iv) type of corrosion that occurs (crevice, filiform, etc.). To this end, basic research was conducted with differentially treated hem joint specimens. Two aluminum alloys were studied, 6111-T4 (high Cu content) and 6022-T4 (low Cu content). All the test specimens were coated with an electrophoretic paint (BASF Cathogard®800) after one of three different surface treatments: (i) no conversion coating, (ii) a zinc phosphate conversion coating (Bonderite® M-ZN 958), and (iii) zirconium-based conversion coating (Bonderite® M-NT 1820). No adhesive bond or sealant was used in any of the joints. The surface treated specimens were then exposed to cyclic accelerated degradation testing according to ASTM G85. Details of the test specimen characterization during and after a 30-day test period are reported herein. Characterization was performed using scanning electron microscopy with energy dispersive x-ray analysis, digital optical microscopy, glow-discharge optical emission spectroscopy, and adhesion testing.

6.2 MATERIALS AND METHODS

Aluminum Alloys and Chemicals.

Hem flange specimens were treated with a conversion coating and/or covered with an electrophoretically-applied topcoat (so-called e-coat). Two commercial conversion coatings (Bonderite M-ZN 958 and Bonderite M-NT 1820) were evaluated. Aluminum alloy 6111-T4 (Si: 0.7-1.1, Mg: 0.5-1, Cu-0.5-0.9, Mn: 0.15-0.45, Fe: 0.4 max) and 6022-T4 (Si:0.8-1.5, Mg: 0.45-0.7, Cu: 0.01-0.11, Mn: 0.02-0.1, Fe: 0.05-0.2) were used to replicate the hem joints in doors and fenders. 12” x 4” flat panels were obtained from ACT Test Panels LLC and were cut into 6” x 4” pieces to prepare the hem flange specimens. Figure 6.2 shows a photograph of the hem flange test specimen used in the studies. In this geometry, the inner panel was manually bent to a 30°- 45° angle and positioned on the outer panel, which was then crimped around the edge of the inner

panel to form the hem joint. No adhesive coating was applied to secure the pieces in place. The hem joint was assembled before applying any conversion coating surface treatment. A hole was punched in the outer panel for hanging the specimens while cleaning, surface treating and e-coating.

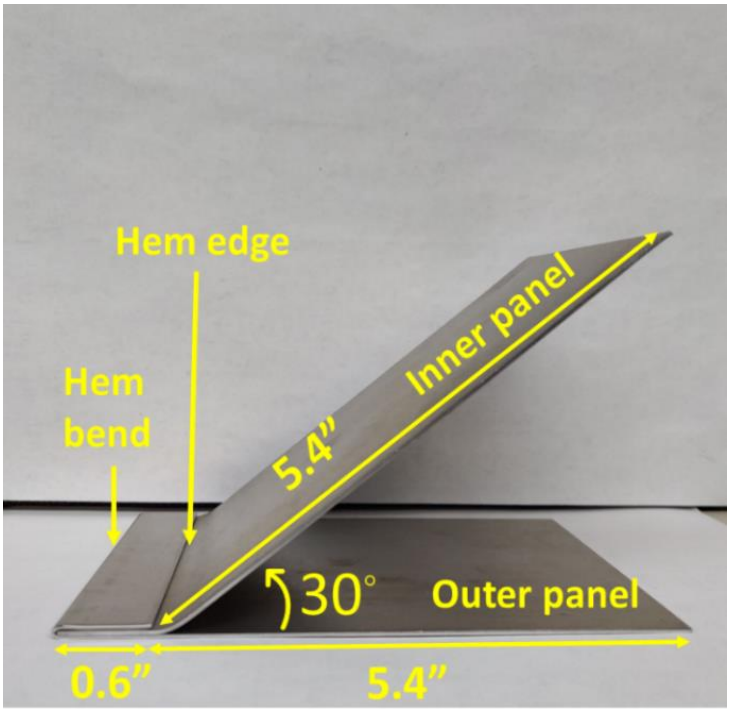

Figure 6.2 Photograph of the hem flange test specimen prepared in-house for ASTM G85 corrosion testing.

Each hem flange test specimen was treated with one of two conversion coatings followed by applying an e-coat (BASF CG-800) top layer before corrosion testing. Hem flanges with just an e-coat layer and no conversion coating were used as controls. The specimens used are identified as follows: (i) no conversion coating + an e-coat layer, (ii) Bonderite M-NT 1820 conversion coating + an e-coat layer, and (iii) Bonderite M-ZN 958 conversion coating + an e-coat layer. Three

specimens of each combination were used for statistical comparison. All cleaning and coating procedures were in accordance with the suppliers' Technical Process Bulletin.

Bonderite M-ZN 958 zinc phosphate conversion coating.

The hem flange specimens were first spray cleaned with Bonderite® C-AK T51 cleaner for 1 min (125 °F) followed by full immersion in a cleaner for 2 min (125 °F). Excess cleaner was removed by a 30-s warm tap water rinse. The cleaned specimens were further processed in Prepalene® X surface conditioner at room temperature for 30s. This surface conditioner was used to create nucleation sites on the clean surface and to promote fine growth of zinc phosphate crystals in the conversion coating. The conditioned specimens were conversion coated by immersion in the Bonderite M-ZN 958 bath for 2 min at 115 °F. This was followed by a 30-s room temperature tap water rinse and post-treatment in Bonderite M-PT 54 NC at room temperature for 30 s. The post-treatment reduces coating porosity and improves the barrier protection against moisture and salt. The post-treated specimens were rinsed with DI water for 30 s and dried with pressurized air. The coating weight for the conversion coated specimens was determined by the traditional Weigh-Strip-Weigh method. The coated panels were immersed in a solution containing nitric acid and sodium nitrate and gently scrubbed for 2 min on each side. The panels were then thoroughly rinsed and dried. The difference in panel weights before and after stripping was determined. The coating weight was similar on both alloys with a nominal value of 1.645 ± 0.036 g/m^2 (n = 3, desired weight: 1-3 g/m^2).

Bonderite M-NT 1820 zirconium oxide conversion coating.

The hem flange specimens were first spray cleaned with Bonderite® C-AK T51 cleaner for 30s (125 °F) followed by full immersion in the cleaner for 1 min (125 °F). Excess cleaner was removed by a 1-min warm tap water rinse followed by a DI water rinse for 1 min. The cleaned

specimens were then conversion coated by immersion in Bonderite M-NT 1820 for 2 min at 90°F. The conversion-coated specimens were rinsed for 1 min in DI water and dried with pressurized air. Zirconium oxide coating weights for the conversion coated panels were measured using an XRF analyser. The coating weights ranged from 60 – 70 mg/m^2 and 75 – 85 mg/m^2 for 6022-T4 and 6111-T4 panels, respectively (n = 3, desired weight: 50-80 mg/m^2).

E-coat (BASF Cathogard-800).

The conversion-coated specimens were wetted with DI water before applying the e-coat top layer under constant voltage. The parameters used for the e-coat deposition were as follows: temperature: 93°F; voltage: 238 V; current: 1A/ 12" x 4" panel (i = 0.15 A/cm^2); and time: 135s. These parameters produced a coating thickness of ~0.75 mil (19μm). The e-coated specimens were thoroughly rinsed with DI water. Excess water was wicked away using a paper towel. The specimens were then cured in an oven for 20 min at 360 °F.

6.3 ACCELERATED DEGRADATION TESTING.

The coated specimens were subjected to a 30-day accelerated degradation test according to ASTM G85 guidelines. The test chamber, maintained at 120 °F, sprays an acidified NaCl (5 wt. %) spray at regular intervals on the specimen surface. A test cycle consisted of the following steps: (i) 45 min of continuous salt spray, (ii) 120 min dry air purge, and (iii) 195 min soak at 95% R.H.

The pH of the NaCl solution was lowered to between 2.8 – 3.0 using acetic acid. The hem flange specimens were positioned vertically in the chamber throughout the 30-day test period. Some specimens were removed from the chamber after 5 days to probe for signs of initial corrosion damage. Specimens were thoroughly rinsed with DI water and air dried before conducting any analyses.

After the 30-day test period, the specimens were evaluated using two test methods. First, the multilayer coating adhesion was evaluated using test method BI 106-01 (Method D). Second, corrosion propagation from a scribe introduced into the specimen was assessed according to test method BI 169-01.

6.4 CHARACTERIZATION.

Scanning electron microscopy (SEM) was performed using a JEOL 7500 scanning electron microscope (JEOL Ltd, Tokyo, Japan). Energy dispersive x-ray spectroscopy was performed with an Aztec system detector (Oxford Instruments, UK) attached to the electron microscope. Spectral data were collected and analysed using the system software (version 3.1). Micrographs and spectra were recorded using a 15 keV accelerating voltage. A digital optical microscope (Keyence VHX 600) was used to capture micrographs of the alloy surface before and after accelerated degradation testing, and to quantitatively assess changes in the surface texture. The micrographs were used to identify pits and other forms of corrosion damage.

6.5 RESULTS

(i) Before G85 – Day 0

Hem flanges of uncoated and treated with Bonderite M-NT 1820 and Bonderite M-ZN 958 conversion coating plus and e-coat top layer were visually examined for surface imperfections before cyclic corrosion testing. The e-coat layer visually appeared to be evenly deposited, with no apparent surface defects on all the specimens irrespective of the alloy type and the conversion coating treatment. The thickness of the e-coat layer was ~0.75 mil (~19 µm) for all specimens. Microscopic examination of the edges of the hem flange specimens, however, revealed less complete, non-uniform e-coat layer coverage. This is perhaps not surprising given the complex hem geometry that could lead to a non-uniform electric field during the e-coat deposition. It is also

likely that the naturally occurring aluminum oxide layer is not completely removed at these corner sites during the conversion coating process, leaving behind electrically non-conducting regions. Such regions are prone to non-uniform electrophoretic deposition of the e-coat layer. Cracking of the e-coat at the hem bend was found on ~50% of all specimens (independent of alloy and conversion coating type) tested. The cracks appear to develop during e-coat at high temperature. Figure 6.3 shows micrographs of e-coat layer defects and cracking along the outer edges of both alloy types.

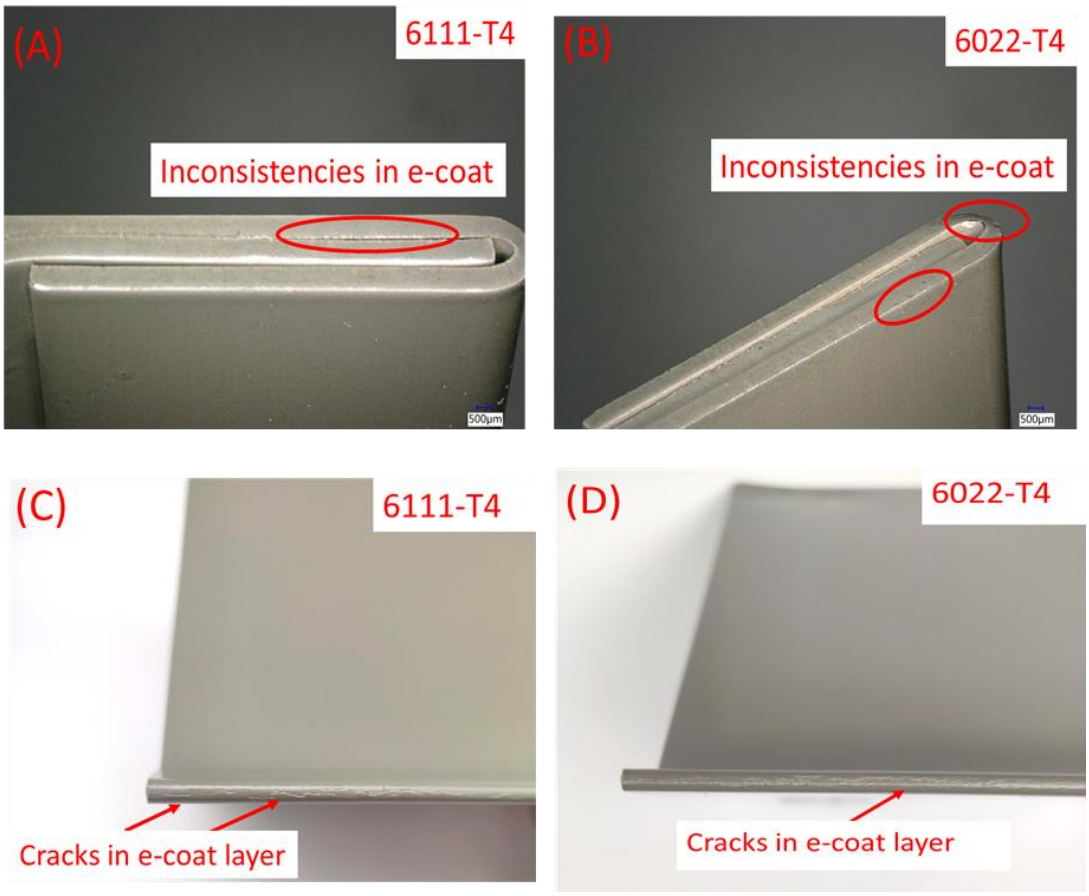

Figure 6.3 Digital micrographs (20x) of Bonderite M-NT 1820 conversion coated and e-coated hem flange specimens showing (A) and (B) inconsistencies in e-coat at the hem bend and (C) and (D) e-coat cracking in (Left) 6111-T4 and (Right) 6022-T4. Images were taken prior to ASTM G85 testing.

Some hem flange specimens were selected before G85 testing to inspect for e-coat coverage underneath the hem. Photographs of opened hem flanges in Figure 6.4 reveal the absence of an e-coat layer under the hem joint. Interestingly, white patches were seen under the joint that appear to be residue from the cleaner not washed away during pretreatment.

Figure 6.4 Photographs of Bonderite M-NT 1820 conversion coated, and e-coated hem flanges separated before G85 testing. Inspection of the photographs reveal no evidence of e-coat under the hem. Arrows and the inset figure indicate cleaner residue.

Sample stubs were punched from metal underneath the hem for chemical characterization. EDX elemental maps revealed no evidence of conversion coating elements such as Zn or Zr

confirming that the conversion coating did not form beneath the flattened hem. (Figure 6.5). This suggests that while the cleaner solution penetrates into the joint, the conversion coating bath apparently does not. The conversion coating and e-coat layer do not effectively form on omplex geometries, like crevices and hem joints.

The maps, however, do show presence of cleaner elements like K and Si. The cleaner residue is not fully washed away in the rinsing methods used hererin. and gets carried over throughout the specimen preparation process. Contents of the cleaning bath include potassium hydroxide, sodium silicate, sodium hydroxide and other surfactants at low concentrations. The origin of K and Si can be traced to the cleaner as no other bath contains these elements. The amount of cleaner solution penetrating the hem depends on the tightness of the joint with every flange retaining varying levels of cleaner. Figure 6.5 shows SEM micrographs and corresponding EDS elemental maps of areas where cleaner residue was found under the hem for both alloy types.

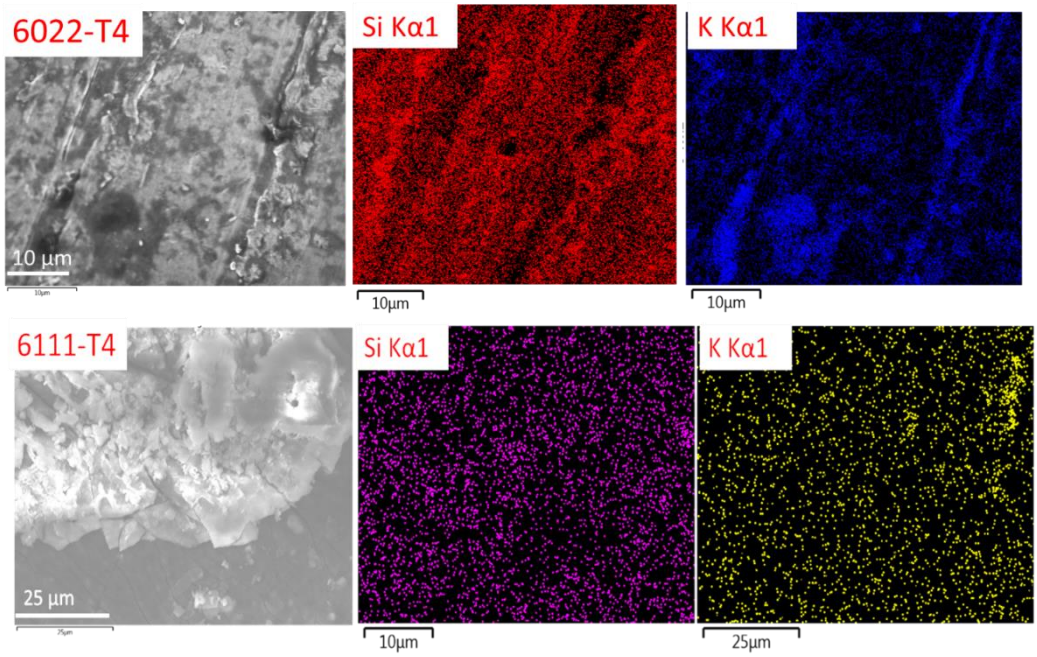

Figure 6.5 Scanning electron micrographs and EDS elemental maps of a AA6022-T4 specimen conversion coated with Bonderite M-ZN 958 (Top) 6022-T4 and AA6111-T4 conversion coated with Bonderite M-NT 1820 (Bottom) 6111-T4. The elements detected were K and Si from the cleaner.

(ii) After G85 test – Day 5

The coated hem joints were subjected to an accelerated degradation test (ASTM G85-Annex II) test for 30 days. Before placing specimens inside the test chamber, each piece was flexed at the hem edge in an outward direction. This was done to provide a pathway for salt penetration under the hem for early onset of corrosion. Care was taken not to damage the e-coat layer during the flexing process. One specimen from each set was removed from the chamber after Day 5 to probe for early-stage corrosion damage.

Specimens inspected after 5 days showed initial signs of corrosion damage along outer edges of the flange and at the hem edge where the outer panel wraps around the inner panel. These damage patterns are revealed in the digital micrographs presented in Figure 6.6. Some salt accumulation was observed at the hem edge. Bulk of the hem joint was unaffected and showed no signs of corrosion damage. Remember, only the bulk of the hem flange is protected by both conversion coating and e-coat. The alloy beneath the hem is unprotected with no conversion coating or e-coat. Corrosion damage was mainly in the form of e-coat delamination and blistering (Figure 6.6). Damage to the e-coat layer along the flange edge provides a pathway for salt solution to undercut under the layer. Undercutting the e-coat exposes the unprotected alloy where anodic reactions like aluminum dissolution, and cathodic reactions like hydrogen reduction, can commence. Over time, the cathodic reaction produces sufficient H_2 gas leading to a pressure build-up at the alloy/e-coat interface creating blisters in the e-coat. Figure 6.6. shows digital micrographs (after Day-5) of various forms of initial corrosion damage observed at the hem joint. One 6111-T4 specimen was chosen to illustrate all damages observed. It was still early in the test to conclude which alloy/conversion coating performed best.

Figure 6.6 Digital micrographs (20x) of a 6111-T4 alloy conversion coated with Bonderite M-ZN 958 and e-coated after a 5-day exposure to a G85 test. Top micrograph: arrows indicate a region where electrolyte creep underneath the e-coat layer occurred resulting in the formation of a blister. Bottom micrograph: an example of e-coat layer delamination along the edge of a hem flange.

Other forms of damage like pitting and filiform corrosion were detected underneath the hem. Figure 6.7 shows evidence for pitting and filiform corrosion underneath the hem. All pitting seems to be occurring near the edge of the joint. The highly acidic conditions within the test chamber also contribute to accelerating corrosion rate resulting in widespread pitting. Worm-like filaments

emerge at the hem edge of AA6022-T4 and continue to grow inwards towards the unprotected alloy. The presence of an e-coat prevents outward propagation of these filaments.

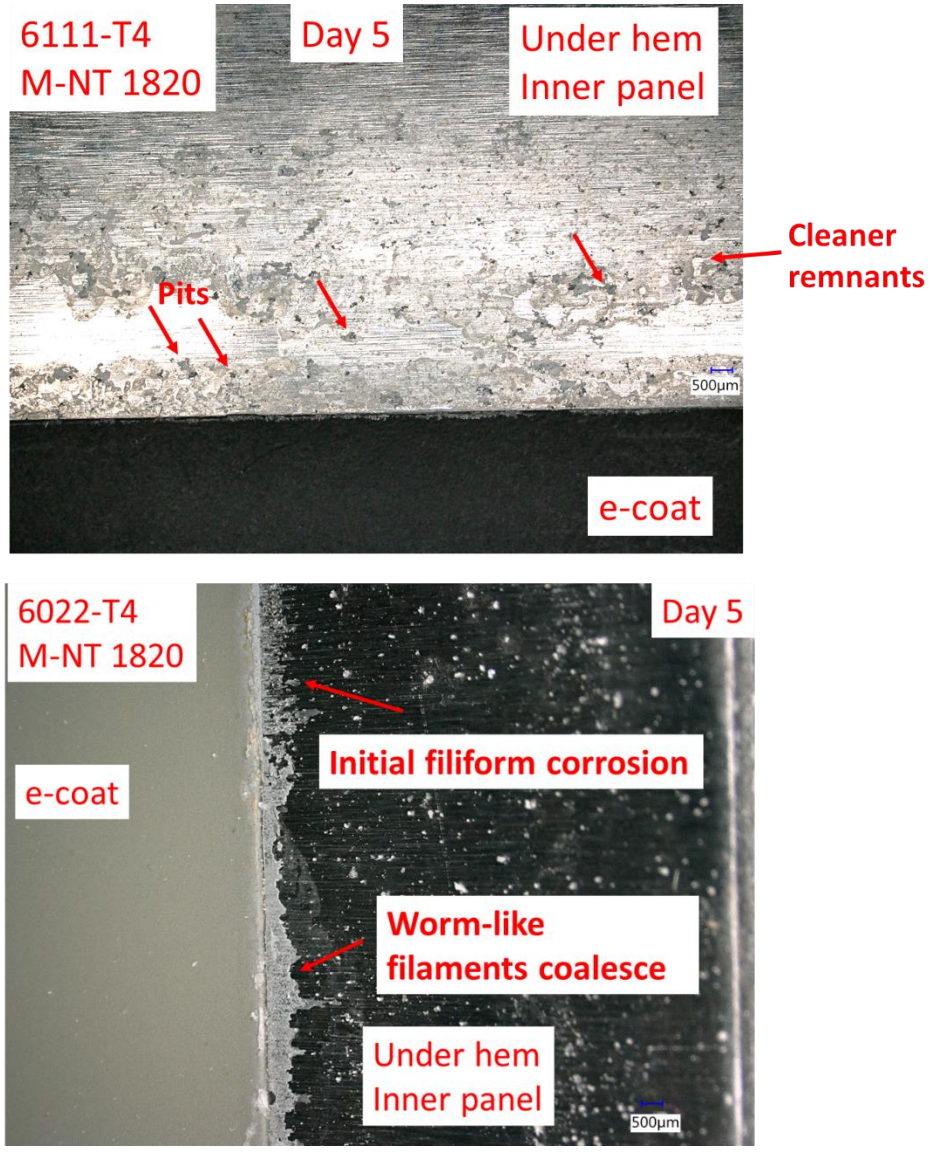

Figure 6.7 Digital micrographs (20x) of Bonderite M-ZN 958 conversion coated and e-coated (A) 6111-T4 inner panel after a 5-day G85 exposure. Arrows indicate pit formation in areas around cleaner residue. (B) 6022-T4 inner panel after a 5-day G85 exposure. Arrows indicate worm-like filaments growing inwards from the hem edge.

(iii) After G85 test – Day 30

Hem flanges removed after 30-day G85 test were characterized for corrosion damage. Figure 6.8 presents micrographs for 6111-T4 and 6022-T4 hem flange specimens with only an e-coat layer. Figures 6.9 and 6.10 present micrographs for hem flange specimens with a conversion coating and an e-coat layer. A quick survey of the microscopy data indicates the hem flangess with only an e-coat layer and no conversion coating exhibit a higher level of corrosion damage (severe blistering and filiform corrosion) as compared to the damage visible on the conversion coated and e-coated counterparts. Qualitatively, there is clear corrosion along the hem edge with blistering on the outer panel and filiform corrosion on the inner panel. It appears that the corrosion damage at the hem edge initiates at the outer edge of the panel, perhaps where the e-coat layer delaminated. The corrosion damage after 30 days exists along most of the underside of the hem joint. The specimens with the conversion coating and e-coat layer show significantly lesser, less e-coat delamination and smaller number of blisters as compared to the specimens with only the e-coat layer. Clearly, the presence of a conversion coating either improves adhesion to the e-coat layer and or improves the barrier layer properties of the overall coating system. Reduced corrosion damage was observed equally on specimens coated with either of the two conversion coatings. The extent of corrosion damage was observed to be dependent on the alloy type and less on the conversion coating type. Amongst the two alloys, 6111-T4, with a higher Cu concentration, exhibited signs of greater corrosion damage (Figure 6.9) than 6022-T4. In fact, Figure 6.10 shows that conversion coated and e-coated 6022-T4 exhibited negligible corrosion after 30 days of G85 test.

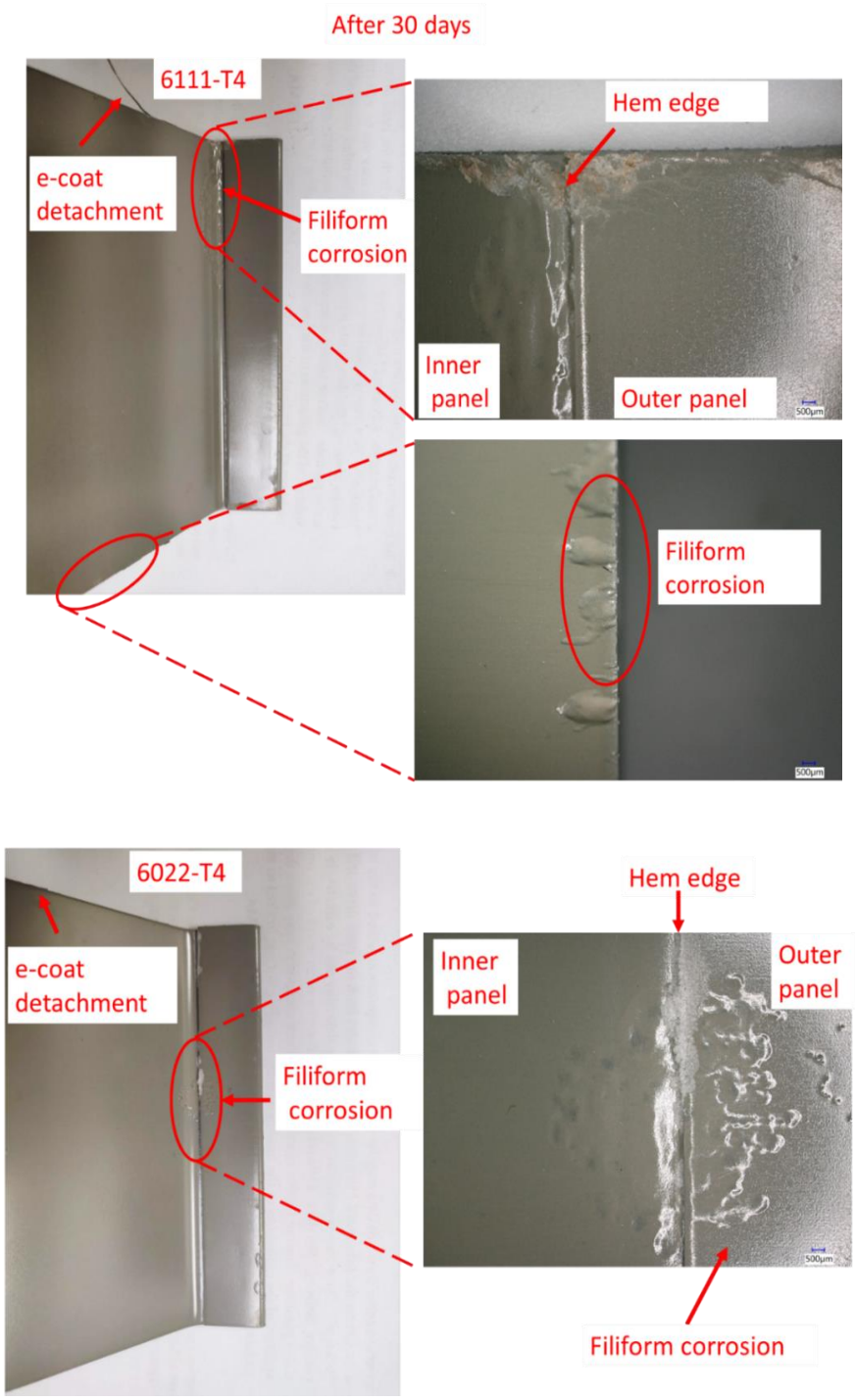

Figure 6.8 Photographs (left) and digital micrographs (right) of e-coated AA6111-T4 and AA6022-T4 hem joints with no conversion coating treatment after a 30- day G85 exposure. Filiform corrosion and widespread blistering are indicated in the as magnified micrographs (20x) on the right. Arrows in the left photographs show areas of e-coat layer delamination along the specimen edge.

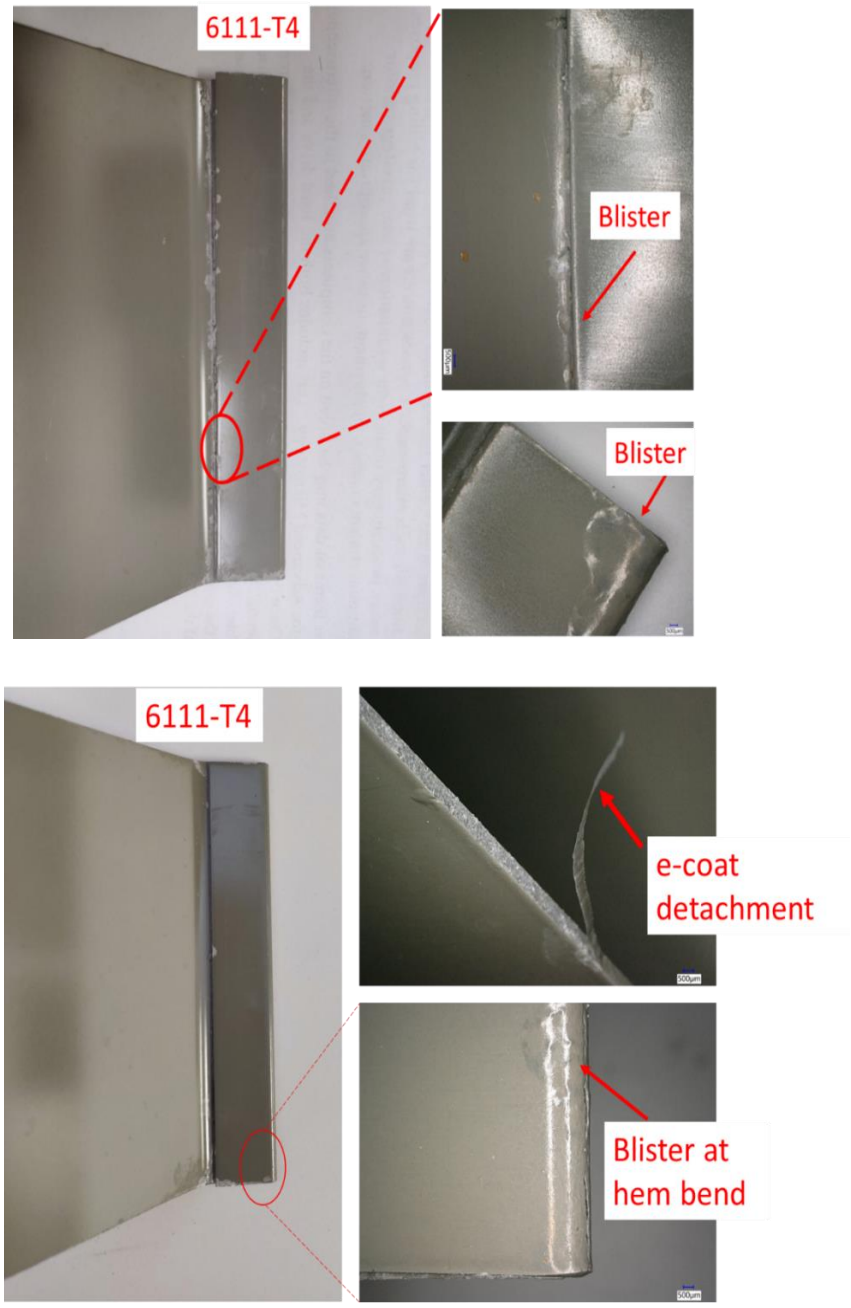

Figure 6.9 Photographs (left) and digital micrographs (right) (20x) of AA6111-T4 specimens with (Top) Bonderite M-NT 1820 and (Bottom) Bonderite M-ZN 958 conversion coatings and an e-coat after a 30- day G85 test. Small blisters are seen at the hem edge (top right) and hem bend (bottom right).

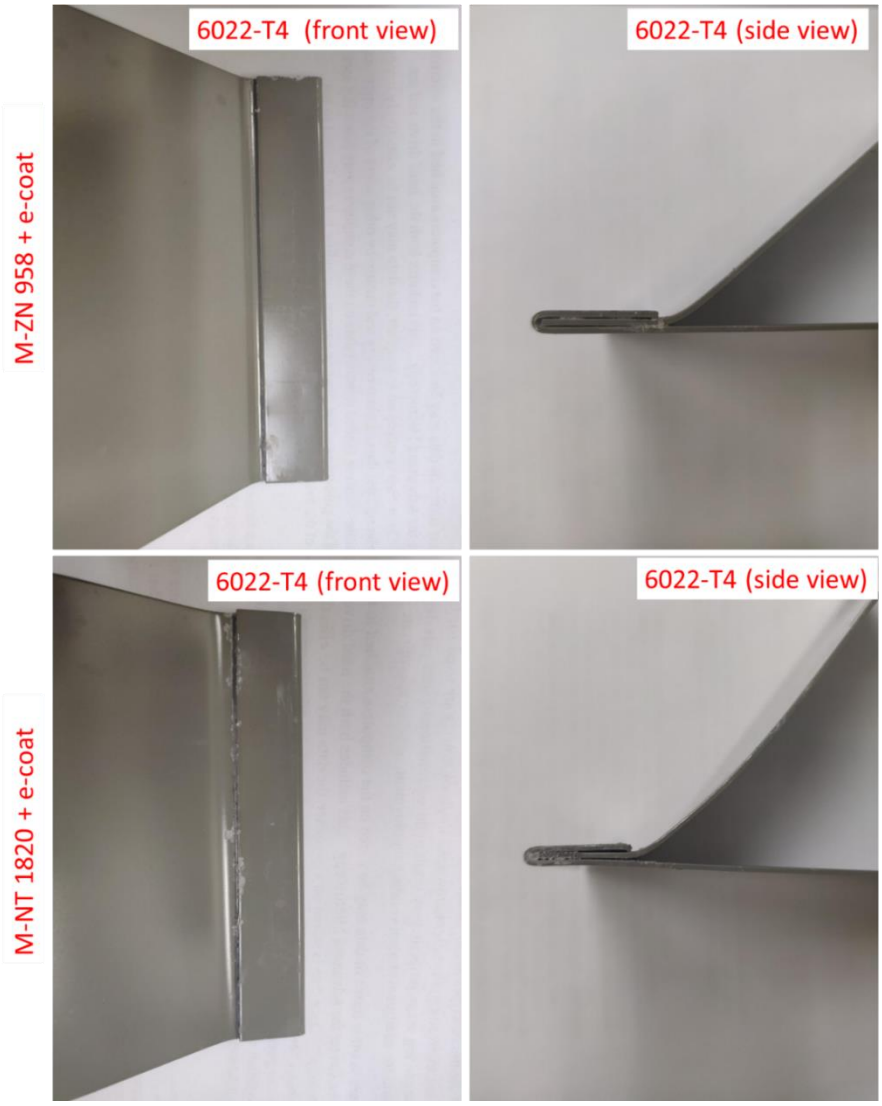

Figure 6.10 Photographs (left) and digital micrographs (right) (20x) of AA6022-T4 specimens with (Top) Bonderite M-NT 1820 and (Bottom) Bonderite M-ZN 958 conversion coatings and an e-coate layer after a 30-day G85 test.

Another interesting observation from the G85 test was the decrease in mechanical strength of the two alloys post 30-Day salt exposure. Figure 6.10 shows photographs of hem joints separated after Day-5 and Day-30 of the test. In the top photograph (Day 5), a wrench was used to separate the hem joint and investigate salt accumulation under the hem. Separation of the joint by hand was impossible at this stage. However, after Day-30 the joints were easily pried open by hand. All panels (conversion coated/non-conversion coated + e-coated) broke off at the hem bend indicating

weakening of the joint due to excessive corrosion caused by salt accumulation under the hem. No tensile or fatigue test was conducted to scientifically prove this observation due to the geometry of the test specimens. Such tests are needed to quantify loss in mechanical strength at the hem bend.

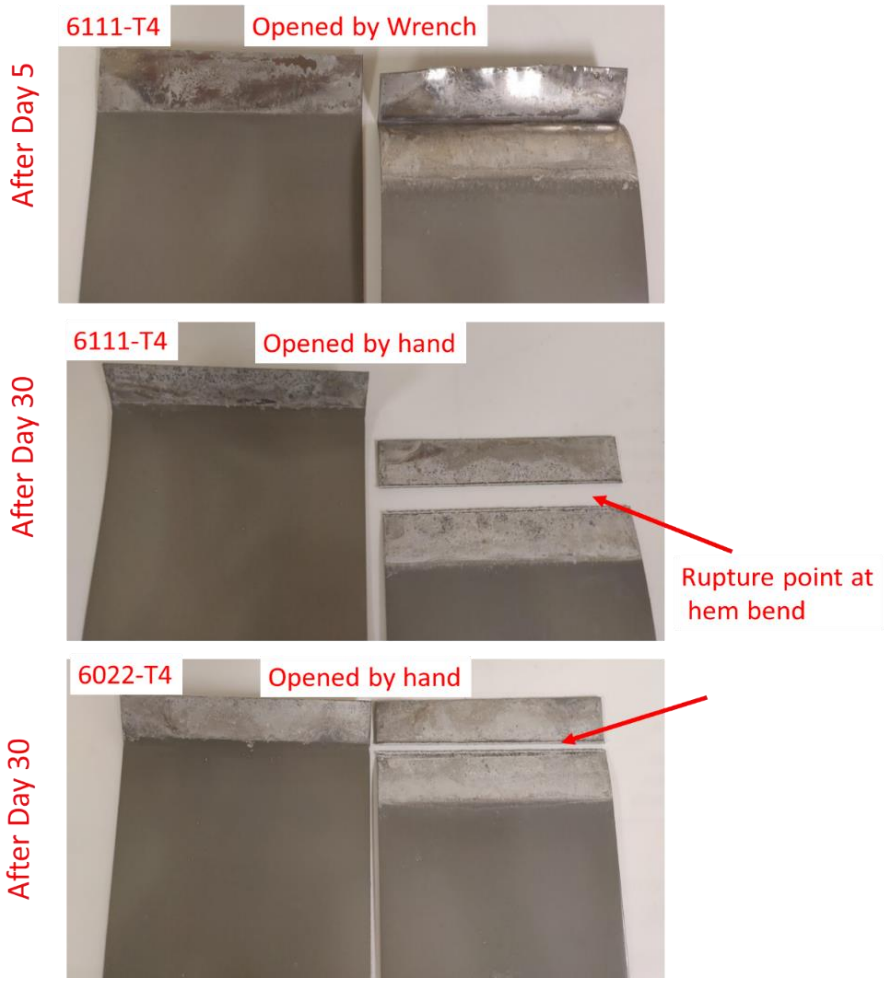

Figure 6.11 Photographs of separated hem flanges after Day-5 and Day 30 of G85 testing. The hem joint was opened using a wrench after Day-5. After Day 30, the hem was could be easily pried open by hand.

(iv) Paint Adhesion and Corrosion Propagation from a Scribe.

Paint adhesion tests were performed was to compare the corrosion resistance provided by the two conversion coatings – Bonderite M-ZN 958 and Bonderite M-NT 1820. Conversion coated and e-coated 6111-T4 and 6022-T4 flat panels (6” x 4”) were subjected to a 5-day G85 test and later assessed for corrosion damage through paint adhesion and corrosion propagation tests.

Table 6.1 summarizes results from the paint adhesion and corrosion propagation tests. Paint adhesion is classified from Grade 0-10 with grade 0 indicating 0% paint removal and grade 10 indicating ~95% removal. All panels passed the adhesion test with 0% paint removal indicating the e-coat adheres well to the conversion coated substrate. Creep from a 90 mm scribe during the 5-day test on 6022-T4 and 6111-T4 panels was-measured. Results from these tests are summarized in Table 6.1. On comparing data presented in Table 6.1, greater creep observed for AA6111-T4 indicates less resistance to corrosion for this alloy type as compared to AA6022-T4. The two conversion coatings perform statistically similar. Data shown above clearly suggest that the low Cu containing 6022-T4 alloy shows a higher creep resistance than 6111-T4 for all three coating conditions. A clear distinction between conversion coating performances, however, could not be made with the above tests.

Table 6.1 Data from the paint adhesion and corrosion propagation tests conducted according to Ford Laboratory test methods. Paint adhesion is classified from Grade 0-10 with grade 0 indicating 0% paint removal and grade 10 indicating ~95% paint removal.

Alloy	Surface Pre-treatment	Creep test (Day 5)	Paint adhesion test (Day 5)	Paint adhesion test (Day 30)
6022-T4	No conversion coating + e-coat	0.1 ± 0.003	Grade 0	Grade 0
	M-NT 1820 + e-coat	0.1 ± 0.004	Grade 0	Grade 0
	M-ZN 958 + e-coat	0.1 ± 0.002	Grade 0	Grade 0
6111-T4	No conversion coating + e-coat	8.2 ± 0.072	Grade 0	Grade 0
	M-NT 1820 + e-coat	3.6 ± 0.011	Grade 0	Grade 0
	M-ZN 958 + e-coat	2.1 ± 0.043	Grade 0	Grade 0

Effects of conversion coating: Corrosion performance of M-NT 1820 vs. M-ZN 958.

The 5-day G85 test of the two conversion coated specimens with an e-coat pain layer revealed no differences in the corrosion resistance and or adhesion. In other words, the conversion coating performance was similar for M-NT1820 and M-ZN 958 even though the coating chemistry is different. A 5-day G85 test was conducted on AA6111-T4 and AA6022-T4 hem flange specimens to compare the corrosion resistance performance of the two conversion coatings. Visual inspection of hem flanges in Figure 6.11 reveal that specimens coated with Bonderite M-NT 1820 show lesser corrosion damage as compared to specimens coated with Bonderite M-ZN 958 for both alloy types. These preliminary results indicate that Bonderite M-NT 1820 performs better than Bonderite M-

ZN 958. More evidence is required to confirm this observation. Again, hem flanges made with aluminum alloy 6111-T4 showed greater signs of corrosion damage as compared to 6022-T4.

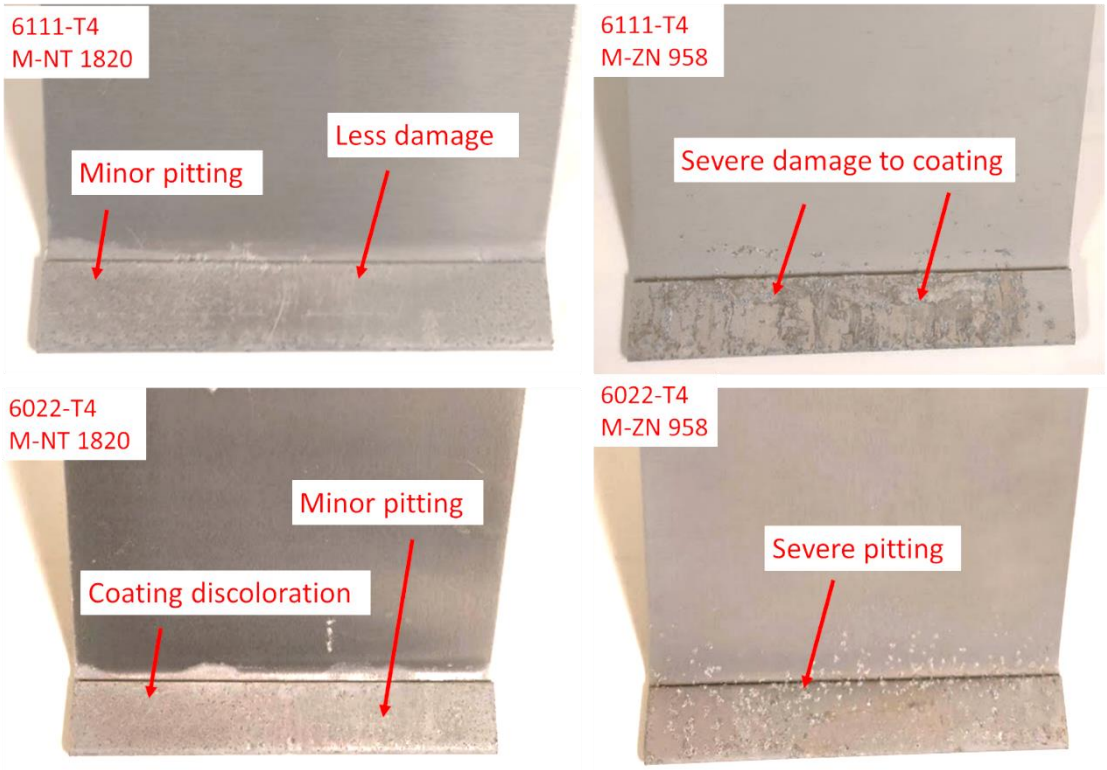

Figure 6.12 Photographs of conversion coated 6022-T4 and 6111-T4 hem flange specimens after 5-Day G85 test. Of the two alloys, 6111-T4 showed more corrosion damage. Bonderite M-NT 1820 conversion coated panels appear less damaged than panels conversion coated with Bonderite M-ZN 958.

6.6 DISCUSSION

The surface preparation method used to make hem flanges does not include a deoxidation step. Some of the naturally occurring aluminum oxide is removed from the alloy surface during formation of the conversion coating. However, not all oxide is removed from the surface, leaving behind non-conducting regions of the oxide, especially along the peripheries of the hem flange and at the hem edge. This results in uneven e-coat deposition. The complex geometry of the hem also creates a non-uniform electric field resulting in a non-uniform e-coat at the hem edges and hem

bend. Such areas as seen in results presented above, act as initial sites for corrosion initiation by allowing moisture and electrolyte ingress at the e-coat/substrate interface. Other points of electrolyte pathways include cracks at the hem bend developed during paint baking and other defects in the e-coat. Once electrolyte reaches the e-coat/substrate interface through these pathways, H-bonds responsible for adhesion between e-coat and conversion coating are dissolved by polar water molecules leading to anodic delamination of the e-coat. [21] Under the e-coat, cathodic reactions are triggered at the exposed intermetallic surfaces which were not previously removed by an etching or deoxidation step. Remember, no conversion coating is formed under the hem and corrosion reactions proceed unhindered. As the rate of oxygen reduction reactions increase, aluminum dissolution occurs around the intermetallic, resulting in pitting corrosion. Evidence for formation of pits is seen in both alloy types. The highly acidic nature of the test chamber provides H^+ ions that get reduced to form H_2 gas. Formation of sufficient hydrogen gas in a confined space under the e-coat creates pressure leading to e-coat blistering.

The high relative humidity and acidity within the test chamber are ideal conditions for filiform corrosion. Individual worm like filaments emerge at the e-coat/substrate interface both at hem edge and outer peripheries and propagate by tunnelling under the e-coat. The difference in oxygen concentration between the filament head and the corrosion initiation site acts as the driving force for corrosion propagation.[22-24] An interesting observation from this study is the role of conversion coating in arresting filiform corrosion. In the absence of a conversion coating, in Figure 6.7, filiform corrosion is seen propagating in both directions from hem edge *i.e.* starting from the e-coat towards the hem bend and away from the hem bend. However, for conversion coated hem flanges (Figure 6.8 and 6.9), filiform corrosion is seen propagating unidirectionally, only towards hem bend where no conversion coating is present. The conversion coating appears to be arresting

spread of filiform corrosion filaments preventing propagation at the bulk. This is because zinc phosphate and zirconium-based conversion coatings are known to form a thin protective layer over cathodic IMPs preventing corrosion reactions from proceeding. [25] Overall, the presence of a conversion coating layer did not introduce any paint adhesion issues as determined by tape tests, instead helped in arresting the rapid propagation of filiform corrosion.

The extent of filiform and pitting corrosion varies with the alloy type. Greater levels of e-coat blistering, creep and pit densities were seen for AA6111-T4 alloy as compared to AA6022-T4. In fact, corrosion damage for AA6022-T4 alloy was limited only to the unprotected surface under the hem. Minimal e-coat delamination and blistering was seen after 30-days of ASTM G85 test for this alloy. Pit density for AA6111-T4 was found to be ~ 9/cm^2 as compared to ~ 4/cm^2 for AA6022-T4. The reason for this is the difference in alloy composition and microstructure between the two alloys. AA6022-T4 is a high Si, low Cu containing alloy with mainly β (Mg_2Si) and S (Al_2CuMg) and few Q ($Al_xCu_yMg_zSi_w$) intermetallic phases. Mg_2Si and Al_2CuMg are anodic as compared to the surrounding matrix resulting in preferential Mg dissolution during corrosion. However, the high Cu-containing AA6111-T4 alloy contains mainly Q, θ (Al_2CuMg), Al_2Cu and Al_7Cu_2Fe intermetallic phases which are cathodic to the surrounding aluminum matrix. [26-28] The presence of several cathodic phases promotes greater cathodic reaction kinetics leading to widespread filiform corrosion.

Another interesting observation from this study is the loss in mechanical strength of the hem joint post 30 days ASTM G85 test. Bending the outer panel to ~180° introduces enormous stress in the hem joint. The U-shaped geometry of the hem flange results in electrolyte accumulation inside the hem. Overtime, the corrosive nature of the electrolyte and the repeated wet-dry cycles of the test, lead to significant loss in mechanical properties of the substrate. On applying sufficient

pressure, the joint breaks off neatly at the hem bend suggesting weakening occurring primarily in this region of the joint. This observation was true for both alloy types. Tensile strength tests are needed to quantify decrease in mechanical properties.

Preliminary data of conversion coated AA6111-T4 and AA6022-T4 hem flanges were collected post 5-day ASTM G85. Visual inspection indicates that the zirconium conversion coating suffers lesser corrosion damage than zinc phosphate conversion coated specimens for both alloy types. The zirconium-based conversion coatings have proven to perform as good as traditional zinc phosphate coatings without compromising adhesion properties. Replacing zinc phosphate coatings with Zr-based conversion coatings can help reduce operational costs by ~ 30%.[25]

6.7 CONCLUSIONS

E-coat forms uniformly (~0.75 mil) throughout the bulk of the hem flange but uneven e-coat deposition occurs at hem peripheries edges. Cracking in e-coat occuring during paint bake later act as corrosion initiation sites. Most corrosion damage is in the form of e-coat delamination and blistering. E-coat delamination provides channels for electrolyte access to the underlying metal that later manifests into filiform corrosion and large blisters during the course of the 30-day G85 test. Some blisters eventually migrate outwards and grow in size. Bulk of the hem flange is unaffected and shows no signs of corrosion damage. The 30-Day G85 test appears to negatively affect the mechanical strength of both alloys, 6022-T4 and 6111-T4, at the hem bend. Excessive salt accumulation under the hem weakens the metal causing it to break easily at the hem bend. Conversion coated and e-coated hem joints suffer lower corrosion damage (less blistering and filiform corrosion) after 30 days of G85 testing as compared to non-conversion coated and e-coated counterparts. Lesser creep was calculated for conversion coated and e-coated panels after 5-day of ASTM G85 test. Among the two alloys studied, 6022-T4 provided greater corrosion resistance

than 6111-T4. This is not surprising as alloys with high Cu content have been historically equated to greater corrosion susceptibility. Preliminary investigation of conversion coated hem flanges with no e-coat after 5-Day G85 test indicate that Bonderite M-NT 1820 provides superior corrosion protection compared to Bonderite M-ZN 958. More experiments are needed to confirm this observation.

REFERENCES

REFERENCES

(1) Arnold, S. A. Techno-Economic Issues in the Selection of Auto Materials. *JOM* **1993**, *45*(6):12-15.

(2) Cole, G. S.; Sherman, A. M. Light Weight Materials For Automotive Applications. *Mater. Charact*. **1995**, *35* (1), 3-9.

(3) Muraoka, Y.; Miyaoka, H. Development Of An All-Aluminum Automotive Body. J. *Mater. Process*. **1993**, *38* (4) 655-674.

(4) Musfirah, A. H.; Ghani, J. A. Magnesium And Aluminum Alloys In Automotive Industry. *Res. J. Appl. Sci*. **2012**, *8* (10) 4865-4875.

(5) Fridlyander, I. N.; Sister, V. G.; Grushko, O. E.; Berstenev, V. V.; Sheveleva, L. M.; Ivanova, L. A. Aluminum Alloys: Promising Materials in the Automotive Industry. *Met. Sci. Heat Treat.* **2002**, *44*, 365-370.

(6) Ghassemieh, E. Materials in Automotive Application, State of the Art and Prospects, **2011**.

(7) Lahaye, C.; Söderlund, J.; Have, D. T.; Schwenk, H. SAE International, **1998**.

(8) Miller, W. S.; Zhuang, L.; Bottema, J.; Wittebrood, A. J.; De Smet, P.; Haszler, A.; Vieregge, A. Recent Development in Aluminium Alloys for the Automotive Industry. Mater. Sci. Eng. A **2000**, *280*, 37-49.

(9) Campestrini, P.; Van Westing, E. P. M.; Rooijen, H. W.; De Wit, J. H.W. Relation Between Microstructural Aspects Of AA2024 And Its Corrosion Behaviour Investigated Using AFM Scanning Potential Technique. *Corros. Sci.* **2000**, *42* (11) 1853-1861.

(10) Buccheit. Jr., R. G.; Moran, J. P.; Stoner, G. E. Localized Corrosion Behavior of Alloy 2090—The Role of Microstructural Heterogeneity. *Corros. Sci*. **1990,** *46* (8) 610-617.

(11) Meng, Q.; Frankel, G. S. Effect of Cu Content on Corrosion Behavior of 7xxx Series Aluminum Alloys. *J. Electrochem. Soc*. **2004**, *151* (5), B271-B283.

(12) Schuman, T. P. Chapter 20 - Protective Coatings for Aluminum Alloys, *Handbook of Environmental Degradation of Materials: Second Edition*. **2012,** 503-538.

(13) Gnedenkov, S. V.; Khrisanfova, O. A.; Zavidnaya, A. G.; Sinebrukhov, S. L.; Gordienko, P. S.; Iwatsubo, S.; Matsui, A. Composition And Adhesion Of Protective Coatings On Aluminum. *Surf. Coat. Technol*., **2001**, *145* (1-3) 146-151.

(14) Rani, B. E. A.; Basu, B. B. J. Green Inhibitors for Corrosion Protection of Metals and Alloys: An Overview, *Int. J. Corros*., **2012**, 1687 - 9325.

(15) Funke, W. How Organic Coating Systems Protect Against Corrosion, Chapter 20. Materials for corrosion protection. *American Chemical Society*, **1986**, 222-228.

(16) Corner, T. Polymeric Materials for Corrosion Control, *Br. Polym. J.* **1986.**

(17) Kadioglu, F.; Adams, R. D. Flexible Adhesives For Automotive Application Under Impact Loading. *Int. J. Adhes. Adhes.* **2015**, *56*, 73-78.

(18) Barnes, T. A.; Pashby, I. R. Joining Techniques For Aluminium Spaceframes Used In Automobiles, Part II - Adhesive Bonding And Mechanical Fasteners. *J. Mater. Process.* **2000**, *99*, 72-79.

(19) Satoh, T.; Miyazaki, Y.; Suzukawa, Y.; Nakazato, K. On The Development Of Structural Adhesive Technology For The Automotive Body In Japan. JSAE Review, **1996**, *17*, 165-178.

(20) Bretz, G. T.; Lazarz, K. A.; Hill, D. J.; Blanchard, P.J. Adhesive Bonding and Corrosion Protection of a Die Cast Magnesium Automotive Door. *Essential Readings in Magnesium Technology*, **2014,** 609-615.

(21) Critchlow, G. W.; Brewis, D. M. Review Of Surface Pretreatments For Aluminium Alloys. *Int. J. Adhes. Adhes.* **1996**, *16* (4) 255-275.

(22) LeBozec, N.; Persson, D.; Thierry, D. In Situ Studies Of The Initiation And Propagation Of Filiform Corrosion On Aluminum. *J. Electrochem. Soc*., **2004**, *151* (7), B440.

(23) Zhou, X.; Thompson, G. E.; Scamans, G. M. The Influence of Surface Treatment on Filiform Corrosion Resistance of Painted Aluminium Alloy Sheet. *Corros. Sci*., **2003**, *45* (8) 1767-1777.

(24) Le Bozec, N.; Persson, D.; Nazarov, A.; Thierry, D. Investigation of Filiform Corrosion on Coated Aluminum Alloys by FTIR Microspectroscopy and Scanning Kelvin Probe. *J. Electrochem. Soc*. **2002,** *149* (9), B403.

(25) Milošev, I.; Frankel, G. S. Review—Conversion Coatings Based on Zirconium and/or Titanium. *J. Electrochem. Soc.*, **2018**, *165* (3), C127-C144.

(26) Yassar, R. S.; Field, D. P.; Weiland, H. The Effect Of Predeformation On The B ″And B′ Precipitates And The Role Of Q′ Phase In An Al–Mg–Si Alloy; AA6022. *Scr. Mater.*, **2005**, *53* (3), 299-303.

(27) Abou Khatwa, M. K.; Malakhov, D. V. On The Thermodynamic Stability of Intermetallic Phases in the AA6111 Aluminum Alloy. CALPHAD, **2006**, *30*, 159-170.

(28) Quainoo, G. K.; Yannacopoulos, S.; Gupta, A. K. Strengthening Characteristics of AA6111 Aluminum. Canadian Metallurgical Quarterly, **2001**, *40* (2), 211-220.

CHAPTER 7. INVESTIGATION OF TRIVALENT CHROMIUM PROCESS CONVERSION COATING AS A SEALANT FOR TYPE II ANODIZED AA2024-T3.

Chapter adapted from *J. Electrochem. Soc*., 167, 111504 (2020).

Article: T. K. Shruthi, Jack Walton, Sarah McFall-Boegeman, Sjon Westre and Greg M. Swain, Investigation of the Trivalent Chromium Process Conversion Coating as a Sealant for Anodized AA2024-T3.

7.1 INTRODUCTION

High strength aluminum alloys (2xxx and 7xxx series) have considerable technological utility due to their lightweight and high mechanical strength.[1] These alloys are comprised of complex metallographic microstructures with various microscopic intermetallic phases dispersed throughout the matrix that contribute to the material's mechanical properties. However, the exposed intermetallic particles also render the alloy susceptible to localized pitting corrosion through the formation of galvanic couples with the aluminum matrix.[2-5] Military aircraft, weapons systems platforms and ground support equipment often use anodization as a surface pretreatment for aluminum alloys. The anodization technique provides more protection against degradation and corrosion than chemical conversion coatings due to the thick oxide coating.[6-10]

Anodizing is an effective electrochemical method to improve the corrosion and wear resistance of aluminum alloys.[6,7] Anodic coatings applied to aluminum and aluminum alloys are classified by several types: Type I and IB – electrolytic anodization in chromic acid; Type IC – electrolytic anodization in a non-chromic mineral acid; Type II – electrolytic anodization in a sulfuric acid bath and Type IIB – thin sulfuric acid anodization for use as a non-chromate alternative for Types

I and IB; and Type III – electrolytic anodization to produce a hard and dense oxide coating such as in sulfuric/boric acids. Key properties of the anodic coating are thickness (0.1 – 2 mils or 2.5 – 25 microns), coating weight (200-2000 mg/ft^2) and hardness/abrasion resistance.[6-8,11-13]

Oxide coatings generally consist of a thick, porous outer layer of alumina overlying a thin, compact inner or barrier layer.[6-10] Although the oxide passivates the surface, the coating is porous, thereby providing pathways for water, electrolyte ions and dissolved oxygen to reach the underlying metal. Cracks or defects tend to form in the oxide around the intermetallic particles that provide pathways for electrolyte penetration through to the underlying metal. Such defects reduce the overall corrosion resistance of the anodized layer.[14] The coatings generally need to be sealed – a process that either reduces the diameter of the outer pores to form a more compact film, or causes blockade of the pores by precipitation or inclusion of salt deposits.

There are several different treatments used to seal anodized aluminum alloys including chromate[15,16], hot water[17] and nickel acetate.[18] Chromate-based sealers are considered the best when maximum corrosion resistance is desired.[15] Water-based sealers are attractive when reduced corrosion performance is acceptable. Both of these processes require operating temperatures of 190 to 200 °F and immersion times of up to 25 min to achieve proper sealing and therefore maximum corrosion resistance.[15] Immersion in hot ultrapure water causes closure of the outer pores by a chemical process that involves the formation of boehmite by hydration of the alumina.[8,19]

$$Al_2O_3 + H_2O \rightarrow 2AlOOH \tag{14}$$

The sealed outer oxide layer is much thicker than the interfacial barrier layer. Several alternate sealing baths based on nickel salts[18,20] rare-earth salts[21,22] and organic compounds[23] have been used

to fill outer regions of the pores with precipitates that increase barrier properties of the coating by inhibiting internal transport of solution species through the porous network, thereby improving the corrosion resistance.

Chromate-based treatments use hexavalent chromium, which is toxic and carcinogenic to humans.[15,19,24] With the recent reduction in Occupational Safety and Health Administration permissible worker exposure limit of hexavalent chromium and world-wide pressure to eliminate use of this chemical species, many suppliers and end-users are pursuing alternative processes that are equally effective without the environmental, safety, and health risks.[15] The chromate-based process is run at a high temperature for a lengthy time. Hot water sealing does not have the environmental, safety, and health risk associated with chromate-based sealers, but it is sensitive to impurities and difficult to maintain as a process.[15] Anodic coatings sealed with chromate generally provide exceptional corrosion resistance. Processes with reduced use of hazardous chemicals, operating temperatures and immersion times are attractive alternatives being sought.

In this project, two trivalent chromium process (TCP) conversion coatings were investigated for their ability to seal sulfuric acid anodized aluminum alloy 2024-T3 and protect it from corrosion in two different degradation tests. TCP baths consist of potassium hexafluorozirconate, chromium (III) sulfate and fluoride at a pH around 3.8.[26] There has been an extensive body of literature published recently on the formation, structure and corrosion protection of TCP-coated aluminum alloys, as exemplified in these citations.[25-29] Other than a DoD report, we are unaware of any published literature on TCP sealants for anodized aluminum.[15] There has been one recent report on sealing oxide coatings on aluminum alloys 2618 and 7175 with a solution containing trivalent chromium Cr(III) and fluorozirconate Zr(IV) salts.[30]

Basic research was performed to investigate the mechanism by which the TCP conversion coatings (TCP-HF and TCP-NP) seal Type II sulfuric acid (SA) anodized layers on AA2024-T3 and the enhanced corrosion resistance these sealants provide. Unsealed anodic coatings are also part of the studies. Electrochemical techniques including open circuit potential measurements (OCP), potentiodynamic polarization curves and electrochemical impedance spectroscopy at the OCP were employed to assess the corrosion resistance of sealed anodized and unsealed anodized alloys. Scanning electron microscopy (SEM) with energy dispersive x-ray spectroscopy (EDS) was used to determine the oxide and sealed oxide morphology as well as the distribution of TCP coating bath constituents, Zr and Cr, within the oxide. SEM with focused ion beam (FIB) milling was used to examine oxide morphology and thickness, and TCP coating thickness, in the cross section. Sealed and unsealed anodized specimens were exposed to a 14-day neutral salt-spray (ASTM B117) and a 5-day full immersion (3.5 wt.% NaCl) test to assess the corrosion resistance of the TCP-sealed specimens.

7.2 MATERIALS AND METHODS

Reagents.

Cleaner 1000, TCP-NP (hereafter referred to as TCP-1) and TCP-HF (hereafter referred to as TCP-2) baths were provided by CHEMEON Surface Technology. The degreaser was prepared to a concentration of 45 g/L and the deoxidizer, HNO_3, was used at 35 wt.% when applying TCP-2. The TCP-2 coating bath was diluted with ultrapure water to 30 vol. % prior to use. TCP-1 was prepared by mixing 0.5 vol. % each of the two components: parts A and B. The pH of both TCP baths was adjusted to 3.85 using 0.25 M NaOH or 0.5 M H_2SO_4, as required. Electrochemical anodization of the AA2024-T3 specimens was performed in 9.8 wt.% H_2SO_4. No filtration step to remove any suspended particulates in the coating bath was applied before use.

Specimen preparation.

Aluminum alloy 2024-T3 specimens were obtained as 2 mm-thick sheets (www.metalsonline.com) and cut into $1in^2$ squares for the experiments. The specimens were prepared for use by first abrading with 1500 grit wet aluminum oxide paper for 2 min. This was followed by hand polishing with 0.3 μm alumina grit (Buehler), slurried in ultrapure water, on a felt pad for 2 min. A final hand polish was performed using 0.05 μm alumina powder slurried in ultrapure water on a separate felt pad. A 20-min ultrasonic cleaning in ultrapure water followed by a 20-min ultrasonic cleaning in purified isopropyl alcohol was applied after each polishing step to remove polishing debris. The polished specimens were then degreased in CHEMEON cleaner 1000 at 55 ℃ for 10 min followed by a 2-min ultrapure water rinse. The degreased specimens were then deoxidized in 35 wt.% HNO_3 for 2 min at room temperature followed by a 2-min ultrapure water rinse. The degreased and deoxidized specimens were then dried with N_2 before being electrochemically anodized.

Electrochemical Anodization.

The degreased, deoxidised AA2024-T3 specimen were anodized according to anodization procedure briefed in Chapter 2 (Section 2.3).

Sealing.

The anodized specimens were sealed by immersion with TCP-1 (TCP-NP) or TCP-2 (TCP-HF). An immersion time of 5 min for TCP-1 and 10 min for TCP-2 was used, both at room temperature. The optimum immersion times were selected to provide the maximum corrosion resistance based on electrochemical measurements in naturally aerated 0.5 M Na_2SO_4 + 0.01 M NaCl using anodized specimens sealed for different times from 1-20 min.

Oxide Coating Weight Determination.

The oxide coating weight was determined using a chromic acid stripping method, as described in ASTM B137. Anodized specimens were air dried for 24 h before chemically dissolving the oxide. Specimens were weighed before immersing in the stripping solution (20 g CrO_3 and 35 mL of concentrated (85 wt.%) phosphoric acid, both diluted with ultrapure water to 1L). Immersion was done in 5-min periods to dissolve the oxide. Specimens were then rinsed with ultrapure water and dried with N_2 before measuring the weight. Typically, a total of 15 min was required to dissolve the oxide and to obtain an unchanging weight. Table 7.1 presents results for three anodized specimens. A nominal oxide weight of 1192 ± 43 mg/ft^2 was found (n=3 anodized specimens). According to document MIL-A-8625F, a minimum oxide coating weight for a Type II sulfuric acid anodization is 1000 mg/ft^2.[7]

Table 7.1 Oxide weights for Type II sulfuric acid anodized AA2024-T3 specimens as determined by ASTM B137.

Anodized Samples	Weight Before Stripping (µg)	Weight After Stripping (µg)	Difference in weight (mg)	Oxide Weight (mg/ft^2)
Specimen 1	1833	1827	6.2	1190
Specimen 2	1758	1751	6.4	1236
Specimen 3	1809	1803	5.7	1150

Anodization was performed for a total of 23 min at 15 VDC. Area of oxide = 0.75 in^2.

CHEMEON Prepared Specimens. Anodized AA2024-T3 specimens, unsealed and TCP sealed, were prepared by a commercial coater. A total of 24, 1" x 1" specimens, were prepared: (i) 8 anodized and TCP-2 sealed, (ii) 8 anodized and hot water sealed and (iii) 8 anodized and unsealed.

Specimen pretreatment prior to anodization included the following: (i) 6-min exposure to CHEMEON cleaner 1000 (45 g/L at 55 ^{o}C), (ii) 1-min tap water rinse, (iii) 2-min CHEMEON Deox 3300 (25 g/L, 5 wt. % H_2SO_4 + 5 wt. % HNO_3 at room temperature) and (iv) 1-min tap water rinse.

The pre-treated specimens were then anodized at 12 A/ft^2 (13 mA/cm^2) in 190 g/L H_2SO_4 (~10 wt. %) at room temperature for a total of 29.4 min. A 3-min linear ramp of the current was used to start the anodization. After anodization, the specimens received two, each 2-min, rinses with deionized water. TCP-sealed specimens were prepared by immersing the anodized substrates in TCP-2 (30 vol. %) for 5 min at room temperature. Hot water sealed specimens were prepared by immersing the anodized substrates in deionized water, pH 5.8, for 30 min at 96 ^{o}C. Oxide thickness was reported to be 10 μm but was measured to be closer to *ca.* 5 μm.

7.3 TESTING & CHRACTERISATION

Electrochemical Characterization.

All electrochemical measurements were performed in a 1 cm^2 flat cell (Bio-Logic Science Instruments, France) as described in Chapter 2. The order of measurements for a particular specimen was the following: Initial OCP, EIS at the OCP, OCP and potentiodynamic polarization curve.

Accelerated Degradation Tests.

5-day Full Immersion Test. Sealed and unsealed anodized AA2024-T3 specimens were continuously immersed at room temperature in 3.5 wt. % NaCl for 5 days. Open circuit potential (OCP) measurements and electrochemical impedance spectroscopy (EIS) at the OCP were performed daily. The purpose for these measurements was to investigate the time dependence of any solution penetration through the sealed oxide to the underlying metal.

Neutral Salt-Spray Test (ASTM B117). The TCP-sealed and unsealed anodized AA2024-T3 specimens were exposed to a 14-day (336 h) neutral salt spray (NSS), according to ASTM B117 (5 wt. % NaCl and 35 ± 1°C), in a commercial 4 ft^3 salt-spray chamber (MX 9204, Associated Environmental Systems). The salt solution in the chamber was refilled daily. Specimens were inspected daily for initial signs of corrosion damage.

Corrosion Damage Assessment. The U.S. ARMY Corrosion Control and Prevention Group has established a new scale for the assessment of corrosion damage and material degradation during accelerated degradation testing.[31] The following scale was used herein: **Stage 0** – shows no visible corrosion. **Stage 1** – sample discoloration and staining. **Stage 2** – loose isolated rust or corrosion product and early stage pitting of the surface along with minor etching. **Stage 3** – more extensive rust or corrosion product, minor etching, pitting and more extensive surface damage. **Stage 4** – extensive rust or corrosion product formation, extensive etching, blistering, deadhesion and pitting that has progressed to the point where the life of the specimen has been affected. This scale was used herein.

7.4 RESULTS

Characterization of the Oxide and TCP-Sealed Oxide Layers.

Figure 7.1 shows scanning electron micrographs of (A) unanodized AA2024-T3, (B) anodized AA2024-T3 and (E and F) TCP-sealed and anodized AA2024-T3. The unanodized alloy, which was degreased and deoxidized, is relatively smooth with etch pits (dark spots) decorating the surface (Figure 7.1A). These pits form mainly during the deoxidation step, but some are present on the as received alloy. The porous oxide morphology is evident in the micrograph for the anodized specimen (Figure 7.1B). Electrochemical anodization of aluminum alloys produces a nanoporous oxide layer with pore diameters in the range of 10 – 50 nm, depending on the acid and

process parameters.[32-37] Oxide coating thickness for this specimen is *ca.* 5 μm, as determined from SEM-FIB analysis (Figure 7.1C). This oxide thickness was reproducibly observed for the sulfuric acid anodization conditions employed herein and is consistent with the thickness estimated (*ca.* 3 μm) from the coating weight and the density of aluminum oxide (3.95 g/cm^3). Cross-sectional analyses of the oxide layer (Figure 7.1D) also shows that the coating consists of some defects most likely caused by dislodged intermetallic particles entrapped within the growing layer. This gives rise to incomplete oxide formation. Such micro-sized defects and heterogeneities have been previously observed in oxides grown electrochemically on 2xxx series aluminum alloys. [30,32,38,39] These defects have been attributed to partial dissolution of copper rich and Al_9FeNi intermetallic phases at the high potentials used for anodization in sulfuric acid.[38] After immersion sealing, both TCP coatings form over the outer oxide layer (Figure 7.1E and F). In other words, the sealant fills in the outer pores. The micrographs reveal continuous TCP coating coverage across the outer surface with so-called mud cracking that forms in the vacuum environment of the SEM. Cracks are not formed during the sealing process and are rather a result of dehydration in the vacuum.[40,41]

The SEM micrograph in Figure 7.1B reveals a porous oxide surface (*ca.* 20 nm pores) that is partially covered by amorphous aluminum hydroxysulfate deposits after anodization. In this case, these deposits were incompletely removed by washing. Immediately after anodization and with no washing, the pores are totally obscured by these deposits (*e.g.* anodization smut) across the surface. The chemical composition of the deposits was confirmed by x-ray microanalysis that revealed signals for Al, S and O. It was found that this smut can be effectively dissolved by a 20-min full immersion in room temperature ultrapure water, as shown in the electron micrographs presented in Figure 7.2.

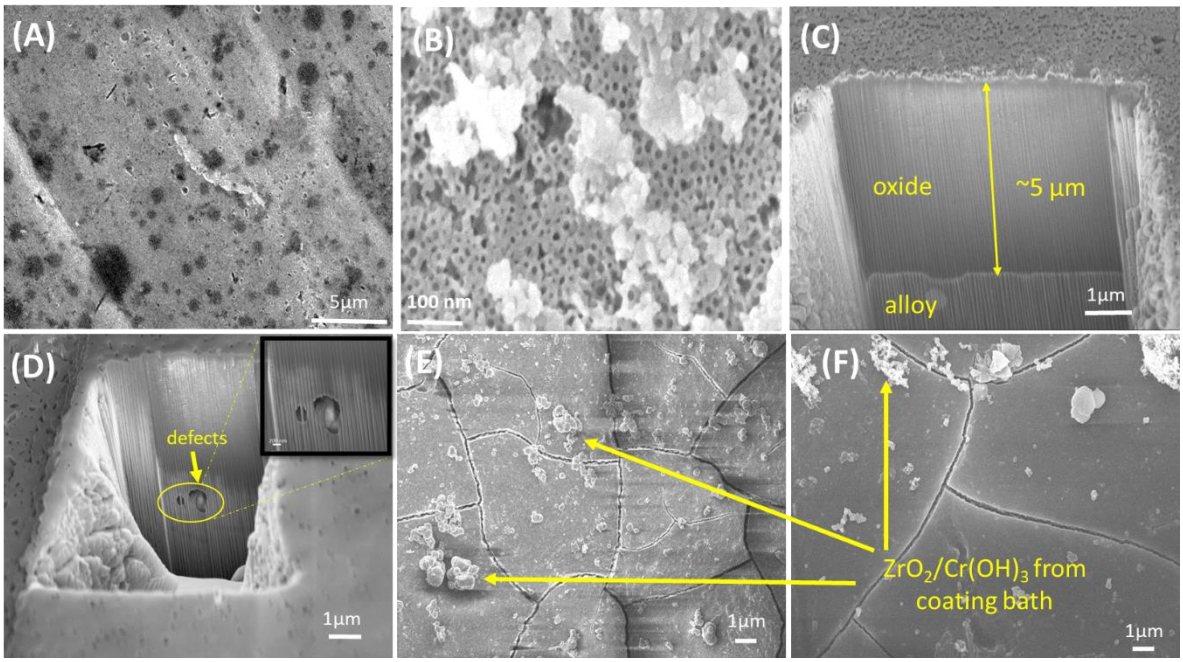

Figure 7.1 Scanning electron micrographs of (A) degreased and deoxidized AA2024-T3, (B) anodized AA2024-T3 in 9.8 wt.% H_2SO_4, (C) FIB-milled cross-section of the oxide layer grown on AA2024-T3 showing micropores and oxide thickness, (D) defect in the oxide layer grown on AA2024-T3 due to a dislodged intermetallic particle, I 10-min TCP-2 sealing of an AA2024-T3 specimen anodized in 9.8 wt. % H_2SO_4, and (F) 5-min TCP-1 sealing of an anodized AA2024-T3 specimen. The specimens were anodized at 15 V DC for a total of 23 min.

Figure 7.2A and B show electron micrographs of an anodized specimen before and after removal of the smut. Figure 7.2C presents a higher magnification micrograph of the smut-free oxide. Clean oxide pores are in the 10-20 nm range. If not removed, the smut could lead to weak adhesion with topcoats. The deposits could also cause incomplete sealing with TCP or other sealants.

Micrographs in Figure 7.1E and F reveal mud-cracks in both TCP sealant layers formed on anodized AA2024-T3. These cracks are caused by dehydration of the conversion coating in the vacuum of a SEM chamber and are not present when the TCP layer forms. This was confirmed through an experiment involving anodized AA2024-T3 specimens sealed with TCP-1 (5-min immersion) and TCP-2 (10-min immersion). Optical microscopy was then performed on the sealed

specimens before and after aging overnight, and once again after exposing the same sealed specimens to the vacuum for 30 min. Figure 7.3 shows optical micrographs of an anodized and TCP-2 sealed specimen before and after vacuum exposure. The optical micrograph in Figure 7.3A shows a crack-free sealant layer before exposure to vacuum. Figure 7.3B shows cracks across the sealant layer after vacuum exposure. Interestingly, the cracks (~1µm deep) in the TCP sealant layer also form in the outer oxide layer, as evidenced in the cross-sectioned micrograph shown in Figure 7.3C. Similar results were observed on anodized specimens sealed with TCP-1. Dark regions in the micrographs are not topographical features (*e.g.*, pits or raised features), as confirmed by 3D optical microscopy. Rather, these are regions of discoloration that reflect light differently than the surrounding metal.

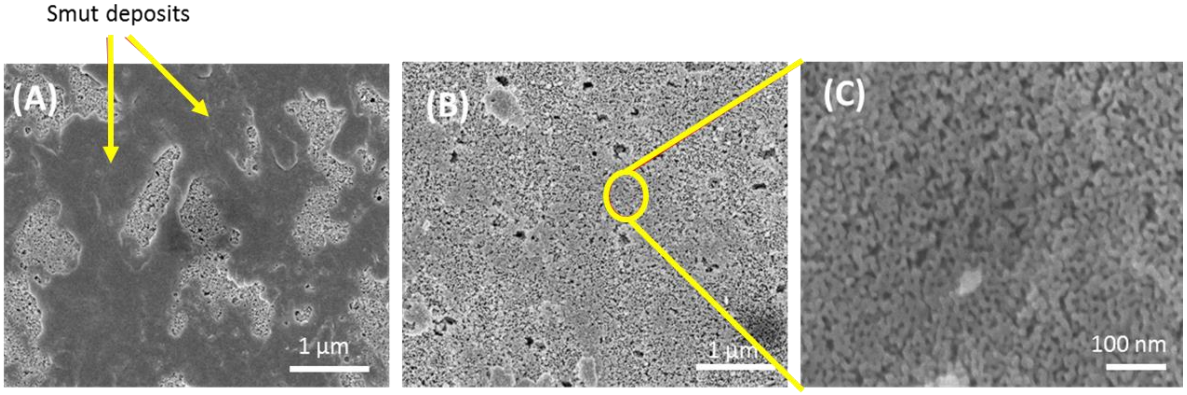

Figure 7.2 Scanning electron micrographs of AA2024-T3 anodized in 9.8 wt. % H_2SO_4 (A) before soaking in ultrapure water showing aluminum hydroxysulfate deposits across the oxide surface, (B) after a 20-min soak in ultrapure water at room temperature that removes the smut and exposes the underlying oxide pores and (C) higher magnification micrograph showing an exposed nanoporous oxide after the 20-min ultrapure water soak. Pore sizes in this outer oxide region are in the 10-20 nm range.

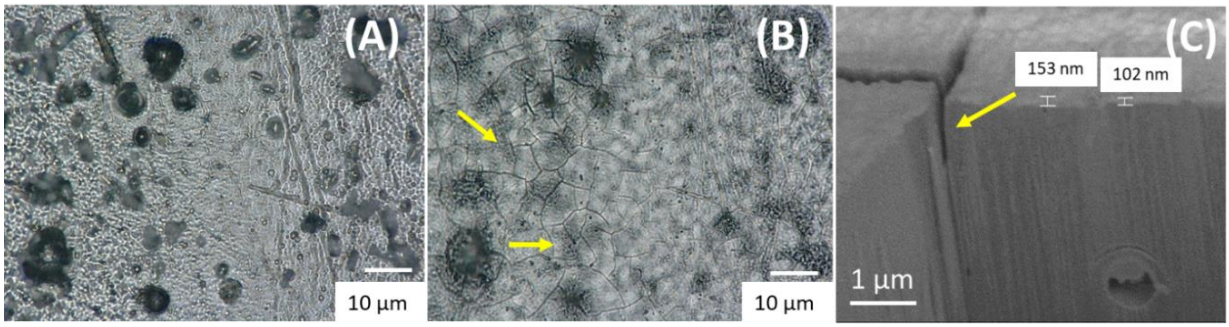

Figure 7.3 (A) Optical micrograph of an anodized AA2024-T3 specimen sealed with TCP-2 after 16 h of atmospheric exposure, and (B) optical micrograph of the same specimen after a ~30 min exposure to the high vacuum of the SEM. The micrograph in (A) prior to vacuum exposure shows a crack-free TCP sealant layer. The micrograph in (B) shows cracks in the TCP layer caused by dehydration (so-called mud cracking). (C) Scanning electron micrograph in the cross-section showing the depth of a crack penetrating the oxide layer that formed during the vacuum exposure. Arrows in the micrographs (B and C) identify the cracks.

An important consideration is to what extent does TCP penetrate pores of the oxide. Micrographs in Figure 7.3 reveal that the sealant forms across the outer oxide surface. These micrographs present an area of the specimen, representative of all areas probed, where the TCP covers the oxide layer. Understanding of how deeply the sealant layer penetrates the oxide was determined from EDS elemental profiles of TCP coating elements through the oxide in the cross-section. Figure 7.4 shows the EDS elemental maps for anodized AA2024-T3 specimens sealed with both TCPs. Shown are elemental signals for Zr, Cr, F, Al with depth through the oxide. Elemental maps indicate both sealants are confined to the outermost region of the oxide and neither penetrates deep within the pores. F is detected at a greater depth into the oxide layer than Zr or Cr. For TCP-1, the apparent thickness of Zr signal is *ca.* 250 nm. For TCP-2, the apparent thickness is *ca*. 300 nm. This is consistent with the coating thickness estimated from SEM-FIB cross-

sectional micrographs (see Figure 7.3C). The thickness of TCP-2 sealant is slightly greater presumably because of the longer immersion time (10 vs. 5 min).

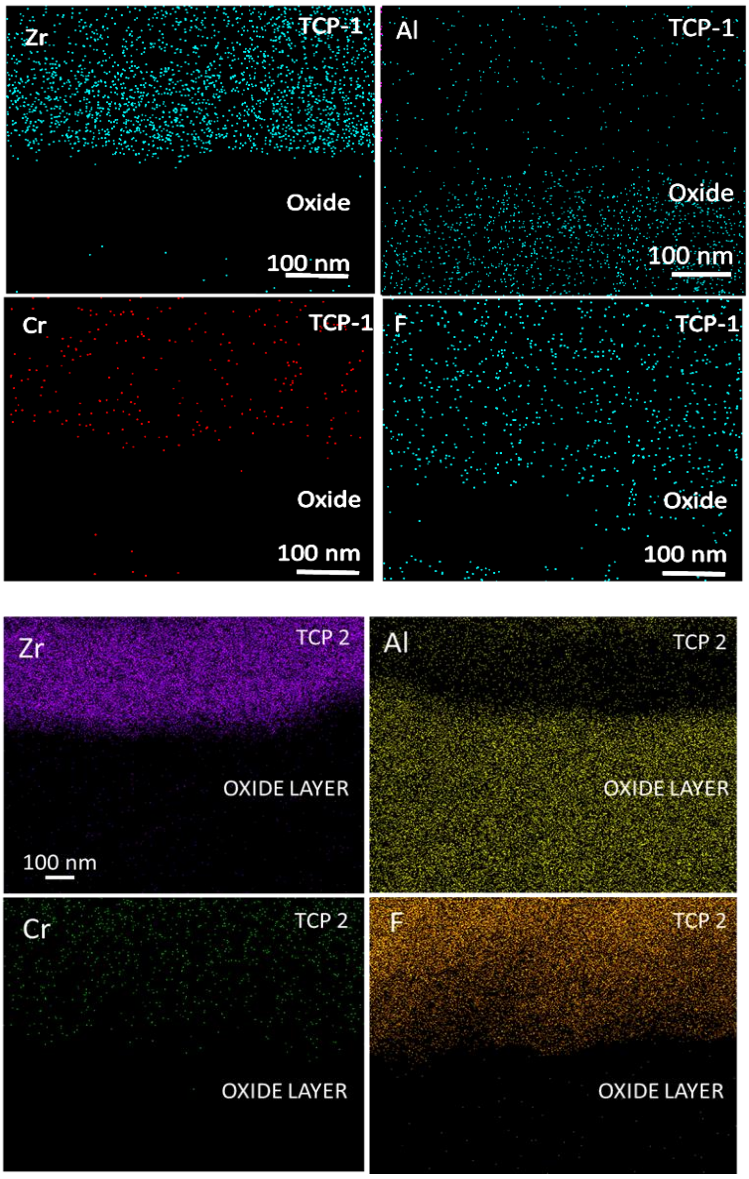

Figure 7.4 Elemental maps for Al, Zr, F and Cr through a cross-section of anodized AA2024-T3 sealed with TCP-1 (top panels) and TCP-2 (bottom panels). The elemental maps were generated using energy dispersive x-ray spectroscopy.

The temporal dynamic of sealant formation was assessed by recording the open circuit potential of the anodized alloy during immersion in TCP. Figure 7.5 shows *in-situ* OCP versus

time curves for anodized AA2024-T3 specimens during immersion in TCP-1 and TCP-2. The potential is initially more positive for the anodized specimen in both coating baths but quickly drifts towards more negative potentials. The drift to negative potentials occurs more slowly for TCP-1 as compared to TCP-2, and the final potential is less negative for the former. Both coating baths contain fluoride so there is some oxide thinning expected due to reactions 15 and 16 (see below) during the sealing process. We do not have hard data on this, but rough assessments reveal that the thinning maybe on the order of 0.5 μm, or less, using the sealing conditions reported herein.

As the TCP bath contains fluoride, it is reasonable to expect that aluminum oxyfluoride chemical species also likely form within the oxide coating, for example AlFO and AlF_2O. Additionally, solution species penetrate pores of the thick oxide coating and dissolve the thin passivating oxide layer on the alloy surface at the base of the pores, thereby exposing the underlying aluminum. This activates the metal and initiates metal oxidation. The rate of metal oxidation is counter balanced by a cathodic reaction that consumes protons (*e.g.*, oxygen reduction and or hydrogen evolution). As a consequence, a solution layer depleted of protons (*i.e.*, elevated pH) grows outward from the base metal through the oxide pores. Eventually, this depletion layer reaches the outer surface of the oxide where interaction with the coating bath precursors occurs. The more alkaline pH environment, estimated to be in the pH 6-8 range, drives the hydrolysis of the coating bath precursors and sealant formation. The sealant species are low-solubility hydrated ZrO_2 and $Cr(OH)_3$, based on prior work with TCP coatings.[25-30,40-43]

Decrease in the OCP during sealing with TCP-1 is more gradual and a less negative potential is reached at the end of the 5-min immersion period as compared with TCP-2. This is consistent with a lower cathodic reaction rate and therefore a less alkaline depletion layer forms at the outer oxide surface. The more negative potential reached for TCP-2 indicates greater cathodic reaction

rate, hence a greater counterbalancing anodic reaction rate. The greater anodic rate likely causes more structural modifications in the oxide coating and the underlying aluminum. Oxide layer damage may be the reason for the greater variability in the electrochemical data presented below for the TCP-2 sealed specimens. The OCP potential profile for TCP-2 shows several sudden changes in potential after 150 s that could be due to the formation and dislodging of H_2 gas bubbles during sealant formation.

$$Al_2O_3 + 6HF \rightarrow 2AlF_3 + 3H_2O \quad (15)$$

$$AlF_3 + 3F^- \rightarrow AlF_6^{3-} \quad (16)$$

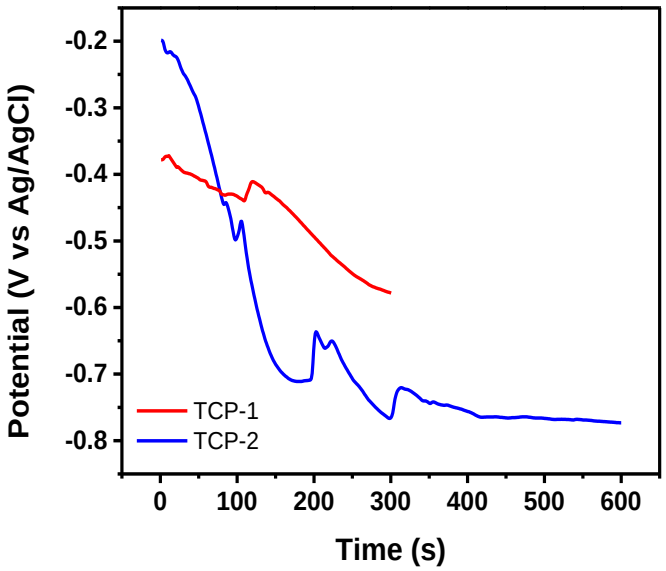

Figure 7.5 Open circuit potential (OCP) versus time curves recorded during the sealing of anodized AA2024-T3 with TCP-1 and TCP-2. The optimum sealing times were determined in separate experiments to be 5 min for TCP-1 and 10 min for TCP-2.

Figure 7.6 shows a scanning electron micrograph and EDS elemental line scans for F, Al, O and Zr acquired through the cross-section of an anodized AA2024-T3 specimen sealed with TCP-1. The electron micrograph shows the organic resin, the oxide coating and the alloy of a cut section

that was mechanically polished. The Zr signal intensity increases starting at the interface between the resin and the oxide, and then decreases progressively with depth into the oxide. The spike in the Zr signal is associated with the sealant layer (hydrated ZrO_2) that forms on the outer oxide.[30,42] The intensity increase spans *ca.* 0.5 μm and is consistent with the sealant thickness determined from SEM-FIB micrographs (Figure 7.1C) and EDX maps recorded from these milled cross sections (Figure 7.4). There is Zr signal above the background detected with depth, but the largest intensity is seen at the outer oxide. The line scan also reveals that the F signal is increased and relatively constant with depth into the oxide. The maximum F signal spans a little over 5 μm. The O signal increases with depth into the oxide. The presence of a TCP sealant on the outer oxide is responsible for this progressive increase in O signal. The presence of both signals for O and F within the oxide is consistent with aluminum oxyfluoride species (*e.g.*, AlFO and AlF_2O) within the coating. The greater depth of F signal is consistent with a fluoroaluminate chemical species (*e.g.*, K_3AlF_6) present at the metal surface. The Al signal is constant with depth through the oxide coating and increases as the metal surface is reached.

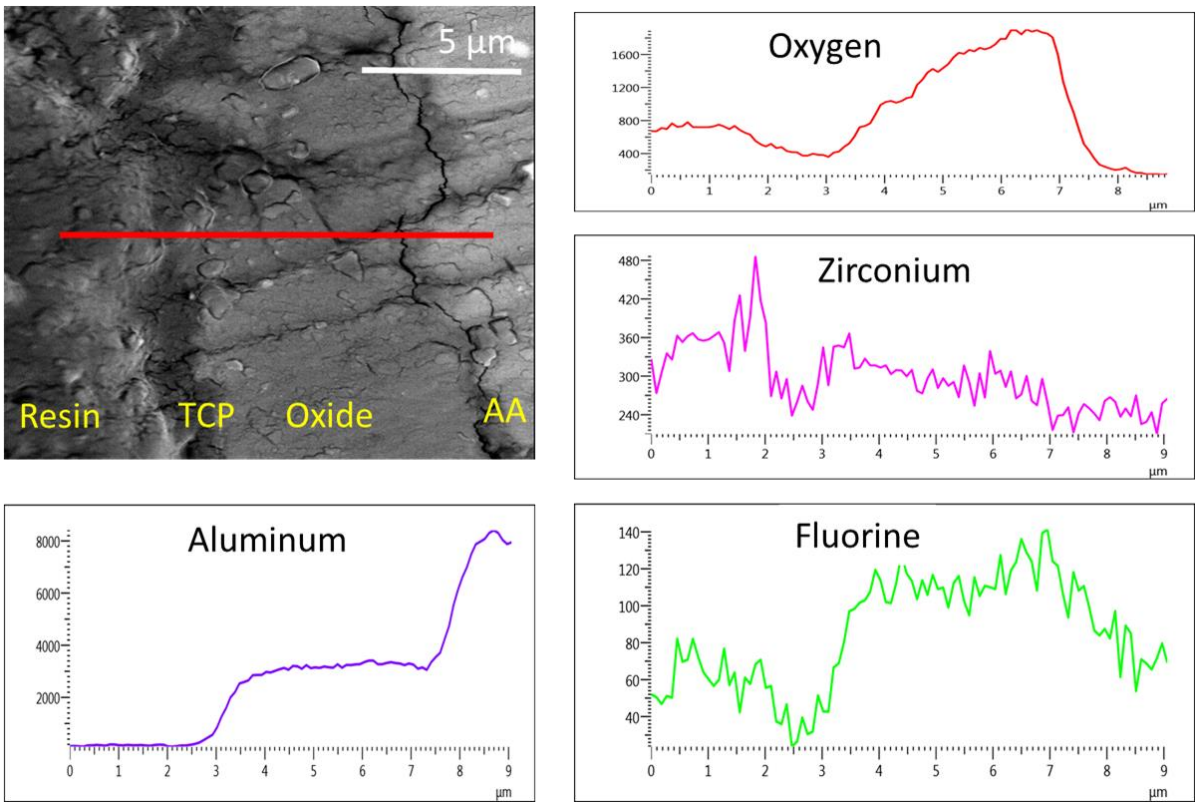

Figure 7.6 Scanning electron micrograph of a cut cross section of an anodized AA2024-T3 specimen sealed with TCP-1 showing the organic resin used for sealing, the oxide coating and the alloy. EDX elemental line scans recorded through the cross section are presented for Al, Zr, F and O. The red line indicates where the line scans were recorded.

Electrochemical Characterization.

The electrochemical properties of anodized specimens, unsealed and TCP sealed, were investigated using OCP measurements, electrochemical impedance spectroscopy at the OCP and potentiodynamic polarization curves; all in naturally-aerated 0.5 M Na_2SO_4 + 0.01 M NaCl at room temperature. Representative impedance data recorded at the OCP are presented as Bode plots in Figure 7.7. Figure 7.7A shows the total impedance as a function of frequency for anodized AA2024-T3 specimens sealed for 5 min with TCP-1 and 10 min with TCP-2. Data for an anodized an unsealed specimen are shown for comparison. The low frequency impedance at $Z_{0.01\ Hz}$ is dominated by the charge transfer (R_{ct}) resistance; a measure of the corrosion resistance. According

to Equation 17, R_{ct} is inversely related to i_{corr} – the corrosion exchange current density at equilibrium potential.

$$R_{CT} = \frac{RT}{nFi_{corr}} \quad (17)$$

The curves reveal similar $Z_{0.01\ Hz}$ values for the two TCP-sealed + anodized specimens with values greater than 10^6 ohm-cm^2. $Z_{0.01\ Hz}$ for the sealed specimens are 5x higher than the value for the unsealed anodized specimen (~5.5 x 10^5 ohm-cm^2), and over 1000x higher than values for a degreased and deoxidized alloy.[25-29,40,41,43,44] Clearly, sealing with either TCP increases the corrosion resistance of the oxide coating by blocking the outer pores. The remainder of the curves in the mid (capacitive) and high frequency (solution and electrode ohmic resistance) regions are overlapping with no distinct differences.

Figure 7.7B shows phase shift versus frequency data for the same specimens. The data indicate two time-dependent processes over the frequency range: one at *ca.* 1 kHz and a second at a lower frequency of *ca.*1 Hz. The most distinct differences however are seen in the low frequency region. The phase angle for the two TCP-sealed + anodized specimens is ≥ 60° suggestive of predominantly capacitive behavior (*i.e.*, blocking of the pores by the TCP sealant). The phase angle is considerably lower for the unsealed specimen (~ 10°). This reflects solution penetration through the pores of the oxide reaching the underlying metal. The TCP sealant serves as an effective barrier to solution penetration through the oxide. Overall, the impedance data show an equivalent level of sealing and corrosion protection afforded by both TCP coatings.

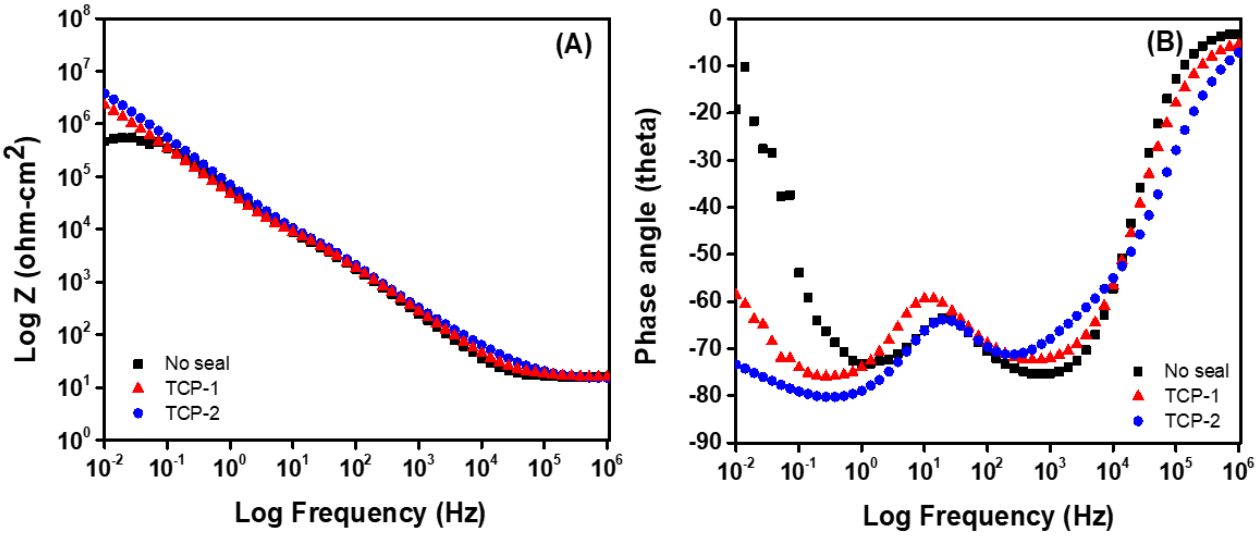

Figure 7.7 Electrochemical impedance spectroscopy data (Bode plots) recorded in naturally-aerated 0.5 M Na_2SO_4 + 0.01 M NaCl for anodized AA2024-T3 specimens sealed with TCP-1 (5 min) and TCP-2 (10 min). Data for an unsealed anodized specimen are shown for comparison. The EIS data were recorded at the OCP using a 10 mV AC sine wave. The figure shows (A) total impedance and (B) phase shift plots over a frequency range from 10^6 to 10^{-2} Hz.

Figure 7.8 shows the equivalent circuit used to model the impedance data for sealed and unsealed anodized alloy.[7,8,30,45-51] The circuit consists of a solution resistance, R_s, in series with an outer porous oxide layer resistance (R_p) in parallel with a constant phase element, (CPE_p) representing the capacitance of the porous region of the oxide coating, in series with an oxide barrier layer resistance (R_b) in parallel with a constant phase element (CPE_b) representing the capacitance of the inner barrier layer of the oxide.[7,8,30,45-51] The fitted data revealed good agreement between experimental and computed data. However, the resulting trends in the values for R_p, CPE_p, R_b and CPE_b were inconsistent with the other electrochemical data (presented below) and the sealant characterization (presented above) and with expected trends, namely that R_p values for the two TCP-sealed specimens would be significantly larger than the value for the unsealed control and CPE_b values would be significantly smaller. The magnitudes of R_p (kΩ-cm^2) and R_b (MΩ-cm^2) determined for the unsealed and TCP-sealed specimens are consistent with other data

reported in the literature.[49-51] The results were such that it is was difficult to draw any meaningful conclusions.

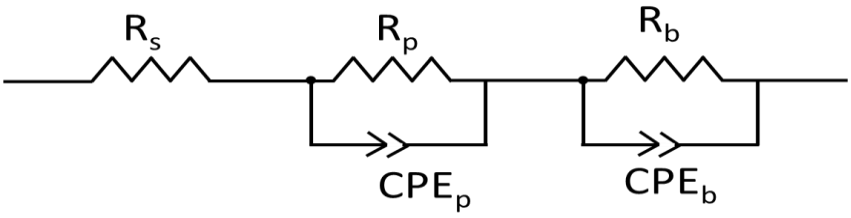

Figure 7.8 Equivalent circuit model used to represent the surface of a TCP sealed and unsealed AA2024-T3.

Figure 7.9 shows the anodic and cathodic potentiodynamic polarization curves for anodized AA2024-T3 specimens, unsealed and TCP-sealed, in naturally aerated 0.5 M Na_2SO_4 + 0.01 M NaCl. The anodic curves shown in Figure 7.9A reveal a passivating current at potentials positive of the OCP. The OCP values were *ca.* -0.25 V for TCP-1 sealed and *ca*. -0.13 V for TCP-2 sealed and unsealed anodized alloy specimens. The anodic current magnitude, for example at -0.1 V, is significantly lower (*ca.* 10x) for the TCP-1-sealed specimen and slightly lower (*ca.* 5x) for the TCP-2-sealed specimen, as compared to the unsealed anodized specimen. There is no clear onset potential for stable pit formation and growth on any of the three specimens, at least to potentials as positive as 0.15 V.

The cathodic curves in Figure 7.9B reveal significantly decreased limiting currents for dissolved oxygen reduction for both TCP-sealed specimens, as compared to the unsealed specimen. In fact, the current suppression across the entire potential range for oxygen reduction (-0.4 to -0.9 V) is similar for TCP-1 and TCP-2 and is 3.5-5x lower than the current for the unsealed anodized specimen. All curves approach one another at the most negative potentials where water electrolysis (*i.e.*, H_2 evolution) commences. It should be noted that the OCP values recorded

initially for some freshly prepared specimens were different from the values recorded after the EIS measurements and after performing each of the polarization curves. This indicates that the condition of the oxide or sealed oxide changed slightly with polarization during an electrochemical measurement.

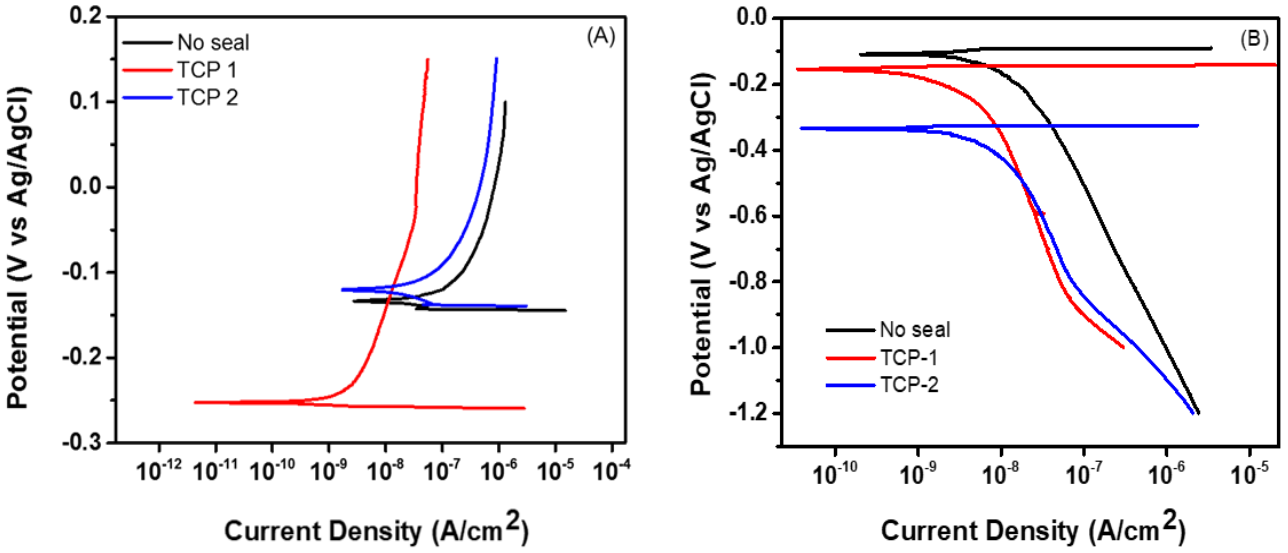

Figure 7.9 Potentiodynamic (A) anodic and (B) cathodic polarization curves for anodized AA2024-T3 specimens unsealed, sealed with TCP-1 and sealed with TCP-2. The measurements were made in naturally aerated 0.5 M Na_2SO_4 + 0.01 M NaCl at room temperature.

Figure 7.10 presents a summary of the electrochemical parameters measured for anodized AA2024-T3 specimens, unsealed and TCP-sealed, measured in naturally aerated 0.5 M Na_2SO_4 + 0.01 M NaCl. Figure 7.10A shows that sealing the oxide layer with either TCP coating shifts the initial (*i.e.*, freshly prepared) nominal OCP towards more noble potentials by 40 to 60 mV. There is, however, no statistically significant difference in the OCP values for specimens sealed with either TCP coating, as compared to the unsealed controls, given the magnitudes of the standard deviations. Comparing the nominal anodic currents at +0.1 V and the cathodic currents at -0.7 V measured from the potentiodynamic polarization curves reveals current suppression by both TCP sealants. Figure 7.10B reveals a 1.5x current suppression at 0.1 V for TCP-2 sealed specimens and

a 10x suppression for TCP-1 sealed specimens, as compared to the unsealed anodized controls. Figure 7.10C reveals that the nominal cathodic current at -0.7 V is lower by 3.5 to 5x for both TCP sealants, as compared to the unsealed anodized controls. Notably, the variability in the measured values is less for TCP-1 than for TCP-2 sealed specimens.

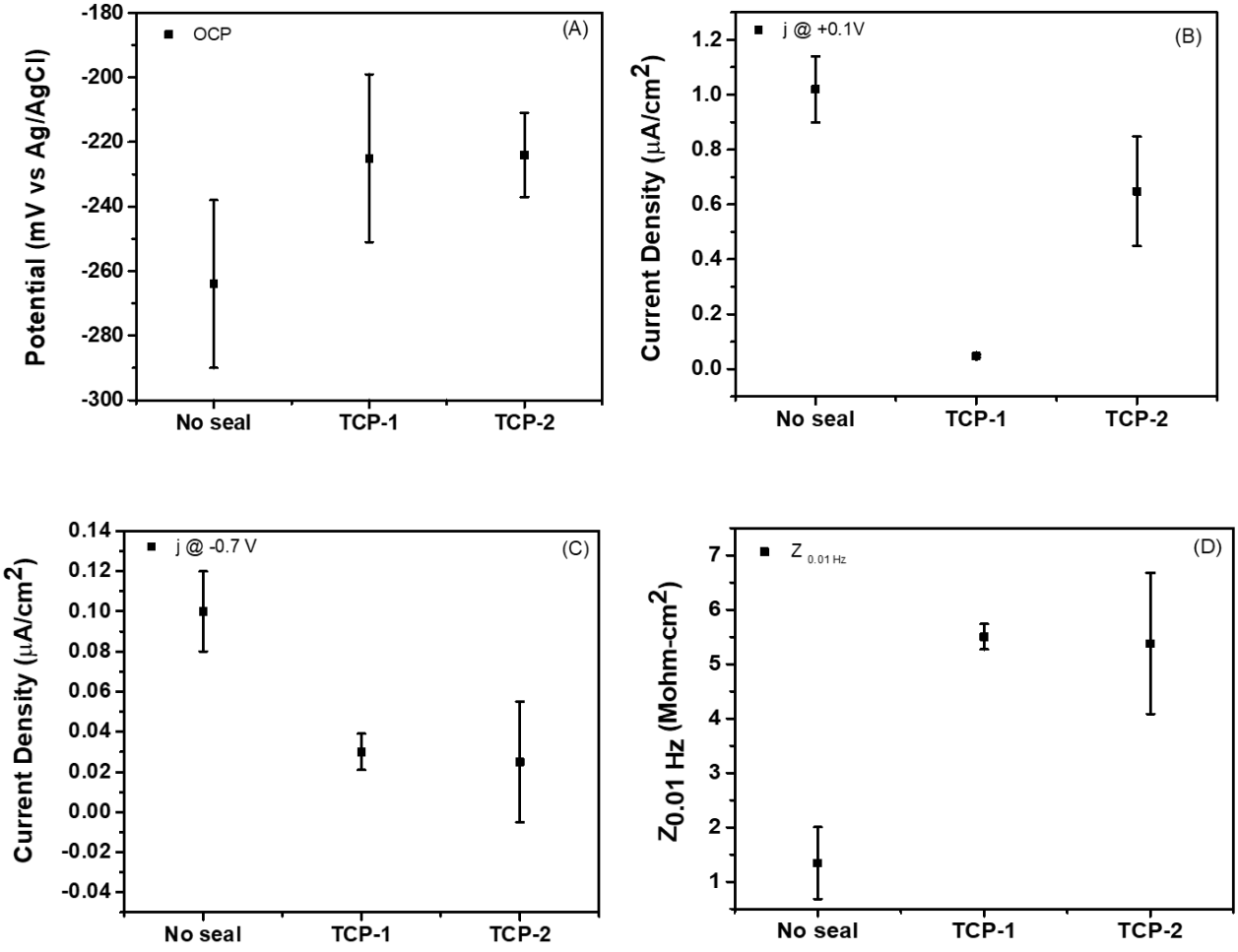

Figure 7.10 Comparison of electrochemical parameters measured in naturally aerated 0.5 M Na_2SO_4 + 0.01 M NaCl for anodized AA2024-T3 sealed with TCP-1 and TCP-2. Data for anodized specimens unsealed are shown for comparison. The following data are presented: (A) open circuit potential (OCP) (B) anodic current density at +0.1 V, (C) cathodic current density at -0.7 V and (D) low frequency impedance modulus, $Z_{0.01\,Hz}$, at the OCP. Data are reported as mean ± standard error of the mean ($n \geq 3$ measurements).

Finally, Figure 7.10D reveals a nominal $Z_{0.01Hz}$ increase by a factor of 5-6x after sealing the oxide with either TCP coating. The greater variability seen in the electrochemical data for the TCP-

2 sealed specimens could be due to oxide coating damage caused by the longer immersion period of 10 min, as compared to 5 min for TCP-1. Remember, the coating bath is acidic and contains fluoride that could etch and damage the oxide layer structure.

Full Immersion Degradation Testing.

Accelerated degradation tests were conducted to assess and compare the corrosion resistance of TCP-sealed and unsealed anodized AA2024-T3. This was also done to determine how predictive the electrochemical data are regarding actual corrosion resistance. Figure 7.11 shows comparison of EIS data recorded for anodized AA2024-T3 specimens sealed with TCP-1 and 2 before and after a 5-day continuous immersion period in 3.5 wt.% NaCl. This test was performed to probe for solution penetration through the TCP sealant layer. Bode plots of total impedance vs. frequency reveal that $Z_{0.01\ Hz}$ is unchanged (~10^6 ohm-cm^2) for anodized specimens sealed with either TCP (Figure 7.11B and C, top panels) after 5 days of exposure. In contrast, a 10x decrease in $Z_{0.01\ Hz}$ is seen for the unsealed anodized specimen after just 3 days (~10^5 ohm-cm^2) (Figure 7.11A). The low frequency impedance for this specimen did not decrease any further through Day 5. The reduced low frequency impedance is likely due to Cl^- penetration through the sealant layer and attack on the oxide layer and the underlying alloy.

To compare the effect of the two TCP sealants on the corrosion resistance, an improvement function (I) was calculated. This parameter is defined as [49]:

$$I = \log\left(\frac{Z_{sealed}}{Z_{unsealed}}\right)_{0.01\ Hz} \quad (18)$$

Z_{sealed} and $Z_{unsealed}$ are the nominal impedance values at 0.01Hz after 5 days of exposure. I for the unsealed anodized specimen decreased to 0.1 consistent with solution penetration through the

oxide and attack on the underlying metal. In contrast, I for TCP-1 sealed is 1.8 and for TCP-2 sealed is 1.1. These values indicate the stability of the sealant after 5 days of immersion. A slightly greater I value is seen for TCP-1 indicating that this sealant provides a greater level of corrosion resistance.

Subtle differences in the Bode plots of phase angle vs. frequency are seen for the sealed and unsealed specimens (Figure 7.11A-C, bottom graphs). The unsealed specimen has a decreased low frequency phase angle from -80 to -20° (after just 3 days of immersion) indicating reduced capacitive behavior. The low frequency phase angle data for the two TCP-sealed specimens remains largely unchanged indicating that both TCPs provide a stable sealant layer that serves as an effective barrier to electrolyte penetration. For TCP-1 sealed specimen, there is a loss of the mid- frequency time constant at ~10^2 Hz after electrolyte exposure indicating Cl^- penetration compromising the capacity of the oxide in preventing electrolyte diffusion.

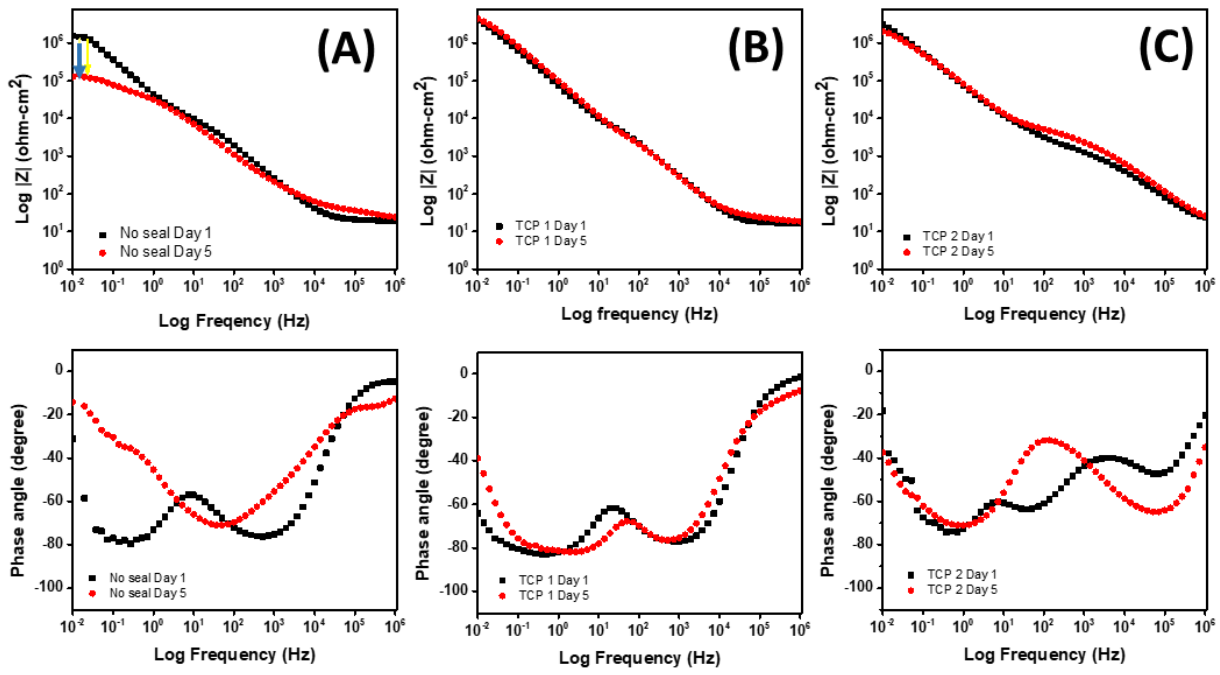

Figure 7.11 EIS spectra showing frequency and phase shift plots for Day 1 and Day 6 of a full immersion period in 3.5 wt. % NaCl for anodized AA2024-T3 specimens (A) unsealed and (B) sealed with TCP-1 and (C) with TCP-2.

Neutral Salt-Spray Testing.

A 14-day neutral salt-spray (NSS) test was conducted according to ASTM B117 to further assess the corrosion resistance provided by the TCP sealants on anodized AA2024-T3 specimens. Camera photographs of the specimens before and after the exposure are shown in Figure 7.12. The arrows (scale bar = 1000 μm) indicate regions with visible corrosion damage on the unsealed specimen. Significant pitting and corrosion damage are observed (Stage 2). In contrast, the two TCP-sealed specimens show no discoloration, pitting or corrosion damage (Stage 0). The unanodized region at the top of each specimen was protected (with corrosion tape) during the test.

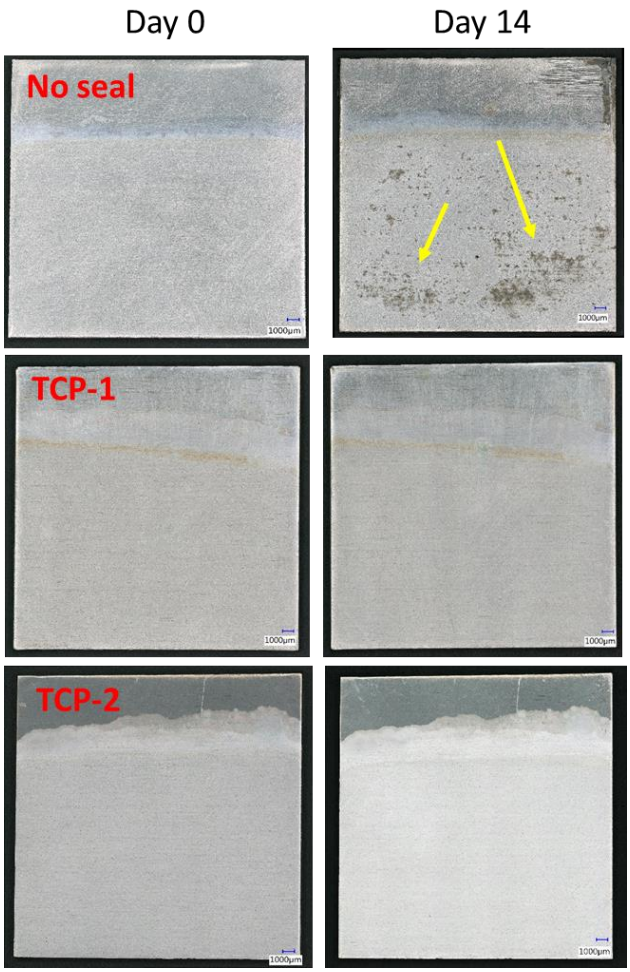

Figure 7.12 Camera photographs of anodized AA2024-T3 specimens unsealed, TCP-1 sealed, and TCP-2 sealed on Day 0 and 14 of a neutral salt-spray exposure according to ASTM B117. The arrows indicate areas of corrosion damage on the unsealed specimen. The bottom three-quarters of each panel was immersed in the sulfuric acid and anodized.

Figure 7.13 presents spatial maps of the specimen surface topography. Deeper regions (*e.g.*, pits), relative to the surface, appear blue in color. Intermetallic particles remaining above the surface appear as red regions. The unsealed specimen (Figure 7.13A) has extensive pitting and corrosion damage widespread across the surface, as evidenced by large increases in pit depth in three distinct regions. The surface roughness increased from 0.46 ± 0.04 to 1.18 ± 0.11 μm over the 1000 x 1000 μm^2 image area. In contrast, the profiles for the two TCP-sealed specimens show

little indication of pitting or surface damage. The yellow-red features in the topographical maps are intermetallic particles. The initial surface roughness of the anodized specimen sealed with TCP-2 is greater than that of the specimen sealed with TCP-1. Both surface roughnesses decrease during the test though. This is because of the dissolution of the TCP coating precipitates that form on the surface during sealing (white aggregates in Figure 7.1E and F). The digital micrographs in Figure 7.13 were analyzed for pit number, depth and area. The results are summarized in Table 7.2. The mass loss of the unsealed specimens was not measured after the 14-day salt-spray exposure as the surface was considerably damaged. Mass loss, however, was measured for the anodized specimens sealed with the two TCPs (n=3 specimens of each). The mass loss arises primarily from corrosion around the specimen edges that were not masked off during the salt-spray exposure. The camera photos in Figure 7.12 show no discoloration, streaking, pitting or other corrosion damage on the surface of either sealed specimen. As a consequence, there are no data reported for pit number, depth or density. Table 7.2 reflects the considerable corrosion damage on the unsealed anodized specimen.

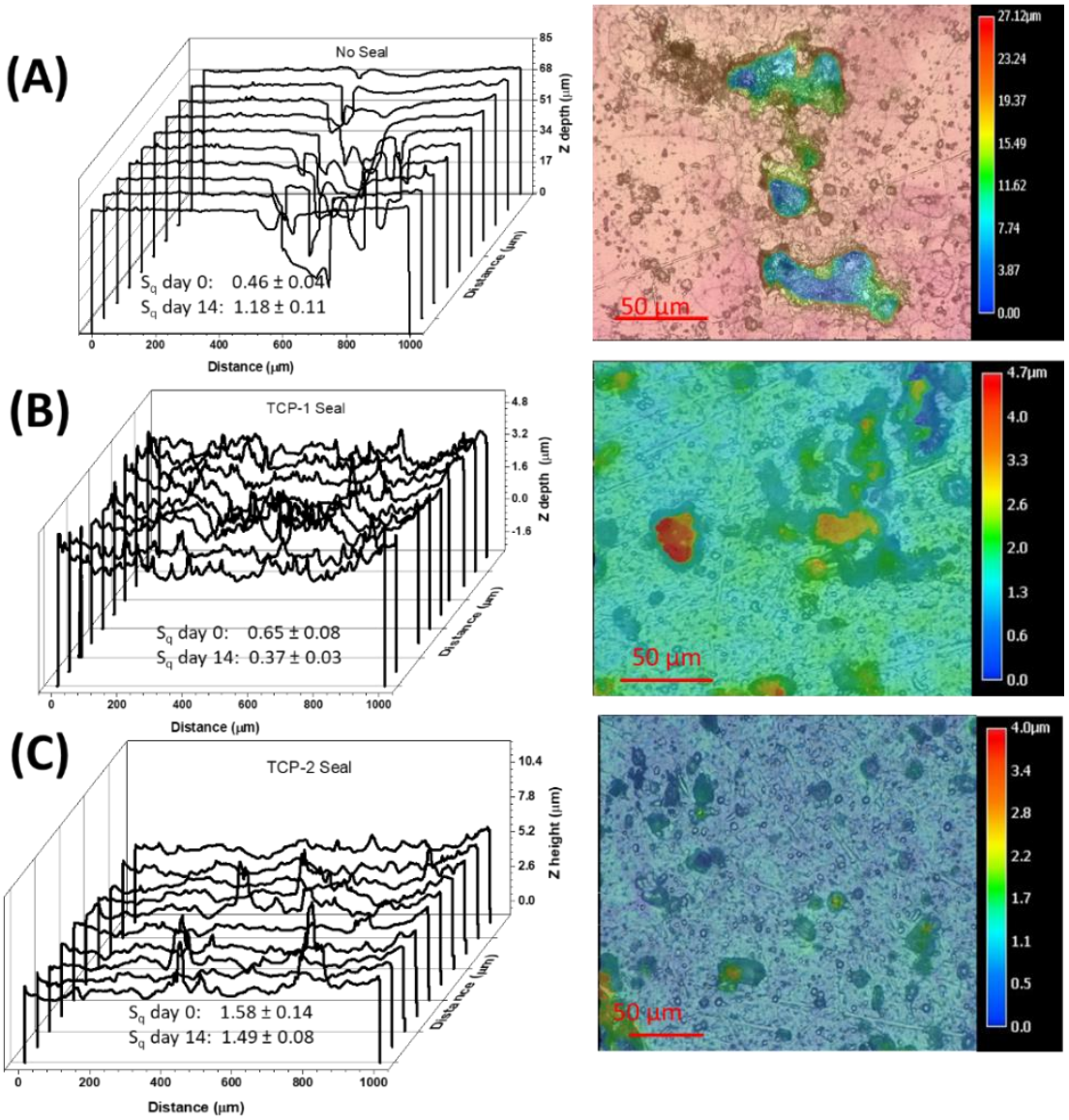

Figure 7.13 3-D surface topography (left) line profiles and (right) spatial maps constructed from digital images of anodized AA2024-T3 specimens (A) unsealed and sealed with (B) TCP-1 and TCP-2 after 14 days of salt-spray exposure. Note the different z-axis scales for each map.

Table 7.2 Quantitative assessment of the damage observed on anodized AA2024-T3 unsealed and sealed with the TCP after a 14-day NSS test. Data are presented as mean ± std dev. Pit number, pit density, average pit area, and % damaged area were calculated for the entire specimen area (n=3 for each sealant). Pit depth for the unsealed specimens was determined from measurements of 15 pits using topographical data from stitched images. Mass loss for the unsealed specimens was not measured.

N = 3	Mass loss (%)	Pit #	Pit Depth (μm)	Pit Density (pits/cm^2)	Average Pit Area (mm^2)	% Damaged Area
Unsealed	-	392 ± 128	40 ± 13	1120 ± 336	(3.8 ± 0.8) x 10^{-2}	5 ± 2.5
TCP-1	0.36 ± .03	0	-	-	-	-
TCP-2	0.24 ± .02	0	-	-	-	-

Figure 7.14 shows scanning electron micrographs and elemental EDS maps of anodized AA2024-T3, unsealed and sealed with TCP, after the 14-day test. The elemental maps shown for Zr, O and Al are for TCP-2 sealed specimen after the exposure period. The purpose for these studies was to determine if the sealant remains intact after the 14-day salt exposure. The micrographs and maps reveal minor loss and detachment of both TCP sealants during the test. Arrows in the micrographs show areas where sealant layer has detached from the surface, exposing the underlying oxide. EDS maps clearly show reduced Zr and increased Al signal intensities in these regions consistent with the loss of the sealant. The damaged area is small, on the order of a few μm^2. Such isolated regions of coating degradation were seen at multiple locations on both TCP-sealed specimens. Upon examining both TCP-1 and TCP-2 sealed specimens, approximately 40% of the TCP sealant detached during the salt-spray exposure. It is important to note that the specimens were subjected to some post-processing treatments prior to performing the EDS analysis including soaking in ultrapure water for 30 min to dissolve excess NaCl and a 20 min ultrasonication in ultrapure water to remove any corrosion product. Control experiments were

conducted to ensure that the coating degradation observed in the micrographs was not caused by these post-processing treatments. SEM micrographs obtained before and after the DI water soak and ultrasonication revealed no damage to the sealant layer.

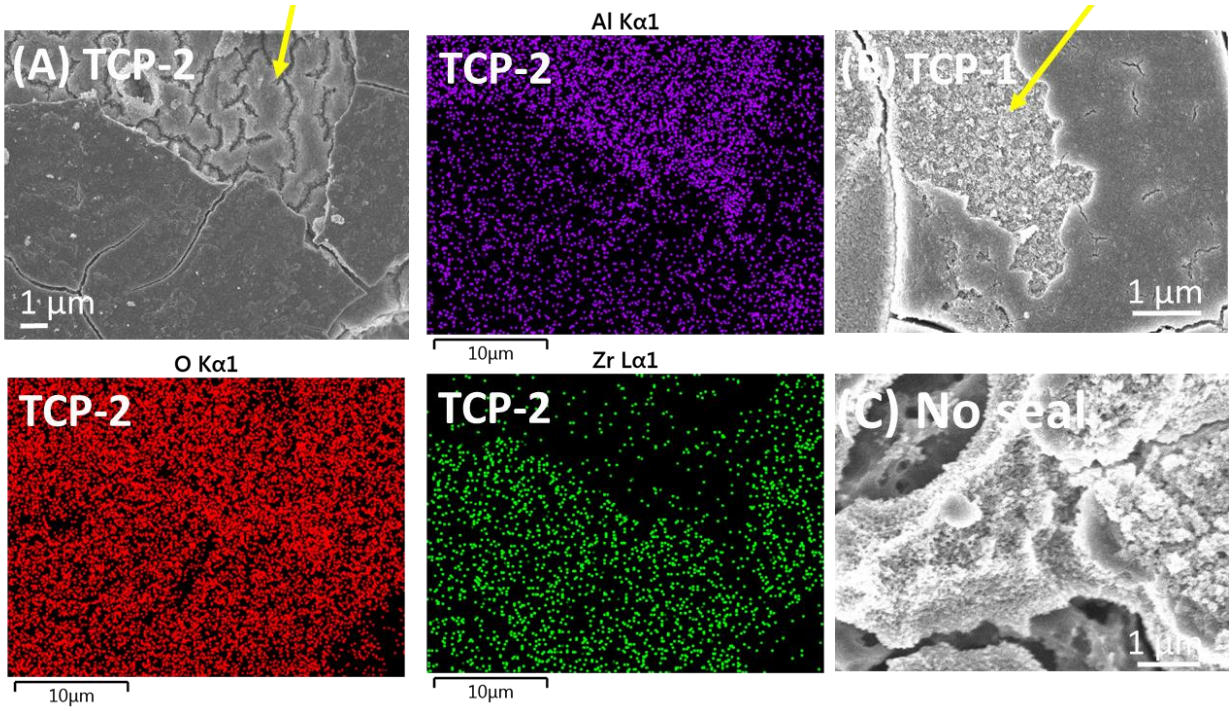

Figure 7.14 Scanning electron micrographs of (A) TCP-2 sealed (B) TCP-1 sealed and (C) unsealed anodized AA2024-T3 specimens after a 14-day salt-spray test. Spatial elemental maps of Zr, O and Al are also shown for TCP-2 sealed + anodized AA2024-T3. Arrows indicate regions of coating degradation.

Comparison with Commercially Prepared Specimens.

All the results presented above are for specimens anodized and TCP sealed in house. It is important to validate the quality of our in-house anodization and sealing processes. This was accomplished by having specimens anodized in sulfuric acid and TCP sealed by a commercial coater. Figure 7.15A-D presents comparison (CHEMEON and MSU) plan view scanning electron micrographs showing the oxide morphology of anodized specimens sealed in hot water (A and B) and with TCP-2 (C and D). Figure 7.15E and F presents cross-sectional electron micrographs of

TCP-2 sealed + anodized AA2024-T3 specimens after FIB milling. Figure 7.15A and B show the oxide morphology of sulfuric acid anodized specimens after hot water sealing. The sealing was performed for 30 min in ultrapure water at 96 ^{o}C. There is no evidence of anodization smut on the surface. However, a more open porosity is seen on the MSU specimen as compared to the CHEMEON specimen. This is attributed to the fact that the MSU specimens were anodized using a constant voltage with no temperature control while the Chemeon specimens were anodized under constant current conditions at a controlled temperature of 70 °F. Figure 7.15C and D show similar TCP sealant layer morphologies for the two specimens. The sealant covers the oxide coating and obscures the underlying pore structure. Both sealant layers are decorated with coating aggregates (white spherical particulates), although they are more visible on the MSU than on the CHEMEON prepared specimen. Dissolution of these particles during salt-spray exposure is the presumed reason for the decreased surface roughness reported in Figure 7.13. Mud cracks are seen in both TCP sealant layers. Micrographs of the TCP specimens milled by FIB reveal cracks extending into the oxide coating. These cracks are 1 – 2 μm in depth. The oxide thickness for both specimens is 5 – 6 μm with a *ca*. 300 nm thick TCP sealant layer. Overall, these results confirm the quality of the anodization and TCP sealing procedures used in-house.

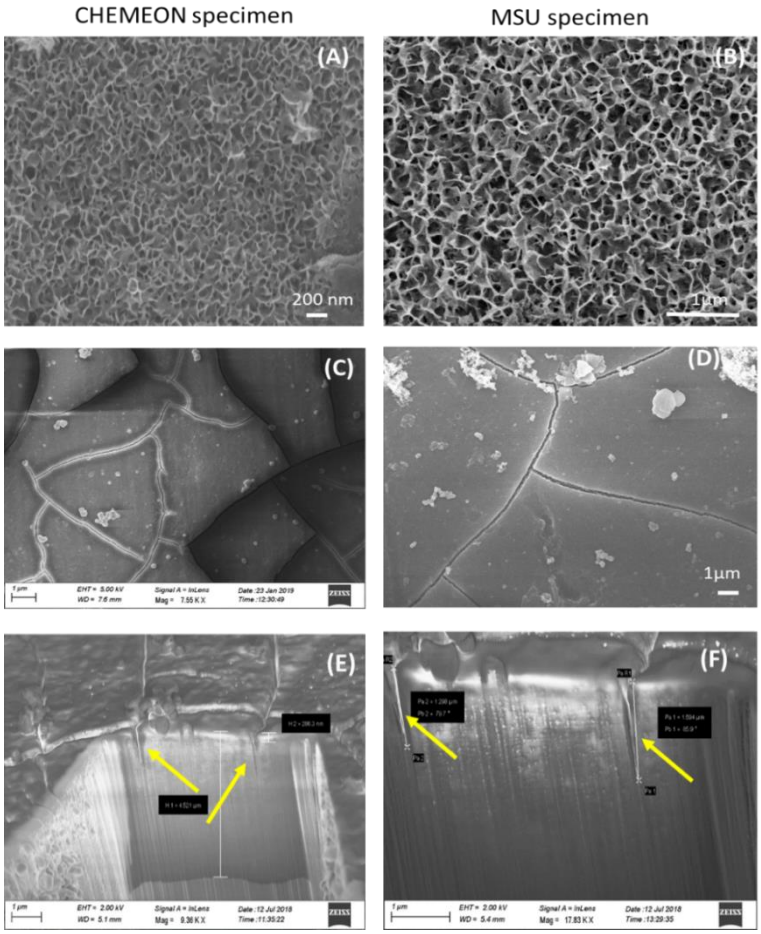

Figure 7.15 Scanning electron micrographs (secondary electron images) showing the oxide morphologies of sulfuric acid anodized AA2024-T3 specimens (A and B) after hot water sealing (ultrapure water, 96 ^{o}C, 30 min) and (C and D) after sealing with TCP-2. (D and E) Cross-sectional scanning electron micrographs obtained after FIB milling that show crack formation in the oxide layers after TCP sealing. Arrows indicate ~1-2 µm cracks that formed in the outer oxide coating. Micrographs A, C and E are for CHEMEON-prepared specimens and B, D and F are for MSU-prepared specimens.

Potentiodynamic polarization and impedance measurements were performed to compare the properties of CHEMEON and MSU-prepared specimens. Figure 7.16 presents electrochemical impedance data recorded at the OCP (Figure 16A and C) and anodic potentiodynamic polarization curves (Figure 7.16B and D) for anodized AA2024-T3 specimens sealed in a similar manner with TCP-2. The measurements were made in naturally-aerated 0.5 M Na_2SO_4 + 0.01 M NaCl. Nearly identical electrochemical data are seen for both specimens. $Z_{0.01\,Hz}$ is *ca.* 6 x 10^6 ohm-cm^2 for both

sealed specimen types and similar anodic currents of ca. 0.05 μA/cm^2 are seen for both specimen types at +0.1 V. Similar electrochemical data are seen for anodized specimens unsealed (Figure 7.16C and D). There are, however, some subtle differences in the low frequency impedance and phase shift for the two unsealed specimen types. For example, $Z_{0.01\ Hz}$ is *ca.* 5 x 10^5 ohm-cm^2 for the MSU anodized specimen unsealed which is about 5x lower than for the CHEMEON specimen. The anodic currents at -0.1 V in the polarization curves are essentially equivalent at 1 μA/cm^2.

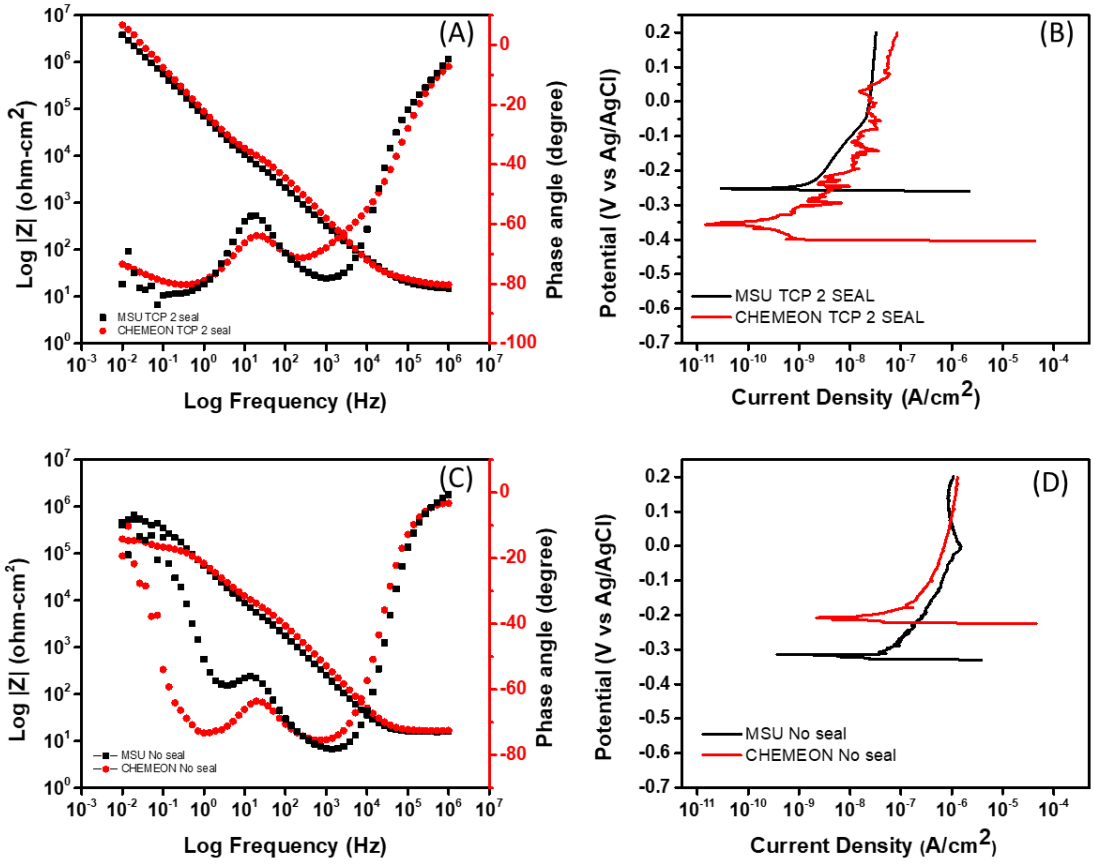

Figure 7.16 Electrochemical data for specimens prepared by CHEMEON compared with specimens prepared in-house at MSU. The data include (A) Z and phase angle data versus frequency at the OCP and (B) anodic potentiodynamic polarization curves for anodized AA2024-T3 specimens sealed with TCP-2. (C) Z and phase angle data versus frequency at the OCP and (D) anodic potentiodynamic polarization curves anodized AA2024-T3 specimens unsealed.

7.5 DISCUSSION

The anodization of AA2024-T3 in sulfuric acid under constant voltage conditions produces an oxide coating that is *ca.* 5 µm thick with a nominal coating weight of *ca.* 1200 mg/ft^2. The oxide layer consists of 10-50 nm-sized pores in the outer coating. Intermetallic phases can be dislodged from the alloy and trapped within the growing oxide. This leads to a defective oxide coating. Solution can penetrate through these defects to reach and corrode the underlying base metal. In order to improve the overall corrosion resistance, the porous oxide coating is typically sealed by one of several methods: hot water immersion, nickel acetate immersion and chromic acid treatment.

In this work, two commercial TCP coatings were evaluated as sealants. TCP is an environmentally-friendlier alternative to chromate-based sealants. Both TCP treatments form a Zr/Cr rich oxyhydroxide layer over the outer oxide. There is minimal penetration of the sealant deep into the pores. The apparent thickness of TCP-1 sealant is *ca.* 250 nm (5-min immersion) while TCP-2 sealant is *ca.* 300 nm thick (10 min immersion). Elemental maps for both TCP-sealed specimens reveal the penetration of fluoride from the coating bath into the oxide coating. Fluoride likely attacks the internal oxide chemically to produce AlOF and $AlOF_2$ species. Dissolved O_2 gets reduced at the activated metal surface causing the consumption of protons and an increase in the solution pH. As O_2 is reduced, a depletion layer forms at and extends from the metal surface. The insoluble ZrO_2 and $Cr(OH)_3$ sealant constituents form because of coating bath precursors interacting with an alkaline solution layer that extends from the metal at the base of the pores to the outer oxide coating. Figure 7.17 presents a schematic representation of the anodization and TCP sealing process. EDS measurements confirm that the TCP sealant is confined to the outer oxide coating and does not penetrate deep within the oxide. This sealing mechanism is different

from that of other conventional sealants like nickel acetate and dichromate in which the sealant constituents form deep within the pores of the oxide. The formation of a TCP sealant layer increases corrosion resistance of the oxide coating based on increases in $Z_{0.01\ Hz}$ and R_p and decreases in anodic and cathodic polarization currents. The degree of increased corrosion resistance is similar for both TCP-1 and TCP-2. There were no significant differences in performance between the two. Results from a 14-day neutral salt-spray exposure are consistent with the predictive electrochemical data – both TCP sealants improve the corrosion resistance of the oxide coating. No pitting, discoloration or other coating degradation was observed on TCP-sealed specimens after the 14-day exposure (Stage 0). In contrast, unsealed anodized specimens showed some pitting, discoloration and streaking after the exposure (Stage 2/3).

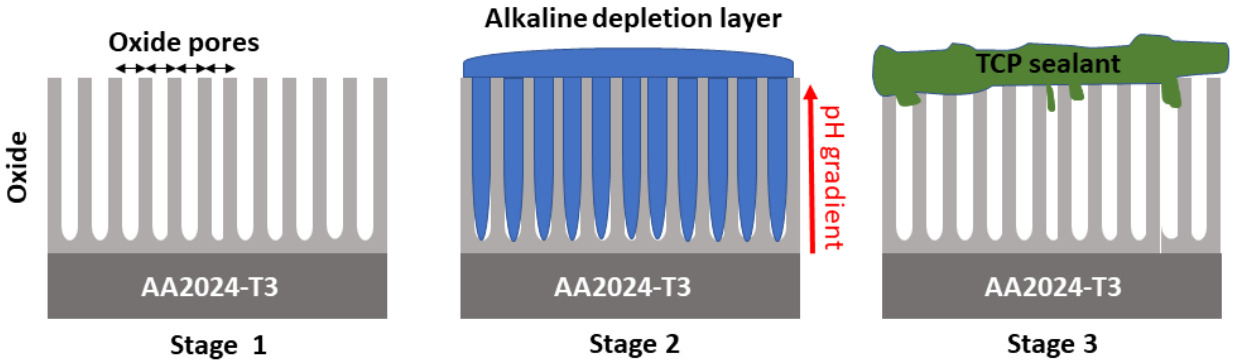

Figure 7.17 Schematic representation of the anodization and TCP sealing process. Stage 1 – anodic coating formed on the aluminum alloy in sulfuric acid. Stage 2 – activation of the base metal and formation of an alkaline depletion layer extending from the base metal to the outer oxide due to proton-consuming redox reactions that occur during the open circuit immersion in the TCP coating bath. Stage 3 – precipitation of coating bath precursors to form the TCP sealant on the outer oxide coating.

In this study, we did not assess the adhesion strength of the sealant layer with the oxide, nor the interaction of the sealant layer with a primer or other topcoat. Both would be important next phases of research. However, it was observed that there was loss of the sealant layer after the salt-spray exposure in some isolated areas (see. Figure 7.14). This suggests that perhaps the adhesion

of the sealant is relatively weak since the layer resides on top of the oxide and there is minimal physical interlocking with the interior pores.

7.6 CONCLUSIONS

Scanning electron microscopy, digital optical microscopy, energy dispersive x-ray analysis and electrochemical methods were used to characterize sulfuric acid anodized AA2024-T3 specimens sealed with TCP-1 and TCP- 2 commercial conversion coatings. This work is the first to investigate how effectively these environmentally friendly coating systems, as compared to traditional chromate sealants, are at forming on and passivating the porous oxide. The following highlight key findings from the study:

1. The oxide layer formed on AA2024-T3 is porous, approximately 5 μm thick (~1200 mg/ft^2) under the anodization condition used and contains some entrapped intermetallic particles.
2. Sealing the oxide layer with either TCP provides enhances corrosion protection of the oxide as evidenced by suppressed anodic currents (2-10x), suppressed cathodic currents (3-5x) and increased $Z_{0.01\ Hz}$ (5-6x).
3. Energy dispersive x-ray analysis of cross-sectioned specimens indicated the TCP coating (Zr, Cr, F) forms across the oxide coating and forms only in the outer regions of the pores. The thickness of the sealant layer based on the Zr signal intensity is ~300 nm for both sealants. F was detected 500 nm into the outer oxide coating.
4. The TCP sealant forms a layer on the outer surface of the oxide increasing the barrier properties of the oxide. Some mud cracking was seen in the TCP layer after exposure to the high vacuum condition of inside a SEM.
5. Results from a 14-day neutral salt spray exposure confirmed the corrosion resistance predicted from laboratory electrochemical data. There was no discoloration, visible pitting or other

corrosion damage seen on either TCP-sealed specimen (Stage 0). In contrast, some minor pitting was observed on the unsealed anodized specimen after just 7 days of salt spray exposure.

6. Full immersion testing in 3.5% NaCl for 5 days revealed that both TCP sealants provided excellent and unchanged corrosion protection to the alloy. In contrast, oxide degradation was observed for the unsealed specimen after 3 days.
7. Similar behavior was observed for MSU anodized and TCP-sealed specimens and CHEMEON-prepared anodized and TCP-sealed specimens in accelerated degradation tests.

ACKNOWLEDGEMENTS

The author would like to thank Mr. Jack Walton and Ms. Sarah McFall-Boegeman for their contributions in obtaining optical and scanning electron micrographs presented in this work.

REFERENCES

REFERENCES

(1) Heinz A.; Haszler A.; Keidel C.; Moldenhauer S.; Benedictus R.; Miller W.S. Recent Development In Aluminium Alloys For Aerospace Applications. *Mater. Sci. Engr*., **2000,** *280*, 102-107.

(2) Scully J. R.; Knight T. O.; Buchheit R. G.; Peebles D. E. Electrochemical Characteristics Of The Al_2Cu, Al_3Ta And Al_3Zr Intermetallic Phases And Their Relevancy To The Localized Corrosion Of Al Alloys. *Corr. Sci*., **1993**, *35*, 185-195.

(3) Buchheit R. G. A Compilation of Corrosion Potentials Reported for Intermetallic Phases in Aluminum Alloys. *J. Electrochem. Soc*. **1995,** *142*, 3994-3996.

(4) Birbilis N.; Buchheit R. G. Electrochemical Characteristics of Intermetallic Phases In Aluminum Alloys: An Experimental Survey And Discussion. *J. Electrochem. Soc*. **2005**, *152*, B140-B151.

(5) Birbilis N.; Cavanaugh M. K.; Buchheit R. G. Electrochemical behavior and localized corrosion associated with Al7Cu2Fe particles in aluminum alloy 7075-T651. *Corr. Sci.* **2006**, *48*, 4202-4215.

(6) Cohen S. M.; Spadafora S. J. A Comparison of Thin Film Sulfuric Acid Anodizing and Chromic Acid Anodizing Process, Report #NAWCADWAR-95023-43, April 25, **1995**.

(7) Anodic Coatings for Aluminum and Aluminum Alloys, Military Specification: MIL-A-8625F, September 10, **1993**.

(8) Diggle J. W.; Downie T. C.; Goulding C. W. Anodic Oxide Films On Aluminum. *Chem. Rev.* **1969,** *69*, 365-405.

(9) Ebihara K.; Takahasi H.; Nagoyama M. Structure And Density Of Anodic Oxyde Films Formed On Aluminum In Sulfuric Acid Solutions. *J. Met. Finish. Soc. Jpn.* **1982,** *33*, 156-164.

(10) Shimuzu K.; Kobayashi K.; Thompson G. E.; Wood G. C. Development Of Porous Anodic Films On Aluminium *Phil. Mag. A.* **1992,** *66*, 643-652.

(11) Curioni M.; Saenz de Miera M.; Skeldon P.; Thompson G. E.; Ferguson J. Macroscopic and Local Filming Behavior Of AA2024-T3 Aluminum Alloy During Anodizing In Sulfuric Acid Electrolyte. *J Electrochem. Soc.*, **2008**, *155*, C387-C395.

(12) Arenas M. A.; Conde A.; De Damborenea J. J. Effect Of Acid Traces On Hydrothermal Sealing Of Anodising Layers On 2024 Aluminium Alloy. *Electrochim. Acta*., **2010,** *55*, 8704 – 8708.

(13) Curioni M.; Skeldon P.; Koroleva E.; Thompson G. E.; Ferguson J. Role Of Tartaric Acid On The Anodizing And Corrosion Behavior Of AA2024-T3 Aluminum Alloy. *J. Electrochem. Soc.*, **2009,** *156*, C147 – C153.

(14) Hao L.; Cheng B. R. Comparative Study Of The Effects Of Sealing Processes On The Wear Resistance And The Sealing Quality Of Hard Anodic Coatings. *Met. Finish.*, **2000**, *98*, 48-55.

(15) Matzdorf C. A.; Beck E.; Hilgeman A.; Prado R. Trivalent Chromium Process (TCP) as a Sealer for MIL-A-8625F Type II, IIB and IC Anodic Coatings, Naval Air Warfare Center Aircraft Division, August, 29, **2008**.

(16) Thompson G. E.; Zhang L.; Smith C. J. E.; Skeldon P. Boric/Sulfuric Acid Anodizing Of Aluminum Alloys 2024 And 7075: Film Growth And Corrosian Resistance. *Corrosion*, **1999**, *55*, 1052-1061.

(17) Carangelo A.; Curioni M.; Acquesta A.; Monetta T.; Belluci F. Application Of EIS To In Situ Characterization Of Hydrothermal Sealing Of Anodized Aluminum Alloys: Comparison Between Hexavalent Chromium-Based Sealing, Hot Water Sealing And Cerium-Based Sealing. *J. Electrochem. Soc.*, **2016**, *163*, C619-C626.

(18) Wei H.; Chen D.; Hu H.; Chang M; Ye X.; Wang M. Insights Into Energy-Efficient And Eco-Friendly Sealing Of Anodic Aluminum Oxide Film Holes With Alkaline Earth Metal Salts. *RSC Advances*, **2017,** *7*, 55653-55667.

(19) Cohen S. M. Review: Replacements for Chromium Pretreatments on Aluminum. *Corrosion.*, **1995,** *51*, 71 – 78.

(20) Dito A.; Tegiacchi F. Cold Sealing Of Anodized Aluminium With Nickel Salt Solutions. *Plat. Surf. Finish.*, **1985**, 72, 72 – 78.

(21) Mansfeld F.; Chen C.; Breslin C. B.; Dull D. Sealing of Anodized Aluminum Alloys with Rare Earth Metal Salt Solutions. *J. Electrochem.* Soc., **1998,** *45*, 2792 – 2798.

(22) Yu X.; Chunan C. Electrochemical Study Of The Corrosion Behavior Of Ce Sealing Of Anodized 2024 Aluminum Alloy. *Thin Solid Films.*, **2003**, *423*, 252 – 256.

(23) Shulman G. P.; Garson P.; Bauman A. J. *Met. Finish.*, **1995**, *95*, 16.

(24) Tiley J. S. 7th Annual Aerospace Hazardous Materials Management Conf., *Session A*, **1992,** 2727.

(25) Shruthi T. K.; Swain G. M. Communication—Role of Trivalent Chromium on the Anti-Corrosion Properties of a TCP Conversion Coating on Aluminum Alloy 2024-T3. *J. Electrochem. Soc.*, **2018**, *165*, C103 – C105.

(26) Munson C. A.; McFall-Boegeman S. A.; Swain G. M. Cross Comparison Of TCP Conversion Coating Performance On Aluminum Alloys During Neutral Salt-Spray And Thin-Layer Mist Accelerated Degradation Testing. *Electrochim. Acta,* **2018,** *282*, 171 – 184.

(27) Qi J.; Hashimoto T.; Walton J.; Zhou X.; Skeldon P.; Thompson G. E. Formation of a Trivalent Chromium Conversion Coating on AA2024-T351 Alloy. *J. Electrochem. Soc.*, **2016,** *163*, C25 – C35.

(28) Guo Y.; Frankel G. S. Active Corrosion Inhibition of AA2024-T3 by Trivalent Chrome Process Treatment. *Corrosion*, **2012,** *68*, 045002-1 – 045002-10.

(29) Li L.; Swain G. P.; Howell A.; Woodbury D.; Swain G. M. The Formation, Structure, Electrochemical Properties and Stability of Trivalent Chrome Process (TCP) Coatings on AA2024. *J. Electrochem. Soc.*, **2011,** *158*, C274 – C283.

(30) Chahboun N.; Rocca E.; Veys-Renaux D.; Augros M.; Boutoba M.; Caldiera N. Sealing of Anodized Multiphase Aluminum Alloys with Cr(+III)/Zr(+IV) Salts: Characterization and Corrosion Behavior. *J. Electrochem. Soc.* **2016,** *163*, C69 – C75.

(31) Department of Defense website: Corrosion Prevention and Control (CPC) Overview **2019**.

(32) Habazaki H.; Shimizu K.; Skeldon P.; Thompson G. E.; Woo G. C.; Zhou X. Nanoscale Enrichments Of Substrate Elements In The Growth Of Thin Oxide Films. *Corrosion Sci*., **1997,** *39*, 731 – 737.

(33) Kim Y. C.; Quint B.; Kessler R. W.; Oelkrug D. Structural Properties Of Electrochemically Designed Porous Oxide Films On AlMg1. *J. Electroanal. Chem*., **1999,** *468*, 121 – 126.

(34) Sulka G. D.; Stroobants S.; Moshchalkov V.; Borghs G.; Celis J. P. Synthesis of Well-Ordered Nanopores by Anodizing Aluminum Foils in Sulfuric Acid. *J. Electrochem. Soc.*, **2002,** *149*, D97 – D103.

(35) Lee W.; Schwirn K.; Steinhart M.; Pippel E.; Scholz R.; Gosele U. Structural Engineering Of Nanoporous Anodic Aluminium Oxide By Pulse Anodization Of Aluminium. *Nat. Nanotechnol.*, **2008,** *3*, 234 – 239.

(36) Choi D.; Lee P.; Hwang W.; Lee K.; Park H. Measurement Of The Pore Sizes For Anodic Aluminum Oxide (AAO). *Curr. Appl. Phys.*, **2006,** *6*, e125 – e129.

(37) Zaraska L.; Sulka G. D.; Jaskula M. Anodic Alumina Membranes With Defined Pore Diameters And Thicknesses Obtained By Adjusting The Anodizing Duration And Pore Opening/Widening Time. *J. Solid-State Electrochem.*, **2011,** *15*, 2427 – 2436.

(38) Fratila-Apachitei L. E.; Duszczyk J.; Katgerman L. Voltage Transients And Morphology Of AlSi(Cu) Anodic Oxide Layers Formed In H_2SO_4 At Low Temperature. *Surf. Coat. Tech.*, **2002,** *157*, 80 – 94.

(39) Fares C.; Hemmouche L.; Belouchrani M. A.; Amrouche A.; Chicot D.; Puchi-Cabrera E. Coupled Effects Of Substrate Microstructure And Sulphuric Acid Anodizing On Fatigue Life Of A 2017A Aluminum Alloy. S. *Mater. Design*, **2015,** 86, 723 – 734.

(40) Guo Y.; Frankel G. S. Characterization Of Trivalent Chromium Process Coating On AA2024-T3. *Surf. Coat. Technol.,* **2012,** *206,* 3895 – 3902.

(41) Walton J.; Shruthi T. K.; Yancey D.; Vlasak P.; Westre S.; Swain G. M. Evaluation of a Trivalent Chromium Process (TCP) Conversion Coating on AA2024-T3 That Requires No Surface Pretreatment. *J. Electrochem. Soc.,* **2019,** *166,* C589 – C599.

(42) Kobayashi T.; Sasaki T.; Takagi I.; Moriyama H. Solubility of Zirconium (IV) Hydrous Oxides. *J. Nucl. Sci. Technol.,* **2007,** *44,* 90 – 94.

(43) Munson C. A.; Swain G. M. Structure And Chemical Composition Of Different Variants Of A Commercial Trivalent Chromium Process (TCP) Coating On Aluminum Alloy 7075-T6. *Surf. Coat. Technol.,* **2017,** *315,* 150 – 162.

(44) Shruthi T. K.; Swain G. M. Detection of H_2O_2 from the Reduction of Dissolved Oxygen on TCP-Coated AA2024-T3: Impact on the Transient Formation of Cr(VI). *J. Electrochem Soc.,* **2019,** *166,* C3284 – C3289.

(45) Carangelo A.; Curioni M.; Acquesta A.; Monetta T.; Belluccia F. Application Of EIS To In Situ Characterization Of Hydrothermal Sealing Of Anodized Aluminum Alloys: Comparison Between Hexavalent Chromium-Based Sealing, Hot Water Sealing And Cerium-Based Sealing. *J. Electrochem. Soc.,* **2016,** *163,* C619 – C626.

(46) Visser P.; Gonzalez-Garcia Y.; Mol J. M. C.; Terry H. Mechanism of Passive Layer Formation on AA2024-T3 from Alkaline Lithium Carbonate Solutions in the Presence of Sodium Chloride. *J. Electrochem Soc.,* **2018,** 165, C60 – C70.

(47) Visser P.; Liu Y.; Zhou X.; Hashimoto T.; Thompson G. E.; Lyon S. B.; Van der Ven L. G. J.; Mola A. J. M. C.; Terrynad H. A. The Corrosion Protection Of AA2024-T3 Aluminium Alloy By Leaching Of Lithium-Containing Salts From Organic Coatings. *Faraday Discuss.,* **2015,** *180,* 511 – 526.

(48) Schem M.; Schmidt T.; Gerwann J.; Wittmar M.; Veith M.; Thompson G.E.; Molchan I.S.; Hashimoto T.; Skeldon P.; Phani A.R.; Santucci S.; Zheludkevich M. L. CeO_2-Filled Sol–Gel Coatings For Corrosion Protection Of AA2024-T3 Aluminium Alloy. *Corrosion Sci.,* **2009,** *51,* 2304 – 2315.

(49) Chahboun N.; Rocca E.; Veys-Renaux D.; Augros M.; Boutoba M.; Caldeira N. Sealing of Anodized Multiphase Aluminum Alloys with Cr(+III)/Zr(+IV) Salts: Characterization and Corrosion Behavior. *J. Electrochem. Soc.,* **2016,** *163,* C69 – C75.

(50) Liu D.; Wei G.; He P. The Effect Of Sealing And Trivalent Chromium Passivating On Anodized Aluminum. *Int. J. Electrochem. Sci.,* **2016,** 11, 2097.

(51) Boisier G.; Pébère N.; Druez C.; Villatte M.; Suel S. FESEM and EIS Study of Sealed AA2024 T3 Anodized in Sulfuric Acid Electrolytes: Influence of Tartaric Acid*J. Electrochem. Soc.,* **2008,** *155,* C521.

(52) Hirschorn B.; Orazem M. E.; Tribollet B.; Vivier V.; Frateur I.; Musiani M. Determination Of Effective Capacitance And Film Thickness From Constant-Phase-Element Parameters *Electrochim. Acta,* **2010,** *55,* 6218 – 6227.

CHAPTER 8. COMPARISON BETWEEN TRIVALENT CHROME PROCESS (TCP) COATING AND INDUSTRIAL SEALANTS FOR AN ANODIC OXIDE FORMED ON AA2024-T3.

8.1 INTRODUCTION

2xxx series aluminum alloys are widely used in the aerospace sector due to their light weight and high strength. The addition of Cu, a primary alloying element in these alloys, forms several microscopic galvanic cells within the alloy matrix which increases overall corrosion susceptibility.[1-4] Anodization is a surface modification technique widely used to improve corrosion resistance of aerospace aluminum alloys. [5-15]

Anodic "oxide" coatings are insulating layers used to passivate aluminum and aluminum alloys. Anodizing is an electrochemical process that converts the metal surface into a durable and corrosion-resistant, anodic oxide finish. Chromic acid anodizing is a well-known process to enhance the corrosion resistance of aerospace aluminum alloys. However, the increased scrutiny around using toxic Cr(VI) has encouraged attempts to find suitable non-toxic alternatives. [16-18] Anodizing in dilute sulfuric acid, sulfuric + boric acid, sulfuric + tartaric acid electrolytes are considered effective alternatives to chromic acid anodizing.[11,13,15] Type II dilute sulfuric acid anodization is currently the most popular industrial choice for anodizing 2xxx aluminum alloys. The oxide formed is biphasic, comprising of a dense barrier layer at the substrate/oxide interface which extends outwards into a columnar porous structure perpendicular to the substrate.[9-12] These anodic coatings are highly porous and tend to absorb chemicals from the surrounding environment which cause structural damages to the oxide. Thus, sealing treatments are employed to prevent oxide damage and improve corrosion protection.[19-23] Hydrothermal sealing in hot water,

dichromate and nickel acetate solutions are among the most commonly used sealing methods.[19-23] However, these processes are energy intensive, time consuming or have a significant environment cost. Several sealing alternatives are being developed to meet demands for high corrosion performance. [24]

Our group has proposed the use of a non-toxic Trivalent chromium conversion coating as a sealing method.[25] Sealing aluminum oxide grown on AA2024-T3 with TCP is a quick, room-temperature, non-toxic process making it an attractive candidate for replacing traditional hydrothermal sealing processes. The TCP conversion coating is a hexafluorozirconate bath with added Cr(III) salts. When anodized AA2024-T3 is immersed in a TCP bath, the fluoride in the coating attacks the oxide and promotes cathodic oxygen and proton reduction reactions at the alloy surface. This leads to an increase in interfacial pH that starts at the substrate surface and extends through the porous oxide structure. This leads to precipitation of coating constituents at the surface of the oxide resulting in the formation of an ~300 nm thick TCP sealing layer. The seal is mostly confined to the outer oxide layer and only partially penetrates the oxide.[25] The TCP seal formed over anodized AA2024-T3 shows superior corrosion protection. So far, no reports have been published comparing the electrochemical and corrosion performance of TCP sealed anodized AA2024-T3 against other industrially used hydrothermal sealing methods.

The key research questions addressed in this work are (i) how do different TCP coatings seal the anodic coating and how deep into the oxide does the sealant penetrate, (ii) to what degree does a TCP sealant increase corrosion resistance of an oxide coating, in comparison with other traditional sealants and (iii) how does any corrosion resistance enhancement predicted by electrochemical measurements compare with what is observed during accelerated degradation testing for all the sealed specimens?

8.2 MATERIALS AND METHODS

Reagents.

All chemicals used were analytical grade quality or better. Sodium sulfate (Na_2SO_4), sulfuric acid (95 – 98 wt. %), potassium dichromate, nickel (II) acetate tetrahydrate, boric acid, sodium carbonate, calcium chloride and sodium chloride were all purchased from Sigma-Aldrich (St. Louis, MO). Cobalt acetate was purchased from Spectrum Chemical Manufacturing Corp. (Gardena, CA). Nitric acid (68 – 70 wt. %) was purchased from Fisher Scientific (Hampton, New Hampshire). All chemicals were reagent grade quality, or better, and used without additional purification. The Cleaner 1000 and one of the commercial TCP baths used as a sealant, TCP-1 (TCP-HF), were provided by Chemeon Surface Technology (Minden, Nevada). TCP-2 (Aluminescent) was obtained from Luster-On (Springfield, MA) and TCP-3 (Bonderite T5900 RTU) was obtained from Henkel Corp. (Madison Heights, MI). All solutions were prepared using ultrapure water (Barnstead E-Pure) with a resistivity >17MΩ-cm.

Specimen Preparation.

Specimens were prepared and anodized exactly as described in Chapter 2.

Sealing Methods.

Anodized AA2024-T3 was sealed using the following solutions:

(i) Hot water: 30 min immersion in ultrapure water at 90°C.

(ii) Nickel acetate: 15 min immersion in 5 g/L nickel acetate + 1 g/L cobalt acetate + 8 g/L boric acid solution at 85°C.

(iii) Potassium dichromate: 15 min immersion in 5% (w/v) potassium dichromate solution at 90°C.

(iv) TCP-1: The TCP bath was prepared by mixing 0.5% (v/v) and 5% (v/v) of parts A and B, respectively, of the two-component system. A 5-min immersion in the TCP bath (pH: 3.85) at room temperature was used for sealing.

(v) TCP-2 and TCP-3: The TCP bath was prepared by diluting the as received coating solution to 30% (v/v). A 10-min immersion in the TCP bath (pH: 3.85) at room temperature was used for sealing.

The sealed specimens were aged overnight at laboratory conditions before testing. The sealing conditions used were optimized for each sealant.

Electrochemical Characterization.

All electrochemical measurements were performed in a 1cm^2 flat cell in naturally-aerated 0.5 M Na_2SO_4 + 0.01 M NaCl at room temperature (23 ± 2 ^oC). The test protocols followed are summarized in Chapter 2. Separate specimens were used for the anodic and cathodic polarization measurements.

Accelerated Degradation Tests.

Neutral Salt-Spray Test (NSS) – ASTM B117, Thin layer mist test (TLM) and 5-day full immersion test were conducted to evaluate the corrosion inhibition performance of the different sealants. Test protocols are summarized in Chapter 2.

8.3 CHARACTERIZATION

Scanning electron microscopy was performed using a JEOL 7500 scanning electron microscope (JEOL Ltd, Tokyo, Japan). Spectra were recorded using a 15 keV accelerating voltage. A digital optical microscope (Keyence VHX 600) was used to obtain 3-dimensional topographical information of surfaces like pit densities and surface roughness surface, before and after the different accelerated degradation tests. The depth resolution was determined to be *ca.* 0.2 µm.

8.4 RESULTS

Morphological Characterization of the Sealed Oxide Coatings.

Figure 8.1 shows plan view scanning electron micrographs of anodized AA2024-T3 hydrothermally sealed with hot water, nickel acetate and dichromate. An unsealed oxide grown on AA2024-T3 by Type II anodization has an open porous structure with pore diameters ranging between 10 – 50 nm. [9,10, 26] Hydrothermal sealing processes significantly modify the structure of the anodized layer. The surface morphology of hot water sealed specimens in the figure below shows a typical flaky oxide structure with pores filled with hydrated alumina. [22-24] This sealing process does not form a distinct protective film over the oxide leaving visible open pores. NiAc sealed oxide shows complete blockage of oxide pores from the simultaneous precipitation of $Ni(OH)_2$ and hydrated alumina. The dichromate sealed oxide layer appears to have little resemblance to the original porous oxide structure. A barrier layer blocking the underlying porous structure is seen. However, this layer is discontinuous, containing several micropores. This is typical for chromate sealed AA2024-T3. [19,27]

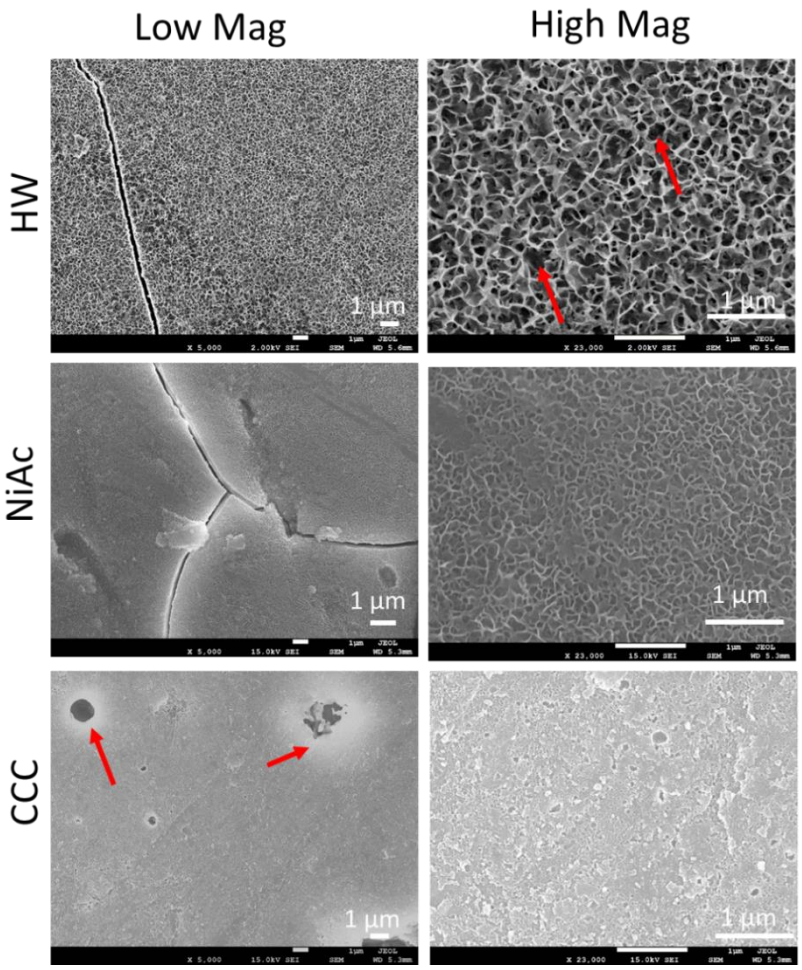

Figure 8.1 Low (left) and high (right) magnification scanning electron micrographs (secondary electron images) of anodized AA2024-T3 sealed with hot water, nickel acetate and dichromate coatings. Arrows are used to highlight open pores in the hot water seal and micropores in dichromate sealed anodized specimens.

Figure 8.2 shows the scanning electron micrographs of anodized AA2024-T3 sealed with the three TCP coatings. The surfaces of the three TCP-sealed oxides are similar with a dense coating occluding pores of the underlying oxide. The surfaces also show presence of excess inhibitor precipitates which usually are Zr and Cr-O. Cracks seen on the coating surface are a result of dehydration caused by high vacuum in the SEM.[25]

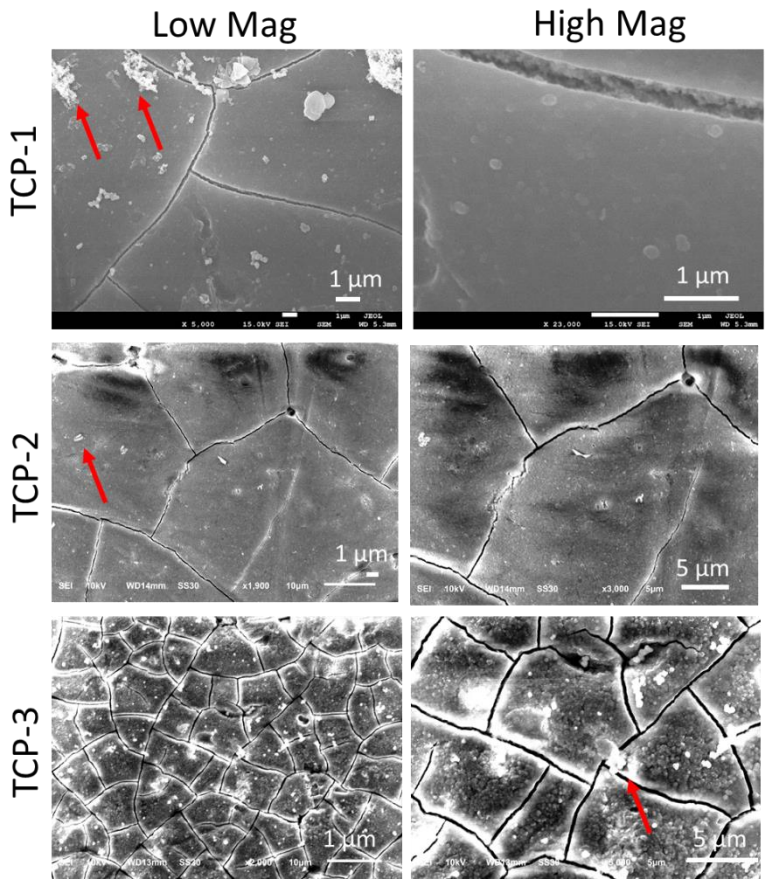

Figure 8.2 Low (left) and high (right) magnification scanning electron micrographs (secondary electron images) of anodized AA2024-T3 sealed with three different TCP conversion coatings. Arrows indicate coating precipitates.

Electrochemical characterization.

Figure 8.3 shows the anodic and cathodic potentiodynamic polarization curves for unsealed and sealed anodized AA2024-T3 specimens. All measurements were made in naturally aerated 0.5 M Na_2SO_4 + 0.01 M NaCl at room temperature. A scan rate of 1 mV/s was used. Figures 8.3A and B reveal stable passivity for all anodized specimens, sealed and unsealed, with low anodic currents and no distinct pit initiation. No sudden current increases were seen indicating absence of pit formation throughout the potential window measured. Sealing the oxide shifts the OCP more positive indicating a higher level of surface passivation as compared to unsealed oxide. Shift in

OCP is most positive (~ 150 mV) for nickel acetate and TCP-2 sealed specimens. Anodic current suppression for sealed specimens ranges from 5 – 1000x as compared to the unsealed specimen, depending on the sealant type. Nickel acetate sealed specimens show better sealing results with greatest level of anodic current suppression, 10x lower than other sealing methods. Dichromate sealed AA2024-T3 shows initial pitting at ~ 0.0 V but the surface immediately re-passivates at ~ 100 mV, likely due to active corrosion inhibition by chromate ions trapped in the oxide pores. TCP sealed AA2024-T3 specimens show current suppression comparable to Nickel acetate seal and a greater suppression as compared to hot water and dichromate seals.

Figures 8.3C and D reveal cathodic current suppression for anodized and sealed specimens. Again, nickel acetate and TCP-2 sealed specimens show greatest current suppression. Sealing blocks oxide pores and prevents oxygen and electrolyte from reaching the alloy surface thus inhibiting cathodic reactions. The performance of the different TCP coatings varies slightly because of the variations in coating formulation from suppliers. Nevertheless, nickel acetate and TCP sealed specimens show better electrochemical performance with greater surface passivation and current suppression as compared to unsealed, hot water and dichromate sealed anodized AA2024-T3. The passivation stability for the anodized specimens decreased in the order:

TCP-2 > nickel acetate > TCP-1 ≈ TCP-3 > dichromate > hot water > unsealed AA2024-T3.

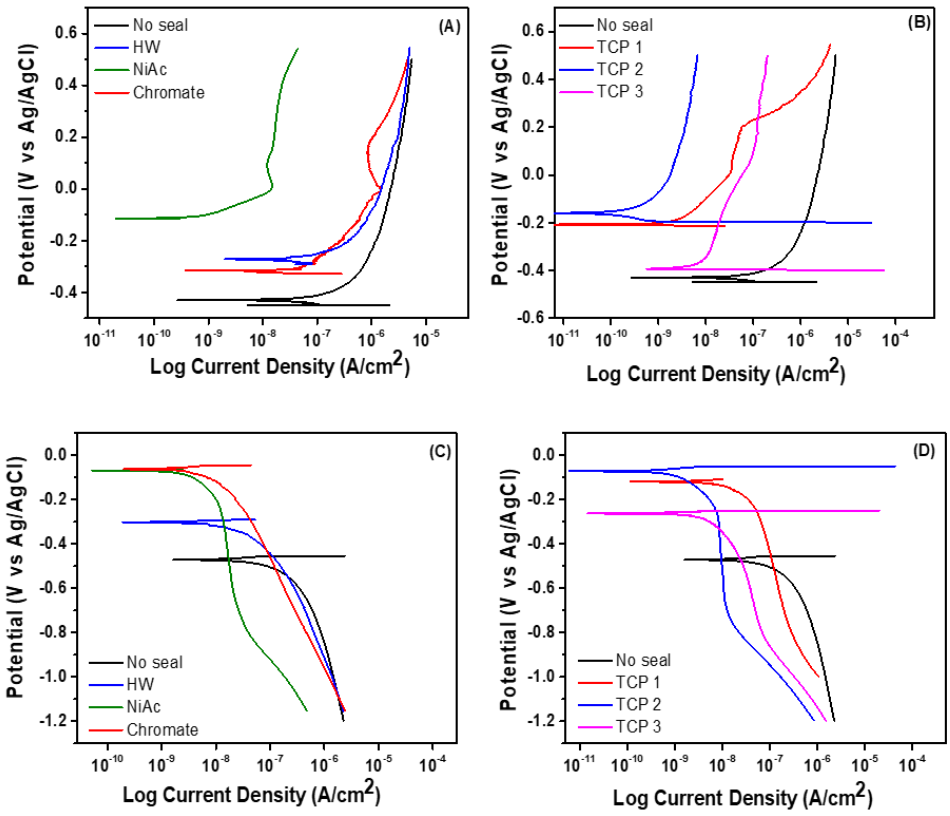

Figure 8.3 Potentiodynamic anodic polarisation curve data for (A) hot water, nickel acetate, dichromate and (B) TCP-1, TCP-2 and TCP-3 sealed anodized AA2024-T3. Potentiodynamic cathodic polarisation curve data for (C) hot water, nickel acetate, chromate and (D) TCP-1, TCP-2 and TCP-3 sealed AA2024-T3. Data for unsealed specimen are shown for comparison.

Figure 8.4 shows Bode plots (log frequency vs. log impedance plot) of unsealed and sealed oxide layers grown on AA2024-T3. High frequency impedance, representing electrolyte resistance, is similar for all specimens. The low frequency impedance represents electron transfer resistance for redox reactions occurring at the alloy/oxide interface at OCP. Higher Z at 0.01Hz indicates greater resistance to electrochemical reactions on the substrate surface which directly translates to a measure of corrosion protection capability of the sealant (REF). On comparing Figures 8.4 A and B, it is evident that nickel acetate and TCP sealing treatments provide slightly higher low-frequency impedance than dichromate and hot water seals. In fact, the latter two sealing

methods have an impedance modulus comparable to an unsealed anodized AA2024-T3. This observation is in agreement with the sealed oxide morphologies observed in Figure 8.1 where an incomplete blocking of oxide pores by dichromate and hot water is seen. Open pores acts as pathways for oxygen and electrolyte penetration through the oxide to the underlying metal. The low frequency impedance for the different sealing methods decreases in the order:

TCP-2 ≈ TCP-3 ≈ nickel acetate > TCP-1 > dichromate ≈ hot water ≈ unsealed AA2024-T3.

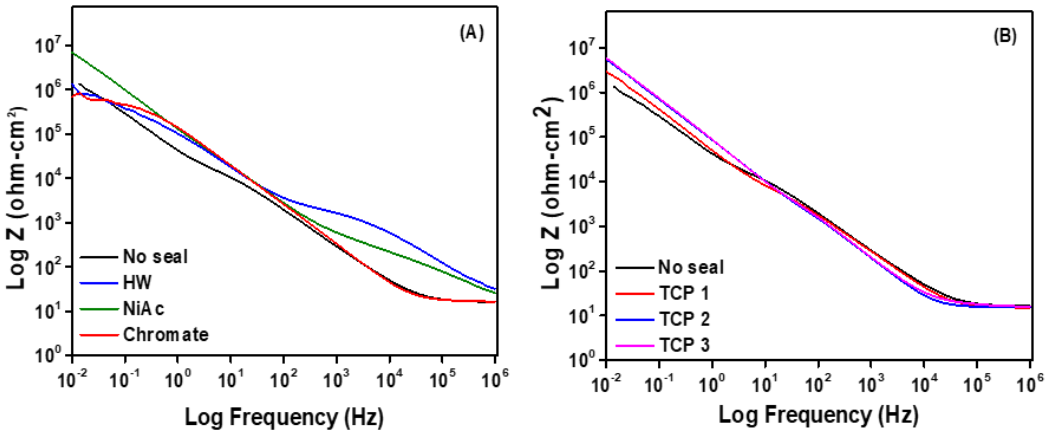

Figure 8.4 Low frequency impedance spectra, $Z_{0.01\ Hz}$ for (A) unsealed, hot water, nickel acetate, dichromate and (B) TCP-1, TCP-2, TCP-3 sealed anodized AA2024-T3 in naturally aerated 0.5 M Na_2SO_4 + 0.01 M NaCl at room temperature.

Figure 8.5 shows the summary of measured electrochemical parameters for sealed anodized AA2024-T3. Data for unsealed AA2024-T3 is shown for comparison. All values are reported as mean ± std. deviation (n = 3). Figure 8.5A suggests that the OCP is statistically more positive for nickel acetate and TCP sealed anodized AA2024-T3 as compared to the unsealed anodized AA2024-T3. Remember, a shift in OCP to positive potentials indicates surface passivation. The OCP, shifts to more negative potentials for hot water and dichromate sealed anodized AA2024-T3. Figure 8.5B shows an increase in low frequency impedance for all sealing methods, except dichromate. The highest improvement in low frequency impedance (5 – 7x) is seen for TCP sealed

anodized AA2024-T3. Similarly, TCP sealed specimens show 5 – 10x suppression in anodic and cathodic currents, the greatest as compared to other sealing methods. Nickel acetate sealed specimens also show current suppression comparable to TCP sealed specimens while, dichromate and hot water sealed AA2024-T3 show no statistical difference from the unsealed specimen. On comparing the electrochemical performance of anodized AA2024-T3 sealed with different sealing treatments, the order of decreasing corrosion performance is as follows:

TCP-2 ≈ TCP-3 ≈ nickel acetate > TCP-1 > dichromate ≈ hot water ≈ unsealed AA2024-T3. The three TCP sealants perform either comparably or better than the currently used industrial sealing methods.

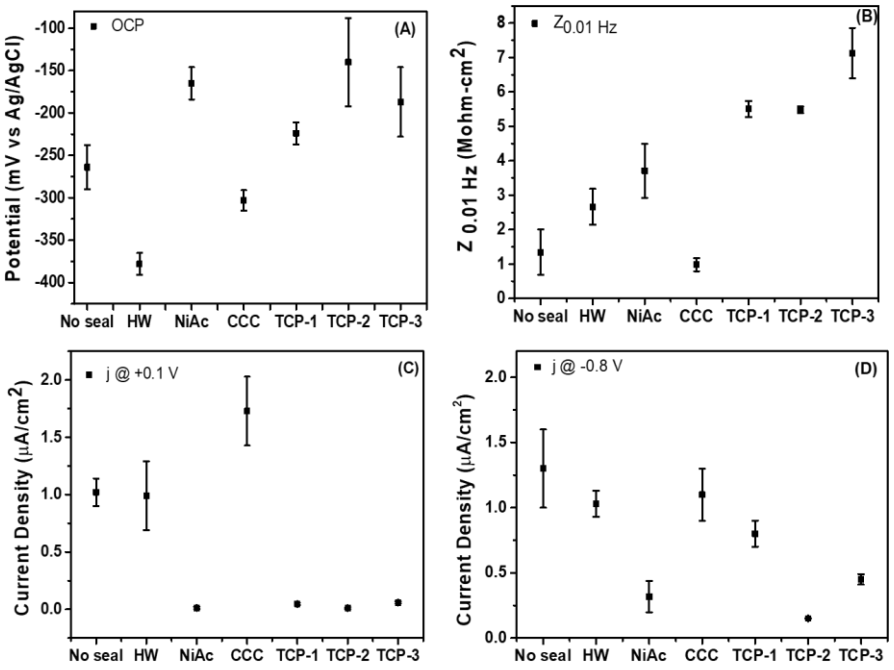

Figure 8.5 Comparison of electrochemical parameters measured in naturally-aerated 0.5M Na_2SO_4 + 0.01 M NaCl for anodized AA2024-T3 sealed with hot water, nickel acetate, dichromate and three TCP coatings. The following data are presented: (A) Open circuit potential (OCP), (B) $Z_{0.01}$ Hz. (C) anodic current density at +0.1V and (D) cathodic current density at -0.8V.

To correlate trends observed from the electrochemical measurements with corrosion resistance properties, a 5-day full immersion test was conducted. EIS was measured before and after the test

to assess the robustness of the sealing layer and its capability in preventing electrolyte penetration through the oxide. Physical transformations occuring at the sealant/oxide interface are reflected by phase shift and changes in low frequency impedance values. A robust sealant would ideally show no difference in initial and final impedance values. A drop in low frequency impedance during the test period indicates sealant breakdown. Figure 8.6 and 9.7 show EIS data recorded for anodized AA2024-T3 sealed with different sealants before and after a 5-day immersion test in 3.5 wt. % NaCl. Data for unsealed specimen is shown for comparison. Two time constants are observed for most specimens. Higher frequency time constant represents the porous layer and lower frequency time constant represents the barrier layer.[25] A third time constant, seen only in few sealed specimens, represents the sealing layer. Figure 8.6A shows a 10x decrease in low frequency impedance for the unsealed specimen indicating electrolyte penetration through the oxide layer during the test. Loss of a high frequency time constant and displacement of low frequency time constant to higher frequencies suggests decrease in barrier properties.

$Z_{0.01\ Hz}$ and phase angle remain unchanged for hot water and nickel acetate sealed anodized AA2024-T3. This indicates superior barrier protection provided by the two sealing treatments. The initial low frequency impedance modulus for dichromate sealed anodized AA2024-T3 is lower than the other sealing techniques, however, the sample still exhibits superior corrosion protection. Infact, a ~10x increase in $Z_{0.01\ Hz}$ was observed during the 5-day test period. Similar observations have also been reported previously and such behavior is attributed to the active corrosion protection offered by chromate anions trapped in the oxide pores.[22,27] This observation is consistent with the anodic polarization curve reporte earlier in Figure 8.3A for dichormate seal anodized

AA2024-T3 where the specimen surface shows signs of surface repassivation at positive potentials likely due to active corrosion protection by chromate ions.

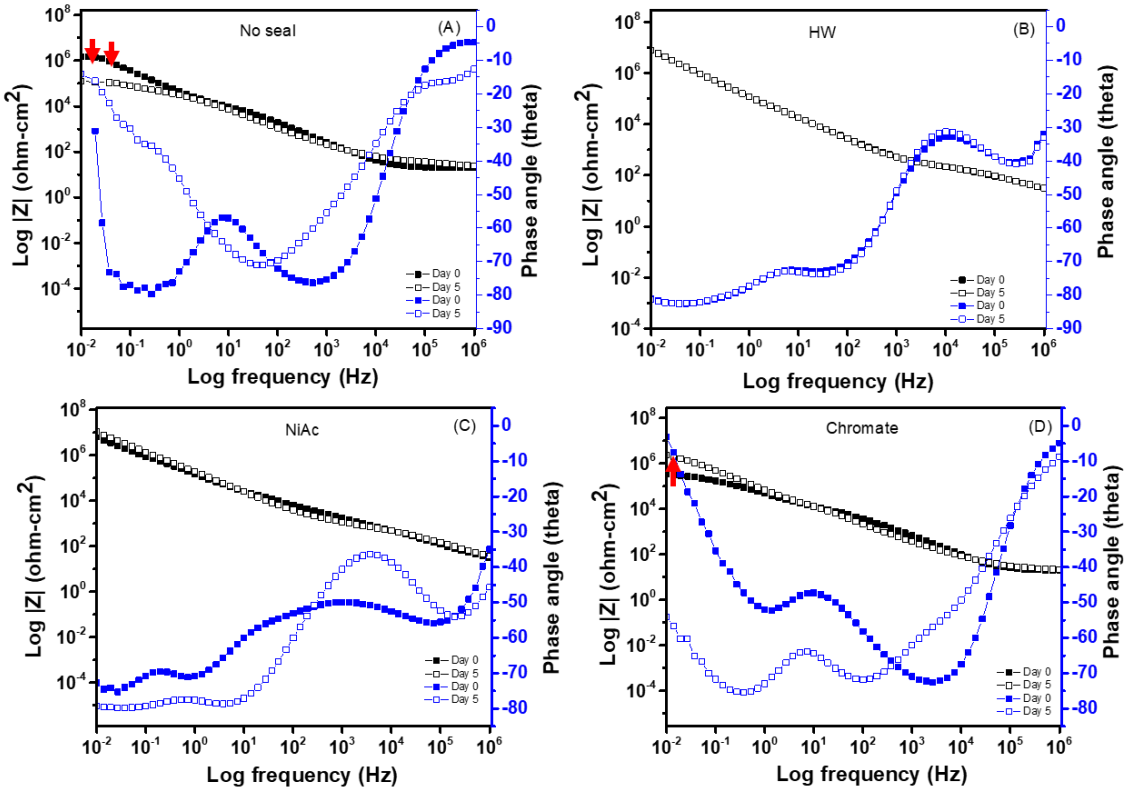

Figure 8.6 EIS data showing impedance and phase angle vs. frequency plots for the sealed and unsealed anodized AA2024-T3 specimens before (Day 0) and after (Day 5) the 5-day full immersion test for (A) Unsealed, (B) Hot water, (C) Nickel acetate, and (D) Chromate sealed anodized AA2024-T3 in 3.5% NaCl.

All three TCP sealing layers show a high initial low frequncy impedance, $Z_{0.01\ Hz}$ at the start of the test (~ 10^7 Ω.cm^2). The impedance remains unchanged during the 5-day period. TCP-3 shows a 5x drop in $Z_{0.01\ Hz}$ after the test indicating a slightly lower corrosion protection provided by this particular TCP. TCP-1 and TCP-2 perform at par with other sealants representing a robust sealing layer capable of preventing electrolyte from entering the porous oxide.

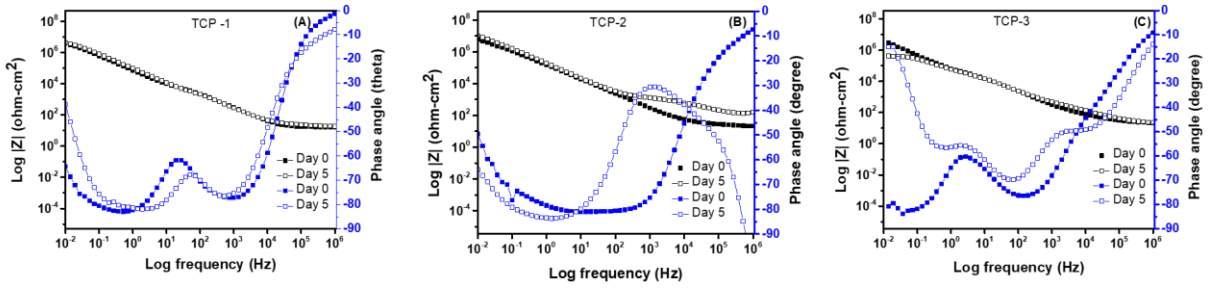

Figure 8.7 EIS data showing impedance and phase angle vs. frequency plots for (A) TCP-1, (B) TCP-2 and (C) TCP-3 sealed anodized AA2024-T3 specimens before (Day 0) and after (Day 5) the 5-day full immersion test in 3.5% NaCl.

Accelerated degradation test.

To further compare the corrosion inhibition performance of TCP sealed anodized AA2024-T3 with other sealing methods, two accelerated degradation tests, namely a 14-day neutral salt spray test (ASTM B117) and a 14-day thin layer mist (TLM) test were conducted. Digital micrographs of specimens before and after the degradation tests are shown in Figure 8.8 and 9.9. No surface pits or corrosion damage were observed on any of the sealed specimens in both tests. Isolated pits were observed on the unsealed specimens during both tests. Sealing anodic oxides with dichromate imparts a green-yellow coloration to the sample due to incorporation of chromate ions in the micropores.

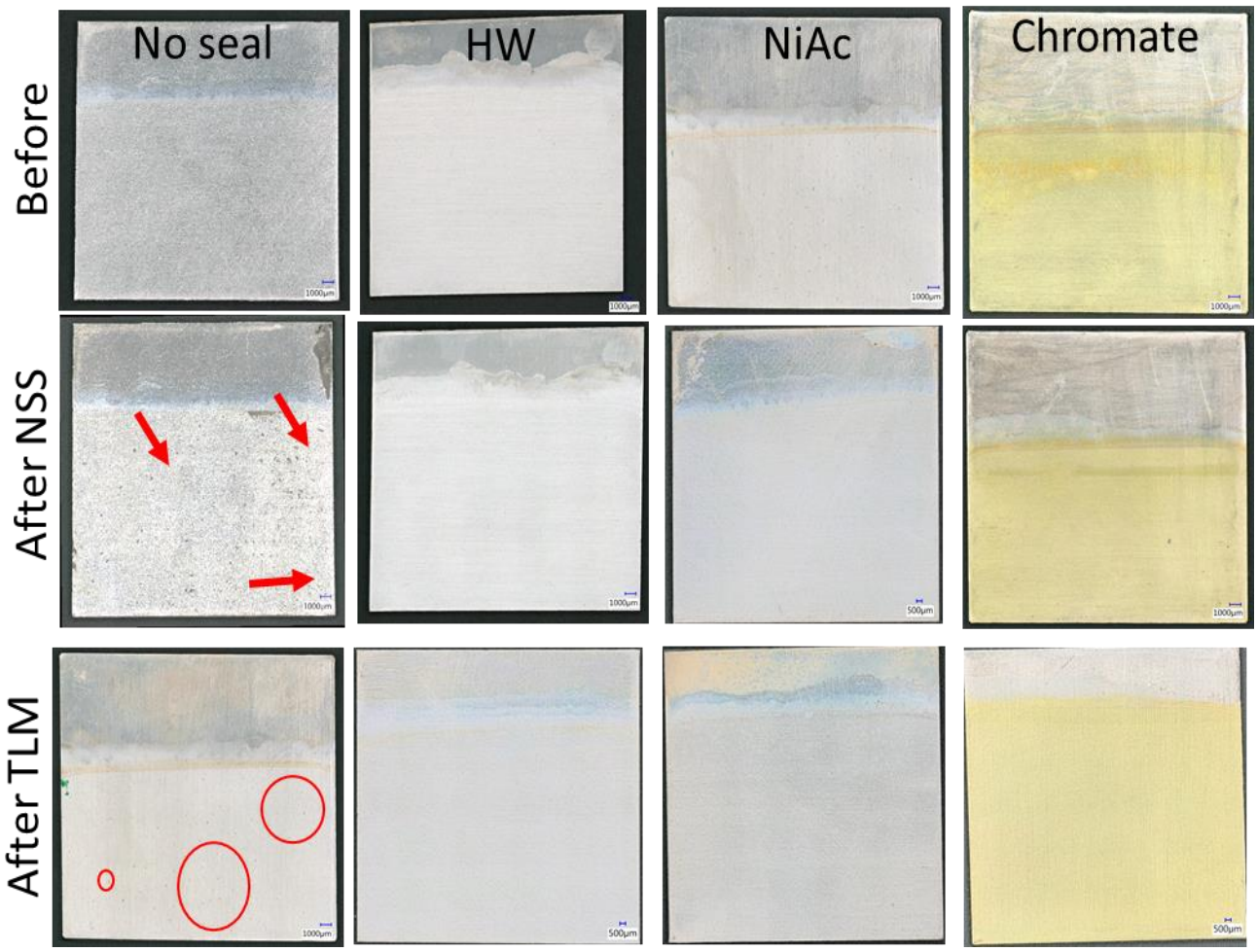

Figure 8.8 Stitched digital micrographs of unsealed and sealed anodized AA2024-T3 before (top) and after 14-day NSS (middle) and 14-day TLM test (bottom). Arrows and circled regions indicate areas of corrosion damage on the unsealed specimen. No damage was observed on sealed anodized AA2024-T3.

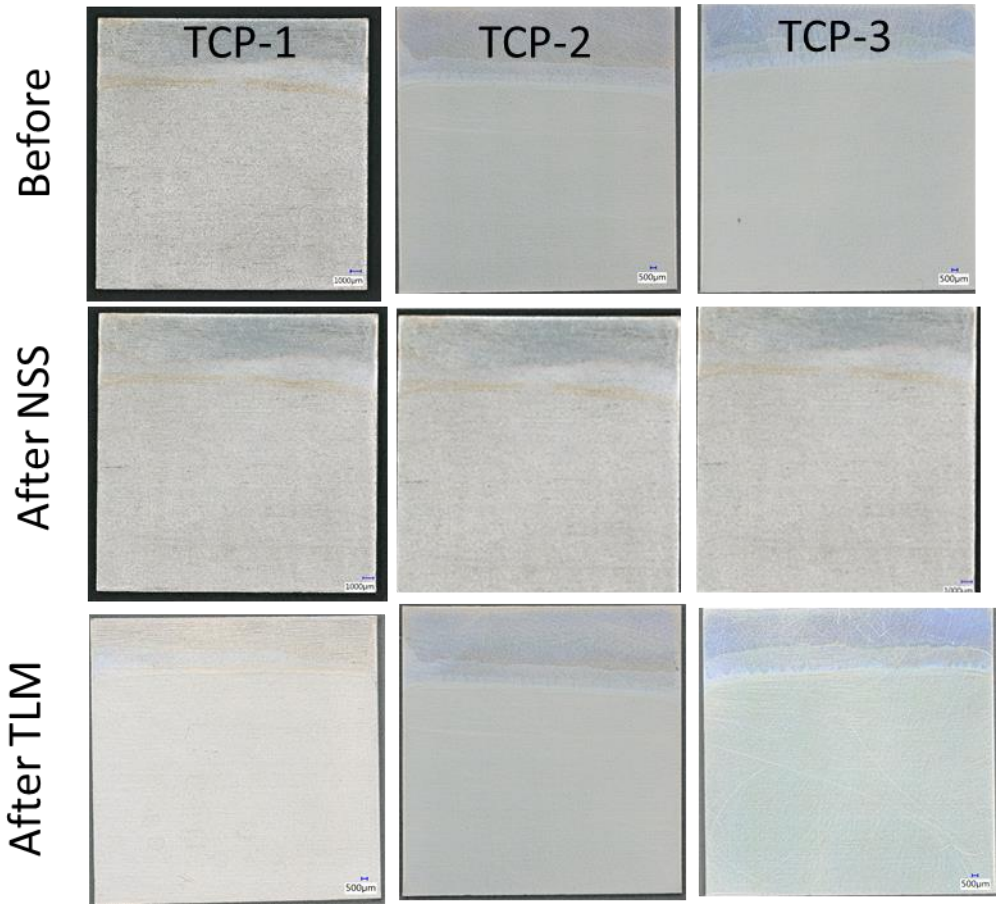

Figure 8.9 Stitched digital micrographs of anodized AA2024-T3 sealed with TCP-1, TCP-2 and TCP-3 before (top) and after 14-day NSS (middle) and 14-day TLM test (bottom). No corrosion damage was observed on any specimens.

Tables 8.1 and 8.2 summarize data for surface roughness, pit densities and mass loss for specimens subjected to 14-day NSS and TLM tests respectively. Mass loss was maximum for the unsealed specimens in both tests. Specimens were soaked in DI water for 30 min after each test to dissolve salt deposits from the test. Initial surface roughness for specimens arise from oxide pores and coating precipitates/ cracks in the sealing layer. A small increase in surface roughness is seen for all specimens, some of which could be from residual salt residing on specimen surfaces. Pitting was observed only in the unsealed anodized specimen with a pit density of 4 pits/ cm^2 and 2

pits/cm^2 for specimens subjected to 14-day NSS and TLM tests respectively. As expected, the greatest mass loss was seen for the unsealed anodized specimen in both tests. Mass loss for sealed anodized AA2024-T3 are statistically similar for all sealed anodized AA2024-T3 specimens.

Table 8.1 Summary of changes in topographical of unsealed and sealed anodized AA2024-T3 before and after 14-day B117 test.

14-day NSS	Pit density Number/cm^2	Rms roughness		Mass loss mg/in^2
		Day 0	Day 14	
No seal	4	0.44 ± 0.02	0.69 ± 0.04	3.3 ± 0.3
HW	0	0.41 ± 0.03	0.44 ± 0.01	1.1 ± 0.03
NiAc	0	0.48 ± 0.04	0.84 ± 0.09	1.7 ± 0.4
Chromate	0	0.62 ± 0.03	0.97 ± 0.13	1.1 ± 1.04
TCP-1	0	0.44 ± 0.02	0.45 ± 0.17	0.6 ± 0.3
TCP-2	0	0.40 ± 0.02	0.44 ± 0.02	1.3 ± 0.4
TCP-3	0	0.43 ± 0.04	0.48 ± 0.01	1.5 ± 0.4

Table 8.2 Summary of changes in topography of unsealed and sealed anodized AA2024-T3 before and after 14-day TLM test.

14-day TLM	Pit density Number/cm^2	Rms roughness		Mass loss mg/in^2
		Day 0	Day 14	
No seal	2	0.44 ± 0.02	0.89 ± 0.19	4.15 ± 0.31
HW	0	0.41 ± 0.03	0.45 ± 0.02	1.45 ± 0.18
NiAc	0	0.48 ± 0.04	0.46 ± 0.01	1.70 ± 0.30
Chromate	0	0.62 ± 0.03	0.44 ± 0.01	1.85 ± 0.29
TCP-1	0	0.44 ± 0.02	0.47 ± 0.05	1.16 ± 0.19
TCP-2	0	0.40 ± 0.02	0.44 ± 0.01	1.19 ± 0.37
TCP-3	0	0.43 ± 0.04	0.47 ± 0.07	1.15 0.02

8.5 DISCUSSION

Porous aluminum oxide electrochemically grown in sulfuric acid has a high specific area of ~100 m^2/g and tends to absorb moisture and aggressive substances from the environment which decreases the corrosion inhibition properties of the anodic coating. Consequently, the micropores are sealed with coatings to increase corrosion resistance. The aerospace industry recognizes hot water, nickel acetate and dichromate sealing as the best sealing methods to protect 2xxx series aluminum alloys. [22,27] This work highlights differences in sealing mechanisms in traditional sealing processes and the TCP sealing process and proposes room temperature TCP sealing as a potential replacement to the existing energy intensive sealing treatments.

All sealing methods involve partial pore wall dissolution coupled with precipitation of sealing products within the oxide pores. High temperature hot water sealing (95°C) produces chemically stable, insoluble boehmite within oxide pores effectively filling most pores and substantially increases corrosion resistance of the oxide layer. No physical barrier layer is formed over the outer surface of the oxide. The fundamental reaction involved during the sealing process is:

$$Al_2O_3 + H_2O \rightarrow 2AlO(OH)\ (bohemite) \qquad (14)$$

Nickel acetate sealing is predominantly used in North America to seal anodized aluminum due to its superior sealing performance. During high temperature (85°C) sealing of anodized aluminum in nickel acetate solution, nickel hydroxide precipitates simultaneously with boehmite. The superior performance of this sealing treatment is attributed to the catalytic role of $Ni(OH)_2$ in converting Al_2O_3 to AlO(OH) within the oxide pores. The co-precipitation of presence $Ni(OH)_2$ and boehmite increases the sealing efficiency of the micropores as compared to hot water sealing and significantly improves corrosion reisstance of anodized aluminum. This sealing treatment,

similar to hot water sealing, only fill micropores an does not form a distinct protective barrier layer over the outer surface of the oxide. Reactions occurring during hydrothermal sealing of anodized AA2024-T3 during nickel acetate sealing are:

$$Al_2O_3 + H_2O \rightarrow 2AlO(OH)\ (boehmite) \tag{14}$$

$$Ni^{2+} + 2OH^- \rightarrow Ni(OH)_2 \tag{19}$$

Dichromate sealing is usually performed at temperatures close to boiling point (95°C). Within the pores, aluminum oxide is converted to aluminum oxydichromate ($AlOHCrO_4$) or aluminum oxychromate ($(AlO)_2CrO_4$). In addition to blocking oxide pores through precipitation of Al-Cr complexes, large reservoirs of Cr(VI) species are trapped within the pores and later released to nearby corroding sites. It has been reported that unlike other sealing methods, the dichromate sealing causes substantial dissolution of the porous oxide skeleton and causes thinning of the barrier layer. This is evident from data in Figure 8.3 showing inferior electrochemical performance of dichromate sealed AA2024-T3. However, dichromate sealed anodized AA2024-T3 does show excellent corrosion protection in full immersion and accelerated degradation tests. The enhanced corrosion protection mainly is due to active corrosion protection provided by the active chromate ions loosely adsorbed to the pore walls. Such claims have been previously reported by other researchers as well. Reactions involved during dichromate sealing of anodized aluminum are:

$$Al_2O_3 + 2HCrO_4^- + H_2O \rightarrow 2AlOHCrO_4 + 2OH^- \tag{20}$$

$$Al_2O_3 + HCrO_4^- \rightarrow (AlO)_2CrO_4 + OH^- \tag{21}$$

Several researchers have been focused on developing ambient temperature sealing treatments to reduce energy and operation costs, and to eliminate residual drying marks from hydrothermal sealing processes. Nickel fluoride was one such commercially successful sealing method. However, similar to Cr(VI), use of nickel salts are under scrutiny due to high toxicity and its ability to cause dermatitis. Thus, the authors of this article propose the use of TCP as a viable candidate for sealing anodized aerospace aluminum alloys.

TCP sealing presents favourable features such as short sealing time (2-5 min), ambient sealing temperature, low energy and operation costs and less smut formation. TCP sealed anodized AA2024-T3 specimens show superior electrochemical performance and excellent corrosion resistance behavior as compared to other sealing techniques. There has been one report in the past showing evidence for trivalent chromium sealed AA2024 and AA7075 withstanding 2000-hr salt spray tests. Boehmite is formed within the oxide only at temperatures above 85°C. During Low temperature sealing, hydrargillite ($Al(OH)_3$) is likely to be precipitated. Fluoride in the coating bath has a strong affinity towards aluminum and promotes oxide dissolution. This induces a pH increase and promotes precipitation of aluminum hydroxide, aluminum fluoride within the oxide pores. The pH gradient grows outwards causing precipitation of zirconium and chromium oxides over the outer oxide surface forming a sealing layer. Evidence for fluoride trapped within the pores has been reported by our group previously. Zr and Cr oxides are however confined to the outer surface and do not penetrate deep within the oxide. Possible reactions during TCP sealing are:

$$Al_2O_3 + 6F^+ + 3H_2O \rightarrow 2AlF_3 + 6OH^- \quad (22)$$

$$Al_2O_3 + 3H_2O \rightarrow 2Al(OH)_3 \quad (23)$$

$$ZrF_6^{2-} + 4OH^- \rightarrow ZrO_2.2H_2O + 6F^- \quad (9)$$

$$Cr^{3+} + 3OH^- + 3e^- \rightarrow Cr(OH)_3 + 5OH^- \quad (10)$$

The enhanced corrosion behavior could be due to the sealing mechanism of TCP where synergistic reactions leading to coprecipitation of AlF_3 and $Al(OH)_3$ within the pores and the formation of a ~300 nm thick sealing layer over the oxide surface. Therefore, in a TCP sealing process, there is a physical barrier protecting the oxide in addition to precipitates blocking the oxide pores.

8.6 CONCLUSIONS

In this study, three TCP conversion coating baths were used to seal aluminum oxide grown on AA2024-T3. Electrochemical and corrosion performance of TCP sealed anodized AA2024-T3 specimens were compared against industrially accepted nickel acetate, dichromate and hot water sealing methods. Electrochemical polarisation and impedance data revealed greater level of anodic and cathodic current suppression for all three TCP seals. Electrochemical performance of TCP sealed anodized AA2024-T3 is comparable to nickel acetate sealed specimens and better than hot water and chromate sealed specimens. Accelerated degradation tests showed that all the sealants exhibited comparable corrosion protection to anodized AA2024-T3. The results confirm that sealing anodized AA2024-T3 with TCP provides a substantial environmental advantage due to non-toxic coating bath formulation of TCP conversion coatings. TCP sealing process is also a less energy intensive, time efficient (5 min sealing time) room temperature method as compared to the other high temperature sealings processes studied in this work that require 15-30 min sealing times.

ACKNOWLEDGEMENTS

The author would like to thank Mr. Jack Walton and Ms. Sarah McFall-Boegeman for their contributions in obtaining optical and scanning electron micrographs presented in this work.

REFERENCES

REFERENCES

(1) Davis, J. Alloying: Understanding the Basics-Light Metals and Alloys. *Mater. Sci. Technol.* **2001**, 192–203.

(2) Polmear, I. J. Light Alloys. *Light Alloy.* **2005**.

(3) Kaufman, J. G.; International, A. S. M. Introduction to Aluminum and Aluminum Alloys. *Met. Handb. Desk Ed.* **2000**, 417–423.

(4) Paul, T. Corrosion of Aluminum and Aluminum Alloys. *Choice Rev. Online* **2000**, *37* (05), 1–24.

(5) Zalnezhad, E.; Sarhan, A. A. D.; Hamdi, M. Investigating The Effects Of Hard Anodizing Parameters On Surface Hardness of Hard Anodized Aerospace Al 7075-T6 Alloy using Fuzzy Logic Approach For Fretting Fatigue Application. *Int. J. Adv. Manuf. Technol.* **2013**, 68, 453–464.

(6) Runge, J. M. Metallurgy Basics for Aluminum Surfaces. *The Metallurgy of Anodizing Aluminum.* **2018,** 191-248.

(7) Macdonald, D. D. On the Formation of Voids in Anodic Oxide Films on Aluminum. *J. Electrochem. Soc.* **1993**, *140* (3), L27 – 30.

(8) Cohen S. M.; Spadafora S. J. A Comparison of Thin Film Sulfuric Acid Anodizing and Chromic Acid Anodizing Process, Report #NAWCADWAR-95023-43, April 25, **1995**.

(9) Anodic Coatings for Aluminum and Aluminum Alloys, Military Specification: MIL-A-8625F, September 10, **1993.**

(10) Diggle J. W.; Downie T. C.; Goulding C. W. Anodic Oxide Films On Aluminum. *Chem. Rev.* **1969,** 69, 365-405.

(11) Ebihara K.; Takahasi H.; Nagoyama M. Structure and Density Of Anodic Oxide Films Formed On Aluminium In Sulfuric Acid Solutions. *J. Met. Finish. Soc. Jpn.* **1982,** 33, 156-164.

(12) Shimuzu K.; Kobayashi K.; Thompson G. E.; Wood G. C. Development Of Porous Anodic Films On Aluminium *Phil. Mag. A.* **1992,** 66, 643-652.

(13) Curioni M.; Saenz de Miera M.; Skeldon P.; Thompson G. E.; Ferguson J. Macroscopic and Local Filming Behavior Of AA2024-T3 Aluminum Alloy During Anodizing In Sulfuric Acid Electrolyte. *J Electrochem. Soc.*, **2008**, 155, C387-C395.

(14) Arenas M. A.; Conde A.; De Damborenea J. J. Effect Of Acid Traces On Hydrothermal Sealing Of Anodising Layers On 2024 Aluminium Alloy. *Electrochim. Acta*., **2010,** 55, 8704 – 8708.

(15) Curioni M.; Skeldon P.; Koroleva E.; Thompson G. E.; Ferguson J. Role Of Tartaric Acid On The Anodizing And Corrosion Behavior Of AA2024 T3 Aluminum Alloy. *J. Electrochem. Soc.*, **2009,** 156, C147 – C153.

(16) Garcia-Vergara, S. J.; Skeldon, P.; Thompson, G. E.; Habazaki, H. A Tracer Investigation Of Chromic Acid Anodizing Of Aluminium. *Surf. Interface Anal*. **2007**, 39, 860-864.

(17) Critchlow, G. W.; Yendall, K. A.; Bahrani, D.; Quinn, A.; Andrews, F. Strategies For The Replacement Of Chromic Acid Anodising For The Structural Bonding Of Aluminium Alloys. *Int. J. Adhes. Adhes*. **2006**, *26* (6) 419-453.

(18) Twite, R. L.; Bierwagen, G. P. Review Of Alternatives To Chromate For Corrosion Protection Of Aluminum Aerospace Alloys. *Prog. Org. Coat*. **1998**, *33* (2), 91-100.

(19) Hao L.; Cheng B. R. Comparative Study Of The Effects Of Sealing Processes On The Wear Resistance And The Sealing Quality Of Hard Anodic Coatings. *Met. Finish*., **2000**, 98, 48-55.

(20) Matzdorf C. A.; Beck E.; Hilgeman A.; Prado R. Trivalent Chromium Process (TCP) as a Sealer for MIL-A-8625F Type II, IIB and IC Anodic Coatings, Naval Air Warfare Center Aircraft Division, August, 29, 2008.

(21) Thompson G. E.; Zhang L.; Smith C. J. E.; Skeldon P. Boric/Sulfuric Acid Anodizing Of Aluminum Alloys 2024 And 7075: Film Growth And Corrosian Resistance. *Corrosion*, **1999**, 55, 1052-1061.

(22) Carangelo A.; Curioni M.; Acquesta A.; Monetta T.; Belluci F. Application Of EIS To In Situ Characterization Of Hydrothermal Sealing Of Anodized Aluminum Alloys: Comparison Between Hexavalent Chromium-Based Sealing, Hot Water Sealing And Cerium-Based Sealing. *J. Electrochem. Soc.*, **2016**, 163, C619-C626.

(23) Wei H.; Chen D.; Hu H.; Chang M; Ye X.; Wang M. Insights into Energy-Efficient And Eco-Friendly Sealing Of Anodic Aluminum Oxide Film Holes With Alkaline Earth Metal Salts. *RSC Advances*, **2017, 7**, 55653-55667.

(24) Ofoegbu, S. U.; Fernandes, F. A. O.; Pereira, A. B. The Sealing Step in Aluminum Anodizing: A Focus on Sustainable Strategies for Enhancing Both Energy Efficiency and Corrosion Resistance. *Coatings*, **2020**, *10*, 226.

(25) Shruthi, T. K.; Walton, J.; McFall-Boegeman, S.; Westre, Sjon.; Swain, G. M. Investigation of the Trivalent Chromium Process Conversion Coating as a Sealant for Anodized AA2024-T3. *J. Electrochem. Soc*. **2020**, *167*, 111504.

(26) Hakimizad, A.; Raeissi, K.; Ashrafizadeh, F. Characterization Of Aluminum Anodized Layers Modified In Sulfuric And Phosphoric Acid Baths And Their Effect On Conventional Electrolytic Coloring. *Surf. Coat. Technol*. **2012**, *206*, 8-9, 2438-2445.

(27) Zuo, Y.; Zhao, P.; Zhao, J., The Influences Of Sealing Methods On Corrosion Behavior Of Anodized Aluminum Alloys In Nacl Solutions. *Surf. Coat. Technol*. **2003**, *166*, 2-3, 237-242.

CHAPTER 9. CONCLUSIONS AND FUTURE WORK

9.1 CONCLUSIONS

Trivalent Chrome Process conversion coatings are the leading replacement to Cr(VI) in the aerospace industry. This dissertation focuses on understanding how alloy microstructure, surface preparation techniques and coating chemistry affect TCP performance formed on AA2024-T3.

Deoxidation of the alloy surface is an important parameter that affects surface roughness, pit depths and densities. Increased deoxidiser exposure can lead to surface roughening and promote pit formation on the alloy. The extent of surface damage, however, is dependent on the type of deoxidiser and varies with the concentration of fluoride ions in the deoxidiser. Excessively deoxidised surfaces do not form a uniform coating and are prone to corrosion attack than a conformally coated surface. The deoxidation pre-treatment step is an important pre-treatment process as it removes unnecessary smut and natural oxide layer required to form a conformal TCP coating. Therefore, the process cannot be eliminated entirely but needs to be controlled to minimize surface roughening and pitting.

Cr(III) present in the TCP conversion coating is key to inhibiting the cathodic half reaction *i.e.* oxygen reduction reaction occurring at the alloy surface. TCP protects AA2024-T3 by the following two mechanisms:

(i) Acts as a non-conducting physical barrier between the alloy and the environment and delaying early pitting of the surface.

(ii) $Cr(OH)_3$ precipitates formed on IMPs block oxygen chemisorption sites preventing oxygen reduction reactions.

Aging TCP coating formed over AA2024-T3 in the presence of oxygen increases corrosion resistance due to the active corrosion protection provided by transiently formed Cr(VI) within the coating. Oxygen reduction reactions occurring on IMPs produce a strong oxidiser, H_2O_2, capable of oxidizing Cr(III) to Cr(VI). Transiently formed Cr(VI) is known to migrate to nearby corroding sites and reduce to form passivating Cr(III) hydroxide and protect the alloy from corrosion propagation. Concentration of transiently formed Cr(VI) is within permissible limits to prevent carcinogenicity.

TCP was investigated as an environmentally friendly alternative to passivating porous oxide formed on anodized AA2024-T3. It was found that sealing the oxide layer with TCP enhances corrosion protection of the oxide by suppressing anodic currents (2-10x) and cathodic currents (3-5x). The TCP forms a layer on the outer surface of the oxide, blocking pores and increasing barrier properties of the oxide. Specimens examined after 14-day B117 test revealed no discoloration, visible pitting or other corrosion damage on TCP-sealed specimens post anodization. Full immersion testing in 3.5% NaCl for 5 days also revealed excellent corrosion protection to the anodized alloy sealed with TCP. In contrast, oxide degradation was observed for the unsealed specimen during both tests.

The effectiveness of TCP sealed AA2024-T3 was compared against industrially accepted sealing methods (nickel acetate, dichromate and hot water sealing methods) through electrochemical and accelerated degradation test methods. Electrochemical data revealed that TCP sealed AA2024-T3 performed as good as or better than the industrial sealants. Accelerated degradation tests showed comparable corrosion protection for all sealants formed over anodized AA2024-T3. Sealing anodized AA2024-T3 with TCP provides a substantial environmental advantage due to non-toxic coating bath formulation of TCP conversion coatings. The TCP sealing

process less energy intensive, time efficient (5 min sealing time) room temperature method compared to the other high temperature hydrothermal sealing processes currently employed in the industry.

9.2 FUTURE WORK

In the recent years, a lot of insight has been generated around formation and corrosion protection mechanisms of TCP formed over aluminum alloys. Research published by our group has shown that TCP is an effective conversion coating as well as oxide sealant. Future work should focus on gaining an in-depth understanding of corrosion protection mechanisms of the TCP seal formed over anodized AA2024-T3. Additional data in the form of high-resolution cross-sectional SEM and TEM images is needed to locate the TCP seal over an oxide and understand its structure. Research also needs to be conducted to understand changes in coating chemistry occurring during accelerated degradation tests and also evaluate robustness of a TCP seal in the presence of a primer over-layer.